Investigation of Exciton Linewidth and Lineshapes in Transition Metal Dichalocogenide van der Waals Heterostructures by Electron Microscopy and Spectroscopies

Fuhui Shao

université PARIS-SACLAY

University of Chinese Academy of Sciences

Investigation of Exciton Linewidth and Lineshapes in Transition Metal Dichalcogenide van der Waals Heterostructures by Electron Microscopy and Spectroscopies

Étude de la largeur de ligne et de la forme des lignes d'exciton dans les hétérostructures de van der Waals de dichalcogénure de métal de transition par microscopie et spectroscopie électroniques

Thèse de doctorat de l'université Paris-Saclay et Institute of Semiconductors, Chinese Academy of Sciences

École doctorale n°572: Ondes et matière (EDOM)
Spécialité de doctorat: Physique
Graduate School: Physique. Référent: Faculté des sciences d'Orsay

Thèse préparée dans les unités de recherche **Laboratoire de Physique des Solides** (Université Paris-Saclay, CNRS) et **Key Laboratory of Semiconductor Materials Science** (Institute of Semiconductors, Chinese Academy of Sciences), sous la direction de **Luiz GALVAO TIZEI**, Chargé de recherche, la co-direction de **Haiqiao NI**, Directeur de recherche, et le co-encadrement de **Mathieu KOCIAK**, Directeur de recherche.

Thèse soutenue à Paris-Saclay, le 15 Décembre 2022, par

Fuhui SHAO

Composition du jury

Membres du jury avec voix délibérative

Zhijie WANG Professeur, Institute of Semiconductors, Chinese Academy of Sciences	Président
Demie KEPAPTSOGLOU Directrice de recherche, SuperSTEM Laboratory, University of York	Rapporteure & Examinatrice
Raul ARENAL Directeur de recherche, Instituto de Nanociencia y Materiales de Aragon	Rapporteur & Examinateur
Pascale LAUNOIS Directrice de recherche, Laboratoire de Physique des Solides (UMR 8502), Université Paris-Saclay	Examinatrice
Toon COENEN Directeur Sciences des matériaux, Delmic B.V.	Examinateur

THESE DE DOCTORAT
NNT : 2022UPASP163

université PARIS-SACLAY

ÉCOLE DOCTORALE
Ondes et matière (EDOM)

Titre: Étude de la largeur et de la forme des lignes d'exciton dans les hétérostructures de van der Waals des dichalcogénures de métaux de transition par microscopie et spectroscopie électroniques

Mots clés: hétérostructures de van der Waals, excitons TMD, élargissement inhomogène de la largeur de raie, forme de raie d'absorption de type fano, spectroscopie et microscopie électroniques, diffraction électronique

Résumé: La spectroscopie de perte d'énergie des électrons (EELS) et la cathodoluminescence (CL) dans un microscope électronique à transmission à balayage (STEM) sont des méthodes extrêmement puissantes pour étudier la physique des excitons des dichalcogénures de métaux de transition (TMD). Dans cette thèse, nous avons étudié la largeur de ligne et la forme des lignes de l'exciton des TMDs sous différentes configurations d'hétérostructures de van der Waals (vdWH). Dans la partie de cette thèse, nous avons démêlé les facteurs d'élargissement inhomogènes de la largeur de ligne de l'exciton en utilisant des EELS combinés à faible perte et à perte centrale, la cartographie de la déformation et les séries d'inclinaison de diffraction à faisceau large. Les TMD encapsulées dans du nitrure de bore hexagonal (hBN) offrent la meilleure qualité de matériau optique, montrant la largeur de ligne excitonique la plus nette, car ce vdWH élimine les variations diélectriques, les désordres de charge, les dommages dus à l'irradiation et les ondulations. Dans la partie suivante, nous avons modifié la forme des lignes d'absorption des excitons par le graphite/graphène. Comme le semiconducteur-métal combine des états d'énergie discrets et continus, le couplage électromagnétique entre les TMD et le graphite a montré une forme de ligne asymétrique de type Fano dans les EELS et l'absorption optique. Ensuite, l'étude STEM-CL de la TMD/graphène encapsulée dans le hBN montre un spectre d'émission qui ne contient qu'une seule ligne amortie, mais nette, provenant de l'exciton neutre.

Title: Investigation of Exciton Linewidth and Lineshapes in Transition Metal Dichalcogenides van der Waals Heterostructures by Electron Microscopy and Spectroscopies

Keywords: van der Waals heterostructures, TMD excitons, homogeneous linewidth broadening, fano-like absorption lineshape, electron spectroscopy and microscopy, electron diffraction

Abstract: Electron energy loss spectroscopy (EELS), and cathodoluminescence (CL) in a scanning transmission electron microscopy (STEM) are extremely powerful methods for investigating the exciton physics of transition metal dichalcogenides (TMDs). In this thesis, we investigated the TMD exciton linewidth and lineshape under various van der Waals heterostructure (vdWH) configurations. In the part of this thesis, we have disentangled the exciton linewidth inhomogeneous broadening factors by using combined low-loss and core-loss EELS, strain mapping and wide-beam diffraction tilt series. TMDs encapsulated inside hexagonal boron nitride (hBN) provide the best optical material quality showing the sharpest excitonic linewidth, as this vdWH eliminates dielectric variations, charge disorders, irradiation damage and corrugations. In the next part, we have modified the exciton absorption lineshape by graphite/graphene. Because the semiconductor-metal combines discrete and continuous energy states, electromagnetic coupling between the TMDs and graphite have shown Fano-like asymmetric lineshape in EELS and optical absorption. Afterwards, STEM-CL investigation of TMD/graphene encapsulated inside hBN shows an emission spectrum which contains only a single damped, but sharp line from the neutral exciton.

Acknowledgements

First and foremost, I am sincerely grateful to my esteemed supervisors Dr. Luiz Galvao Tizei and Dr. Haiqiao NI for their invaluable advice, continuous support, and patience during my PhD study. Their immense knowledge and plentiful experience have encouraged me in all the time of my academic research and daily life. I would also like to thank Dr. Mathieu Kociak for his mentorship, who had raised many precious guidance and help during our discussion. Additionally, I would like to express gratitude to Dr. Steffi Y. Woo for her treasured support which was really influential in shaping my experiment methods and critiquing my results. The doors to them were always open whenever I ran into a trouble spot or had a question about my research. This work would not have been possible without them.

In particular, the technical assistance for electron microscope provided by Alexandre Gloter, Marcel Tencé, XiaoYan Li, Jean-Denis Blazit, and other members of the team was valuable and appreciated. Without their upgrading, developing and repairing the microscope, the experiment could not have been successfully conducted. Furthermore, I wish to thanks Ashish Arora, Robert Schneider, Javier García de Abajo, Andrea Konečná and Nianjheng Wu for our cooperation over the last few months and ongoing.

My sincere thanks also goes to Prof. Zhijie Wang, Dr. Demie Kepaptsoglou, Dr. Raul Arenal, Dr. Pascle Launois and Dr. Toon Coenen, for their insightful comments and encouragement, but also for the questions which prompted me to widen my research from various perspectives. I would like to take this opportunity to express gratitude to Prof. Eric Charron, Prof. Zhijie Wang and Prof. Odile Stéphan for their support and kindness in the administration of both organizations. Taking this opportunity, I would like to express my sincere gratitude to thank my colleagues for their assistance in day-to-day lab activities, their sympathy, congeniality, and their wit. In the STEM group I experienced a very friendly and welcoming atmosphere, which is very valuable for me.

Last but not the least, I also appreciate all the support I received from my family and friends for providing me with unfailing support and continuous encouragement throughout my study over the past years. I also place on record, my sense of gratitude to one and all, who directly or indirectly, have lent their hand all along.

Fuhui
25, Dec. 2022

Contents

List of Figures

List of Tables

Chapter 1

Synthèse en français

Les dichalcogénures de métaux de transition (TMD) font partie de la famille des matériaux bidimensionnels (2D). Leurs monocouches présentent une bande interdite directe dans la gamme des longueurs d'onde visibles, ce qui permet une émission de lumière efficace. En raison du faible écrantage diélectrique de l'environnement local, la réponse optique des TMD est déterminée par les résonances d'exciton, qui correspondent à des paires électron-trou liées par des forces de Coulomb. Plus important encore, l'intégration de TMD avec d'autres matériaux bidimensionnels aux propriétés spécifiques sous la forme d'hétérostructures de van der Waals (vdWH) a mis en évidence des interactions lumière-matière uniques, qui peuvent être adaptées pour obtenir de nouvelles fonctionnalités. Il est donc nécessaire de contrôler les propriétés optiques des vdWH atomiquement minces pour diverses applications futures en optoélectronique.

Cependant, les propriétés des matériaux 2D, et en particulier ses monocouches, sont fortement affectées par l'environnement local dans lequel il se trouve, car les monocouches ont une surface spécifique élevée qui les rend très sensibles à son environnement, comme le désordre externe et l'environnement diélectrique. Des expériences préliminaires ont montré que le désordre contient des facteurs tels que la déformation, la rugosité, les absorbants, les impuretés, les charges piégées, l'oxydation. En plus de la propreté de l'interface et de l'environnement diélectrique homogène, l'encapsulation des monocouches dans d'autres couches de matériaux 2D garantit leur planéité à l'échelle de dizaines de picomètres. Outre ces effets "positifs" et la reduction de la désordre diélectrique, le couplage en champ proche entre couches joue également un rôle important dans les performances de ces structures en couches minces. Donc, les propriétés optiques du matériau peuvent être modérées par le couplage au substrat. Récemment, ces questions ont été abordées par des chercheurs dans de nombreux domaines, notamment l'évolution mobilité-température, le comportement de supraconductivité et la photoluminescence (PL) de monocouches 2D sous différentes configurations.

Une quantité considérable d'ouvrages a été publiée sur l'étude des propriétés optiques des matériaux 2D. Cela a conduit à des progrès rapides dans l'étude de nombreux nouveaux dispositifs optiques quantiques basés sur les vdWH, tels que les émetteurs de photons uniques, les dispositifs émetteurs de lumière flexibles, les biocapteurs, les cellules solaires, etc. Les

techniques optiques telles que les spectroscopies d'extinction/émission optiques sont utilisées depuis longtemps pour étudier les TMDs. Selon le critère de Rayleigh, la longueur d'onde de la source lumineuse détermine la résolution spatiale, de sorte que les techniques qui utilisent la lumière comme source d'excitation peuvent difficilement atteindre une résolution inférieure à quelques centaines de nanomètres. Bien que le microscope optique basé sur la super-résolution puisse surmonter la limitation de la résolution due à la diffraction et réaliser des mesures optiques avec une résolution inférieure à la longueur d'onde. Cependant, ces techniques fournissent des types limités d'informations à l'échelle nanométrique de l'échantillon. En effet, l'hétérogénéité des matériaux et de l'environnement se produit à l'échelle de moins de 100 nm, ce qui justifie la nécessité d'explorer les TMD par microscopie et spectroscopie électroniques.

Technique particulièrement puissante, la microscopie électronique à transmission à balayage (STEM) utilise des électrons libres comme source d'excitation et peut cartographier les variations optiques, structurelles et chimiques des échantillons avec une résolution spatiale à l'échelle nanométrique. Il a été prouvé expérimentalement que la spectroscopie de perte d'énergie des électrons (EELS) et la cathodoluminescence (CL) mesurées dans un STEM sont des contreparties parfaites à l'échelle nanométrique des technologies optiques. Dans cette thèse, diverses méthodes de caractérisation en STEM sont utilisées, y compris l'acquisition d'informations sur la déformation du réseau et la contrainte basée sur la diffraction des électrons, les propriétés optiques basées sur la spectroscopie de perte d'énergie des électrons (EELS) et la cathodoluminescence (CL), la contamination et l'épaisseur de l'échantillon à partir de la perte de cœur, afin d'étudier systématiquement les propriétés optiques et structurelles des TMD monocouches dans différentes configurations de vdWH.

Dans cette thèse, l'effet des hétérostructures sur les propriétés optiques des TMD a été étudié à l'échelle nanométrique. Une variété de troubles associés aux TMD monocouches ont été examinés et leurs effets négatifs sur la largeur de ligne excitonique ont été clarifiés par microscopie électronique et spectroscopies. Il a été démontré que les TMD encapsulées entre deux couches de matériau 2D sont préservées de la meilleure manière possible. Afin d'étudier les propriétés optiques des TMD monocouches, les spectres EELS et CL de diverses TMD monocouches à base de hBN, de graphène et de graphite vdWH sont étudiés, tels que ***hBN/TMDs/hBN***, ***graphite/TMDs/graphite***, ***hBN/TMDs/graphite*** et ***hBN/TMDs/graphite/hBN***.

Les principes expérimentaux pour les matériaux 2D par les techniques STEM sont présentés dans le chapitre 3. Des échantillons de TMD monocouches dans diverses hétérostructures sont préparés par la méthode de transfert à sec par estampage viscoélastique par mes collègues Nianjheng Wu et Steffi Woo, comme présenté dans le chapitre 4. En outre, la physique de la vallée de spin des TMD et la transition de résonance de l'exciton sont présentées dans le chapitre 7. Différents matériaux diélectriques à bande interdite, à savoir le hBN et le nitrure de silicium amorphe (Si_3N_4), le graphite non dopé sous différentes configurations, sont étudiés en tant que matériaux de support ou d'encapsulation pour les monocouches de TMD afin d'étudier l'influence du substrat/diélectrique sur la forme des lignes d'absorption des excitons dans les TMD à l'aide de la spectroscopie de perte d'énergie électronique (EELS) dans un

microscope électronique à transmission à balayage (STEM). Tout d'abord, les rugosités des monocouches sont déterminées à partir d'une série de clichés de diffraction électronique à faisceau large en évaluant l'élargissement des taches de diffraction en comparaison avec les simulations effectuées à l'aide du logiciel QSTEM dans le chapitre 5. Pour mieux comprendre l'élargissement inhomogène dans les TMD monocouches (chapitre 7), des expériences de cartographie chimique, de cartographie de la déformation et de contrôle de la dose par EELS sont menées. Dans le chapitre 8, ***graphite/WS_2/graphite*** sont mesurés à la fois par EELS et par absorption optique, afin d'évaluer leur pertinence dans l'observation de la forme des lignes de Fano. Pour ***hBN/graphène/WSe_2/hBN*** vdWH, les mesures EELS et CL sont conçues pour étudier la neutralisation complète des monocouches de TMD par le graphène, ainsi que le transfert sélectif non radiatif d'espèces excitoniques à longue durée de vie comme le trion vers le graphène. L'absorption optique est réalisée à l'Université de Münster par les collaborateurs Robert Schneider et Ashish Arora. Ces formes de lignes sont interprétées dans le cadre de la résolution de l'équation de Maxwell pour une couche 2D infiniment mince, qui est développée par F. Javier García de Abajo à l'ICREA-Institució Catalana de Recerca i Estudis, et Avançats et Andrea Konečná à l'Université de technologie de Brno. Toutes les expériences STEM/EELS/CL et les analyses associées ont été réalisées au Laboratoire de Physique des Solides à Orsay. Enfin, les principales contributions de ce travail et les travaux futurs seront discutés dans le chapitre 9 et le chapitre 10, respectivement.

Chapter 2

Introduction

Transition metal dichalcogenides (TMDs) are members of the two-dimensional (2D) materials family, and their monolayers have a direct energy bandgap at visible wavelength range, leading to efficient light emission [1]. Due to the weak dielectric screening from the local environment, the optical response of TMDs is determined by **exciton resonances**, which correspond to electron-hole pairs bonded by Coulomb forces [2]. More importantly, the integration of TMDs with other two-dimensional materials of specific properties in the form of van der Waals heterostructures (vdWH) has demonstrated unique light-matter interactions, which can be tailored to further obtain novel functionalities. It is therefore necessary to control the optical properties of atomically-thin vdWH for various future applications in optoelectronics.

However, the properties of 2D materials, and in particular its monolayers, are highly affected by the local environment in which it is located, because monolayers have a high specific surface area which make them highly sensitive to its environment, such as the external disorder and dielectric environment. Preliminary experiments have shown that the disorder contain factors including strain [3], roughness [4], absorbates [5], impurities [6], trapped charges [7, 8], oxidation [5]. In addition to interface cleanliness and homogeneous dielectric environment [9], encapsulating the monolayers within other 2D material flakes ensures its flatness down to the tens of picometer-scale [10, 11]. Besides these "positive" environments and reduced dielectric disorder effects, interlayer near-field coupling also plays a significant role in the performance of such thin layered structures, and therefore the material's optical properties can be moderated by coupling to the substrate [12]. Recently, these questions have been addressed by researchers in many fields including the mobility-temperature evolution [13, 14, 15], superconductivity behaviour [16] and photoluminescence (PL) [17, 18] of 2D monolayers under different configurations.

A considerable amount of literature has been published on the investigation of the optical properties of 2D materials. This led to rapid progress in the study of many novel quantum optical devices based on vdWH, such as single photon emitters [19, 20], flexible light-emitting devices [1, 21], biosensors [22], solar cell [23] and etc.

Optical techniques such as optical extinction/emission spectroscopies have been used for a long time to study TMDs. According to Rayleigh's criterion [24], the wavelength of the light source determines the spatial resolution, resulting in the techniques that use light as excitation source can hardly achieve resolution below hundreds of nanometers. Although the optical microscope based on super-resolution can overcome the diffraction limitation to resolution and realize optical measurement with subwavelength resolution [25, 26, 27]. However, these techniques provide limited types of nanoscale information of the sample. As a matter of fact, material and environment heterogeneity occurs in the <100 nm scale [28, 29], justifying the need to explore TMDs with electron microscopy and spectroscopy.

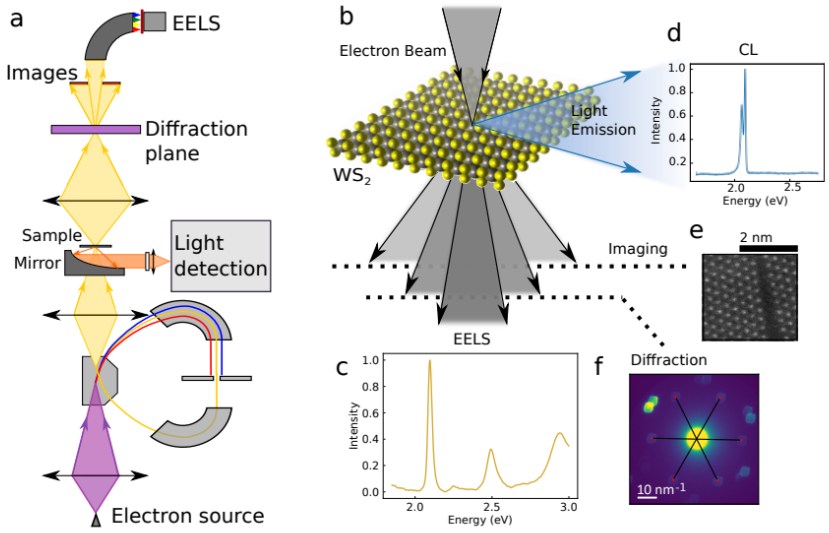

Figure 2.1: **Information available in the STEM:** 1) optical information, including (c) low-loss EELS and (d) CL; 2) structural information, including (e) images and (f) diffraction; 3) chemical elemental distribution retrieved from core-loss EELS. Reproduced from ref. [28].

A particularly powerful technique, scanning transmission electron microscopy (STEM) uses free electrons as excitation source and can map the optical, structural and chemical variations of samples with nanoscale spatial resolution [28, 30, 31, 32, 33]. It has been experimentally proven that electron energy loss spectroscopy (EELS) and cathodoluminescence (CL) measured in a STEM are perfect nanoscale counterparts of optical technologies [34]. In this thesis, a variety of characterization methods in STEM are used, as partially shown in Fig. 2.1, including acquiring information on lattice deformation and strain based on electron diffraction, optical properties based on low-loss EELS and CL, contamination and sample thickness from core-loss, to systematically investigate the optical and structural properties of monolayer TMDs under various vdWH configurations.

2.1 Statement of my work

In my thesis, the effect of heterostructures on the optical properties of TMDs was investigated on nano-scale. A variety of disorders associated with monolayer TMDs were examined and their negative effects on excitonic linewidth were clarified by electron microscopy and spectroscopies. It was demonstrated that the TMDs encapsulated between two 2D material flakes are preserved in the best possible manner [35, 17, 5, 9]. In order to investigate the optical properties of monolayer TMDs, its EELS and CL spectrum in various hBN-, graphene-, and graphite-based monolayer TMDs vdWH are studied, such as ***hBN/TMDs/hBN***, ***graphite/TMDs/graphite***, ***hBN/TMDs/graphite*** and ***hBN/TMDs/graphite/hBN***.

Disorder and excitons in the TMD monolayers

As mentioned previously, one particular property of TMDs is that they display bright luminescence when their thickness is down to atomically thin monolayers, possessing a direct bandgap, as opposed to its multi-layers and bulk [1, 2]. Since TMD monolayers have been studied by optical extinction/excitation techniques, local shift of emission/absorption line lead to an inhomogeneous linewidth broadening is observed due to the average response on micron-sized scale [17, 18].

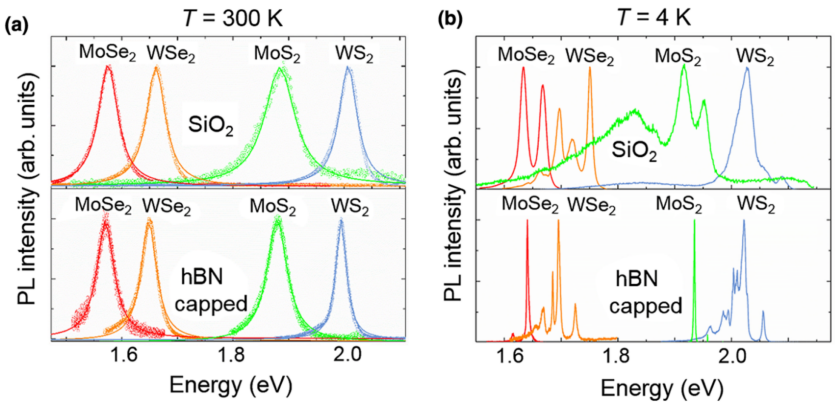

Figure 2.2: **PL spectrum of TMD monolayers (a) 300 K and (b) 4 K**: the monolayer $MoSe_2$, WSe_2, MoS_2 and WS_2 on SiO_2 (top); encapsulated by hBN (bottom). Reproduced from ref. [17].

The broad linewidth can obscure the intrinsic properties of monolayer TMDs and cover other weaker characteristic peaks at energies close to it. Broad linewidth was sometimes attributed to SiO_2 substrates which introduce substantial extrinsic disorder to TMDs monolayer [5], such as intrinsic disorder, surface contamination and charge traps. These external disorders have been shown to hugely affect 2D materials, particularly monolayer graphene and TMDs [5]. It is therefore necessary to understand and control extrinsic disorders in order to maximize the potential of 2D monolayers.

It has been observed that the hexagonal boron nitride (hBN) encapsulation can protect the properties of TMDs from extrinsic and intrinsic disorders, leading to a better electronic mobility and sharper emission/absorption excitonic linewidths approaching the homogeneous broadening limit [17, 35, 36]. An example of this is the study carried out by Cadiz et al. [17, 36] in which the linewidth of neutral exciton is as narrow as 2 meV in hBN/MoS_2/hBN, significantly reduced from the 10 meV of MoS_2 monolayer on bare SiO_2 at T = 4 K as shown in Fig. 2.2. Table 2.1 summarized the selected absorption/emission of TMD excitons measured in varouis literatures by different techniques at room temperatures (RT) and below. Here, linewidth is defined as the value of the full width at half maximum (FWHM), which is derived from exciton peak features fitted by Gaussian, Lorentzian, hyperbolic secant functions, or simply estimated at the energy axis at half the value of the maximum resonance intensity.

Table 2.1: **TMDs monolayer (MoS_2, $MoSe_2$, WS_2, WSe_2) exciton spectrum measured by different technologies.** The temperature reported is an approximate representation of the actuarial temperature, which can be found in the cited references.

Configuration	Temperature	Technique	Linewidth	Energy center	Reference
freestanding MoS_2	LN_2	EELS	>100 meV	1.88 eV	Ref. [37, 29, 38, 39, 40]
freestanding MoS_2	RT	EELS	>200 meV	1.88 eV	Ref. [38, 41, 42, 43, 40]
MoS_2 on SiO_2 or sapphire	2-10 K	Reflectivity	~ 40 meV	~ 1.95 eV	Ref. [44, 45, 46]
MoS_2 on SiO_2	RT	PL	~ 40 meV	~ 1.87 eV	Ref. [17, 47]
hBN/MoS_2/hBN on SiO_2	4 K	Reflectivity, PL	<5 meV	~ 1.95 eV	Ref. [17, 18, 35]
hBN/MoS_2/hBN on SiO_2	RT	PL, CL	~ 30 meV	~ 1.87 eV	Ref. [17, 35, 48]
freestanding $MoSe_2$	LN_2	EELS	> 100 meV	~ 1.62 eV	Ref. [37, 29, 38], this work
hBN/$MoSe_2$/hBN	LN_2	EELS	~ 20 meV	~ 1.64 eV	This work
$MoSe_2$ on SiO_2	< 55 K	PL	~ 10 meV	~ 1.69 eV	Ref. [17, 49, 50, 46]
$MoSe_2$ on SiO_2	RT	PL	~ 40 meV	~ 1.57 eV	Ref. [17, 51]
hBN/$MoSe_2$/hBN on SiO_2	4 K	PL	<5 meV	~ 1.64eV	Ref. [17, 18, 35, 50]
hBN/$MoSe_2$/hBN on SiO_2	RT	PL	~ 30 meV	~ 1.57 eV	Ref. [17, 35]
freestanding WS_2	LN_2	EELS	>100 meV	~ 2.15 eV	Ref. [37, 39], this work
hBN/WS_2/hBN	LN_2	EELS, CL	<40 meV	~ 2.11 eV	Ref. [28, 52], this work
WS_2 on SiO_2	4-10 K	Reflectivity, PL	~ 20 meV	~ 2.04 eV	Ref. [17, 44, 46]
WS_2 on SiO_2	RT	PL	~ 30 meV	~ 2.01 eV	Ref. [53, 17]
hBN/WS_2/hBN on SiO_2	4 K	PL	<5 meV	~ 2.00 eV	Ref. [17, 18, 35]
hBN/WS_2/hBN on SiO_2	RT	PL,CL	~ 30 meV	~ 2.03 eV	Ref. [17, 35, 48, 53]
freestanding WSe_2	LN_2	EELS	>100 meV	~ 1.83 eV	Ref. [37, 43, 39, 40], this work
hBN/WSe_2/hBN	LN_2	EELS	~ 30 meV	~ 1.76 eV	Ref [39], this work
hBN/WSe_2/hBN	RT	CL	~ 50 meV	~ 1.65 eV	Ref. [48, 54]
WSe_2 on SiO_2	4-30 K	PL	~ 10 meV	~ 1.75 eV	Ref. [17, 55, 36, 46]
WSe_2 on SiO_2	RT	PL	~ 40 meV	~ 1.66 eV	Ref. [17, 53]
hBN/WSe_2/hBN on SiO_2	4-10 K	PL	<5 meV	~ 1.70 eV	Ref. [17, 18, 36, 35]
hBN/WSe_2/hBN on SiO_2	RT	PL	~ 30 meV	~ 1.73 eV	Ref. [17, 35, 53]

Even if the optical properties have been widely studied by optical measurements [17, 18, 36], STEM/EELS/CL has not been widely used to probe the optical properties of TMD monolayers, with only a handful of reports in the literature [29, 37, 38, 40, 41, 42, 43, 52], as its measured exciton linewidth presented in Table 2.1. A large part for the lack of interest in this technique was the observation of large absorption linewidths (above 150 meV) for suspended monolayer TMDs on nano-scale at low temperature, which is considerably larger than one would expect even for room temperature optical measurements on SiO_2 substrates at micro-scale.

Unlike PL experiments [17], the CL signal on TMD monolayers in an electron microscope is not detectable, unless they are encapsulated in two hBN flakes [28, 48, 52].

Recently, EELS experiments of hBN encapsulated WS_2 have shown that the exciton linewidths can be much narrower at around 30 meV [28], approaching values comparable to those measured using optical absorption at similar temperatures around 110 K [35], as shown in Table 2.1.

It is noteworthy that no comprehensive and systematic comparison experiments so far have been conducted to determine the specific role of hBN or other substrates, but negative aspects such as the broadening in exciton linewidth induced by charge disorder [35], as well as dielectric environments variation [5] have been described separately. Instead of straightforward and evidence controlled experiment, most works are generic attribution of linewidth broadening to factors as mentioned above and sample protection [17, 36].

Previous works on TMDs by electron microscope missed 1) how does the linewidth is influenced by the substrate? 2) what are the origin of inhomogeneous broadening for excitons in TMDs? 3) Why encapsulation with hBN improves the optical quality of TMDs in both optical and EELS study? 4) Is hBN encapsulation of TMDs is the only heterostructures that have the most sharpest linewidth in EELS measurements?

In view of the limited amount of research on electron spectroscopies studies of TMDs, the first part of this thesis project was set out to disentangle the negative factors to the optical properties of TMDs, that can induce exciton inhomogeneous broadening. With this purpose, I used many combined technologies inside STEM to study the absorption spectra of TMDs on various substrates, namely insulators vaccum, amorphous Si_3N_4 and hBN. The variability of these substrates and configurations allows one to obtain the effects of TMDs roughness, charge disorder, sample cleanliness and damage on exciton absorption linewidth, respectively.

Excitons in TMD monolayers engineered by graphite

As a two-dimensional material, graphite provides the same level of surface flatness for two-dimensional monolayers [10, 56]. In addition, since graphene is a metallic material [57], it has the capability of resolving charge disorder of TMDs. Therefore, TMDs vdWH configurations involving graphene, graphite/hBN or double-graphite encapsulation provides the same atomic flatness, surface protection, and other benefits for TMD monolayers as hBN encapsulation. Despite that, no previous study has investigated the absorption spectra of TMDs encapsulated by graphite flakes, thus there is no knowledge of the exciton linewidth for such heterostructures. Investigating the optical properties of TMDs inside graphite-based heterostructures is a continuing concern within the inhomogeneous broadening schemes in previous section.

First of all, the Fano-like line profile was observed for the first time in both EELS and

optical absorption for graphite encapsulated TMDs. As a result of quantum interference between two competing optical absorption channels in such vdWHs, one discrete and the other continuous, asymmetric lineshapes are produced akin to the Fano effect [58, 59]. There are only a few reports of TMDs/metal system leading to Fano-like lineshapes, and they are all have different mechanisms than the one presented here. For example, monolayer TMDs have been shown to exhibit strongly exciton-plasmon coupling that Fano lineshape is achieved in the reflection or the scattering spectrum with metal nanostructures such as gold triangles [60] and silver bowtie [61]. Other than that, graphene/MoS_2 hybrid structures exhibit sharp Fano resonances between planar waveguide polaritons and surface plasmons in Kretschmann's configuration [62].

Since semiconductor/metal combines discrete and continuous energy absorbers, it is a good candidate to observe optical Fano-resonances in absorption measurement. Although the optical properties of monolayer TMDs/graphite heterostructures possess all the elements to show Fano effect, but this has not been extensively explored [63]. Thus, monolayer TMDs heterostructure based on graphite is investigated in this thesis under electron excitation to study its optical response in nano scale.

A further effect of graphene in TMD-based vdWH has been shown to be a filter of light emission, causing only single, narrow-line PL emission to arise solely from neutral excitons instead of both charged and neutral excitons [18]. Remarkably, the linewidth of monolayer TMDs on graphite substrates is as sharp as those in the hBN encapsulated monolayers in excitation spectra, indicating that the exciton lifetime is not largely influenced by the presence of the graphite layers [18, 64, 65]. It is unexpected, as damping from the conductive graphene should increase non-radiative decay of excitons, leading to wider linewidths.

Here I accordingly designed the hBN encapsulated WS_2/graphene as the ref. [18] and attempts to achieve both measurable neutral exciton emission and trion filter effects at the nanoscale at liquid nitrogen temperature. This part of work is an attempt to study the excitons in TMD monolayers engineered by graphite under different configurations, with the objective to understand the possible effects leading to absorption/emission lineshapes in electron spectroscopies.

2.2 Outline of this thesis

In this thesis, the optical and structural properties of TMD monolayers in various heterostructures by means of electron microscopy and spectroscopies were explored . The experimental principles for 2D materials by STEM techniques are presented in chapter 3. Samples of monolayer TMDs in various heterostructures are prepared by viscoelastic stamp dry transfer method by my colleagues Nianjheng Wu and Steffi Woo as introduced in chapter 4. In addition, the spin-valley physics of TMDs and the exciton

resonance transition are introduce in chapter 7.

Various bandgap dielectric materials, namely hBN and amorphous silicon nitride (Si_3N_4), undoped graphite under different configurations are investigated as support or encapsulation materials for TMD monolayers to study the substrate/dielectric influence on the exciton absorption lineshape in TMDs using electron energy loss spectroscopy (EELS) in a scanning transmission electron microscope (STEM). Firstly, monolayer roughnesses are determined from tilt series of wide-beam electron diffraction patterns by assessing the broadening of diffraction spots in comparison with simulations using QSTEM software in chapter 5. To gain a better understanding of the inhomogeneous broadening in monolayer TMDs (chapter 7), chemical mapping, strain mapping, and dose-control EELS experiments are conducted.

In chapter 8, ***graphite/WS_2/graphite*** are measured both though EELS and optical absorption, in order to evalute their relevance in the Fano-like lineshape observation. For ***hBN/graphene/WSe_2/hBN*** vdWH, the EELS and CL measurements are designed to study the complete neutralization of the TMD monolayers by graphene, as well as the selective non-radiative transfer of long-lived excitonic species such as trion to graphene. The optical absorption is performed at University of Münster by collaborators Robert Schneider and Ashish Arora. These lineshapes are interpreted in the frame of solving the Maxwell equation for a infinitely thin 2D layer, which is developed by F. Javier García de Abajo at ICREA-Institució Catalana de Recerca i Estudis, and Avançats and Andrea Konečná at Brno University of Technology. All the STEM/EELS/CL experiment and related analysis were performed in the Laboratoire de Physique des Solides in Orsay. Finally, the main contributions of this work and future work will be discussed in chapter 9 and chapter 10, respectively.

Chapter 3

Experimental technique: electron microscope and spectroscopies

This thesis investigates the properties of excitons in TMDs and how they are affected by various dielectric environments. Through the combination of scanning transmission electron microscopy (STEM) with electron energy loss spectroscopy (EELS) and cathodoluminescence (CL), also known as STEM/EELS/CL, I gathered a significant amount of spatially-resolved information through electron-matter interaction to obtain information about the sample, including imaging mechanisms, diffraction patterns, low-loss and core-loss electron energy-loss spectra (EELS) and CL spectra [30]. It is only by understanding the physical mechanisms that one can develop novel devices and improve the repeatability based on these existing material systems. This chapter introduces the technique, equipment, and data processing method that will be used in subsequent chapters. This chapter does not contain any original results.

3.1 Introduction

STEM and scanning electron microscopy (SEM) work very similar: a focused electron beam with its size from nanometer to sub-atomic scale is scanned over the sample, while a detector measures the signal intensity I(x,y) at each scan point. Unlike the SEM, which records the secondary electron and back scattering signal, the STEM records the transmitted electron after it passes through the sample. STEM uses multiple detectors to collect the signals from the sample, including circular detectors, annular detectors, and an electron energy spectrometer. The instrument could also be equipped with a CL detector to collect the luminescence signal of the sample under high-energy electron excitation. Additionally, the energy dispersive X-ray (EDX) detector system can also be used in electron microscopy for elemental analysis or chemical characterization. [1]

At the nanoscale, it is difficult to find any setup other than STEM that can perform multiple test methods and provide such a wide range of information for materials [31, 66].

[1] There are no X-ray related experiment in this thesis.

The purpose of this chapter is to provide details of electron-matter interaction (section 3.2), STEM setup (section 3.3), imaging and spectroscopy for materials (section 3.4), practical experiment details (section 3.5), and algorithms related to data processing (section 3.6).

3.2 Elastic and inelastic electron-matter interaction

As electrons traverse the sample in an electron microscope, they interacted with the sample through Coulomb forces. The force changes the direction of the fast incident electrons. Typically, electrons fall into two categories: elastic scattered and inelastic scattered. STEM setup is built based on that these scattered electrons which contains sample information. Therefore I will discuss the various mechanisms of electron interaction with matter as well as the various types of damage that can be caused by fast electrons in this section.

3.2.1 Elastic scattering

The charge of an atomic nucleus produces a strong electric field in its vicinity, and the interaction between the incident electron and this field is known as **elastic scattering**. The scattered electrons, however, are deflected to different angles by Coulomb forces and the distribution is similar to the Rutherford scattering of alpha particles [67]. The angular distribution of these elastically scattered electrons in the far field is detected by several different detectors in STEM to obtain information about the sample.

In fact, the majority of the incident electrons go through large impact factors b (far from the nucleus) experiences a weaker electrostatic attraction, correspond to small scatted angle θ. Whereas electron back scattering at small impact factors (near the nucleus of the target atom) will go through large deviation. For a fast electron with kinetic energy E_0 deflected by the electrostatic field of a stationary nucleus with mass M by an angle θ, the electron transfers an amount of energy E to the nucleus as a result of the conservation of energy and momentum, as below:

$$E = E_{max}\frac{1-cos\theta}{2} \tag{3.1}$$

where $E_{max} = E_0(E_0 + 2m_0c^2)/Mc^2$ is the maximum energy transfer. Actually, only the scattered angle within the collection aperture of EELS will contribute to the EELS spectrum in the practical experiment. [2] So in term of the energy lost of the collected trans-

[2] The EELS setup within the STEM will be described in section 3.4.3, where we focus on the electron-matter interactions that contribute to the collected EELS signal.

mitted electron though elastic scatteing scheme, it is collection angle dependent. It will cause the zero energy loss peak in terms of inelastic scatterings, (as illustrated in 3.4.3.3) is located differently in terms of various θ [68].

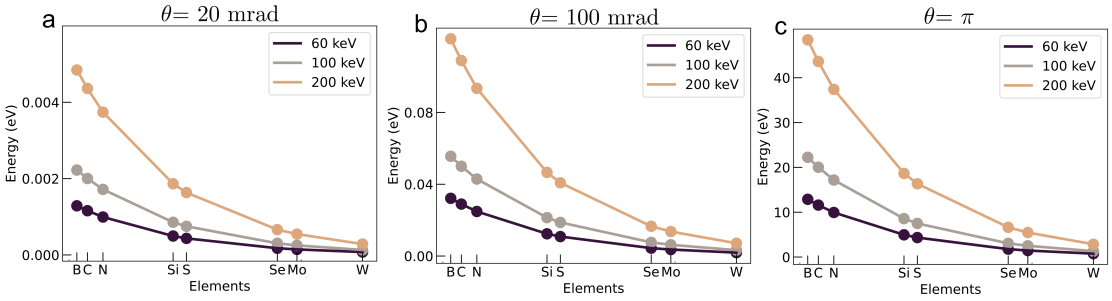

Figure 3.1: **Energy loss of incident electrons of 60 keV, 100 keV and 200 keV at scattering angles**: (a) 20 mrad, (b) 60 mrad and (c) π rad. Only elements contained in the samples that I tested is calculated, including B, C, N, Si, S, Se, Mo, W.

As shown in Fig. 3.1 and Eq. (3.1), increasing acceleration voltage and decreasing atomic number lead to an increase in maximum energy transfer. In this thesis, I used the STEM at the acceleration voltage of 60 keV to minimize the **knock-on radiation damage**, since if the E_{max} is greater than the displacement energy of an atom, the atom will be removed from its lattice site. As shown in Fig. 3.1(a), the maxium energy gain by the most light atom among WS_2, WSe_2, MoS_2, $MoSe_2$ is 16.3 eV at 200 keV, and reduces to 4.3 eV at 60 keV.

The collection semi-angle is set to 21 mrad from the EELS entrance aperture, as I will introduce later. Thus as shown in Fig. 3.1(c), the energy exchange is limited to a few meV, so electron energy loss through elastic scattering is negligible in this situation as it is within the zero loss peak in the EELS spectrum. Typically the collection semi-angle of the scattered electrons is only up to 100 mrad in (S)TEM [3], and the energy exchange is also very small as shown in Fig. 3.1(b). The summary of the electron energy lost through elastic scattering under different deflection angles at 60 keV is presented in Table 3.1.

Table 3.1: **Energy transfer of few elements at 60 keV through elastic scattering.**

Element	B	C	N	Si	S	Se	Mo	W
$E_{max}\,(eV)$	12.9	11.6	9.9	4.9	4.3	1.8	1.45	0.75
$E_{\theta=100mrad}\,(eV)$	0.032	0.029	0.025	0.012	0.011	0.004	0.003	0.002
$E_{\theta=20mrad}\,(eV)$	1.29e-3	1.16e-3	0.99e-3	0.49e-3	0.43e-3	0.18e-3	0.14e-3	0.007e-3

[3]Except for HAADF for imaging, which will be introduced later in section 3.4.

3.2.2 Inelastic scattering

As a result of Coulomb interaction between a fast incident electron and atomic electrons that surround each nucleus, **inelastic scattering** occurs. Inelastic processes in the inner shell can be explained by the excitation of an individual electron into a Bohr orbit which having a higher quantum number. The inelastic processes occurring at the outer shell can be understood in terms of energy band theory, which is located at a higher energy level. The main mechanisms of energy loss can be divided into the following categories with an increasing trend in energy:

- **Phonon Scattering:** the interaction of an incoming electron with an array of atoms results in an excited state for the quantum mechanical quantized modes of the the periodic atomic vibration, which are known as phonons. Energy associated with the phonons are below few hundard meV and are not resolved by the usual electron microscope/spectrometer system in the past. The magnitude of these phonon energies is around $k_B T$, where k_B is the Boltzmann constant, T is the absolute temperature [69].
- **Excitons:** an electron can be excited from the valence band of an insulator or semiconductor to a Rydberg series of states situated just below the conduction band's minima, resulting in an energy loss $E_x = E_g - E_b/n^2$, where E_g is the energy gap, E_b is the exciton binding energy, and n is a integer labeled analogous to hydrogen series [70].
- **Interband transition:** the interaction between an incoming electron and outer-shell electrons may cause a valence electron to undergo an interband transition in semiconductors and insulators.
- **Plasmon resonance:** an incoming electron interact with outer-shell electrons, may also cause collective oscillations with collective electron density in the valence shell.
- **Inner-shell electron excitation:** the ground state energy of inner electrons outside the nucleus are generally hundreds or even thousands of eV below the Fermi level. In the case of interaction of an incoming electron with the inner-shell electron in a atom, since the unoccupied energy states of the atom are all above the Fermi energy level, the inner electron can only transit upward. According to the conservation of energy, when such inelastic collisions occur, the incident electron losses hundreds or even thousands of eV. As a result of this absorption, the atom becomes excited and the outer electrons drop into the electron vacancy, releasing the energy as electromagnetic radiation (characteristic X-rays) or electron kinetic energy (Auger electron) [71].

Unlike elastic scattering that can extend to a large range of solid angles (θ), the inelastic scattering is only concentrated into smaller angles (up to only few mrad for carbon atom at 100 keV) than elastic scattering according to Bethe theory [71]. In some materials the

electrons in the valence band may not revert to their original positions after absorbing energy, which can result in permanent damage to the chemical bond, which is known as **ionization damage**. It is evident that there is a direct relationship between the extent of damage and the required electron dose. There is an increased risk of radiation damage to the sample in the event of high electron exposure (high current density) [71].

3.3 Scanning transmission electron microscope

The purpose of this section is to provide a detailed description of the illumination system in the STEM before introducing the various detectors and techniques in next section. The Fig. 3.2(a) provides a schematic representation of a STEM microscope, which consists of several components:

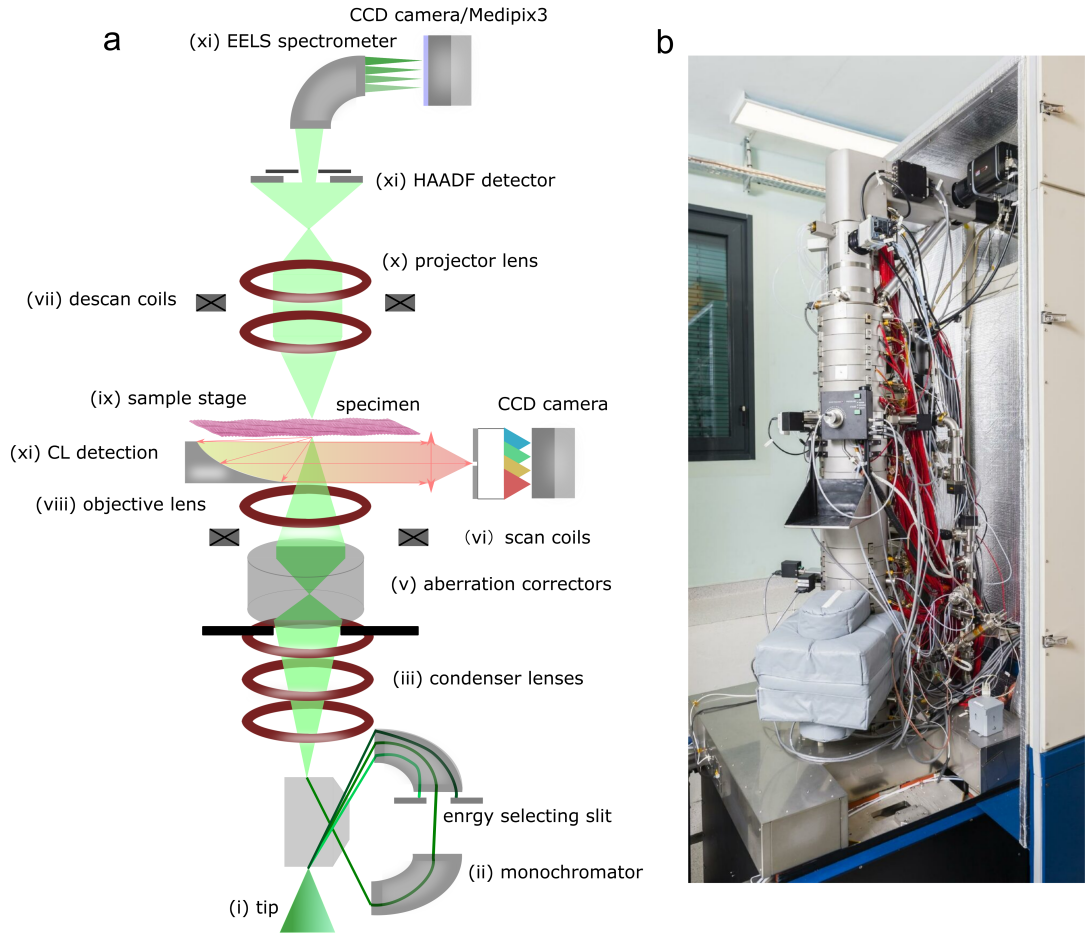

Figure 3.2: **Scanning transmission electron microscope system**: (a) A scheme of a STEM microscope. (b) A photograph of the ChromaTEM, and its monochromator is covered by a grey fabric box.

- **(i) Electron gun:** electrons are extracted from a metallic tip. Consideration of electron source for high-performance STEM should consider both **high brightness** and **small energy distribution**. Using an electron gun with high brightness ensures that all signals in the STEM are intense and that noise fluctuations are less noticeable, and monochromator is used for high energy resolution EELS. The electron source can be obtained in a variety of ways, among thermionic emission, Schottky emission, and cold field emission guns (cFEG). This thesis work uses a STEM called ChromaTEM equipped with a cFEG that has high brightness and good monochromaticity, with 300 meV energy spread range without a monochromator.

- **(ii) Monochromator:** for optical studies, it is not sufficient to use a STEM with an energy fluctuation range of 300 meV for measuring the EELS spectrum of excitons in monolayer TMDs, because the exciton resonances would remain hidden in the ZLP tail. Further improving the monochromaticity of the electron beam requires a STEM equipped with a monochromator. In general, monochromators are essential in STEM-EELS systems to achieve high energy resolution. The monochromator has the capacity to filter out the electrons that have an energy deviation away from the central energy, thus enhancing the monochromaticity of the electron beam while at the same time decreasing some of the brightness as a consequence of the filtration. Electron beam monochromatien makes use of various methods to spread electron beams in space and then filter the energy through a small slit. It is generally assumed that the energy resolution of the system is defined by the full width at half maximum (FWHM) of the elastic scattering peak without any sample in vacuum as a reference.

- **(iii) Condenser lenses:** an electron beam is collected from the accelerating system by means of a focusing system built by the condenser lenses. It consists of several electromagnetic lenses that adjust the focal length, brightness, and semi-convergence angle α of incident electrons, the size of which is determined by the aperture in the focusing system. As a result, the ChromaTEM consists of three lenses in the condensing system, providing three independent degrees of freedom for the current, convergence angle, and focal length.

- **(vi) Scan coils**: focused electron probe is formed on the sample surface after high-speed electrons are ejected from the electron gun after they have been accelerated and focused. Through two dipole electromagnetic lenses, the probe is scanned across the surface of the sample. Similarly, a **(vii) descan coil** controls the electrons transmitted through the sample to be collected by the detectors.

- **(v) Aberration correction system**: it is important to note that photons and electrons are wave-like particles, and a phase that is not ideal can result in poor image quality. There is a direct relationship between the aperture size and the beam size: as the aperture size increases, the converging electron beam becomes smaller, but the aberration becomes more noticeable. Electromagnetic lens are not ideal, having strong aberrations, which limit the beam size (spatial resolution). It is for this reason that a variety of methods have been investigated to correct aberrations,

including correction of the higher order aberrations. C_3 and C_5 aberration are corrected by quadrupole and octupoles electromagnetic lenses in ChromaTEM.

- **(viii) Objective lens**: the objective lens is one of the most important components of STEM. The objective lens consists of two symmetrical polepieces at a distance of about 5 mm between them, and the objective lens converges electrons strongly with the sample between them. ChraomaTEM however, has pole-pieces with a 6 mm gap that have been designed specifically for the insertion of the CL mirror.

- **(ix) Sample stage**: inside the objective lens, the sample stage controls the entry and exit of the sample and its height can be adjusted. The mechanical stability of the sample holder is crucial for high-resolution imaging of samples. The sample stage can be rotated to accommodate the tilting of the sample during an experiment. Furthermore, the sample stage can be equipped with a temperature control system for low-temperature measurements. It should be noted that the tilt angle of the sample is limited inside ChromaTEM to near 400 mrad as a result of the stage clearance between two pole-pieces. The temperature-control sample holder in ChromaTEM is designed and constructed by HennyZ [72]. It has a cooling system linked to a liquid nitrogen (LN_2) dewar with a conductive braid that allows for cooling the samples down to 110 K.

- **(x) Projector lenses**: the equivalent distance between the transmitted electron beam and the detectors is controlled, which, in turn, regulates the different round and annular detectors to collect scattered electrons across a wide range of solid angles, as shown in Fig. 3.3. In TEM, it influence the magnification of image/diffraction patters.

- **(xi) Detectors**: a variety of detectors may be employed depending on the type of information that is being collected. In addition to bright-field (BF) and annular dark-field (ADF) imaging systems, CL and EELS cameras are also available for measuring the emission and absorption spectra (section 3.4). The exciton study in monolayer TMDs employed HAADF, CL detectors and also the electron energy spectrometer and EELS detectors as introduced later in section 3.4.3.

All my experiments are performed on the ChromaTEM microscope, a modified Nion HERMES200 equipped with a spherical aberration corrector and an electron monochromator, as shown in Fig. 3.2(b), which equipped with C_3 and C_5 aberration correctors, CL mirror and a Merlin electron detector (Medipix3). During my PhD study at LPS, the ChromaTEM was equipped with Merlin detectors in 2021, so the earlier EELS for TMDs linewidth study was conducted using Princeton KURO CMOS detectors and more recent data for fano-like lineshape were recorded by Merlin detectors. Camera detective quantum efficiency (DQE) and modulation transfer function (MTF) responses in MerlinEM [73] are near-ideal, allowing for the detection of very weak signals with no additional readout noise. To have more of a degree of confidence, I will only draw conclusion on data acquired on the same detector.

3.4 Various Detectors in STEM

The purpose of this section is to provide a detailed overview of electron beam detection after introducing the physics of electron-matter interaction. Essentially, elastically scattered electrons are used to build high-angle dark field (HAADF images, diffraction patterns, and also make up the zero-loss peaks in EELS. Inelastic scattering is mainly used for optical spectrum and chemical element analysis in EELS.

In STEM, there are two basic types of detectors: a single pixel detector, signals within which are integrated as one number, and an array detector (also called configuration detector), in which electrons arrive in different regions to produce different signals. Single detectors of different shapes are used for image detection as described in section 3.4.1, while array detectors are used for recording diffraction patterns and EELS detection as described in section 3.4.2 and section 3.4.3, respectively. In addition, a CL collection system including a parabolic mirror and coupling optics, can be optional added inside STEM to collect the cathodoluminescence radiative deexcitation signal as introduced in section 3.4.4.

3.4.1 Imaging in STEM

Most of the electrons hitting the sample pass away from the nucleus, and most of the electrons are scattered only at a small angle. In the case of 60-100 keV incident electrons, most of them are scattered between 10 mrad and 100 mrad. As shown in Fig. 3.3(b), STEM imaging detectors usually are sorted by spatial segregation in angular in increasing order: bright field (BF), annular bright field (ABF), low-angle annular dark field (LAADF), middle-angle annular dark field (MAADF), high-angle annular dark field (HAADF). A scintillator/photomultiplier combination is used in STEM as a single detector. As the electrons arrive at the scintillator, they are converted into photons, and then the photomultiplier converts the weak signal into an electrical signal that can be recorded.

During the beam scanning process, each single detector collected the signal and summed up the transmitted electrons within its own areas, and provide a number called counts for each pixel. By observing the intensity of scattered electrons, one obtains the image contrast of the sample. Since the incident electrons are scattered by the specimen at various angles, the image contrast arises from the various scattering schemes of the incident beam as follow:

- **Bright field:** the bright field (BF) image is composed of an image with contrast given by the intensity of the signal collected at the detector angle β, of $0 < \beta < \alpha$, where α is the convergence angle of the probe. As the name suggests, a bright field image is one whose intensity is highest when no object is present, and decreases

when a sample is present. This portion of the signal gives the similar contrast as phase contrast in the TEM, except that the convergence angle is close to zero in the TEM. BF images are coherent, and contrast depends upon the sample's structure, such as thickness and atomic arrangement.

- **Annular dark field:** an annular dark field image is an image composed of the intensity given by the signal collected by the detector angular range at $\alpha < \beta < 80$ mrad as a contrast.[4]

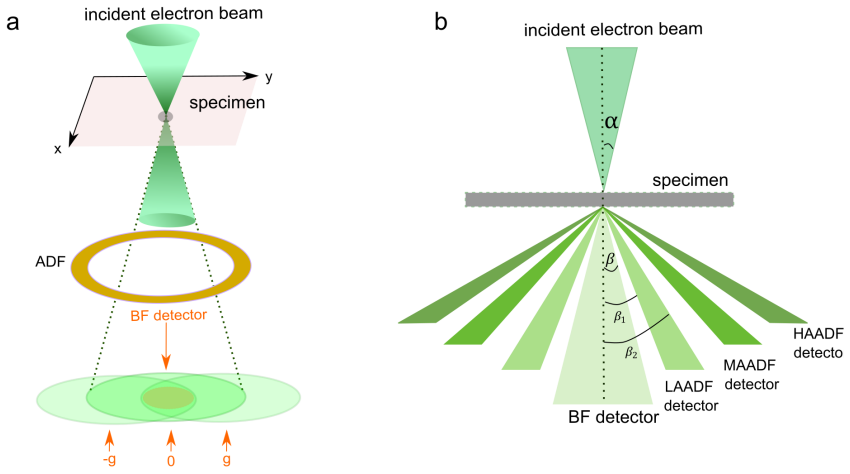

Figure 3.3: **There are several imaging mechanisms commonly used in STEM:** the electron beam scans along the x-y plane of the sample (a), and scattered electrons are collected by different detectors: bright-field detectors (BF) and annular dark-field detectors (ADF). (b) A variety of detectors are used for STEM imaging, including bright fields (BF), low-angle annular dark fields (LAADF), medium-angle annular dark fields (MAADF), and high-angle annular dark fields (HAADF).

- **High-angle annular dark field:** high-angle annular dark field (HAADF) images are produced by the intensity of the signal collected by the detector at an angle of $\beta > 80$ mrad. Electrons are scattered by Rutherford scattering in this case, and the scattering cross-section is proportional to Z^r, r ≈ 1.6, thus HAADF is also called "Z-contrast" image according to ref. [74]. Due to its simple and strightford contrast transfer mechanism, nowadays HAADF is the most frequently used imaging method in STEM.

3.4.2 Diffraction in (S)TEM

[4]The annular dark field image is referred to as either a medium-angle annular dark field (MAADF) or a low-angle annular dark field (LAADF) image depending on the outer annular collecting angle β_2. In general, MAADF is diffraction contrast imaging, where the detector collects transmitted electrons in the angular range determined mainly by diffraction effects. When the internal angle is further reduced to contain a portion of the transmitted electron beam that is not scattered by the material, one call this image an annular bright field image, which is mainly used for imaging light atoms.

In the case of crystals, it is necessary to take into consideration the wave nature of the incident electrons. Due to interference between scattered electron waves, the intensity of scattered electrons changes from a continuous distribution to one that is scattered at a specific angle. This elastic scattering is then called diffraction, and its pattern is recorded by the same detector as the ronchigram, which is a scintillator/CMOS coupled array detector with fibre optic plates in the middle in our microscope set-up.

Specifically, the electron processes the wave-particle duality, so that when its wavelength is sufficiently short to be of the order of the atomic structure periodicity or smaller, diffraction patterns are produced. In a typical (S)TEM, the electron beam has a wavelength that is in the pm range such that the crystal lattice acts as a diffraction grating [75]. Thus, the electron beam incident on the atomic lattice can be seen as a planar wave, which is re-transmitted by each atom as a spherical wave. In a crystal lattice, the constructive interference at the angles θ_n satisfies the Bragg condition:

$$2d_{hkl} \cdot sin(\theta_n) = n\lambda \tag{3.2}$$

where the integer n represent the diffraction order, d_{hkl} is the interplanar distance of plane with Miller indices (hkl) depicting a cubic system for simplicity, λ is the wavelength of the electrons, and θ_n is the diffraction semi-angle.

3.4.2.1 The Ewald sphere and relrod

It is known that the incident plane wave propagating through the crystal has a wave vector whose length is $\mathbf{k_1}$, and its diffracted plane wave has a wave vector $\mathbf{k_2}$. During the diffraction process, which is elastic, no energy is gained or lost, therefore, $\mathbf{k_1}$ and $\mathbf{k_2}$ have same length $|\mathbf{k_1}| = |\mathbf{k_2}| = 1/\lambda$. Diffracted electron waves differ from incident electron waves by a scattering vector $\mathbf{K} = \mathbf{k_2}$ - $\mathbf{k_1}$, as shown in Fig. 3.4(a). Due to their equal lengths, $\mathbf{k_1}$ and $\mathbf{k_2}$must lie on a sphere of radius $1/\lambda$, which is known as an **Ewald sphere**. In this case, Bragg condition can be write as

$$\frac{2 \cdot sin(\theta_n)}{\lambda} = \frac{n}{d_{hkl}} = |\mathbf{g}_{hkl}| \tag{3.3}$$

where $\mathbf{g}$ is the reciprocal lattice vectors linked to interplanar distance d_{hkl}. It can be seen that constructive interference can only occur when $\mathbf{K} = \mathbf{g}$. In the Ewald sphere, direct beams pass through the origin of the reciprocal lattice (point O) and if any other point within the reciprocal lattice intersects the surface, the planes corresponding to that point satisfy the Bragg condition, and so the planes will diffract strongly, as shown in Fig. 3.4(a).

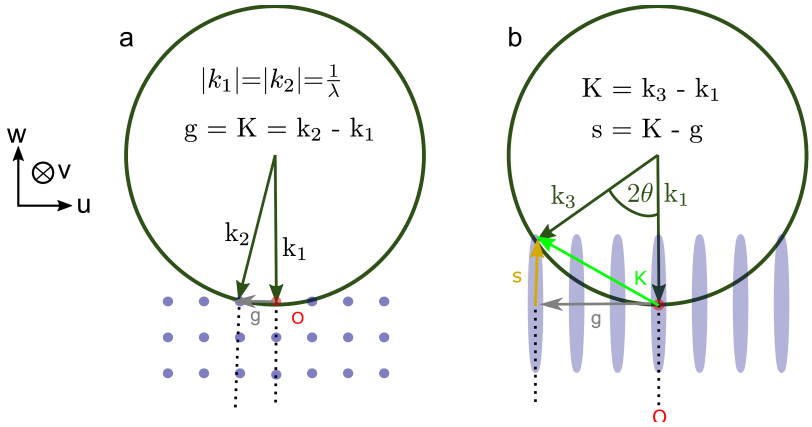

Figure 3.4: **The geometric relationship among incident electron wave, diffracted electron wave, diffraction angle and reciprocal lattice in:** (a) a thick sample and (b) a thin sample. An Ewald sphere in reciprocal space of radius $1/\lambda$ which passes through the origin of a reciprocal lattice point O in both (a) and (b).

Based on the point of view of momentum, creating constructive interference in a diffraction experiment implies that in reciprocal space, the values of momentum transfer where constructive interference occurs form a reciprocal lattice as well. And the reciprocal lattice represents a 3D array of points, each of which represents an atomic plane.

TMDs are 2D atomic structures, and because the dimensions of these thin objects are small along the beam propagation direction (**w**), their reciprocal lattice points extend further along this direction. As shown in Fig. 3.4(b), the reciprocal lattices of a thin material are elongated into reciprocal lattice rods, known as **relrods** [75]. Accordingly, the Bragg diffraction condition is relaxed such that the Ewald sphere intersects the relrods with an excitation error $\mathbf{s} = \mathbf{K} - \mathbf{g}$ in this case, where **g** is the exact Bragg diffraction condition and **K** is the relaxed Bragg diffraction condition.

3.4.2.2 Reciprocal space of rough materials

The reciprocal lattices of a flat and rough material are very different as shown in Fig. 3.5(e) and (f), respectively. [5] For a flat 2D nanosheet, the reciprocal space consists of a set of relrods arranged perpendicularly to the reciprocal lattice. For atomically rough sheets, however, a superposition of diffracting beams from microscopic flat areas causes the relrods to become cone-shaped volumes. For this reason, diffraction spots blur at large sample tilt angles as shown in Fig. 3.5(c), and the effect is more pronounced when the diffraction spots are more away from the sample tilt axis.

A diffraction pattern of WS_2 at different levels of roughness is shown schematically in

[5] The reason why suspended monolayers are rough and hBN encapsulation is flat will be investigated in chapter 5.

Fig. 3.5, and the size of the diffraction spots can be used to assess the roughness of the sample. In chapter 5, these basic concept will be used to study the reciprocal lattice and diffraction patterns of TMD monolayers under different vdWH configurations.

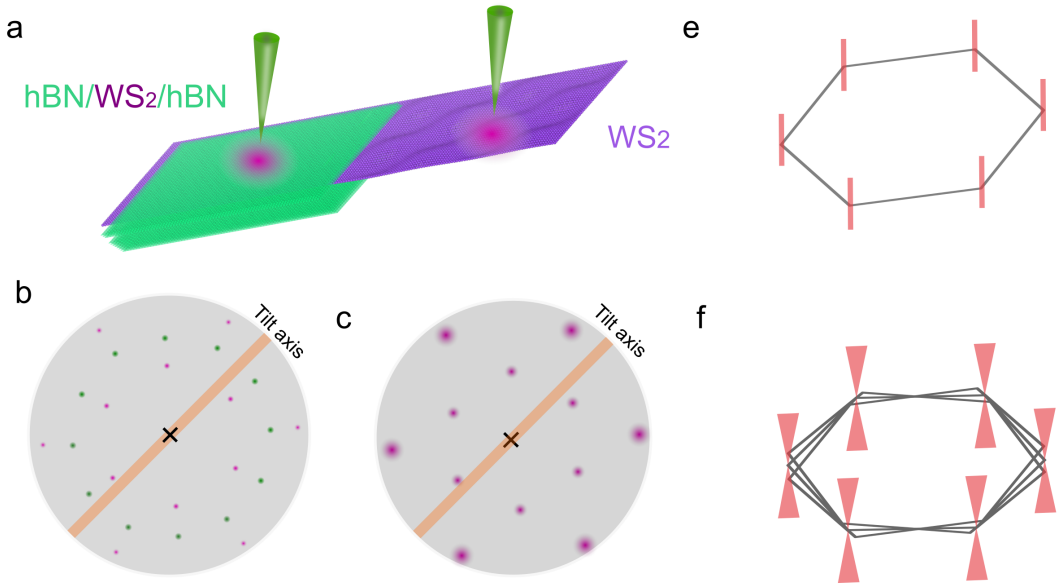

Figure 3.5: **Electron diffraction pattern of WS_2 monolayer:** (a) diffraction of suspending WS_2 monolayer and hBN/WS_2/hBN flakes at incidences angle isn't vertical to the sample surfaces; (b) and (c) are the schematic diffraction patterns on two different regions at (a); (e) and (f) are the corresponding reciprocal space of (b) and (c), respectively.

3.4.2.3 4D-STEM

The basic idea behind 4D-STEM is to run many electron diffraction experiments sequentially, so that the diffraction pattern obtained at each probe position is determined by the local sample structures. In Fig. 3.6, (b) and (c) are the diffraction patterns of the pixel marked by red and green squares on (a). Nowadays, it is highly common to capture an image of the diffracted electron beam at each probe position, usually arranged in a 2D navigation grid.

As a result, the datasets of 4D-STEM are rich in information [31, 32], including local structure, orientation, deformation, electromagnetic field, that can be determined for each probe position.

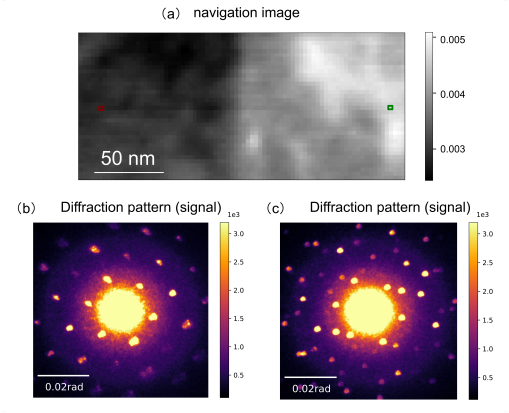

Figure 3.6: **An example of 4D STEM experiment on monolayer WS_2.** The red and green squares marked position where were measured for (b) the diffraction pattern of freestanding WS_2 and (c) hBN/WS_2/hBN, respectively. Purple dots represent the diffraction pattern of WS_2, and green dots represent the diffraction pattern of hBN.

3.4.2.4 Strain mapping by scanning nanodiffraction

The convergence semi-angle α should be chosen carefully based on the particular requirements of each scanning nanodiffraction experiment. As a reminder, α is the radius of the bright-field disk within the diffraction plane, as well as the radius of each diffracted Bragg disk within a crystalline sample. Real-space probe sizes are inversely related to convergence angles; larger convergence angles correspond to finer probes, and overlapping diffraction disks is the requirement of a sublattice-sized probe, enabling the acquisition of information at atomic level resolution [76].

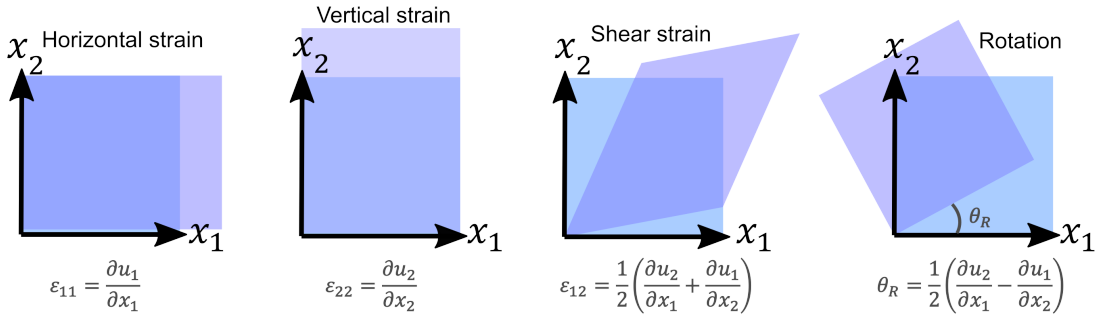

Figure 3.7: **Example of square unit cell to illustrate different axial strain and displacement.** The blue and transparent squares are the standard unit cell and single deformed unit cell. The single deformation including: horizontal, vertical and shear stain. The rotation is just displacement of the object without any strain.

A non-overlapping disk diffraction under small α (scanning nanodiffraction) is used to extracting a strain map, since strain can only be defined on length scales equal to or greater than individual unit cells. Considering a system with ordinate (x, y) and

deformed state characterized by displacement field (u, v), the infinitesimal strain matrix can be expressed as:

$$\epsilon = \begin{pmatrix} \epsilon_{xx} & \epsilon_{xy} \\ \epsilon_{yx} & \epsilon_{xx} \end{pmatrix} = \begin{pmatrix} \frac{\partial u}{\partial x} & \frac{1}{2}\left(\frac{\partial u}{\partial y} + \frac{\partial v}{\partial x}\right) \\ \frac{1}{2}\left(\frac{\partial u}{\partial y} + \frac{\partial v}{\partial x}\right) & \frac{\partial v}{\partial y} \end{pmatrix} \tag{3.4}$$

A 2D strain map of each strain component can be decomposed from Eq. (3.4), as shown in Fig. 3.7. For details of calculation refer to ref. [31, 32] for converting deformation from reciprocal lattice to real lattice.

Aside from non-overlapping nanodiffraction, geometrical phase analysis (GPA) based on high-resolution image is also a very common local displacement analysis method in (S)TEM that the lattice displacement vector could be extracted from the geometric phase component in the back Fourier transform of a filtered Fourier transform of an HREM image [77, 78]. By analysing the derivative of the displacement field, local strain could be obtained. For more details about the GPA, refer to ref. [79], which includes the dedicated theory and data process details. A comparison of different nanoscale strain measurements in terms of precision and accuracy are detailed in ref. [80].

3.4.2.5 Diffraction pattern simulation

In electron crystallography, one of the major challenges has been quantifying the diffraction pattern and determining the crystal structure to a greater degree. Modern analytical software enable one to perform such quantitative analysis. The difficulties for calculating the diffraction patterns quantitatively come from the electrons interact with samples in a complex manner. Even perfect crystals are not stationary, and their vibration increases with temperature, and this vibration means that the atoms within the crystal are not perfectly ordered, and phonon scattering occurs between the spots in the diffraction pattern.

The QSTEM simulation software is a popular tool for analyzing quantitative diffraction patterns and producing high-resolution atomic images [81]. Using a multislice algorithm, the software implements a graphical user interface for quantitative simulations of STEM/TEM/CBED images, and details about the software can be found in the doctoral dissertation of the developer, Prof. Christoph Koch [82]. Due to the popularity and dominance of python for data processing, the open source abTEM code [83] was recently developed for diffraction and image simulation as well. Images and diffraction patterns can be obtained easily with the combination of abTEM and Atomic Simulation Environment (ASE) module [84]. Compared to abTEM, QSTEM based on C++ is much faster due to the limitations of the underlying logic and working principles of

the programming language. Nevertheless, abTEM is capable of increasing computation speed by utilizing GPUs or memory-intensive computing techniques [83]. It was QSTEM rather than abTEM that I chose to simulate diffraction images in this thesis.

3.4.3 Electron energy loss spectroscopy (EELS)

Electron energy loss spectroscopy (EELS) is a technique for analysing the energy distribution of incident electrons after they pass through an object. In (S)TEM, the optical and chemical information provided by EELS complements the structural information provided by imaging and diffraction. Here, I will firstly describe the EELS setup inside the STEM column (section 3.4.3.1). As a next step, I will describe the typical data classification in section 3.4.3.2, followed by illustrate a typical EELS spectrum and describe how it is partitioned in section 3.4.3.3. Finally, the thickness measurement technique based on elastic/inelastic scattering ratio will be given in section 3.4.3.4.

3.4.3.1 Dispersion and detection

The BF electron detector and the CCD or CMOS camera of Ronchigram must be moved out of the way so that this fraction of scattered electrons may enter the electron energy less spectrometer system in order to obtain the EELS signal. The electron energy analysis system will contain a collection entrance aperture, whose physical size is 1-2 mm to limit the maximum solid angle of the electron beam entering the EELS system. The electron beam then enters a magnetic electron prism to disperse in energy the transmitted electrons. Based on the relationship between the radius of curvature and electron velocity, electron beams of differing energies are separated spatially according to their energies, as shown in Fig. 3.8(d).

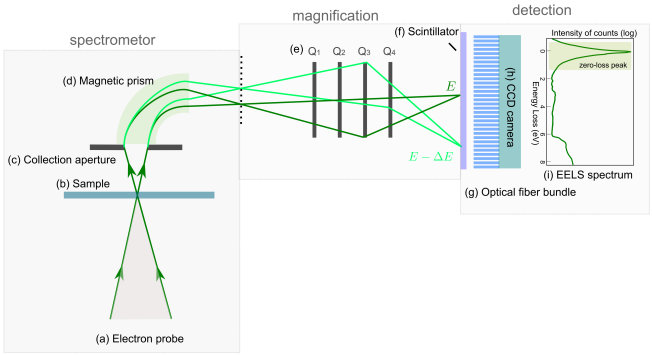

Figure 3.8: **Electron energy loss spectrometer operating principle diagram:** (a) the electron beam is transmited (b) the sample and passes through (c) the aperture; under the influence of (d) magnetic prism and (e) the quadrupole lenses, (f) the scintillator detector converts the electrical signal into an optical signal, and the light passes through (g) the optical fiber bundles to record the (i) EELS spectrum on (h) the CCD.

A scintillator converts electrons into photons, and these photons going through optical fiber, which are then detected by a CCD or CMOS camera. [6] In this part, the energy-dispered electrons are recorded on the detector as the number of electrons on each channel with energy dispersion ΔE. A set of quadrupole lenses lies between the magnetic prism and the detector device, whose function is to amplify the distance of the energy spatial dispersion and its focal length must correspond precisely with that of the scintillator detector as shown in Fig. 3.8(e). Additionally, scintillator and CCD/CMOS detectors can be replaced with a direct electron detector (DED) that produce less noise, such as MerlinEM [73], K3 cameras [85], etc.

3.4.3.2 Signal classification and visualization

The logic for classification of a typical signal recorded inside STEM is based on a benchmark data processing library commonly used for electron microscopy: Hyperspy [86]. The dataset measured inside the STEM is first exported from hardware to Python as a multidimensional array in this process. The multidimensional arrays are indexed with two types of dimensions in Hyperspy: the **navigation dimensions** of the scan and the **signal dimensions** of the quantity measured.

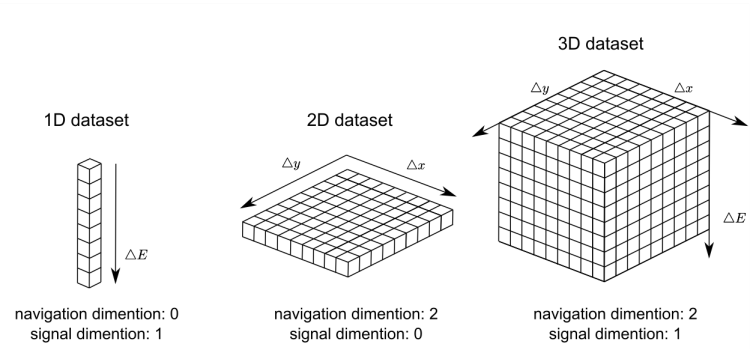

Figure 3.9: **A scheme of dataset nomenclatures for navigation dimension and signal dimension is provided:** (a) one-dimensional dataset (1×1024); (b) two-dimensional dataset ($1024 \times 1024 \times 1$); (c) three-dimensional dataset ($1024 \times 1024 \times 1024$).

The dimension N of the dataset can be represented by the navigation dimension (n) of the sampling and the signal dimension (m) of the result: $N = n + m$. Intuitively, the **navigation dimension** is the image one see with spatial information, while the **signal dimension** is an energy spectrum with a single signal set for each pixel point in the navigation dimension. This definition can be generalized: the navigation dimension can be a temporal dimension or any dimensions, while the signal dimension can be one-dimensional or two-dimensional or even higher.

Datasets with several commonly used dimensions are illustrated in Fig. 3.9. A spectrum

[6] With Medipix3, it can directly measure the dispersed electrons and record the spectrum.

is a one-dimensional data set (N=1, n=0, m=1), and if its spectra has a length of 1024 pixels, it can be represented as (1; 1024), where before the semicolon is the number of pixels in each **navigation dimension**, and after the semicolon is the number of pixels in each **signal dimension**. For an image, it is a two-dimensional array (N=2, n=2, m=0), taking a 1024×1024 image as an example, it can be represented as $(1024, 1024; 1)$. For a spectrum image (SPIM), that is, the spectrum is measured at each point of the image, which is an array of three dimensions (N=3, n=2, m=1), along the above image and spectrum dimensions, at this time the spectrum image can be expressed as $(1024, 1024; 1024)$. If one perform scanning nanodiffraction test on the sample, make 1024×1024 scans on the sample and record a 512×512 diffraction pattern at each scan point, the data dimension is $(1024, 1024; 512, 512)$. In order to visualize the spectrum image, one must select a specific energy range to plot.

3.4.3.3 Electron-energy loss spectrum

As illustrated in Fig. 3.10, an electron energy-loss spectrum is typically divided into three parts: zero-loss peak, low-loss region and core-loss region:

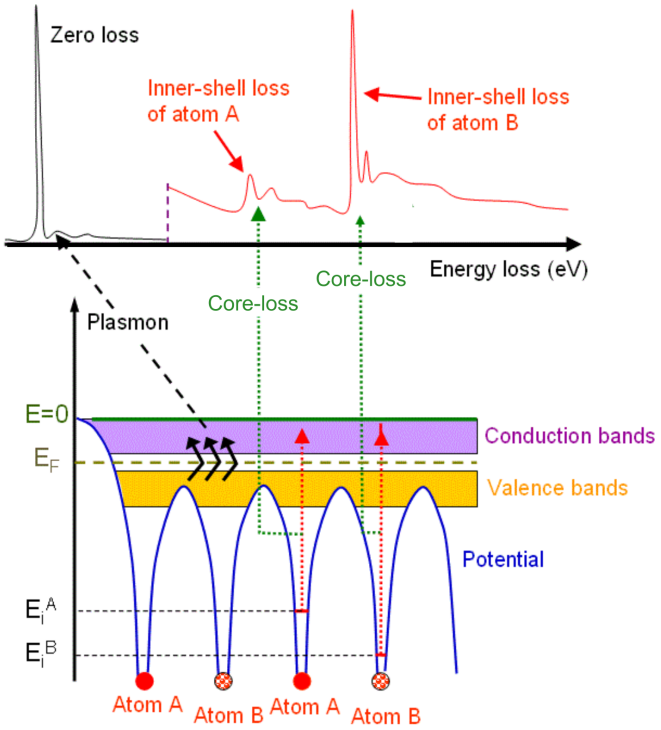

Figure 3.10: **An illustration of the electron energy loss spectrum.** The above diagram shows a typical EELS spectrum with zero loss peak, plasmons, and two core-loss edges of atoms A and B. A lower plot illustrates an energy band of a semiconductor material, showing both the absorption peaks of plasmons and the deep electron excitations in the inner shell. Reproduced from ref. [87].

- **Zero-loss peak (ZLP):** as described in previous section 3.2.1, the incident electrons collide elastically with the sample, and almost no energy is lost; therefore, an EELS system's resolution is generally defined by its ZLP full-width at half-maximum (FWHM). In addition, ZLP can be reduced in width using by several electron monochromator schemes [88, 89], for example, in ChromaTEM, the FWHM is reduced from 300 meV to 5-20 meV after passing through an energy-selecting slit in the monochromator. Due to the fact that most electrons pass through the sample without losing energy, the ZLP is the most intense peak on the EELS spectra.

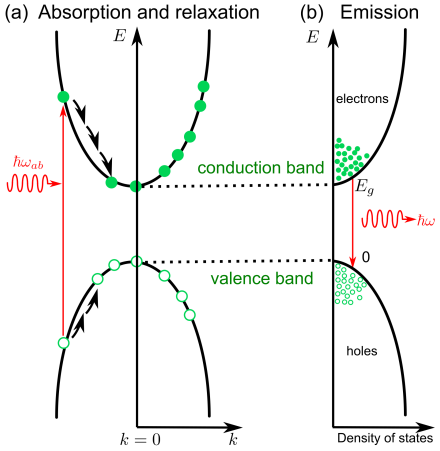

Figure 3.11: **Semiconductor materials with bandgap E_g are excited by electromagnetic waves with frequency $\omega_{ab} > \frac{E_g}{\hbar}$ and de-excited in the following order:** (a) the material first absorbs energy, then electrons leap from the valence band to the conduction band, leaving holes in the conduction band, which corresponding to optical absorption spectrum or EELS; the electrons and holes interact with the phonon, moving towards the extremes of the energy bands, which are indicated by the black arrows in (a); (b) the occupancy of excited electrons and holes in the energy band follows a Fermi-Dirac distribution over time, at which point the electrons and holes recombine, and part of them will go though radiative decay, then give rise to PL or CL emission.

- **Low-loss region:** the energy loss of electrons below 50 eV is mainly determined by the energy band structure of the material, such as excitons, phonons, plasmon, etc.; low-loss regions are generally used to measure the optical properties of the sample, such as excitons, bulk plasmon, surface plasmon, and energy band structures. It includes single electron excitation and plasmon excitation when fast incident electrons scatter inelastically with the outer electrons surrounding the nucleus, as described in section 3.2.2. Actually, the electromagnetic field accompanying the point charge can be considered an evanescent source of radiation, thus **an electron beam could be regarded as a spatially nanoscale, but energetically broad band light source** [34].

In the case of single electron excitation as shown in Fig. 3.11, electrons in the valence band of a semiconductor or insulator can absorb energy to jump to the conduction band, and similarly, electrons in the conduction band of a metal will absorb energy to jump to the conduction band at a higher energy position. Energy absorbed by the sample is released as electromagnetic radiation (for example, electrons in the valence band returning to the conduction band) or heat (electron-phonon interaction).

- **Core-loss region:** the energy loss of electrons is in excess of 50 eV due to the absorption of incident electrons and electron interactions in the inner shells of a atoms. At the ionization threshold, there is a sharp rise in EELS, which approximates to the binding energy of the respective atomic shell. A further characteristic of core-loss in EELS is not peaks but edges, where the inner-shell intensity increases rapidly and falls more slowly with increasing energy loss. By using the initial core state, one can classify absorption edges according to the atomic shell nomenclature according to principle quantum numbetr, n; K for n=1 states, L for n=2 states, etc. By performing core-loss EELS, one can determine both the elemental and chemical composition of the samples.

3.4.3.4 Measurement of specimen thickness: log-ratio method

In addition to optical and elemental information, EELS could be used to measure the thickness of the specimen. The log-ratio method will be introduced here for the purpose of determining the thickness of graphite and hBN in some samples. As the log-ratio thickness measurement assumes that incident electrons going through inelastic scattering events are independent, the Poisson statistic can be used to calculate the probability (denoted as P_n) that electrons will experience inelastic scattering n times.

One electron incident a sample with thickness t, the probability of it undergoing inelastic scattering is t/λ, where λ is mean free path for inelastic scattering, representing the average distance between two collisions. According to the assumption that electrons going through inelastic scattering inside the specimen is independent of each other, the probability of electron being inelastically scattered follow a binomial distribution: $X \sim B(n, t/\lambda)$. When the number of electrons N is large enough, binomial distribution can be approximate into Poissonian distribution:

$$P_n = \frac{(t/\lambda)^n}{n!} e^{-t/\lambda} \tag{3.5}$$

I_t and I_n is given by the specific elastic scattering events (counts of energy loss $t\Delta E$) and sum of inelastic scattering events (counts of all channels), respectively. Thus P_n, the probability of being scattered n times is:

$$P_n = \frac{I_n}{I_t} = \frac{(t/\lambda)^n}{n!} e^{-t/\lambda} \tag{3.6}$$

In practice, the zero-loss peak is always intence and easy to fit. One can fit the ZLP through many models and take its integrated area sum as I_0. Importantly, one needs to make sure that the recorded ZLP peak does not saturate. When $t = 0$, intensity of the ZLP is maximal representing only unscattered events. So when $n = 0$, Eq. (3.6) gives:

$$ln\frac{I_t}{I_0} = \frac{t}{\lambda} \tag{3.7}$$

But this only provides relative thickness, so λ need to be estimated for obtaining the absolute thickness. A precise and easy estimation for λ is based on the dipole approximation when $\beta \ll (E/E_0)^{1/2}$ [71]:

$$\lambda \approx \frac{106F(E_0/E_m)}{ln(2\beta E_0/E_m)} \tag{3.8}$$

Eq. (3.8) gives λ in nm, where E_0 is the incident energy in keV, E_m is the mean energy loss which depends on the chemical composition of the specimen in eV, β is the collection semi-angle before the detector in mrad. According to Malis et al. [90], when average atomic number Z is known, $E_m \approx 7.6Z^{0.36}$, and F in Eq. (3.8) is a relativistic factor defined by: $F = 1 + E_0/1022/(1 + E_0/511)^2$. The mean free path of a 60 keV fast electron inside the hBN and graphene flakes is around 72 nm, which is larger than the thickness of the vdWH samples, thus preventing multiple-scattering. In this regard, electron microscopy is particularly well suited to the study of 2D materials, which by definition have small vertical dimensions.

3.4.4 Cathodoluminescence (CL)

CL signals are collected using a parabolic mirror with a hole that allows the incident electron beam to pass through. As shown in Fig. 3.12, ChromaTEM has a 2 mm CL mirror with numerical aperture of 0.5, inside the 6 mm gap polepiece. This mirror has a focal spot that covers a hole in the grid of 500 nm radius easily. Obtaining CL signals requires the alignment of the beam limiting aperture, the electron beam position, the height and lateral position of the parabolic mirror, and the position of the collection system's fiber.

An optical spectrometer is connected directly to the CL system by inserting the optical fiber bundle. Rather than using mono-mode fibers, fiber bundles can increase the collection of CL light while maintaining spectral resolution. In one experiment, semi-convergence angle α for EELS and CL are same. However, the monochromator slit is removed for CL in order to improve its collection efficiency by providing more current. Since EELS monochromated uses a lower dose, concurrent images suffer more from noise, CL produces a better ADF image than EELS.

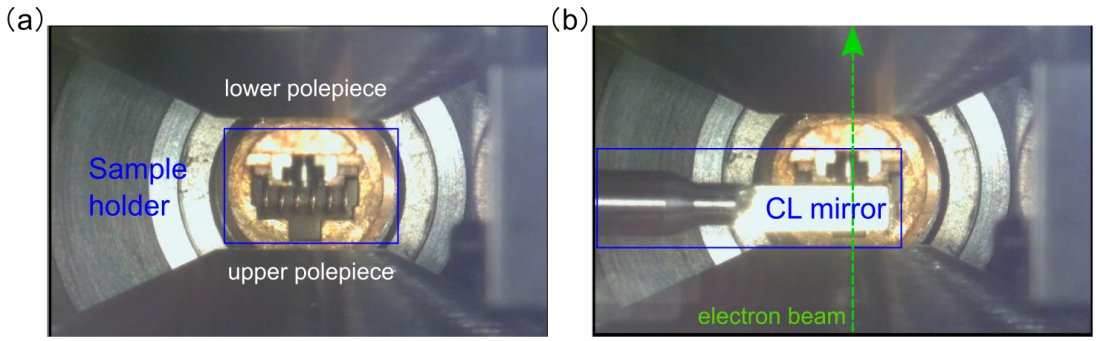

Figure 3.12: **The CL mirror inside ChromaTEM:** (a) ChromaTEM sample chamber: the gap between two polepieces is 6 mm; (b) ChromaTEM sample chamber with a CL mirror inserted that is 2 mm tall.

3.5 Alignment of the electron microscope

ChromaTEM can adjust the focal length, convergence angle and current of the electron illumination independently, because of the presence of three condenser lenses as I described in section 3.3. There are mainly four different mode that I used in this thesis, and their essentially different is convergence angle α as shown in Fig. 3.13. Based on the condenser and projector lenses, the electron microscope can be switched back and forth between EELS mode, diffraction mode and standard mode, while not necessary to tune the focal length. Usually, standard mode (Fig. 3.13(a)) is used to get high-resolution images as reference for EELS and diffraction experiment. Scanning and wide-beam diffraction modes are used to get the lattice deformation and roughness of TMD monolayers in this thesis, respectively. Additionally, CL is also measured at the same condition as EELS mode with the monochromator slit out.

The electron beam energy is set at 60 keV for all measurements, and the wavelength of the electrons is 4.9 pm [91]. Because of the cryogenic-capable sample holder, samples are able to be cooled down to liquid nitrogen temperature LN_2 (110 K) for EELS and CL measurement. The convergence and collection half-angles for the EELS measurement is 21 mrad which is corresponding to 1 mm entrance aperture. The convergence half-angle was set to 1 mrad to approximate an almost parallel beam in TEM for the diffraction measurements, and 1 or 5 mrad for nano-scale diffraction. It is important to note that

when using near-parallel-beam (also called wide-beam illumination) diffraction mode, a Köhler illumination is used, which ensures a uniform distribution of electrons over a large specimen area and <1 mrad diffraction spots. To achieved the Köhler illumination, it demanded to tune the electron beam crossover before the polepiece to the front focal point of it, thus the uniform and parallel distribution of electrons can be achieve within the polepieces. Other modes are diffraction-limited, which means the spatial resolution is either limited by aberrations or sampling. In the experiments, the sampling step in general is set at 2-10 nm, which is very far from the diffraction limit.

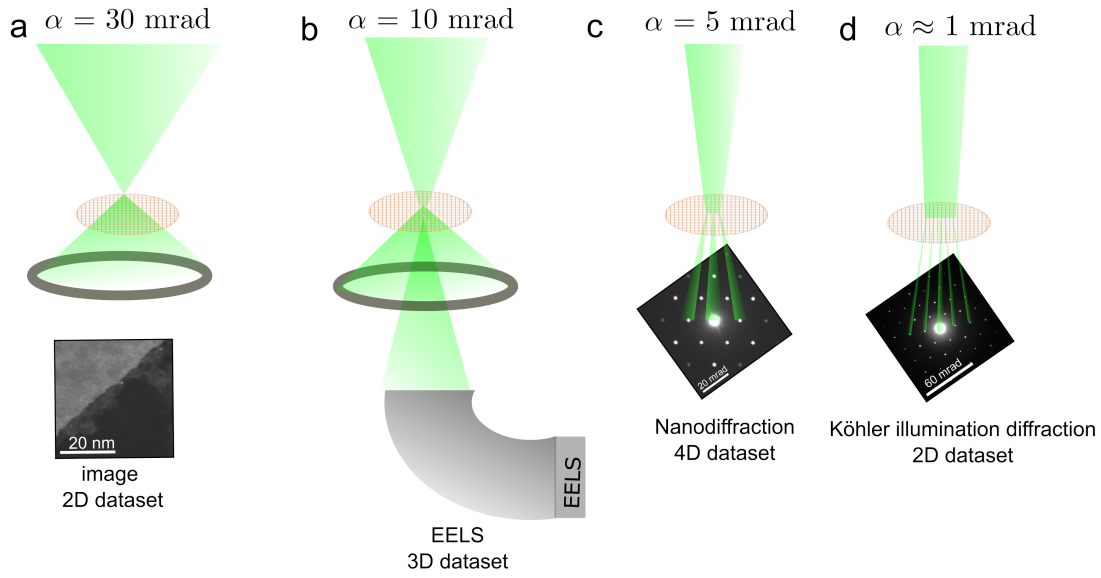

Figure 3.13: **Operating modes defined by the convergence angle:** (a) 30 mrad standard mode in ChromaTEM for imaging; (b) 10 or 15 mrad for EELS mode. (c) 1 mrad or 5 mrad nanodiffraction mode for strain mapping. (d) 1 mrad wide-beam diffraction mode.

Control software AS2 for ChromaTEM can store multiple operating modes which can be freely selected by a simple click on the computer after calibration of each candidate setting. But there are still fine tuning to be made, such as beam shifts, astigmatism and focal length.

EELS scan mode

Two types of EELS spectra are measured in this paper: **slow-scan** and **fast-scan** EELS. Typical exposure time for slow-scan is 150–500 ms per pixel, with the CMOS/Merlin detector exposure time the same as the sample dwell time, typical of a scanning/detector scheme for STEM-EELS spectrum imaging (SPIM). For fast-scan, the beam rasters on top of the sample at a speed of several μs per pixel and detector is accumulating for 150-500

ms like in slow-scan, such that each spectrum is averaged across the full scanned area from a few passes on few hundred square nanometers, as shown in Fig. 3.14.

In order to distinguish beam scan rate and detector accumulating period, **sampling dwell time** and **exposure time** are used to describe how long the beam dwells at each scan position before moving to the next position, and the time taken to accumulate the spectrum, respectively. The low-loss, and core-loss EELS spectrometer dispersion is around 5 meV/pixel and 1.06 eV/pixel, recorded onto a Princeton Instruments KURO CMOS detector with 2048×2048 pixel array or Merlin detector with 1024×256 pixels. The monochromatic zero-loss peak of EELS used for the experiments is around 5-20 meV.

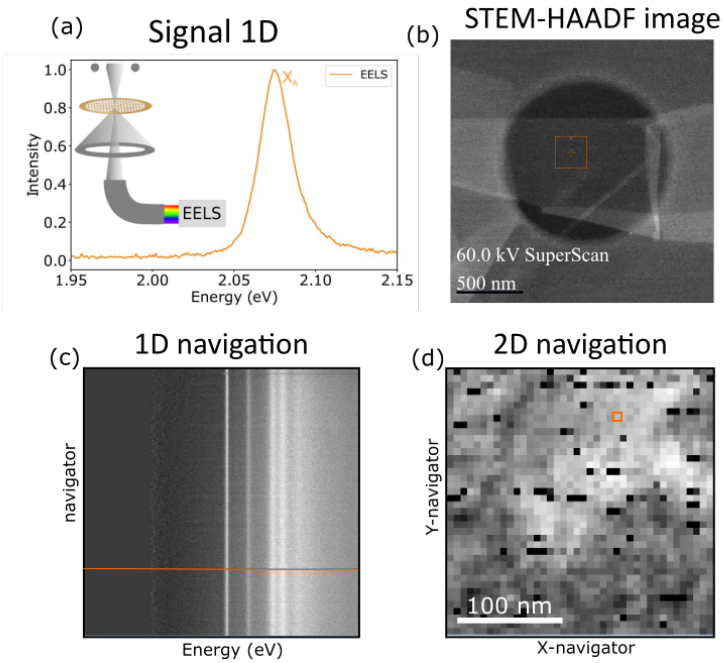

Figure 3.14: **Slow-scan and fast-scan mode for EELS.** (a) EELS spectrum either corresponding to orange line profile in (c) or one SPIM pixel in (d). (b) is the scan area reference image for both (c) fast-scan and (d) slow-scan.

Electron diffraction

In the wide-field illumination diffraction experiments of monolayer TMDs, the beam diameter was around 100 nm wide, which provides a good compromise of not only containing few corrugation periods but also providing some local information. As the accurate size measurement of the beam is unachievable, the HAADF image under this setting enables one to estimate the beam diameter is larger than 100 nm. In the scanning nanodiffraction experiments, the convergence semi-angle α was set to 5 mrad. The beam size is around a few nanometers, and so is the raster sampling step used to extract local

strain and deformation.

3.6 STEM Data analysis

The raw spectrum-image and diffraction data must be processed before interpretation. A majority of the data treatment tools used for EELS/CL are available in Hyperspy or Gatan DigitalMicrograph, including zero-loss peak alignment, gain calibration, background remove, multi-fit, as described in section 3.6.1. For the scanning nanodiffraction datacube, the direct-peak centralization, peak finding and center of mass determination using Pyxem library will be explained in section 3.6.2, which are the basic steps before the deformation and roughness analysis.

3.6.1 EELS/CL spectrum image data process

Gain correction, hot-pixel removal and ZLP alignment of EELS

In ChromaTEM, it is four 256×256 pixelated-detectors (Medipix) arranged together into a 1024×256 array detector. For direct electron detectors, the gain (accounting for variation in sensitivity of different channels) of each pixel point is fixed at the same acceleration voltage. It is therefore possible to apply gain correction to each spectrum to obtain a better signal, which is achieved by measuring a gain reference under uniform illumination. In addition, a hot pixel is generated at the joint of every two detectors, and this hot-pixel is the result of the physical seam and edge of individual detector chips in Fig. 3.15(a). This pre-processing step is required for all acquired spectra on the Merlin detector. Additionally, there are some small spikes in the test results that are also hot pixels arising from the electronics.

For the 1 mm EELS aperture, only half area of the detector is activated. Specially, each column is integrated into a single pixel along the non-energy-dispersive direction. Therefore the gain correction also only takes the sum of the unilateral half-lengths in y direction as a reference. In Fig. 3.15(c), as compared to the spectrum before gain correction (blue and orange), the spectrum after gain correction (green) is less noisy. EELS spectra can shift as a result of voltage instabilities on the camera over time. This is reflected in a shift in the ZLP position from one pixel to another in the spectrum image, as shown by blue curve in Fig. 3.15(b). An alignment procedure is applied in order to correct the ZLP shift by aligning all maximum intensity pixel to same energy position $E = 0$ eV, as shown by orange line in Fig. 3.15(b). Using software Hyperspy or Digital Micrograph, this alignment procedure was automatically performed. The gain-corrected, hot-pixel removed and ZLP-aligned spectrum is shown in Fig. 3.15(c), and it indicates that it is less noisy after the treatment.

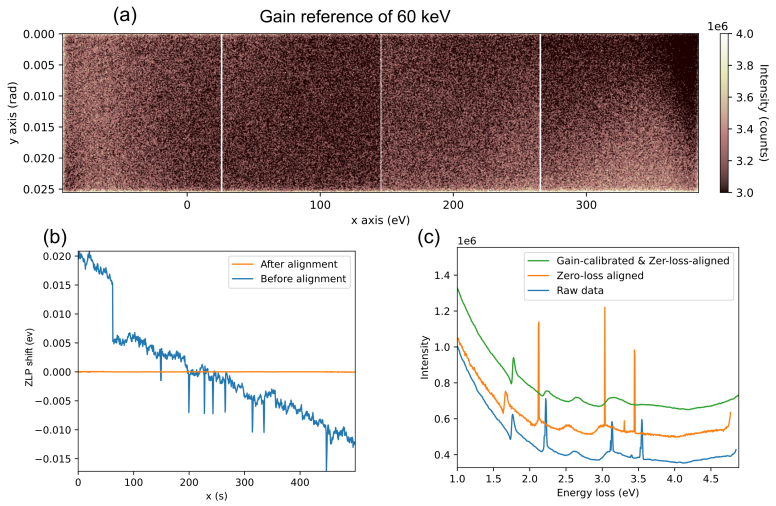

Figure 3.15: **Gain reference, calibration and zero-loss peak alignment.** (a) Gain reference measured on the Merlin detectors at 60 keV. (b) The ZLP position before and after the alignment. (c) Spectrum of TMDs excitons before and after the gain-correction, hot-pixel removal and ZLP-alignment, the spectrum is the sum of 1000 fast-scan spectra.

Background removal of EELS

As seen in the EELS spectra of Fig. 3.16, the sample's response is located at the tail of the ZLP. In order to obtain the response of TMD excitons, ZLP must be extracted after the alignment as mentioned. Various methods can be used for ZLP subtraction, such as Gaussian/Lorentzian fitting, reflected tail, power-law background tail.

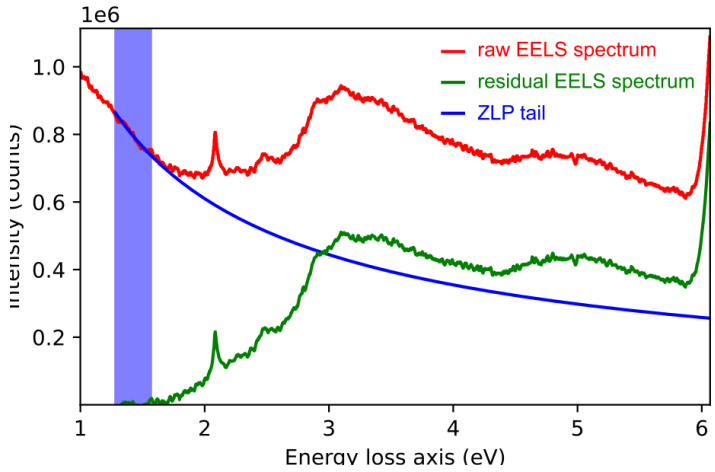

Figure 3.16: **EELS background extraction by power-law model**: the residual spectrum (in green) is extracted from raw data (in red) subtracts the ZLP tail (in blue).

Generally, one selects a method based on the setup and the quality of the data (signal-

to-noise ratio). The right-hand side of the ZLP can be subtracted by reversing the left-hand side of the ZLP for a (S)TEM equipped with a monochromator, and it is known as reflected tail subtraction, but this method may add artifacts if the ZLP is not highly symmetric. In the case of Gaussian/Lorentzian methods, one must fit the shape of ZLP by either methods, and then subtract it to obtain the residual spectrum.

In this thesis, Gaussian/Lorentzian are used to fit the ZLP background for log-ratio thickness calculation. However, for low-loss spectra, the logarithmic tail is a straightforward and direct method as one can customized choose the range of the tail for the fit. Logarithmic tail considers that the tail of the ZLP is estimated by the elastic scattering and that obeys an exponential distribution. As illustrated in Fig. 3.16, a power-law background model separates the raw spectrum into ZLP tails and residual spectrum of monolayer TMDs.

Read-out noise and calibration of CL

A wavelength-dispersive dispersion grating with 150 grooves per mm was used to measure the CL signal, and the resolution is 0.34 nm/pixel or 0.8 meV at 720 nm. In order to obtain a better signal, an EMCCD is used for CL detection, and read-out noise should be subtracted. Aside from that, there are also cosmic X-rays that keep randomly hitting on the camera in the form of spikes on CL spectra. The derivative method allows to identify and remove these spikes by providing appropriate threshold. As mercury-argon light sources provide accurate gas emission lines, they are used to calibrate the CL spectrometer.

In this thesis, CL data f(λ) recorded on EMCCD in intervals of wavelength need to be plotted in energy units. Thus it is necessary to convert signal in wavelength f(E) to energy $f(\lambda)$. From conservation of energy, $f(E)dE = f(\lambda)d\lambda$, thus

$$f(E) = -f(\lambda)\frac{hc}{E^2} \tag{3.9}$$

where hc/E^2 is called Jacobian transformation factor. One can make this non-linear transformation by Lumispy [92] python library or Gatan DigitalMicrograph.

Smoothing and denoise

As the energy loss increases, the signal intensity of EELS decreases [68]. Thus, the signal-to-noise ratio (SNR) is small and the signals are heavily affected by noise. Therefore, several methods are necessary to remove the noise and extract the signal. In many cases, noise can be understood as rapid, random fluctuations in amplitude from point to point within the signal. Several methods can be used to reduce noise, including sliding-

average, weighted, and Savitzky-Golay smoothing, which is the least-squares fitting of polynomials to segments of the data. It should be noted, however, that low-frequency noise remaining in the signals still interferes with the precise measurement of peak position, height, and width even after smoothing. If smoothing is applied on some of the low-loss EELS data for noise reduction, it will be indicated.

Principal Component Analysis (PCA)

Additionally, principal component analysis (PCA), which is a dimensionality reduction method, is often employed to reduce the dimensionality of the spectra being studied. A better interpretation of spectra can be achieved by focusing on the most important key components. PCA is accomplished by transforming a large number of variables into a smaller subset that still represents most of the information from the large set based on the following steps: i) standardize the dataset X; ii) calculate the covariance matrix XX^T; iii) calculate the eigenvalues and eigenvectors for the covariance matrix through singular value decomposition method $X = USV^T$; iv) sort eigenvalues v of V in decreasing order; v) construct the projection matrix from the chosen number of top eigenvalues. PCA is applied in the weak core-loss EELS signals to map the contamination and low-loss EELS on monolayers at room temperature.

Model fitting

Spectrum imaging (SPIM) has the advantage of allowing the creation of various maps based on the information generated at each pixel. Models can be used to fit the selected region of the EELS/CL spectrum to study the energy position and FWHM of the excitons throughout different regions of the sample. In this thesis, I used the Lorentzian/Gaussian distribution to fit the excitons in EELS/CL spectrum.

3.6.2 Diffraction pattern

To study the lattice deformation and roughness from scanning diffraction and tilt-series diffraction, a dataset is processed as follows. First, align all direct beam to the center position through cross correlation by measuring the similarity of all direct beam as a function of the displacement and shift them all to the center of same origin point. One needs to check the radius of the direct beam is in the range for searching. Secondly, several blob detection algorithms such as the Laplacian of Gaussian (LoG), difference of Gaussian (DoG) are used to locate diffraction spots. Since there is a compromise between spatial and reciprocal resolution, diffraction peaks are disks instead of dots. In this case, refinement of the spot location is necessary through center of mass. One can index all the peaks through coordinates and magnitudes, and select two pairs for base vectors of strain mapping or lattice deformation. In the case of tilt-series diffraction patterns, they were stacked together to create a 3D dataset after the above-mentioned processing. The scale of diffraction patterns is calibrated using a standard sample of gold. Besides Pyxem, Py4dstem and Libertem are also available Python library for pixelated 4D STEM processing tasks.

Chapter 4

Sample preparation of van der Waals heterostructures by viscoelastic stamping

The purpose of this chapter is to introduce the sample preparation method for the monolayer TMD Van der Waals heterostructures (vdWH): **viscoelastic stamping**. As a tool for transferring and stacking 2D materials, a viscoelastic polymer stamp [93, 94] is commonly used. It is important to remember that this method, along with maintaining clean interfaces, allows one to create different vdWHs at will.

In order to make the TMD samples for (S)TEM, one not only needs to prepare the monolayer but also transfer the fragile monolayer/multilayer membranes onto microscope-compatible grids. As a matter of fact, TMD monolayers are easily available, either direcly grown using chemical vapor deposition (CVD), or as a result of mechanical exfoliation using Nitto blue tape. The above methods for preparing monolayer 2D materials are well-established. In addition, the yield of monolayers by exfoliation can be improved by a gold-mediated process because of gold have of strong affinity for chalcogens which can preferentially obtain large areas of TMD monolayers [95].

In this chapter, it will be first discussed how to prepare a viscoelastic polymer stamp in section 4.1. For the selection of target thickness of 2D materials, for example hBN, graphite and TMDs, their thickness can be identified by imaging contrast differences caused by material thickness in optical microscope, as shown in section 4.2.

Several robust electron microscopy grids that can withstand stamping is concluded in section 4.3. In fact, an optical microscopy-based sample transfer stage is necessary (section 4.4) for the preparation of vdWH, which is detailed in section 4.5. This chapter concludes with the presentation of all TMD heterojunction samples studied in this thesis in the last section 4.6.

4.1 Viscoelastic polymer stamp preparation

In terms of materials, viscoelasticity refers to the combination of viscous and elastic characteristics when the materials are deformed. Viscoelastic materials behave elastically under slow deformations, whereas they only exhibit viscosity under rapid deformations [93, 96]. A polydimethylsiloxane (PDMS) film is a viscoelastic and optically transparent material that allows flakes to be aligned during the stacking process under an optical microscope, as well as different ways to touch a substrate depending on its speed.

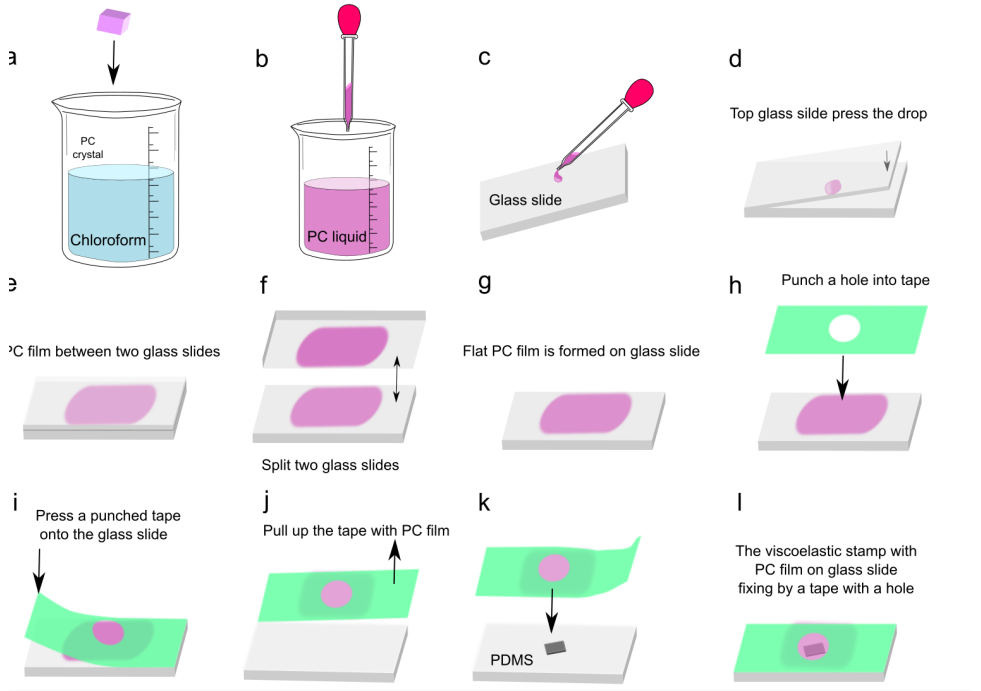

Figure 4.1: **Scheme of a viscoelastic stamp preparation:** (a) PC crystal dissolved inside the chloroform to make PC solution, the weight ratio between chloroform and PC crystal is 19:1; (b) take a drop a PC liquid by a pipotte; (c) put a drop of PC liquid on the glass slide; (d) take another glass slide and press the PC solution drop; (e) two glass slides are fully contacted and PC drop squeezed into thin liquid film; (f) split two glass slides, PC film are at both sides; (g) choose the flatter one, usually both of the PC films are flat on the slide; (h) take a punched tape, align the center of the hole with the center of the PC; (i) press the tape to the PC film; (j) pull up the tape with the PC film; (k) take the tape with PC film and align the center of its hole with a small PDMS on glass slide and press the tape on the glass slide; (l) an intact viscoelastic stamp with PC film on glass slide fixing by a tape with a hole is ready.

Glassy substance can go through glass transition at T_g (glass transition temperature), which is a reversible transition between the glassy and highly elastic states . At temperatures below T_g, the material exhibits a rigid "glassy" state, while at temperatures

above T_g, the material exhibits a viscous or rubbery state. Polymers, such as polycarbonate (PC), polypropylene carbonate (PPC), etc., all have this reversible glass transition [97]. But the glass transition temperature of materials is very different, like polystyrene (PS), polymethyl methacrylate (PMMA) these materials have T_g higher than room temperature, so at room temperature these materials are glassy and inelastic; while some materials such as polyisoprene, polyisobutylene (PIB), their T_g is lower than room temperature, so at room temperature is soft and flexible on the other hand [97, 98].

A viscoelastic stamp used for samples preparation in this thesis consists of a small PMDS block adhered between a glass slide and a polycarbonate (PC) film by tape in the case of high-temperature capable transfer technique [99]. The process of this stamp preparation is presented in detail as shown in Fig. 4.1. In general, the polymer of a viscoelastic stamp could be either PC (T_g = 147°C) or PPC (T_g = 40°C) [98].

Compared with some other methods [100, 101], the viscoelastic stamp avoids the direct contact between the heterojunction interface and the solution or polymer, so the adsorbates at the interface are greatly reduced, which guarantees the cleanliness of the heterojunction interface [102, 103]. It was shown that the contacting process between 2D flakes generate many small bubbles, which converge with each other to form large bubbles within a few seconds when the temperature increases (the movement process can be seen in the video in reference [102]).

In the preparation of heterojunctions by the viscoelastic stamp method, the viscoelastic stamp is in contact with the material on the substrate at a certain inclination angle (see section 4.5 for details), and the viscoelastic stamp pushes small bubbles containing interfacial impurities toward the boundary of the heterojunction. At high temperatures, the migration rate of bubbles and impurities is faster than it is at low temperatures, so **the heterojunction interface is cleaner at high temperature**, as shown in Fig. 4.2. Also, the quality of the heterojunction interface is affected by the speed of contact between the two, and in general, **slower contact results in fewer impurities** [102].

Therefore, we chose the PC with higher T_g temperature as the polymer in the viscoelastic stamp. Both PC and PDMS in the viscoelastic stamp are transparent, so that through it one can still visualize the flaky 2D materials on the substrate and can choose whether to image the viscoelastic stamp or the substrate by changing the optical microscope focal length (see section 4.4 for details).

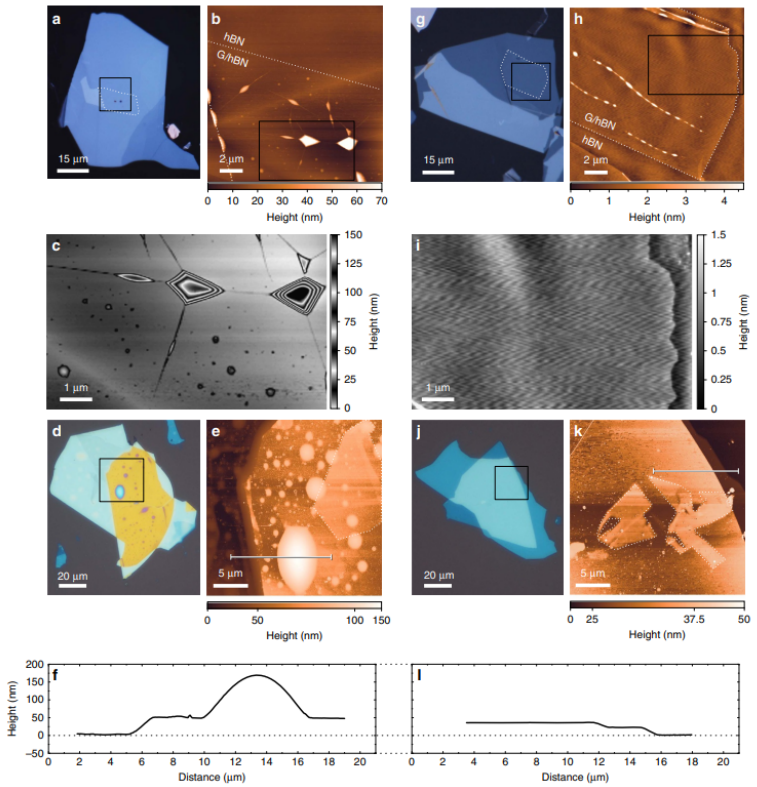

Figure 4.2: **Interfacial quality of vdWH at different assembly temperatures:** (a) microscope view of a graphene/hBN heterojunction on a PPC, where graphene is brought up by hBN on the PPC at 40°C. (b) Atomic force microscope (AFM) in the area marked in (a); (c) magnified view of the area marked with a black box in (b). (d) At 40°C, many bubbles are clearly visible when hBN/graphene is placed on another piece of hBN. (e) Corresponding to the AFM map marked by the box in (d). Graphene is clearly visible due to the extra blisters, and the graphene heterojunction is marked by the dashed line. The height difference of the white straight line range in (e) is given by (f). (g) At 110°C, otherwise the same as in (a). (h) AFM shows that the maximum height difference of graphene/hBN on the substrate is less than 5 nm with almost no bubbles. (i) The region marked by the black box in (h), compared with (e). (j) At 1100°C, hBN/graphene is placed on another piece of hBN, and no impurities can be seen under the optical microscope. (k) AFM plot corresponding to the black boxed region in (j), with the height difference of the white straight line range (i) given in (l). Reproduced from ref. [102].

4.2 Flake identification in the optical microscope

The selection of materials is crucial for the production of 2D vdWH. In most cases, there is a requirement for the thickness of the material to be specified, e.g., monolayer TMDs, graphene and tens of nanometers hBN and graphite, etc. The hBN, graphite and most of the TMDs are thinned by mechanical exfoliation onto SiO_2/Si substrates. However, this approach will result in a very wide range of material thicknesses, generally from monolayer to several hundred nanometers.

It has been reported that the color and contrast of 2D flakes are thickness-dependent [104, 105, 106, 107], one could identify the thickness combination with theoretical calculation by Fresnel equation [104, 106, 108]. A simple and convenient technique was developed to observe and identify the number of layers of 2D materials on substrates under an optical microscope [104, 105, 106, 107]. This is because even a single layer increases the light path of reflected light sufficiently so that a change in interference color with respect to the color of the empty substrate occurs (phase contrast).

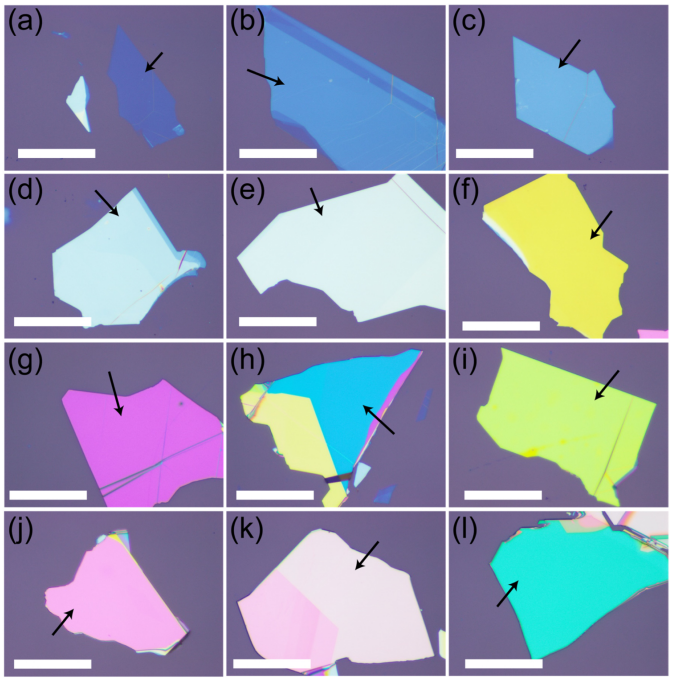

Figure 4.3: **Optical images of hBN flakes on 90-nm SiO_2/Si substrates.** The scale bars are 50 μm. The thickness of the regions indicated by the arrows are (a) 3.6, (b) 8.1, (c) 11.5, (d) 37.3, (e) 52.1, (f) 95.6, (g) 130.7, (h) 147.9, (i) 194.2, (j) 244.4, (k) 319.4, (l)398.4 nm. Reproduced from ref. [104]

.

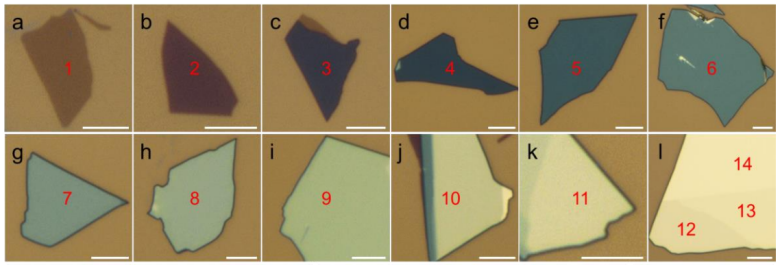

Figure 4.4: **Color optical images of 1 to 14 layers of WSe_2 nanosheets on 90-nm SiO_2/Si.** The scale bars are 5 μm. The digits shown indicate the number of layers of WSe_2. Reproduced from ref. [105].

In this thesis, this fast and facile method was used to estimate flake thickness under the optical microscope. Thickness could be measured more precisely in the electron microscope by t/λ if needed, as detailed in ref. [104, 106, 108] and section 3.4.3.4. Fig. 4.3 gives the color benchmark of hBN thickness ranging from 3.6 nm to 398.4 nm on 90-nm thick SiO_2/Si substrate under white light illumination [104]. In Fig. 4.4, optical contrast used to identify various thickness of WSe_2 on 90-nm SiO_2 is also presented.

The 2D materials used for the vdWH stacks are provided by our collaborators including: MESO group at LPS (France), University of Münster (Germany), Imperial College London (United Kingdom), International Center for Materials Nanoarchitectonics (Japan), National Taiwan University of Science and Technology (Taiwan).

4.3 (S)TEM grids for electron microscope

For performing experiments on very thin 2D vdWH in an electron microscope, the sample needs to be transferred to an appropriate (S)TEM support grid. The grid consists of two parts: a conductive grid and a support film. The conductive grids include but not limited to: Au, Mo, Cu, Ni, doped/coated Si_3N_4 and other materials. There are two main types of support films: continuous support films and porous (holey) support films, typical materials including: carbon porous films (holy carbon) and amorphous Si_3N_4 films.

It is necessary to transfer the stack on top of the relatively more fragile (S)TEM grids for electron microscopes, as opposed to most optical work involving dropping stacks onto silicon or sapphire substrates. This places two demands on TEM grids: support membrane that are tough which wouldn't break during several temperature change processes; membranes that are flat which undertakes uniformly stress with the melting PC, so they wouldn't break when immersed inside solution. A number of types of grids meet the above requirements. Below are the grids that have met the above requirements after several tests, which can also provide different dielectric environments:

- The Quantifoil Mo/Au-supported holey carbon film grid. In this case the sample is self-supporting, with vacuum on the top and bottom sides of the material;
- The PELCO silicon-supported holey 200-nm Si_3N_4 film with 10-20 nm thick carbon film is deposited on the back side of the grid to ensure its electrical conductivity. In this case the sample is self-supporting, with a vacuum on the top and bottom sides of the material.
- The PELCO silicon-based 15-nm thick Si_3N_4 continuous film support grid: monolayer or stack are on top of 15 nm-thick amorphous Si_3N_4.

4.4 Temperature controlled transfer stage

A setup was developed by the MESO group at LPS to perform the 2D materials transfer process, as shown in Fig. 4.5. It consists of an optical microscope with a sample stage, and an additional heating stage with 3D micromanipulators. In practice, the slide with viscoelastic stamp itself is usually inverted on the the sample stage of microscope , while the substrate with the 2D material to be picked up is placed on the heating stage, as shown in the embedded image of Fig. 4.5.

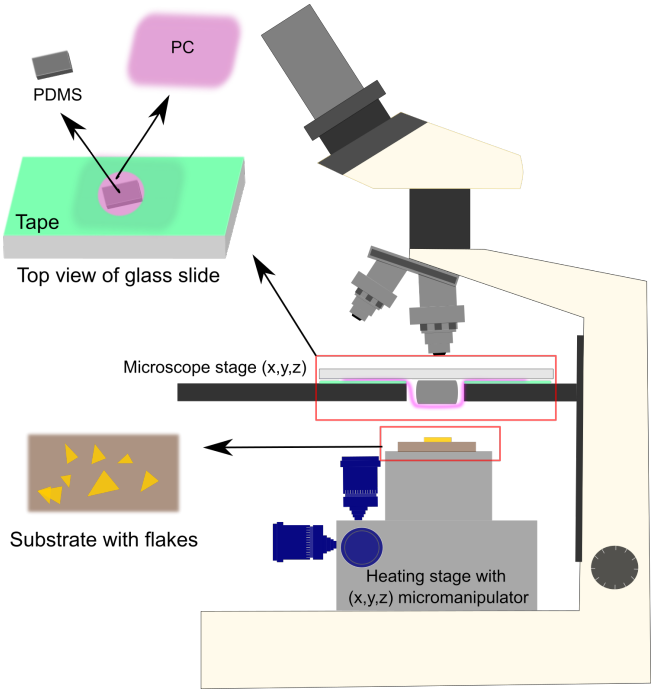

Figure 4.5: **A modified optical microscope with an additional heating stage for 2D materials stacking transfer and alignment.** Substrate and stamp are at their position ready for contact.

The first step of stacking is to focus the microscope on its own sample stage, and then adjust the height of the heating stage so that the 2D materials on the substrate is also visible, thus identifying the candidate flake. By slowly raising the heat stage, flakes on heating stage will come in to focus and then touch the upper stamp. It is important not to allow the 2D material on the substrate to come into full contact with the viscoelastic stamp. Therefore, the microscope needs to be kept slightly overfocused with respect to the substrate, and then slowly warm the heating stage. In this way, the desired flake on the substrate can be aligned with the flake on the stamp so that the two overlap each other to form a heterojunction. Due to the magnetic base on which the heating stage is mounted, the stage's position is relatively stable during the whole process.

4.5 Stacking transfer process and alignment

The stacking and transfer process are made by viscoelastic stamp method in a transfer stage as mentioned. A flowchart of a hBN/$MoSe_2$/graphite stack on top of Mo-based grid as shown in Fig. 4.6 is exemplified as follows:

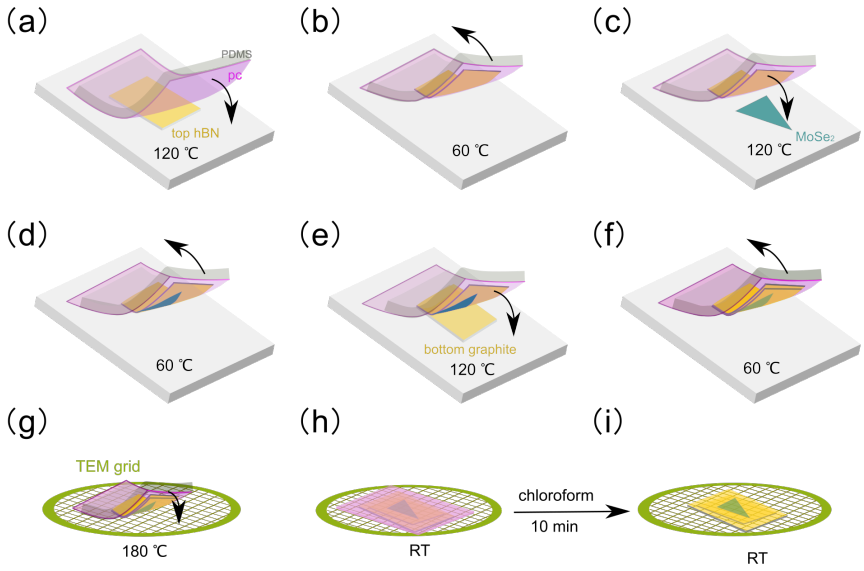

Figure 4.6: **Scheme of fabrication process for the hBN/$MoSe_2$/graphite vdWH.** (a) PC film (light purple) is pressed by PDMS (grey) to contact hBN (yellow) on the Si substrate (white). (b) The hBN flake has been picked up by PC. (c) PC film with hBN is ready to pick up monolayer $MoSe_2$ (dark green). (d) Monolayer $MoSe_2$ has been picked up by PC with top hBN layer. (e) hBN with monolayer $MoSe_2$ is ready to pick up lower graphite flake. (f) The bottom layer graphite is picked up from the Si substrate. (g) The whole stack is ready to be dropped on top of grid by PDMS. (h) The stack is dropped on top of TEM grid at 180 °C and PDMS is withdrawn. (i) PC is dissolved in chloroform and the whole stack is firmly attached on top the grid.

(a) Slowly raising the height of top hBN layer, it will contact the PDMS/PC stamp. Then heat the substrate on heating stage to 120°C.

(b) Cool the substrate down to 60°C, then stamp withdrew slowly with the hBN attached to PC and picked up from its original substrate.

(c) stamp with top hBN is ready to pick up $MoSe_2$ monolayer at 120°C;

(d) cool the substrate down to 60°C, then withdraw the stamp with the hBN and $MoSe_2$.

(e) Drop the stamp to contact with the bottom graphite and heat the substrate up to 120°C.

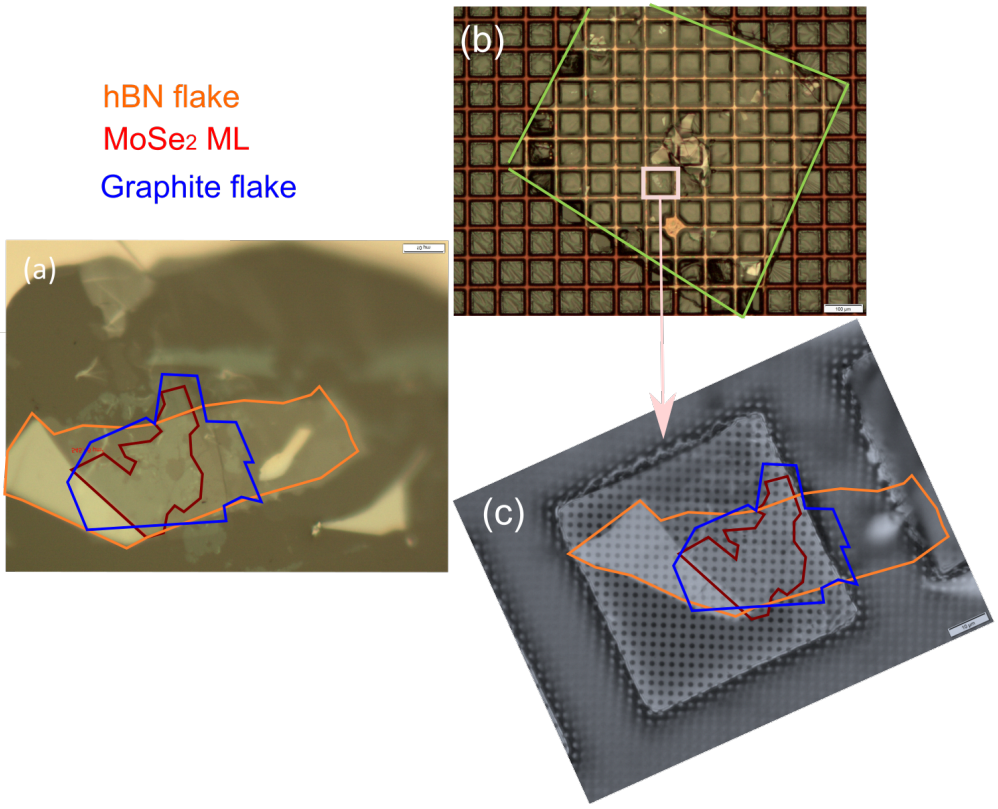

Figure 4.7: **The vdWH stake image at different stages of transfer:** (a) stack on PC (image mirror inverted), scale bar 10 μm; (b) stack is covered by PC on TEM grid, stack is on the window marked by pink square, big green square is the area of PC film; (b) stack on TEM grid after PC removed by chloroform.

(f) Pull back the stamp with the whole stack at 60°C, optical image of the whole stack as shown in Fig. 4.7(a).

(g) Drop the stamp with whole stack on top of the TEM grid at 180°C.

(h) Wait the temperature to decrease below 90°C, then withdraw the stamp quickly. There will be only a PC-covered stack left on grid. Fig. 4.7(b) shows the optical image of the whole stack covered with PC, the large square is the size of PC. Stack is on the grid window marked by pink square.

(i) Put the grid inside chloroform for 10 min to remove the PC film. Finally, the clean stack is on top of grid. The optical image of the whole stack on TEM grid as shown in Fig. 4.7(c).

4.6 Summary of samples

All samples related to this thesis are summarized with their stack configuration, TMD source, and purpose of fabrication in Table 4.1. There seems to be a great deal of work involved in the preparation of these samples, but some of the different types of stacks

are made at one time, and the upper or lower layers only partially cover the TMD monolayers, so at least part of the workload has been reduced. The composition of the vdWH at different areas on the same sample can be identified by the diffraction pattern, the characteristic EELS peak. Dr. Steffi Y. Woo and Dr. Nianjheng Wu made some of these samples at LPS, while Dr. Robert Schneider at the University of Münster provided others.

Table 4.1: **Summary of TMDs vdWH samples in this thesis.** There are three different TMDs studied: WS_2, WSe_2, $MoSe_2$.

TMD type	Stack	TMD source	Purpose
WS_2	WS_2	Exfoliation	Linewidth
	WS_2	CVD	Linewidth
	WS_2/hBN	CVD	Linewidth
	hBN/WS_2/hBN	CVD	Linewidth
	WS_2/Si_3N_4	CVD	Linewidth, damage, charging
	hBN/WS_2/Si_3N_4	CVD	Linewidth, damage, charging
	WS_2/Gr	CVD	Fano
	graphite/WS_2/graphite	CVD	Fano
WSe_2	WSe_2	Exfoliation	Fano
	WSe_2/hBN	Exfoliation	Fano
	hBN/WSe_2/hBN	Exfoliation	Fano, CL
	graphite/WSe_2/graphite	Exfoliation	Fano
	graphite/WSe_2/hBN	Exfoliation	Fano
	hBN/WSe_2/graphene/hBN	Exfoliation	Filtering trion in CL
$MoSe_2$	$MoSe_2$	Exfoliation	Fano
	$MoSe_2$/hBN	Exfoliation	Fano
	hBN/$MoSe_2$/hBN	Exfoliation	Fano
	graphite/$MoSe_2$/graphite	Exfoliation	Fano
	graphite/$MoSe_2$/hBN	Exfoliation	Fano

Chapter 5

Lattice deformation and corrugation of two-dimensional monolayers

There are numerous van der Waals layered materials, including hexagonal boron nitride (hBN), transition metal dichalcogenides (TMDs), graphite, phosphorus, which can be exfoliated into monolayers [109, 110]. Graphite, for example, is a two-dimensional (2D) materials that is build up from graphene layers through van der Waals interaction [111]. Exfoliation from bulk crystal and epitaxy are both very well established methods for synthesizing these monolayers [112, 113, 114]. In this chapter, I examined the influence of substrate on TMD monolayer roughness through electron diffraction.

Section 5.1 provides background and motivation for the study of roughness in 2D monolayers. The structural properties of 2D material are presented in section 5.2, including the crystallography of graphene, TMDs and hBN. The wide-beam diffraction-based roughness measurement method and research topics linked to it are presented in section 5.3. Then, the experimental results and simulation details of sample tilt-series electron diffraction are introduced in section 5.4.

In section 5.5, an investigation of the temperature dependence of the corrugation of monolayer freestanding TMDs is presented. In section 5.6, comparison is performed between freestanding and hBN encapsulated WSe_2 with respect to lattice deformation. In the last section 5.7, a summary is provided of the roughness of TMDs monolayers under different vdWH configurations.

5.1 Background and motivation

Initially, a portion of physicists believed that monolayer 2D freestanding materials were unlikely to exist stably [115]. In the 1930s, it was argued that if a strictly 2D material existed, its lattice would collapse due to its inability to withstand the vibrations caused by thermal fluctuations, forming other relatively stable disordered or three-dimensional configurations [10, 116]. Calculations have demonstrated that carbon possesses a large

number of energetically lower 3D structures than graphene, and so it would seem unlikely that graphene could exist by itself [117, 118], as shown in Fig. 5.1.

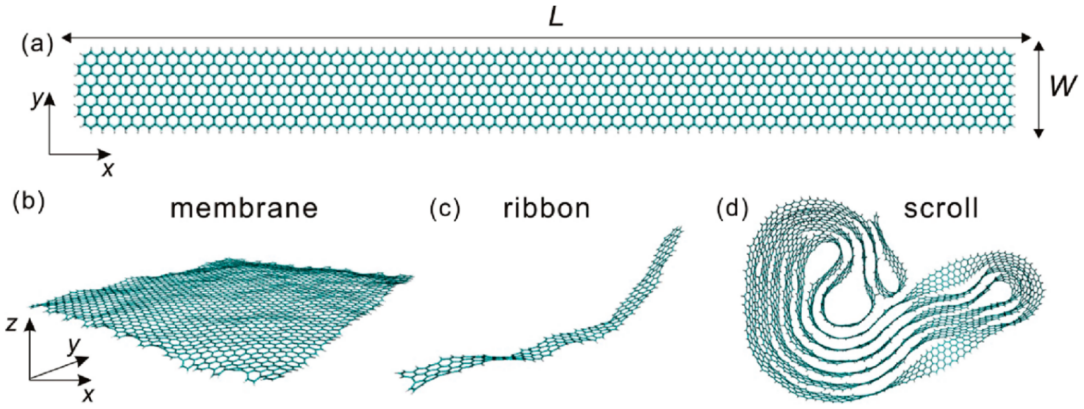

Figure 5.1: **Various 3D structures of graphene at room temperature:** (a) atomic structure of zigzag-edged graphene sheet with width W, length L; (b) ripped membrane; (c) bent and twisted ribbon; (d) nanoscroll stabilized by van der Waals interaction between adjacent graphene layers. Reproduced from ref. [117].

Considering it in terms of entropy, just as a tangled cord is rarely able to be straightened absolutely, tends to bend and twist, a thin film of atoms will always crumple and curl in order to increase its entropy [117, 118]. It has been found that when thin films of atomic thickness are grown, the atoms tend to aggregate into nano-dots rather than uniform films, in an effort to reduce surface tension. Thus, even if a single layer of graphite (graphene) is prepared, it will eventually appear as scrolls and balls, in a favorable manner. It was also found in early experiments that the melting point of many thin film materials decreases sharply as the thickness becomes smaller [119], so it was believed that monolayers can not stably exist [115].

Why, given the present situation, have these factors not prevented the emergence of graphene in 2004 [111]? First, to achieve thermal-mechanical stability, the suspended 2D material can be bent and the height of carbon atoms can displace in an out-of-plane direction though phonon vibrations [11, 118]. Secondly, although 2D configurations have higher energy than other configurations, the 2D materials can still be stable as long as the potential for reconstruction is not exceeded [117]. Thirdly, the van der Waals force between the 2D material and the substrate prevents the material from coiling [11]. As can be seen from the above discussion, the surface of a single layer material does not appear to be absolutely ideal flat. The main reason for this is, as stated in the first point, suspended 2D materials are subject to corrugation to increase entropy [118]. In addition, their interaction with the substrate is strong [4, 11, 120, 121, 122, 123, 124].

There is a lack of studies on the roughness of TMD monolayers that show how the sub-

strates and heterogeneous structures affect the roughness. This lack of research is due to the fact that one lacks, firstly, methods to prepare samples that do not require a supporting substrate or are not affected by the substrate [125, 126], and secondly, a method to experimentally obtain information on the morphology of monolayer materials.

Here a STEM is used in a near-parallel-beam diffraction mode to measure the roughness of monolayer WS_2 in different substrate configurations, including freestanding, 15-nm hBN supported, 5-nm and 15-nm hBN encapsulated, 15-nm Si_3N_4 supported, 15-nm Si_3N_4 and 50-nm hBN encapsulated WS_2 monolayers by electron diffraction under sample-tilt conditions. By assessing the broadening of diffraction spots with comparisons to simulations calculated in QSTEM [82], the roughness of TMD monolayers in different configuration are semi-quantified. Furthermore, the effect of temperature on the intrinsic roughness and lattice deformation using freestanding monolayer WSe_2 are performed.

5.2 Crystallography of 2D materials

Graphene can be rightly considered the "father" of all 2D materials [111]. The scientific community has started considering the possibility of experimentally obtaining alternative 2D materials only since the discovery of graphene in 2004. So when it comes to 2D materials, the first thing to introduce is graphene, because other 2D materials have structural properties very similar to it. Graphene is an atomically thin layer of sp^2-bonded carbon atoms arranged in a 2D honeycomb lattice. Each atom in a graphene sheet is connected to its three nearest neighbors by a strong σ-bond, and the length of these bonds is 0.142 nm [127]. Graphite consists of stacked layers of graphene held by relatively weak van der Waals intralayer bonds, interplane distance 0.335 nm.

Transition metal dichalcogenides (TMDs)

Similar to graphite and hBN, TMDs are a group of layered materials that are covalently bonded within the planes, which interact with each other by van der Waals forces between layers. Both monolayer and multilayer TMDs can be obtained by CVD epitaxy or by exfoliation from bulk crystals. A special property of TMDs is that they show bright luminescence when exfoliated as atomically thin monolayers, whereas when they are multilayers or bulk materials, which have indirect band gaps, the luminescence is reduced [128, 129]. The optical properties of TMDs on different substrates will be presented in the next two chapters.

TMDs of the type MX_2 have a lattice structure similar to that of graphite and are given in Fig. 5.2(a,b) as 2H-phase bilayer. TMDs with a $P6_3/mmc$ space group of Bravais lattices and six atoms in the unit cell [130]. In particular, two transition metal atoms denoted by M, such as tungsten (W) or molybdenum (Mo) and four chalcogen group element

atoms denoted by X, including sulfur (S), selenium (Se) or tellurium (Te). Large distinction between graphene and TMD monolayers is that the former is truly made up of a single layer of carbon atoms, where one TMD monolayers represents three atomic layers made up of two X-atom layers sandwiching one M-atom layer. The transition metals in TMDs are typically +4 in valence and the chalcogenide group elements are -2 in valence.

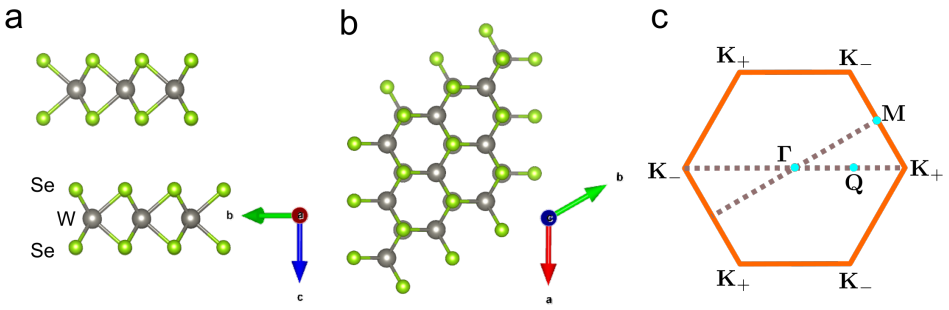

Figure 5.2: **Sketch of the bilayer WSe_2 in the 2H phase:** along (a) a axis and (b) c axis. (c) First Brillouin zone, labeled with the characteristic points **K**, **Γ** and **M**.

In monolayer TMDs, the absence of inversion symmetry results in a space group of $P\bar{6}m2$ with a trigonal prismatic 1H crystalline phase and a point group symmetry of D_3h. Common TMD materials include: $MoSe_2$, MoS_2, WSe_2, WS_2 and their lattice constants are listed in Table 5.1. Here, all of my research is focused on the 2H-phase 2D materials or 1H-phase monolayer TMDs as shown in Fig.5.2, because heterostructures are 2D sheets material stacked with each other in the crystallographic orientation like Fig. 5.2(a) along the c-axis.

Table 5.1: **Lattice constants of four different TMDs [131].**

Lattice parameter	$MoSe_2$	MoS_2	WSe_2	WS_2
a (Å)	3.327	3.190	3.327	3.190
c (Å)	15.451	14.879	15.069	14.202

Hexagonal boron nitride (hBN)

BN presents four polymorphs, arising from different bonding configurations of boron (B) and nitrogen (N) atoms: cubic (cBN), hexagonal (hBN), rhombohedral (rBN) and wurtzite (wBN). The variety of properties of BN materials are strongly related to these crystal structures. Hexagonal boron nitrogen (hBN) is the most stable form of crystalline BN and has an energy gap that ranges from 5.95 to 6.47 eV depending upon its thickness [132]. hBN is also a layered material with hexagonal crystal structure as $P6_3/mmc$ space group, lattice constants a=b=0.2504 nm, c=0.6661 nm, bond angles

α=β=90° , γ=120° [109]. The flake size of commercially available hBN ranges from hundreds of nanometers to tens of microns.

2D van der Waals heterostructures (vdWHs)

In general, the vdW force is several orders of magnitude weaker than the in-plane covalent bonding, making it feasible to obtain monolayers through top-down routes including mechanical [133] and liquid phase exfoliation [134]. This unique way in which 2D materials bind allows them to be assembled into heterostructure stacks of different layers combined like Lego bricks, as shown in Fig. 5.3. One could obtain the desired number of layers or thickness of hBN, graphite or TMDs by peeling off from thick flake material. The combination of various 2D flakes provides the possibility of using nanosheet building blocks to create vdWH with unprecedented properties.

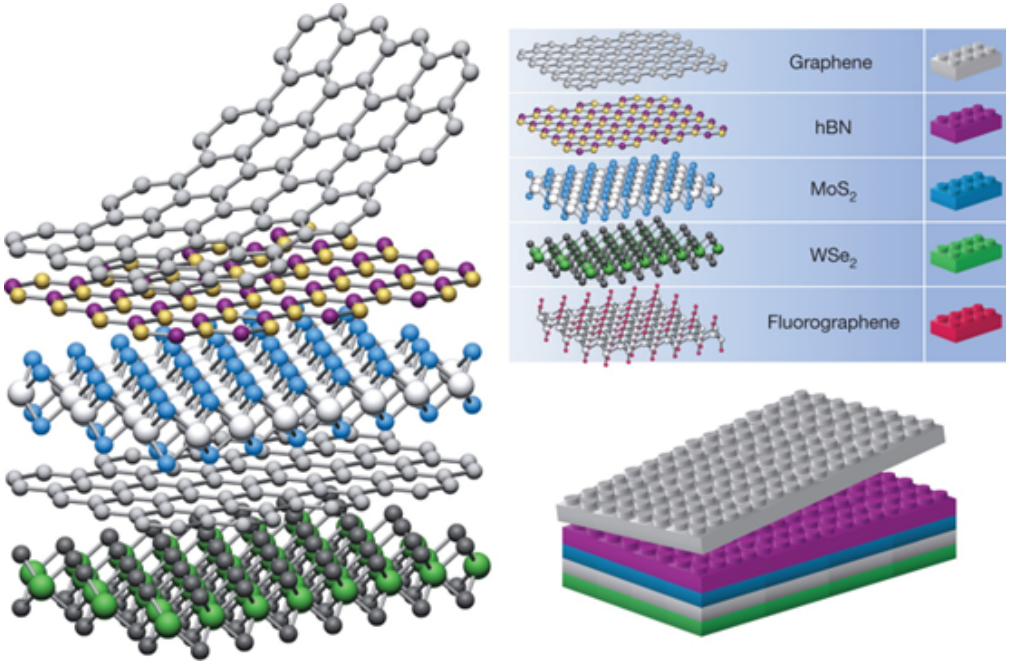

Figure 5.3: **2D crystals can be viewed as Lego blocks (right panel), enabling the construction of a wide variety of layered structures.** The basic principle is very simple: one takes a monolayer, places it on top of a monolayer or few-layer crystal, adds another 2D crystal, etc. Reproduced from ref. [135].

5.3 Roughness analysis based on diffraction

As mentioned, suspended 2D monolayers have an intrinsic nanoscale corrugation arising from their low-dimensional nature [4, 10, 11, 120, 136]. In addition, sample preparation and transfer protocols to substrates or (S)TEM grids can also result in increased surface corrugation due to changes in temperature and surface tension from solvents

used. Suspended atomically thin monolayer corrugation can be detected using electron diffraction, as it can give access to information from the full 3D reciprocal space [75]. Here, we simplify take the roughness as a product of two same trigonometric functions $(h \times cos(2\pi x/L) \times cos(2\pi y/L))$, where h and L denote as the corrugation height and lateral corrugation period, respectively. But the corrugation pattern in reality is most probably more complex.

5.3.1 Principle of roughness measurement in electron microscope

To apprehend the roughness measurement in STEM, two points about electron diffraction in thin, corrugated materials need to be understood. First of all, because the dimension of the object along the beam propagation direction is small, the reciprocal lattice points along this direction extends more significantly than in thick materials.

As shown in Fig. 5.4(k) and (l), the green dots are the reciprocal lattice points of thick WS_2, whereas they are elongated into reciprocal lattice rods (or relrods as introduced briefly in section 3.4.2.1) [75] in thin WS_2. Because they are extended in reciprocal space, the Bragg condition for diffraction is relaxed, meaning that electrons are diffracted even if they are not exactly at the diffraction condition. Thus the Ewald sphere intersects the reciprocal lattice points or relrods with excitation error $\mathbf{s} = \mathbf{K} - \mathbf{g}$ in this case, where $\mathbf{g}$ is the exact Bragg diffraction condition and $\mathbf{K}$ is the relaxed Bragg diffraction condition.

For this reason, an atomically thin monolayer can be tilted substantially and still show large diffracted intensity and sharp diffraction spots. For a corrugated material, instead of relrods only perpendicular to the real-space atomic plane, the reciprocal lattice consists of the superposition of relrods due to the angular distribution of real-space lattice normal vectors tilt, leading to the formation of diffuse cones such as the red cones in Fig. 5.4(i,j) in *u*-*w* plane.

The schematic in Fig. 5.4(i, j) and Fig. 5.5(b) illustrate how the Ewald sphere intersects with the reciprocal lattice cones of a rippled monolayer when electrons are incident perpendicularly (zero sample tilt) and non-perpendicularly on the sample (tilted sample). If the sample is not tilted, the Ewald sphere (blue plane in Fig. 5.4(b)) intersects the vertices of the conjoined cones, marked by the blue hexagon in Fig. 5.4(b). Whereas if the sample is tilted, the Ewald sphere (yellow plane in Fig. 5.4(b)) intersects the cones at a certain height along the *w*-axis, denoted by the yellow ovals on the cones. In Fig. 5.4(i,l), only one relrod/cone is drawn to show the relaxed Bragg diffraction for flat and corrugated thin material at no sample tilt and tilted sample diffraction configurations.

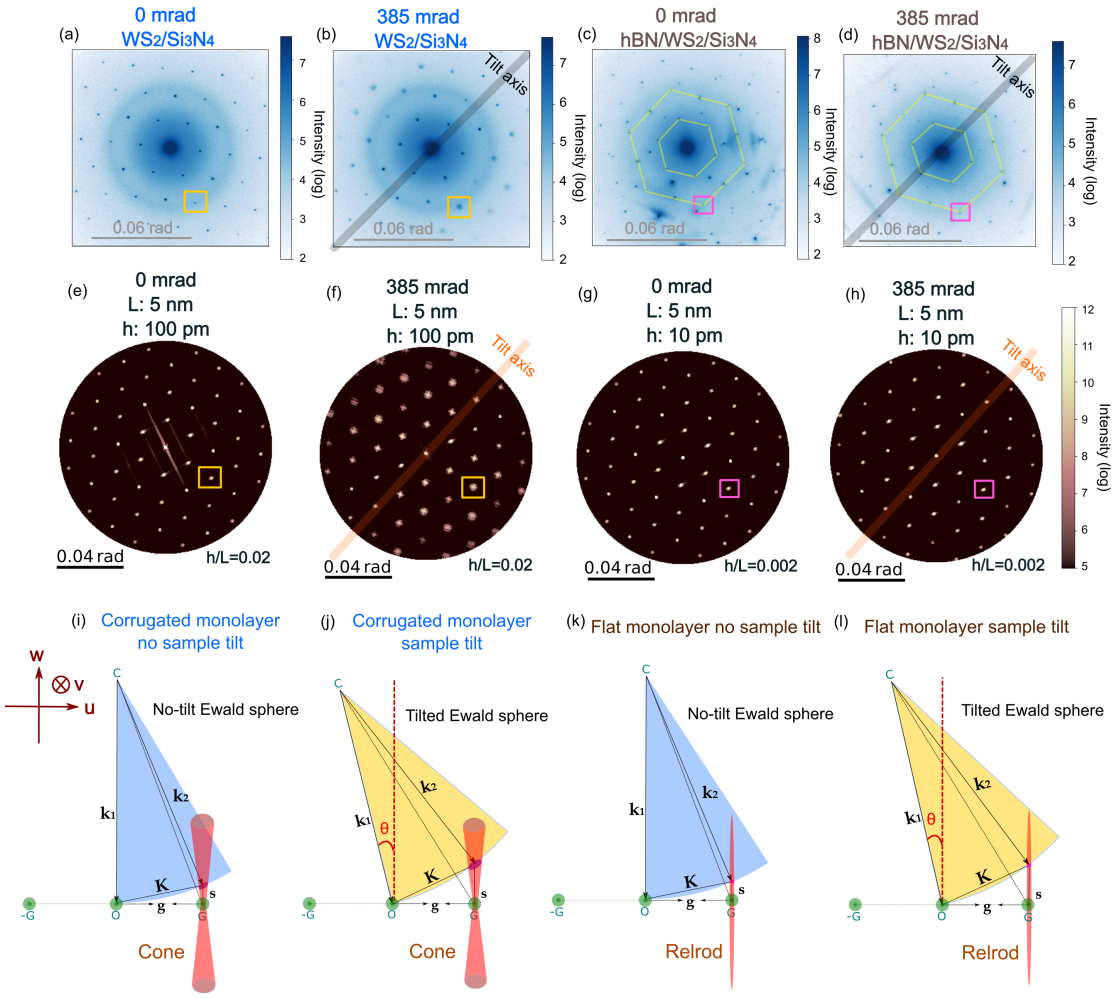

Figure 5.4: **Diffraction patterns and reciprocal lattices of flat and rough WS_2:** (a) and (b) are experimental diffraction patterns at 0 mrad and 385 mrad for WS_2 monolayers supported by Si_3N_4; (c) and (d) are experimental diffraction patterns at 0 mrad and 385 mrad for WS_2 monolayer encapsulated by Si_3N_4/hBN; (e) and (f) are the simulation results of h/L= 0.02 corrugation at 0 mrad and 385 mrad. Its peak size increased consistently with (a) and (b), as highlighted by the $\langle 02\bar{2}0 \rangle$ spots boxed in yellow; (g) and (h) are the simulation results of h/L= 0.002 corrugation at 0 mrad and 385 mrad. Its peak size didn't increase, consistent with (c) and (d), also highlighted by the $\langle 02\bar{2}0 \rangle$ spots boxed in pink. The in-plane rotation and the tilt axis with respect to the first-order reflections in the simulations were chosen arbitrarily, only the tilt axis direction matches with the experiments in this case; (i) and (j) are the reciprocal space of a corrugated monolayer, corresponding to the diffraction patterns in (a), (e) and (b), (f); (k) and (l) are the reciprocal space of a flat monolayer, corresponding the diffraction pattern in (c), (g) and (d), (h). The Ewald sphere is plotted with radius $\mathbf{k}$ (the difference between incident electron momentum $\mathbf{k_1}$ and deflected electron momentum $\mathbf{k_2}$ is very small, so $k = |\mathbf{k_1}| \approx |\mathbf{k_2}|$) in yellow (tilted sample) and blue (no sample tilt), θ in red is the sample tilt angle in (j) and (l). Bragg diffraction condition is relaxed in all atomically thin materials, whether it is flat or corrugated. $\mathbf{K} = \mathbf{g} + \mathbf{s} = \mathbf{k_2} - \mathbf{k_1}$, where the value of $\mathbf{g}$ is the inverse of the $\langle 02\bar{2}0 \rangle$ interplanar distance and $\mathbf{s}$ is the vector to describe how far $\mathbf{K}$ deviates from the exact Bragg condition.

5.3.2 Corrugation of suspended monolayers

Through the diffraction method as described, we have found that freestanding (suspended) TMD monolayers produced by CVD or mechanical exfoliation are not flat as graphene [10, 116], as shown in Fig. 5.5(a). Once again, a corrugated monolayer would show broadening of diffraction spots as a function of tilt angle (Fig. 5.5(c)), while a perfectly flat monolayer should have diffraction spot widths that do not change as the monolayer is tilted with respect to the electron beam. The roughness measurement results and quantification of TMD monolayers in different configuration will be reported later in section 5.4.

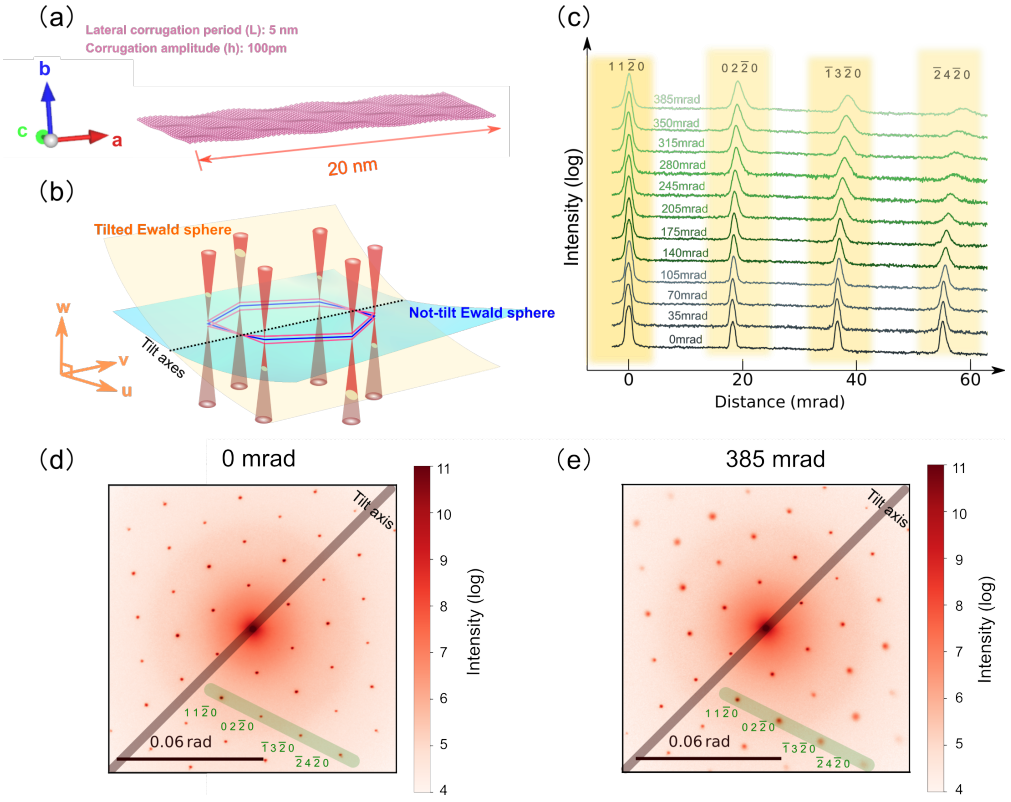

Figure 5.5: **Schematic of corrugation in freestanding WS_2 and the geometry between its reciprocal lattices and Ewald sphere:** (a) model for a rippled WS_2 monolayer (only W atoms shown for visibility) displayed using Vesta [137]; (b) the reciprocal lattice of a rippled TMD monolayer is a set of cones (in red) due to the angular distribution of real-space lattice normal vectors. Also shown are two curved planes which approximate the surface of the Ewald sphere, indicating the points of intersection with the reciprocal space lattice to form the diffraction pattern. The blue plane shows the intersection at zero sample tilt, while the yellow plane shows the intersection at a non-zero tilt angle; the intersection geometry leads to two distinctly different diffraction patterns (d) for zero tilt and (e) for a tilted sample where the spots have become diffuse for a freestanding exfoliated WS_2 monolayer; (c) the intensity profiles of the four diffraction spots, which are indicated in (d) and (e) by the green bar are plotted in log scale. The tilt angle is from 0 mrad to 385 mrad with a step size of 35 mrad.

Whether 2D monolayer membranes are stable, and how 2D materials can exist stably, has been a subject of theoretical debate as mentioned in section 5.1. The existence of suspended 2D materials through rippling was predicted decades ago [10, 116]. It has been successively demonstrated by using probe-type experiments that graphene on conventional silica substrates has nanoscale roughness [10, 11, 120] of the order of 100 pm.

By using a flatter material as substrate, such as hBN [11] or mica [123], the flatness of the graphene can be greatly improved to the same level as the atomically flat substrate. As demonstrated later, TMD monolayers can also be smoothed by contacting them with a flat material such as A dozen nanometers of hBN or graphite. Electron diffraction experiments have revealed that freestanding graphene and TMD monolayers maintains thermodynamic stability by undergoing elastic deformation, that is corrugation, rather than by forming defects [118].

5.3.3 State of the art

Atomic force microscopy (AFM) is the most commonly used method for determining roughness. It is simple and convenient for monolayers with robust substrate support, but less feasible for monolayers that are self-supporting and buried within a vdWH. As the purpose of this study is not merely to examine the roughness of the sample, but also to determine the optical properties of the material buried the corresponding structures and the correlation between the two, the use of noncontact AFM testing is not an ideal solution. The following is an overview of the history of the corrugation study using electron diffraction, which can be used to determine the roughness of monolayers inside the vdWH.

Corrugation in graphene/graphite

The experimental method of measuring roughness based on electron diffraction as a function of sample tilts was first reported in 2007 by J.C. Meyer et al. [10, 56] on the same principle as that described in section 5.3.1 and only two other reports based on transmission electron beam diffraction have been published [11, 120]. These three works didn't correlate the roughness behavior to the electrical or optical properties.

Besides the transmission electron beam experiments as described above, other diffraction techniques including X-ray diffraction, grazing incidence fast atom diffraction (GIFAD or FAD) and microprobe low-energy electron diffraction (μ-LEED) [4, 136], can also be used to get information on reciprocal space, in our case that is to obtain the corrugation or roughness of the sample. μ-LEED is attributed to the expression: $\Delta\theta = \Delta k_{||}/2k_0$, where $\Delta\theta$ is the standard deviation of the local surface normal, $\Delta k_{||}$ is the linewidth of the central diffraction spots, and $k_0 = \sqrt{2m_eE}$ is the momentum of incident electron momentum. By varying the acceleration voltage of the incident electron beam (E) and linearly fitting the slopes of $k_{||}$ and k_0, the local surface normal deflection angle related

to the roughness can be obtained. The GIFAD and X-ray technique is not described in detail here, those interested can refer to ref. [4, 121].

In addition to reporting that corrugation occurs in suspended monolayers of graphene such that the surface normal varies by several degrees and out-of-plane deformations reach 1 nm [10, 56], it is also found that the intrinsic roughness of graphene decreases with increasing number of graphene layers and it becomes flat and ripple-free when it reaches fifty layers in thickness.

It was found in 2011 that the slope of the linear correlation between the intensity of the diffraction spot and the size of the inverted lattice is proportional to the amplitude of the rippling graphene for a certain degree of approximation [120]. However, this theory is based on the fact that the intensity of the same diffraction spot does not change much during the tilting of the sample. The corrugating amplitude and period of the suspended graphene determined by this method are 0.17 nm and 10 nm [120], respectively.

Roughness of graphene inside hBN encapsulation

The sandwich structure of hBN/graphene/hBN leading to a significant reduction in roughness of the encapsulated graphene compared to suspended was demonstrated by diffraction methods in 2017 [11] though using the fitting method as ref. [120]. It shows that the root mean square (RMS) roughness of graphene under suspension, hBN-support, and hBN-encapsulation are 114 pm, 21 pm and 12 pm, respectively. The roughness of graphene between two hBN flakes is considerably less than that previously reported for both suspended graphene and graphene on any substrate, corresponding to the thermal vibration amplitude of carbon atoms in bulk graphite.

Other than these, μ-LEED technique in ref. [4] similarly verified that the roughness of graphene decreases with increasing thickness as ref. [10], but also found that suspended graphene exhibits significantly smoother surface than those supported on SiO_2. Moreover, μ-LEED-IV demonstrated that suspend 2H-$MoSe_2$, another 2D material also has this intrinsic rippling nature and the surface corrugation amplitude decreases with increasing number of layers [136].

Substrates influence on the roughness of monolayers

Aside from looking at the roughness of suspended monolayer, efforts have been made to study the roughness and properties of monolayers on various substrates including: hBN [11], amorphous carbon [120], SiO_2 [4], mica [123], 6H-SiC [121], Ir(111) [122], Ru(0001) [121], and graphite [10] by using various methods, covering techniques such as AFM, X-ray, scanning tunneling microscopy (STM) and electron diffraction. These studies are all pointing to the fact that the roughness of a monolayer material is determined by the substrate: **monolayers on a rough substrate (for example amorphous materials) will be rough, but that on a cleaved surface or comparable parent materi-**

als will be flatter. This is because of supported monolayers is mainly determined by their conformation to the underlying substrate topography. Bare SiO_2/Si substrates can lead to the roughness of monolayer 2D materials on top of it in the range 150-200 pm as measured by AFM [123].

5.4 Monolayer WS_2 roughness in different vdWHs

After the explanation of the physics of roughness measurements in last section, this section turn to the measurements of WS_2 under different substrates (section 5.4.1), including freestanding, 15-nm hBN supported, 5-nm and 15-nm hBN encapsulated, 15-nm Si_3N_4 supported, 15-nm Si_3N_4 and 50-nm hBN encapsulated WS_2 monolayers. Besides the experiments, to semi-quantify the amplitude and period of the corrugation at different vdWH, I tried to relate the experimental diffraction patterns to that of atomic structures with given roughness in section 5.4.2. Also, the details of the atomic model generation and simulation softwares are introduced in section 5.4.2.1.

5.4.1 Experiment: roughness measurement

To reveal the effect of monolayer roughness, tilt series of electron diffraction patterns were acquired, with the sample tilted along the primary sample holder axis from 0 mrad to 385 mrad ($\approx 22°$) with 35 mrad ($\approx 2°$) step as demonstrated similarly for graphene [10, 11, 120] with liquid nitrogen cooling to reach 110 K. The exposure time is 100 or 300 ms for the diffraction patterns. In these wide-beam illumination diffraction experiments, the beam diameter was around 100 nm, which not only contains few corrugation periods as suggested in ref. [10, 11, 120, 121, 136], but also provides the local information within the region.

To compare the roughness of TMD monolayers when placed on or encapsulated in different substrates, the diffraction spot width evolution from the tilt series was measured as shown in Fig. 5.6. The width of the diffraction spots were retrieved from the FWHM of a 2D Gaussian fit. The 2D Gaussian fit was made at linear intensity scale as they are true values, whereas the plot of all diffraction patterns covered in this thesis is shown in log intensity scale to suppress the central spot and enhance weak higher-order spots, so that they can be visualized on the same plot.

For the two freestanding monolayers and Si_3N_4 supported monolayer, the width of the diffraction spots quickly increased, with a maximum width when the monolayer is tilted to the maximum angle of 385 mrad, as shown in Fig. 5.6 (green, yellow and blue lines). The large variation of the peak width of WS_2 on Si_3N_4 in Fig. 5.6 can be attributed to the statistic issue, but their size remains greater than the others. This is probably due to the weak intensity of these diffraction spots, that attribute to both the boarding effect (large diffraction spot size at high sample tilt angle) and the presence of Si_3N_4.

However, the diffraction spot width barely changes as a function of tilt when the monolayer is encapsulated or supported by hBN as in Fig. 5.6 (red, purple and brown lines) and Fig. 5.4(c,d). Both a single thin layer of 15-nm hBN (supported monolayer) or full hBN encapsulation reduces roughness, producing a flat WS_2 monolayer, as shown in Fig. A.2. In addition, the graphite have the same effect to ensure the flatness of monolayers, as diffraction patterns shown in Fig.A.6. The roughness of a WS_2 monolayer in different configurations from the roughest to flattest is: Si_3N_4 supported, freestanding, hBN on one or both sides.

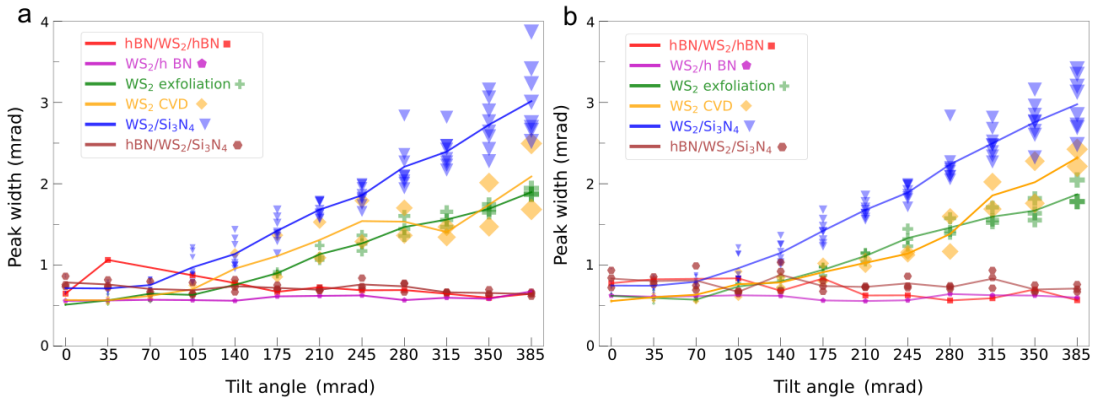

Figure 5.6: **Roughness measurement of WS_2 monolayers under various vdWH configurations:** hBN encapsulated (red), hBN supported (purple), freestanding exfoliated (green), freestanding CVD-grown (yellow), Si_3N_4 supported (blue), and Si_3N_4/hBN encapsulated (brown) cases. The peak width is extracted from a 2D Gaussian fit of specific diffraction spots in each diffraction pattern, represented by different geometries and colors. The lines indicate the average value of the peak width on different substrates at each angle in the cases of multiple measurements from different regions. (a) FWHM of peak width change with tilt angle along x direction. (b) FWHM of peak width change with tilt angle along y direction.

For the data analysis of diffraction spots, I did not adopt the linear fit between intensity and inverse lattice as in ref. [11, 120], because in the presence of other materials, the intensity of the diffraction spots of monolayer TMDs is significantly altered, as shown in Fig. A.2(e,f) and Fig. 5.7(m,n) and the equipment we used doesn't have a beam blocker like ref. [11] to suppress the central beam. The reason why the fitted analysis was suitable for graphene encapsulated in hBN and not for TMDs is that the graphene lattice structure is all carbon atoms, hence it is a true weak phase object. Whereas monolayer TMDs, with its three atomic layers, already violates's Friedel's law such that conjugate reflections will give different intensities ($I_{hkl} \neq I_{\overline{hkl}}$) [138], thus the size of diffraction spots are inherently different [136]. In addition, when hBN is present, the moiré diffraction spots can appear as shown in the Fig. 5.4(c,d) and Fig. A.2(a-f), and the diffraction spots of WS_2 under different tilt angles appear irregular with asymmetrical deformations but with relatively constant size as shown in Fig. 5.7(a-l). The specific reasons

regarding this change may be due to the structure factors of the heterogeneous structure is very complex [75].

Nevertheless, this is not a concern in this experiment as it is more important to determine the roughness of the material based on its trend rather than its subtle changes during tilting. As an overview, monolayer roughness in each configuration can be easily determined from tilt series of electron diffraction patterns led by comparing the broadening of diffraction spots with simulations rather than analytical diffraction analysis depending of the stacking structures.

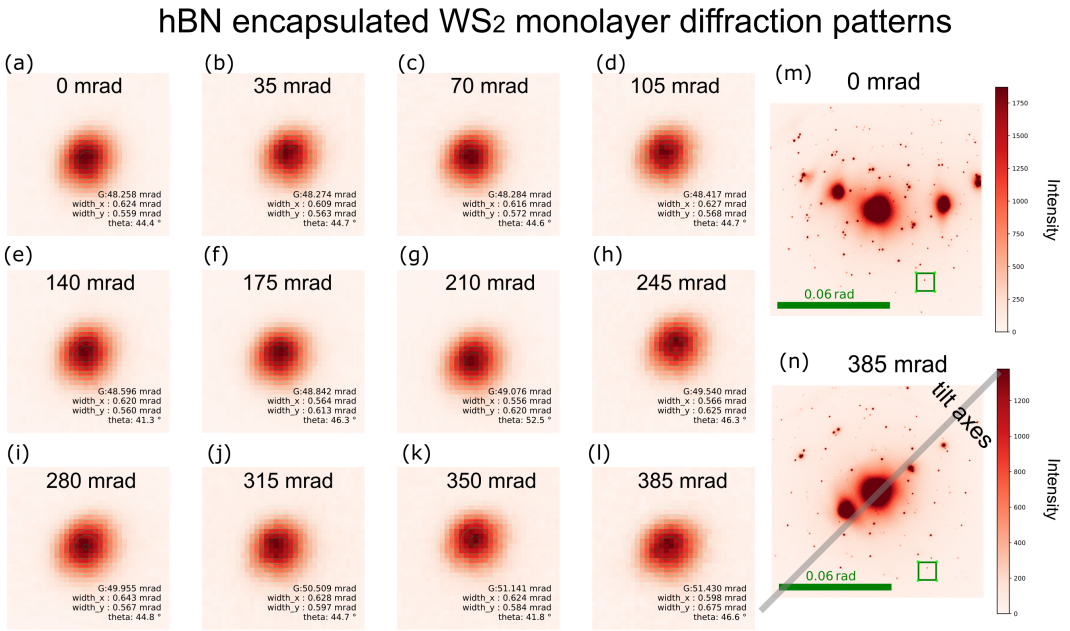

Figure 5.7: **2D Gaussian fit of hBN encapsulated WS_2 monolayer diffraction pattern tilt series.** (a)-(l) Two dimensional Gaussian fit of the selected peak from 0 mrad to 385 mrad sample tilt angle. The FWHM, rotation angle, and intensity are given at the bottom right corner. The candidate peak selected, $\langle \bar{2}3\bar{1}0 \rangle$, is marked by a green rectangle in (m) and (n).

5.4.2 Diffraction pattern simulation by QSTEM

To confirm that the diffraction spot broadening can be explained by the TMD monolayer roughness, numerical calculations were performed for the expected diffraction pattern of rough and flat monolayers in QSTEM [82]. The aim of the simulations is not only to confirm that the TMD monolayer roughness will have a wider diffraction spot at high sample tilt angles, but also to semi-quantify the roughness of TMD monolayer under

diffraction configurations.

5.4.2.1 Atomic models and parameters for simulation

The atomic monolayer models are built by Atomic Simulation Environment (ASE) [84] library in Python. The model for a rough monolayer was produced by displacing the atoms along the out-of-plane direction (along the c-axis, or [0001] direction), while keeping the total projection area of the layer constant. This is achieved by iteratively dispersing atoms along the surface tangent, which is defined by the corrugation height (h) and lateral corrugation period (L). The value of roughness was given by a product of two same trigonometric functions ($h \times cos(2\pi x/L) \times cos(2\pi y/L)$), but the corrugation pattern in reality is most probably more complex. One could have a very clear atomic model in VESTA [137] and make customized color and visualized orientation as Fig. 5.5(a).

Despite not being relaxed, these model structures are sufficient to view the effect of roughness on the diffraction patterns and to estimate the amplitude of the monolayer rippling. The rough model might explain why the symmetry of the spots observed in experiments does not always match the symmetry observed in simulations in later sections. The presence of these noises (artefacts) reflecting additional periodicity in the atomic structure models does not affect our ability to compare the experimental results with the simulation results. One can simply ignore them or suppress the presentation of the noise by plotting in log intensity scale, as shown later.

Basic parameters

In QSTEM, the beam acceleration voltage and convergence angle was set to 60 keV and 1 mrad. The astigmatism, spherical aberration and chromatic aberration was set to 1 nm, 10 μm and 1.0 nm. The brightness is $5 \times 10^8 \mathrm{A}/cm^2$ sr. These are consistent with the experimental parameters in ChromaTEM to simulate the exact same conditions as the experiment. The window size is 500 Å with 0.24 Å resolution for the potential calculation, thus the biggest scattering angle is 66.4 mrad. 500 slices was set to multi-slice the atomic model because of the high sample tilt angle and a 1024×1024 diffraction pattern image with 0.13 mrad/pixel was presented as the simulation result.

Thermal diffuse scattering

The atoms in any real material at a particular instance of time are not exactly located at their symmetrical lattice points due to thermal and zero-point vibrations. The frozen phonon approximation is a simple and somewhat brute-force approach to numerically simulate the effects of thermal vibrations in the specimen. In the Frozen phonon approximation, the simulated image or diffraction pattern is the intensity averaged over several different configurations of atoms with different random offsets. This type of scattering may be referred to as thermal diffuse scattering (TDS) [139].

Accounting for TDS is quite time consuming and memory intensive because for each round of calculation a random number of displacement needs to be generated for all the atoms, then diffraction simulations are performed, and afterwards all the results are added up and averaged. And minimum rounds of TDS calculation in the simulation is related to the thickness of the sample and requires a diffraction pattern to converge (highly symmetrical as the real lattice).

The simulation in later section all does not take into account TDS, because the experiments were performed at a low temperature of 110 K, the atoms are less off-centre and there is little effect of TDS on diffraction. It could decrease the noise to some extent with TDS applied, but it doesn't play a key role in conventional TEM diffraction. In this case, TDS is only considered as "background intensity". When it comes to high collection angle scattered electrons, TDS will compete with Rutherford (elastic) scattering [140], thus has a decisive influence on the simulation results in Z-contrast images.

5.4.2.2 Corrugation amplitude and period quantification based on simulation results

The results of the simulations for lateral corrugation period size, L = 2 nm, 5 nm, 10 nm with the h (corrugation amplitude) 0.002, 0.01, 0.02, 0.04 times L is presented in Fig. 5.8. The results of the simulations will be plotted in the same figure as the experimental results to find the roughness of the TMDs under different configurations. For better visualization, all experiment and simulation diffraction patterns are plotted in log scale. This can suppress the central disk while showing more clearly the weak high-order diffraction peaks.

Discussion of artefacts and maximum plot intensity

There are some artefacts which are quite difficult to interpret when the minimum log intensity for plotting is set to V_{min}= 1 as shown in Fig. A.1, especially in Fig. A.1(a). It is reasonable to have this artefacts because the model use to calculate diffraction pattern has intrinsic long-range periodicity, and cannot be as ideal as the random real world. The atomic model is also not relaxed so some noise (artefacts) also introduced. To suppress this, simulation results are plotted at V_{min} = 3 or 5 (minimum log intensity) for the simulated diffraction patterns. This could suppress the artefacts, whereas the peak width at the high-order peaks of weak intensity are a bit smaller, as shown in Fig. A.1. For the simulation of $h/L = 0.01$ with $L = 2$ nm corrugated WS_2 monolayer diffraction pattern at 385 mrad sample tilt angle, there are some artefacts at V_{min} = 1 in Fig. A.1(a). By plotting it at V_{min} = 3, the artefacts became weaker. Comparing with others in Fig. A.1, the peak size shrinks a bit but this is not so evident in (c) and (b), but peak size shrink too much in (d). Thus, all simulation results are plotted with V_{min} = 3 or 5.

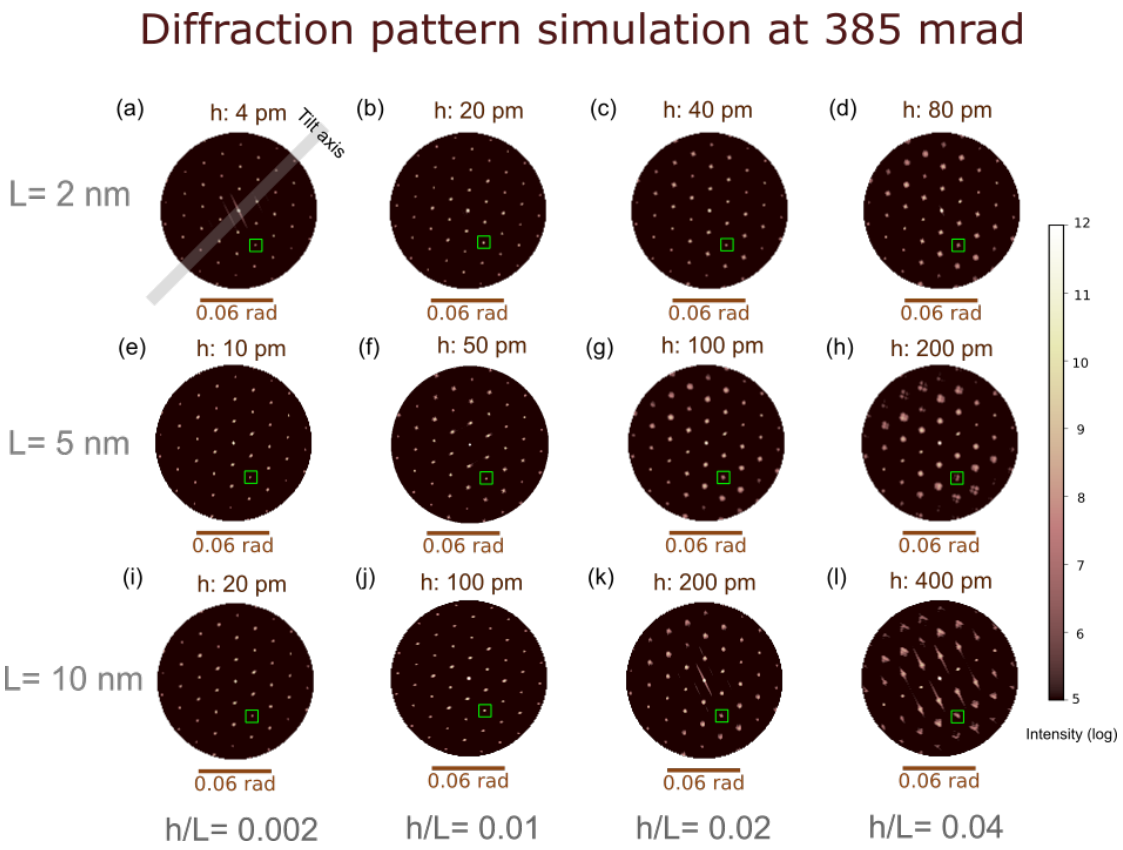

Figure 5.8: **Diffraction pattern simulation at 385 mrad sample tilt angle of corrugated WS_2 monolayer with different ratios between corrugation height (h) and lateral corrugation period (L).** h/L = 0.002 in first column (a), (e) and (i); h/L = 0.01 in second column (b), (f) and (j); h/L = 0.02 in third column (c), (g) and (k); h/L = 0.04 in last column (d), (h) and (l). The first row (a)-(d) has the same L= 2 nm; the second row (e)-(h) has the same L= 5 nm; the third row (i)-(l) has the same L= 10 nm. The tilt axis for all diffraction patterns is denoted in (a) by the grey line.

h/L semi-quantify through diffraction patterns comparison between experimental results and simulation

The simulation of the diffraction pattern at 0 mrad sample tilt angle is not presented, because there isn't any difference among different h/L ratios. The tilt axis is only marked in Fig. 5.8(a) , and (b-l) maintain the same tilt axis as it. The diffraction patterns in Fig. 5.8 proved that the corrugation is the reason why peaks became larger at high sample tilt angle, comparable to the experimental patterns in Fig. 5.4, Fig. 5.5, and Fig. 5.6. The diffraction peaks became broadened as the value of h/L increase at 385 mrad sample tilt angle as shown in Fig. 5.8. This means at least in the range of corrugation period of 2-10 nm, it is the h/L ratio instead of the discrete L or h values that dictate the width of diffraction peaks at large sample tilt angle, as described by previous reports [4, 10, 136]. This is very different from previous studies on freestanding graphene that its diffraction peak size and intensity at high sample tilt angle are described to be governed only by the rippling amplitude [11, 120].

The results of the simulations indicate that the typical height (h) for the corrugation roughness equals to 0.01 times the lateral corrugation period (L), or $0.01 \times L$, for the freestanding monolayer, $0.02 \times L$ for the monolayer on Si_3N_4, and less than $0.002 \times$ L for the monolayer supported by and encapsulated in hBN, as shown in Fig. A.3 and Fig. 5.8. Diffraction patterns in Fig. A.2 indicate that hBN as substrate suppresses the intrinsic roughness of TMD monolayers thus ensure the flatness of a TMD monolayer, showing at least 20× reduction in roughness even when used in conjunction on top of rough substrates such as Si_3N_4. This is expected, in view of previous experiments with hBN-encapsulation of graphene and optical experiments of encapsulated TMDs [141, 101, 142, 143, 35].

A WS_2 monolayer on top of the Si_3N_4 is expected to be rough, as this amorphous substrate is not flat. Because amorphous materials cannot be as flat as an atomically flat crystal (eg. thick hBN and graphite), although it can still be a very "flat and smooth" surface. For SiN_x, its roughness can vary a lot depending on the deposition condition [144]. To obtain the accurate surface topography of SiN_x films on the TEM grid, AFM measurements were performed. The result were shown in Fig. A.5 that the amplitude of the roughness is in the range of 0.3-0.8 nm assuming the monolayer on Si_3N_4 reflects well the roughness of the Si_3N_4 itself, thus an $h/L = 0.02$ and the lateral corrugation period L is around 15-40 nm. From the line profile in Fig. A.5(b), one can easily find there are in the range of 5-15 oscillations in each 250 nm interval, from which one can deduce the lateral rippling period in the same 10 times range.

A separate region of the same WS_2 monolayer on Si_3N_4 covered by a thin hBN layer shows a diffraction pattern with similar spot widths to the hBN encapsulated monolayer, at all sample tilts as shown in Fig. 5.4(c,d) and Fig. 5.6. This allows the construction of high-quality devices on top of different substrates, even if the substrate itself is rough (at least with roughness comparable to that of the amorphous Si_3N_4), to obtain a flat TMD monolayer by the use of single top layer hBN.

5.5 Temperature dependence of freestanding monolayer TMDs corrugation

Further investigation of the temperature dependence of the corrugation of monolayer TMDs from LN_2 (110 K) to RT (300 K) was performed. As in the previous section 5.4.1, same experimental method was employed to study freestanding monolayer WSe_2 on a 500 nm radius holey membrane grid. Accordingly, all roughness measurements are taken on the same sample, so the distance in mrad is used in place of tilt angle to plot the results.

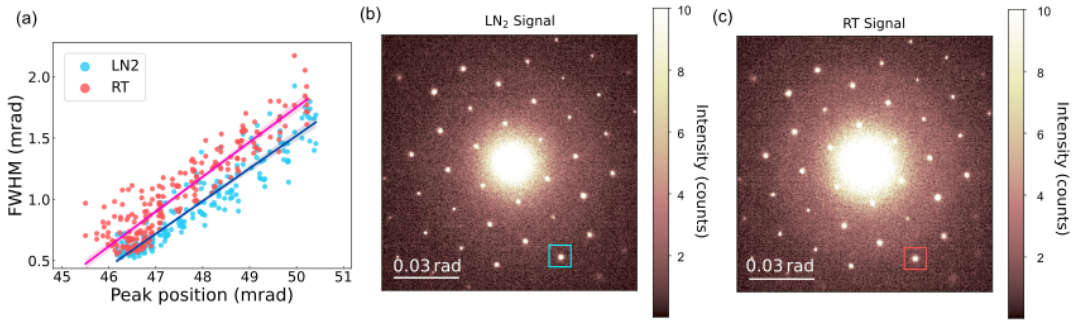

Figure 5.9: **Diffraction peak width of freestanding monolayer WSe_2.** The blue symbols correspond to 110 K, whereas those red correspond to 300 K in (a). The peak position is given by radial position in mrad from 2D Gaussian fit. It is shown in (b) and (c) how the 385 mrad sample-tilt diffraction patterns are at 110 K and 300 K, and squares represent the candidate peak for fit. Intensity of (b) and (c) are in log scale and multiplied by 1000.

As shown in Fig. 5.9(a), slops and FWHM indicate that the corrugation increased a bit under 190 K temperature change. Separate measurements over different areas of the sample gave the data points in Fig. 5.9(a). But the diffraction peaks are only a bit wider at RT (red dots) than at LN_2 (blue dots), around 5-10 pixels as shown in the y axes in Fig. 5.9(a), which makes it difficult to make an accurate assessment of h/L, as the peak fitting also contains some errors.

In ref. [120], graphene has demonstrated that it has an increase in the corrugation at 150 K, compared with 300 K. It is most likely that this deviation from intuition is due to graphene's very large, but negative coefficient (-2×10^{-5} K^{-1}) of thermal expansion [145]. By arranging the overcrowded atoms in the suspending form by ripples, the tension is released as the temperature decreases (increase) for graphene (TMD monolayers) [146, 147].

However, the monolayer WSe_2 shows not very significant change in roughness in the 190 K temperature window. Therefore, the roughness of the monolayer TMDs might be observed to vary more dramatically with temperature when the temperature window increased to few times of 190 K, as the thermal expansion coefficient of monolayer $MoSe_2$ is 3 times smaller than graphene [148].

5.6 Scanning nano-diffraction and lattice disorder

Scanning nanodiffraction (also called 4D STEM) techniques as described in section 3.4.2 can provide useful information of the local lattice parameter variations. In an attempt to map lattice and strain at the nano-scale, canning diffraction experiments are preformed

on some samples with near-parallel illumination to study the strain and lattice disorders.

From a projection perspective, strain is interpreted from a single projection along the direction of the incident beam. For instance, during nanodiffraction mapping or GPA of HRTEM images, this can lead to false in-plane strain measurements.

5.6.1 Errors of strain mapping by nanodiffraction

In this thesis, the first-order diffraction peaks of TMDs were located about 290-300 pixels away from the central diffraction peak (direct beam) in the experimental conditions used. These first-order diffraction peaks have a diameter of approximately 10-20 pixels. Usually, one define the coordinate origin in the diffraction image by the center of the direct beam, and it is determined by blob detection. On the basis of this absolute coordinate system, the positions of the other diffraction peaks are determined.

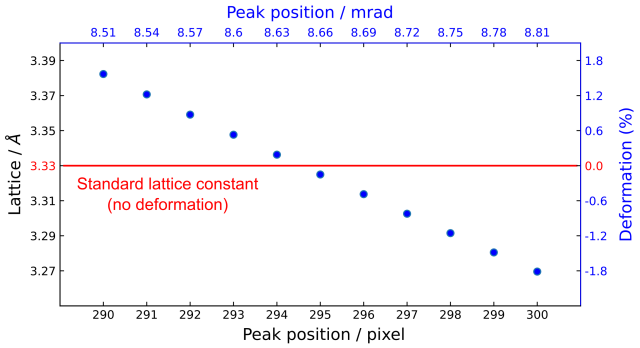

Figure 5.10: **Accuracy and reliability of scanning nanodiffraction**: peak position in diffraction pattern changed by one pixel equates to about 0.015 Å changed in lattice parameter. The deformation is calculated based on 3.33 Å as indicated by red line.

However, the center of the direct beam always jitters around a few pixels, because not only the saturating intensity of the direct peak but also the desan coil of STEM is not well aligned will cause its position can not be defined precisely. Due to these limitations, even with the parameters of the blob detection algorithm adjusted, the center point of the direct beam cannot be located adequately. A more accurate way to locate the coordinates of one diffraction spot should though subtracting its arbitrary absolute coordinates from its conjugate reelection spots. Fig. 5.10 presents that one pixel deviation could result in the misconception that the lattice has deformed by 0.5%.

The intensity-weighted averaging method is used to obtain subpixel accuracy in this section, and therefore the error caused by peak finding can be roughly estimated reduced to one-tenth from 0.5% to 0.05% though 10-square center of mass refinement.

5.6.2 Structural disorders of WSe_2 in freestanding and hBN encapsulated at RT and LN_2

It can be seen in Fig. 5.11 that the hBN encapsulated WSe_2 have a much sharper normalized distribution when compared to freestanding WSe_2 at both RT and LN_2. Since the WSe_2 in both samples are of different origins and TEM grids, it is impossible to tell whether the difference in their lattice parameter sizes and the presence of hBN are related. In Fig. 5.11(a), the lattice parameters are extended by 0.03 Å, and it is not clear how much is caused by the projection of the corrugation, and how much is the really in-plane lattice parameter disorders. Fig. 5.11(b) illustrates that WSe_2 encapsulated in hBN has a more concentrated distribution when hBN is applied, as the variance much smaller, and this is because of both the absence of corrugation and a more homogeneous in-plane structure than freestanding WSe_2.

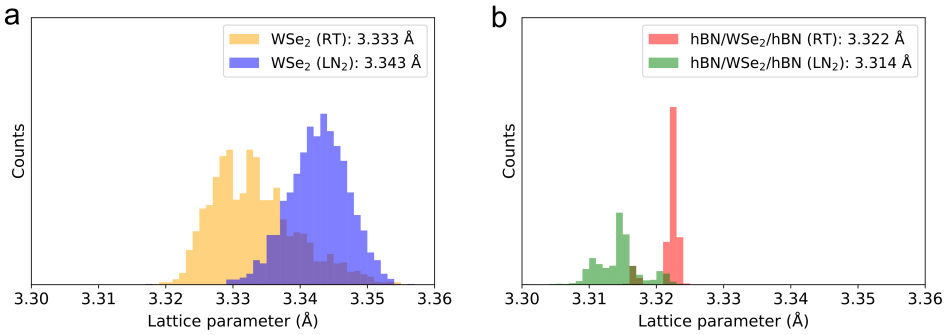

Figure 5.11: **The lattice parameters histogram of freestanding and hBN encapsulated WSe_2 at RT and LN_2.** There are 3600 data points for both (a) and (b). The mean is given in the legend.

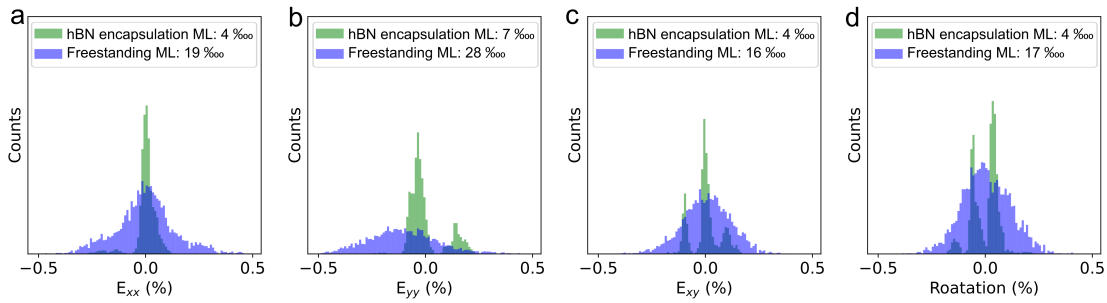

Figure 5.12: **The strain distribution in freestanding WSe_2 and hBN/WSe_2/hBN:** (a) E_{xx}, (b) E_{yy}, (c) E_{xy} and (d) rotation. For comparison, the mean values are set to zero and the variations are listed in the legends.

In more detail, the strain components on two samples at LN_2 are compared: $\mathbf{E_{xx}}$, $\mathbf{E_{yy}}$, $\mathbf{E_{xy}}$ and rotation. The focus here is not on the spatial distribution of the strains, but

rather on their statistical distribution in the form of histograms. Fig. 5.12 shows that all distributions are more centralized and sharp for the hBN encapsulated WSe_2, consistent with the results in Fig. 5.11, indicating that strain disorder is less prevalent among the hBN encapsulation sample. While the strains on our TMD samples are small, TMDs are extremely rigid, as experiments have shown that even when the stress/strain of TMDs exceeds 7.3%, the materials do not break [149].

In Fig 5.12 (b-c), there are more than one peaks in each of the strain tensor distribution, and this come form the sample preparation being conducted by the viscoelastic stamp that induced the strain disorders. In fact, the encapsulated monolayers prepared by this method showed strain variations even at nano scale as shown in Fig. B.1. Recently, it was observed that the EELS and CL variations of WS_2 inside hBN encapsulation can be attributed and correlated to strain maps [28]. This work was established on the basis that the WS_2 monolayers encapsulated in the middle of two hBN flakes is flat (no corrugation), therefore the results of the stain maps are reliable at this point.

5.7 Conclusion

In this chapter, the structural information of WS_2 monolayer in various substrates are studied. The monolayer TMDs is confirmed to have an intrinsic corrugated nature on TEM grid by sample-tilt diffraction experiment. 2D Gaussian fit of the diffraction spots was used to compare the roughness of TMD monolayers in decreasing order is: Si_3N_4 supported, freestanding, hBN on at least one side. And at liquid nitrogen and room temperature, the difference for the corrugation in freestanding WSe_2 sample is not very obvious.

Diffraction patterns of several single-layer TMDs with different ripple periods and amplitudes were calculated theoretically using a multi-slicing algorithm based program QSTEM. Using the simulated diffraction patterns and the experimental results, following roughness ranking are obtained as shown in Table 5.2.

Table 5.2: **Summary of WS_2 monolayer roughness in different configurations**

Configuration	hBN/WS_2/hBN	Si_3N_4/WS_2/hBN	WS_2/hBN	WS_2/Si_3N_4	ExfoliatedWS_2 (freestanding)	CVD-grown WS_2 (freestanding)
Roughness	$0.002 \times L$	$0.002 \times L$	$0.002 \times L$	$0.02 \times L$	$0.01 \times L$	$0.01 \times L$

In this study, the in-plane stain disorders of samples with hBN encapsulation are one magnitude less varied as compared to freestanding samples. Although the roughness experiments and strain mapping in this chapter are all based on a single TMD material, all the conclusions are generalizable to other TMD species and even other 2D materials. In this chapter, both roughness and strain measurement show the importance of hBN

for TMD monolayers from a structural stand point. But I didn't manage to analyse both the roughness and strain under one single scanning nanodiffraction experiment for 2D monolayers. Especially, I have not found a systematic way to decouple the intensity changes in diffraction patterns varying due to corrugation and strain. For this reason, wide-beam sample-tilt series diffraction are used to probe the corrugation of the layers and scanning nanodiffraction was employed for strain mapping separately.

In the next two chapters, the effect of hBN and graphite on the optical properties of TMD monolayers will be invertigated and a systematic study of the many factors that affect the properties of TMDs will use the findings of this chapter. To date, hBN is the most ideal substrate for 2D materials, more specifically, the hBN/TMDs/hBN and hBN/graphene/hBN heterostructures are the basic routine production of high-performance devices for the following reasons:

i) encapsulation structure protects the intermediate layers from chemical reactions and contamination;

ii) multilayer hBN is as flat as an atomically flat crystal, smoother than conventional silica substrates;

iii) hBN as insulator will not damp the optical and electrical tests results, thus still reflects the intrinsic properties of graphene and TMDs.

Chapter 6

Interband transitions of transition metal dichalcogenides monolayers

Transition metal dichalcogenides (TMDs) monolayers are stable room-temperature light emitting and absorbing materials. One particular property of TMDs is that they display bright luminescence when their thickness is down to atomically thin monolayers, possessing a direct bandgap, as opposed to an indirect bandgap in multi-layers and bulk. They are one of the potential candidates for many novel quantum optical devices, such as single photon emitters [19, 20], flexible light-emitting devices [1, 21], and biosensors [22].

The optical properties of TMDs have been extensively explored using optical measurements, particularly by means of absorption and photoluminescence ref. [150, 50, 151, 51, 46]. On the other hand, TMDs can be excited in ways other than optical probe and also lead absorption and luminescence, such as fast electron excited electron energy-loss and cathodoluminescence signals. Aside from having sub-wavelength spatial resolution for optical property investigation [68], the benefit of electron probe is the ability to offer various in-suit signals on the same region, such as chemical mapping and structural arrangements can be provided inside a scanning transmission electron microscope (STEM).

It is the purpose of this chapter to establish the fundamentals of the physics of TMDs materials and their related optical measurements, which will be the basis for the following two chapters. The first section 6.1 reported the joint density of states (JOS) calculation and it was included in this chapter for several reasons: it is the JOS for the initial and final electron bands decides the optical transitions rather than the simple summation over discrete levels of the solid; it is the basis for understanding the relationship between the energy band gap, dielectric function, absorption spectra. Then, the spin-valley physics of TMDs is introduced in section 6.2, and the fundamentals covered here will be needed in the next two chapters. Finally, the spectra comparison between the optical and electron spectroscopy for hBN encapsulated TMDs will be given to show why EELS is the optimal approach to study INhomogeneous broadening of TMDs excitons in section 6.3.

6.1 Interband transitions: absorption and emission

Bands are formed by the electronic states of semiconductors. It is therefore the transitions between energy bands that determine the optical properties of semiconductors rather than discrete levels that determine them. The transitions between between the valence band states $\mathcal{C}$ and the conduction band states $\mathcal{V}$ are generally referred to as interband transitions.

The **joint density of states** (JOS) function, it defined as the number of optical transitions between the occupied (unoccupied) electronic states of the valence band and the (un)occupied electronic states of the conduction band, and it reveals how optical properties of solids give the information about the energy band structure in detail. For absorption and emission process, valance and conduction band states are involved at the same time, and the JOS gives the number of states available for photons of energy $\hbar\omega$ to interact with. In brief, the JOS provided an intuition into the relationship among complex dielectric function, energy band gap and optical observables.

To begin with, the expression for the joint density of states will be obtained from Fermi's golden rule in section 6.1.1, thus one can grasp the connection between the energy band gap and the JOS. On top of that, the expressions of direct interband absorption and emission will be given in the form of JOS in the section 6.1.2. Additionally, the relationship between the absorption and emission transition will be discussed as well. Next, the similarities and differences between the optical and electronic spectra will be introduced clearly in section 6.1.3 and section 6.1.4.

6.1.1 The joint density of states and Fermi's golden rule

The interband transition process is quantum mechanical in nature as it is depend on the coupling between the valence and conduction bands. This coupling results from Fermi's golden rule, that the probability per unit time $W_{\vec{k}}$ that a photon of energy $\hbar\omega$ makes a transition between the valence band state $\mathcal{C}$ and the conduction band state $\mathcal{V}$ at a given Brillouin zone point $\vec{k}$ is [152]:

$$W_{\vec{k}} \cong \frac{2\pi}{\hbar} \left| \left\langle v \left| \mathcal{H}' \right| c \right\rangle \right|^2 \delta\left[E_c(\vec{k}) - E_v(\vec{k}) - \hbar\omega \right] \tag{6.1}$$

where the $\mathcal{H}' = -e\vec{A} \cdot \vec{p}/mc$ is the matrix element Hamiltonian for the electromagnetic perturbation between the $\mathcal{V}$ valence and $\mathcal{C}$ conduction band Bloch states at momentum k, $\vec{p}$ is the optical field and $\vec{A}$ is the vector potential due to the optical fields with only spatial dependence. The energy conservation is considered as the delta function in Eq.6.1. The interband transition probability W for energy $\hbar\omega$ is the integration of Eq. 6.1 over k-space [152]:

$$W = \frac{2\pi}{\hbar}\int \left|\left\langle v\left|\mathcal{H}'\right|c\right\rangle\right|^3 \frac{2}{8\pi^3}\delta\left(E_c(\vec{k}) - E_v(\vec{k}) - \hbar\omega\right)d^3k \tag{6.2}$$

For simplicity, one can consider $|\langle v|\mathcal{H}'|c\rangle|^2$ is approximately independent of k, and because the electronic states in the Brillouin zone are quasi–continuous functions of k, then the joint density of states between the valence and conduction bands is [152]:

$$\rho_{cv}(\hbar\omega) = \frac{2}{8\pi^3}\int \delta\left[E_c(\vec{k}) - E_v(\vec{k}) - \hbar\omega\right]d^3k. \tag{6.3}$$

Eq.6.3 definds the joint density of states as **the number of states per unit volume per unit energy range which occur with an energy difference between the conduction and valence bands equal to the photon energy**. Though the constant energy surface $\mathcal{S}$ in k-space, and wave vector k_n normal to it, the joint density of states can be expressed as integral over energy surface as [152]:

$$\rho_{cv}(\hbar\omega) = \frac{2}{8\pi^3}\iint \frac{dS}{|\nabla_k (E_c - E_v)|_{E_c - E_v = \hbar\omega}}. \tag{6.4}$$

6.1.2 Interband transitions of direct band gap material

The definition of **absorption coefficient** $\alpha_{\text{abs}}(\omega)$ for the solid at frequency ω is the power removed from the incident beam per unit volume per unit flux of electromagnetic energy. It can be expressed by the joint density of states $\rho_{cv}(\hbar\omega)$, occupied conduction states $f(E_c)$ and occupied valence states $f(E_v)$ as [152]:

$$\alpha_{\text{abs}}(\omega) = \frac{16\pi^2 e^2}{m^2 c\tilde{n}\omega}|\langle v|p|c\rangle|^2 \rho_{cv}(\hbar\omega)\left[f(E_v) - f(E_c)\right] \tag{6.5}$$

where $|\langle v|p|c\rangle|^2$ matrix is the coupling between the valence and conduction bands, $\tilde{n}$ denotes the index of refraction. Combined Eq. 6.4 and Eq. 6.5, at joint critical points (also called Van Hove singularities) k_{Von} in the Brillouin zone where $(E_c(k_{Von}) - E_v(k_{Von}))$ is stationary, the $\rho_{cv}(\hbar\omega_{k_{Von}})$ is extremely large at the corresponding frequency ($\hbar\omega_{k_{Von}} = E_c(k_{Von}) - E_v(k_{Von})$), thus the absorption is very efficient.

Luminescence refers to the emission of radiation by a solid in excess of the amount emitted in thermal equilibrium. In view of the fact that luminescence is essentially a

non-equilibrium phenomenon, it requires external excitation by means of light, electron beams, current injection, etc., that can act to create an excess of electrons, holes, or both electrons and holes. A recombination radiation or luminescence is produced when electrons and holes recombine. If one assumed that the material is in thermodynamic equilibrium near a particular point, the luminescence (light emission) rate $R_{cv}(\hbar\omega)$ for the transition from the conduction band $\mathcal{C}$ to the valence band $\mathcal{V}$ is related to the absorption rate by the Planck distribution $\rho(\omega)$ [152]:

$$R_{cv}(\omega) = P_{vc}(\omega)\rho(\omega) = \frac{2}{\pi}\frac{\omega^2\tilde{n}^3 P_{cv}(\omega)}{c^3\left[\exp\left(\hbar\omega/k_B T\right)-1\right]}, \tag{6.6}$$

where the absorption rate can be expressed by absorption coefficient as $P_{cv}(\omega) = \frac{\alpha_{\text{abs}}(\omega)c}{\tilde{n}}$, so that the frequency and temperature dependence of the emission rate is [152]:

$$R_{cv}(\omega) = \frac{2}{\pi}\frac{\omega^2 n^2 \alpha_{ab}(\omega)\omega}{c^2\left[\exp\left(\hbar\omega/k_B T\right)-1\right]}. \tag{6.7}$$

Eq. 6.7 denotes that one material exhibits high emission rate at frequencies where absorption coefficient is large, as another way of putting it, **the prerequisite for a good emitter is that it is a good absorber.** The luminescent efficiency can be defined as the ratio between the energy associated with the radiative process and the total input energy. When excitation energy is provided, the radiative recombination process is in direct competition with the non-radiative processes. Thus, it is the luminescent efficiency rather than luminescent rate determines the optical response. Therefore, materials that are efficient luminescent are those in which radiative transitions prevail over nonradiative transitions.

6.1.3 Optical absorption and electron energy loss spectra

For absorption, electrons are promoted from the valence band to the conduction band, leaving holes in the valence band, thus the transitions take place at the Brillouin zone determined by the excited probe. Associated with optical absorption measurements, one measure the light intensity $I(z)$ after traversal of a thickness z of material as compared to the incident intensity $I(0)$. This gives rise to the following expression [70]:

$$\mathcal{A}(\omega) = \frac{I(z)}{I_0} = e^{-\alpha_{\text{abs}}(\omega)z}, \tag{6.8}$$

where the absorption coefficient can be expressed in terms of the imaginary part of the

complex index of refraction $\tilde{k}$ [1] as:

$$\alpha_{\text{abs}}(\omega) = 2\frac{\omega\tilde{k}(\omega)}{c}. \tag{6.9}$$

According to the conservation of energy, the incident light will be reflected, absorbed and transmitted, thus $1 = \mathcal{R}(\omega) + \mathcal{A}(\omega) + \mathcal{T}(\omega)$, where $\mathcal{R}(\omega)$, $\mathcal{A}(\omega)$, $\mathcal{T}(\omega)$ are the fraction of the power is reflected, absorbed and transmitted, respectively.

Electron energy loss spectroscope technique is conceptually similar to the optical absorption spectrum: an incident fast electron with energy E_i is scattered by an electron in the material, taking energy $\hbar\omega$ from the incident fast electron. According to the conservation of energy, low-loss region of EELS measured the energy loss of the fast electron as the absorption for the sample: $E_i - E_f = \hbar\omega$. Likewise momentum is conserved to yield the relation:

$$\vec{k}_i - \vec{k}_f = \vec{q} \tag{6.10}$$

where $\vec{k}_i$ and $\vec{k}_f$ are the initial and final momentum of the fast electron, and E_i and E_f are the initial and final energy of the incident electron, and $\hbar\omega$ and $\vec{q}$ is the energy and momentum transferred form the incident electron to the sample. The energy loss probability Γ_{EELS} of the fast electron can be described as the response of the sample by $\mathrm{Im}(-1/\epsilon(\vec{q},\omega))$ [34, 71]. The exact expression for EELS probability of thin TMDs heterostructures will be given in later section 8.2.1.

For optical measurement, the momentum transfer from the light source to the sample could be ignore as the wavelength of photon source is around 600 nm, corresponding to the wavevector $10^{-2}\, nm^{-1}$. For semiconductors, such as TMDs, a typical dimension across the Brillouin zone is one over the lattice parameter about 1.5 nm^{-1}. For EELS measurement, the spectrum could be recorded using a sufficiently small collection aperture, thus $\vec{q}$ transfer is minimized. As an alternative approach, one could consider the interaction of a transmitted electron with the entire solid is as a function of the dielectric response function $\epsilon(\vec{q},\omega)$. However, in the case where spectrum collection angle is small, $\epsilon(\vec{q},\omega)$ varies little with $\vec{q}$ and can be replaced by the optical value $\epsilon(0,\omega)$ [68].

Nevertheless, the EELS under small collection angle and optical absorption are not identical transition as a result of the different excitation probe but can show similar spectra.

[1] The relations between the optical constants and dielectric function [70]: $\varepsilon_1 + i\varepsilon_2 = (\tilde{n} + i\tilde{k})^2$, where $\varepsilon_1 = \tilde{n}^2 - \tilde{k}^2$ is the real part of the dielectric function, and $\varepsilon_2 = 2\tilde{n}\tilde{k}$ is the imaginary part of the dielectric function. The quantities $\tilde{N} = \tilde{n} + i\tilde{k}$ is called the optical constants of the solid, where $\tilde{n}$ is the index of refraction and $\tilde{k}$ is the extinction coefficient. It is necessary to emphasis that ε_1, ε_2, $\tilde{n}$, $\tilde{k}$ are all frequency dependent.

The importance of absorption measurements in the study of energy band structure is due to the spectrum emphasis on band extremes (Eq.6.5), which reveals details about the energy bands at certain locations in the Brillouin zone.

6.1.4 Cathodoluminescence and photoluminescence

The schematic representation of the interband luminescence process in a direct gap semiconductor is provided in Fig 6.1. For emission to occur, there must be an electron in the conduction band and an unoccupied level (i.e. a hole) in the valence band. These electrons and holes are generally injected into their respective bands by laser or fast electron excitation, which correspond to photoluminescence (PL) and cathodoluminescence (CL), respectively. In terms of the excited process for the luminescence, PL is the resonant narrow-band excitation at the exact k point as specific emission dominate its spectrum, while CL is the off-resonant broadband excitation among a large range of k resulting in many possible emissions.

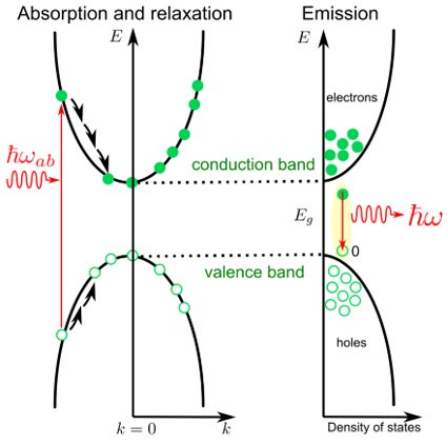

Figure 6.1: **Interband luminescence process in a direct gap semiconductor**: 1) electrons are injected into excited state band under electromagnetic wave with energy $\hbar\omega_{ab} > E_g$ (red arrow); 2) the hot electrons and holes are relax to the lowest and top available levels by interacting with lattice casued phonon emission as indicated by the black arrows in the left diagram; 3) the electrons and holes are located at the band edge as shown in the right diagram; 4) since the momentum of the photon can be neglected, the electron and hole that reombine must have the same k vector; 5) the electron and hole can be bounded by Columb force located in the middle of the forbidden band, as introduced in the section 6.2.2; 6) the electron and hole can decay into photons with energy $\hbar\omega$, which is represented by downward red vertical arrow on the right band diagram.

After the electrons (holes) are injected, they relax very rapidly to the bottom (top) of the condition (valence) band by emission of phonons. Thus the injected carriers are called hot electorns and holes, and after the phonon relaxation, they became cold electrons and holes. Moreover, the radiative transitions take place at energies very close to the

band-gap energy E_g no matter how the technique creates the hot electrons and holes in the first place.

The emission linewidth is either determined by thermal dispersion of charge carriers within their bands or inhomogeneous broadening effects. At temperature T, the linewidth contributed by the carrier dispersion at band edge is of order k_bT. Additionally, if the environments in which the sample finds itself within the probe size are not totally uniform, the emission spectrum will be modified by the interaction between the sample and their various local disorders. As a result, the inhomogeneous broadening is also referred to as environmental broadening.

6.2 Energy band structure of TMDs

Materials often derive new properties and exhibit a wealth of physical phenomena as the dimensionality of the system is reduced [135, 110, 130]. For TMDs, when they are reduced from multilayers to monolayers, the energy band changes from an indirect bandgap to a direct bandgap. The band structures of single-layer, double-layer and bulk MoS_2 materials based on Density Functional Theory (DFT) [2, 153] calculation are given in Fig. 6.2(a) and Fig. 6.3(c).

The optical properties of the TMDs are mainly determined by the **K**, **Γ** and **Q** points in the first Brillouin zone (FBZ) as in Fig. 6.2(b). There are six **K** points in the FBZ, containing two nonequivalent types of energy valleys, $\mathbf{K}^-$ and $\mathbf{K}^+$, that cannot be simply seen as the same kind. Spin-orbit (SOC) coupling is strong due to the presence of heavy transition metal atoms in TMDs resulting in the outer electrons having d-orbitals. This coupling causes the valence band to split into two subbands with an energy splitting of Δ^v_{SOC} of magnitude around a few hundred meV [154]. Similarly, a splitting occurs in the conduction band, but the energy difference Δ^c_{SOC} is only around a few tens meV, as shown in Fig. 6.3.

6.2.1 Spin bright and dark excitons

The spin-orbit coupling is slightly different for metallic elements Mo and W. In MoX_2, Δ^v_{SOC} has a different sign from Δ^c_{SOC}, while Δ^v_{SOC} has the same sign as Δ^c_{SOC} in WX_2. In MoX_2, the lowest energy transitions are spin allowed, while they are spin forbidden in WX_2 as shown in Fig. 6.3(a,b). That means the ground (frst excited) exciton state in the Mo- and W-based TMDs is bright (dark)- and spin-forbidden dark (bright)-state, respectively. Thus Mo-based monolayers emit light more efficiently than W-based as at low temperature carriers (created by photons or fast electrons) mainly populate the ground state of the exciton [155]. It is a common practice to ignore the difference in the conduction band Δ^c_{SOC}, which translates into an equivalent value of Δ^v_{SOC} for the experimentally measured SOC of the gap between X_A and X_B, ass shown in Fig. 6.3 (c).

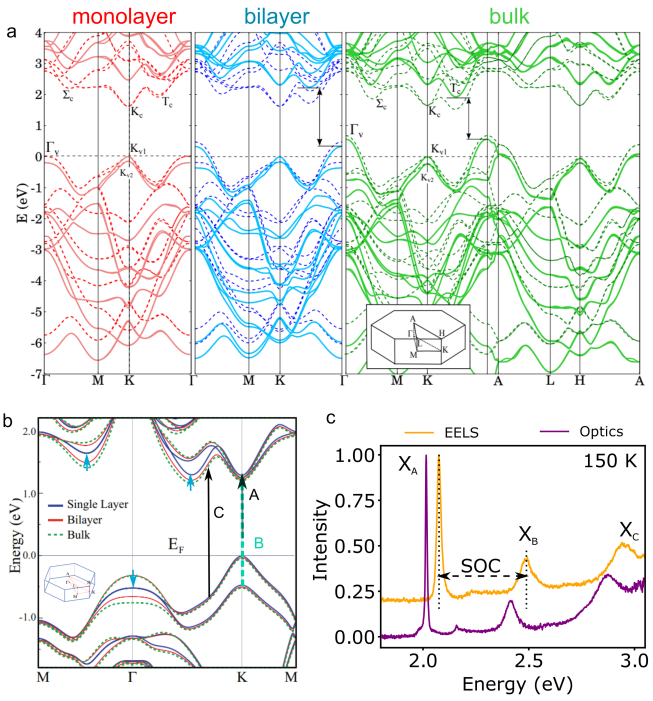

Figure 6.2: **Band structures of TMD materials:** (a) band structure calculation for MoS_2 based on DFT for a monolayer (red), bilayer (blue), and bulk (green). Reproduced from [129]; (b) DFT calculations of bulk materials, bilayer and monolayer WSe_2 energy band structures, where the variation of the extreme point is indicated by the blue arrow. Reproduced from [153]; (c) low-loss EELS (orange) and optical (violet) absorption spectra of hBN encapsulated monolayer WS_2. X_A, X_B and X_C peaks correspond to excitons formed at positions A, B and C in (b): bounding electron-hole pairs originates from Coulomb force interactions, as described in section 6.2.2. The energy difference between the EELS and optical absorption of X_A, X_B and X_C is mainly due to the measurement are conducted on two different samples and the electron beam could cause local heating. The energy difference between X_A and X_B is the spin-orbit coupling (SOC). Optical absorption measurements was reproduced from [35].

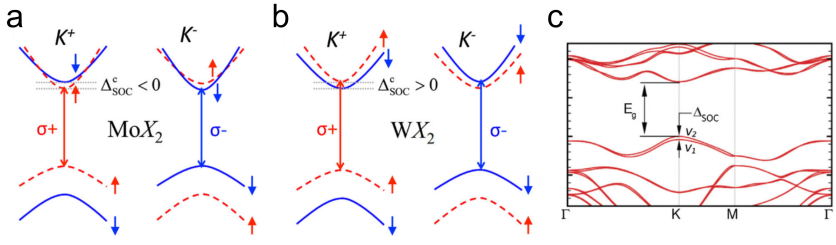

Figure 6.3: **Spin-orbit coupling in MoX_2 and WX_2:** (a) in Mo-based TMDs, the highest point of the valence band and the lowest point of the conduction band have the same spin; (b) in W-based TMDs, the highest point of the valence band and the lowest point of the conduction band have different spins; (c) theoretically calculated band structure and valence band-orbit spin coupling split in Mo-based (X denotes chalcogen group element atoms). Reproduced from ref. [2].

6.2.2 Multiple exciton species in TMDs: X_A, X_B and X_C

Materials excited by fast electrons or photons undergo interband absorption, thus producing electrons in the conduction band and holes in the valence band. The resulting electrons and holes can be attracted to each other by the Coulomb interaction, forming bonding electron-hole pairs, which are called excitons, as shown in Fig. 6.5 (b,c). Excitons can interact with phonons, decouple bounding electrons and holes to become free carriers, escaping from the Coulomb force. When the binding energy of the exciton is less than the energy of the phonon, k_BT, the exciton cannot exist stably. Excitons can be observed in many materials by reducing the phonon energy k_BT, that is, by lowering the temperature of the material [156].

When a photon interacts with matter, the momentum of the photon is negligible, so the excited electron and hole possess the same magnitude of momentum $|\mathbf{k}|$. Excitons can only be formed when electrons and holes have the same velocity, because no relative motion between electrons and holes occurs when $v_e = v_h$. The velocities of electrons and holes are expressed in terms of group velocities as:

$$v = \frac{1}{\hbar} \cdot \frac{\partial E}{\partial \mathbf{k}}. \tag{6.11}$$

At the extreme point positions in the valence and conduction bands, the partial differentiation of energy with respect to momentum is zero. Thus from these energy positions, one can observe very strong exciton effects, which is called band Nesting. As presented in in section 6.1, another interpretation of the excitons can be made by JOS that the strong absorption occurred at joint critical points.

The positions labelled in Fig. 6.2(b) satisfy the condition that electrons and holes have the same velocity: where the excitons formed at A and B move with $\partial E/\partial \mathbf{k} = 0$; for position C, the valence and conduction bands are parallel to each other but $\partial E/\partial \mathbf{k} \neq 0$. At this point the derivative of energy to momentum is not zero but has the same value, and also forms stable electron-hole pairs. The exciton optical absorption responses corresponding to the A, B and C energy band positions in Fig. 6.2(b) are labelled in as X_A, X_B and X_C in Fig. 6.2(c), respectively. For all TMDs, the excitons are named X_A (or X^0 for the neutral exciton), X_B and X_C, respectively, depending on their energy ordering from lowest to highest, and I keep following this notation for TMD absorption spectra in this thesis.

6.2.3 Exciton binding energy and hydrogenic Rydberg series

The exciton has slightly less energy than the unbound electron and hole (band gap) due to the Coulomb force. The interaction produces a series of internal exciton states, and en-

ergy level of bound state is hydrogenic, that have ground and excited states, and they can likewise be characterized by the principal quantum number. As presented in Fig. 6.4, there are ground and first excited excitons for both X_A and X_B in the calculated absorption spectrum. Several studies have reported excited exciton series for various exciton species inside TMD monolayer, such as excited X_A series[157], excited trion (charged exciton) [141], excited biexciton (quasi-particle formed from two excitons) [158].

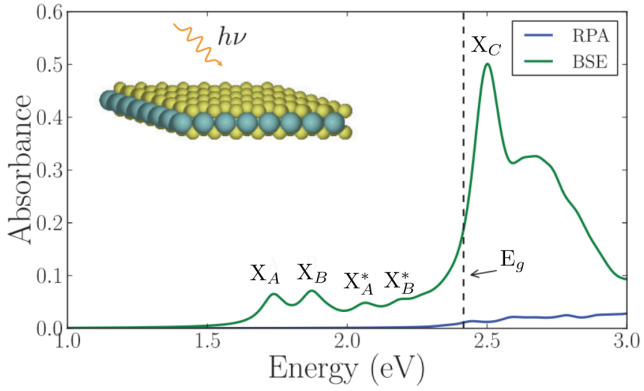

Figure 6.4: **Calculated optical absorption spectrum of Mo_2 with and without the direct electron-hole interaction.** Considering and neglecting the electron-hole direct interaction correspond to Bethe–Salpeter equation (BSE) based on many-body perturbation theory and Random phase approximation (RAP), respectively. The ground state of X_A, X_B and their first excited Rydberg states X^*_A, X^*_B. The dashed line indicates the quasiparticle band gap E_g. Reproduced from ref. [159].

Compared to bulk materials, electrons and holes forming excitons in monolayer TMDs are strongly confined within the plane of the monolayer and, in addition, are subject to reduced screening as a result of the change in the dielectric environment, as presented in Fig. 6.5(c). According to a simple hydrogenic model (Rydberg series) , the effective mass Hamiltonian of exciton in 2D system is [157]:

$$H = -\hbar^2\nabla^2_{\mathbf{r}}/2\mu + V_{eh}(r) \tag{6.12}$$

where $\mu = 1/\left(m_e^{-1} + m_h^{-1}\right)$ is the exciton reduced mass, $V_{eh}(r) = -e^2/\varepsilon r$ is a locally-screened attractive electron-hole interaction and ε is the complex dielectric constant. Based on Eq. 6.12, the n^{th} exciton resonance binding energy in TMDs is dererminded by: [160, 157]:

$$E_b^{(n)} = \frac{\mu e^4}{2\hbar^2\varepsilon^2(n-1/2)^2} \tag{6.13}$$

which can reaching up to 30% of the energy band gap E_g. The reason of 2D materials have a large binding energy is because of the geometric confinement and reduced dielectric screening [159].

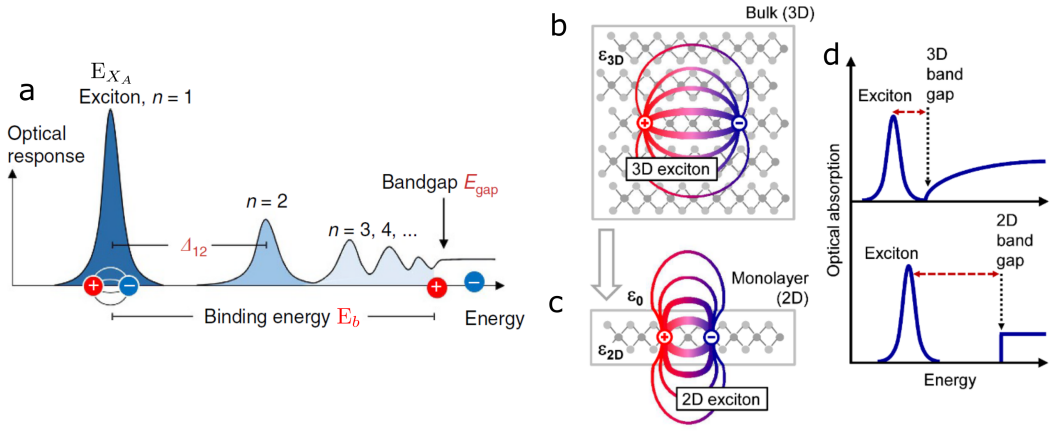

Figure 6.5: **Exciton energy levels and binding energy:** (a) The relationship between exciton Rydberg states and the electronic bandgap. Reproduced from ref. [161]. A schematic illustration of real-space of electrons and holes bound by Coulomb interaction into excitons in (b) a bulk and (c) a 2D material. (d) The effect of dimensionality on electronic and excitonic properties, as represented schematically by optical absorption. Both the band gap and the exciton binding energy are expected to increase as the evolution from 3D to 2D occurs (indicated by the red dashed line). (b-d) are reproduced from ref. [157].

Dielectric environment will strongly influence the properties of exciton through dielectic function ε in an atomically thin semiconductor because excitons lie close to a surface. This model also provides a straightforward estimate of the unusually large exciton binding energy in TMD monolayers, which has been determined to be a few hundred meV [157]. The large binding energy is due to the 2D nature and the weak dielectric screening from the environment, thus the Coulomb interaction is significantly enhanced in TMDs (Fig. 6.5 (c)). According to different reports, the exciton binding energy in monolayer TMDs is in the interval of 200-700 meV [157, 158], allowing they can stably exist at room temperature. In contrast, the GaAs bulk material has a large permittivity (around $13\epsilon_0$) and a small binding energy in the region of 5 meV [162], which is unable to survive at room temperature.

6.2.4 Netural and charged excitons

Coulombic interactions between two-dimensional materials are not only limited to one electron and one hole interactions. In fact, three charged particles can also be bound together by Coulomb interaction to form a charged exciton called trion, which consists

of two types: X^+ (one electron plus two holes) and X^- (two electrons plus one hole). In optical experiments, one generally controls the concentration of carriers in the material by applying a bias to the TMDs, which in turn artificially controls the formation of the two types of trions [163].

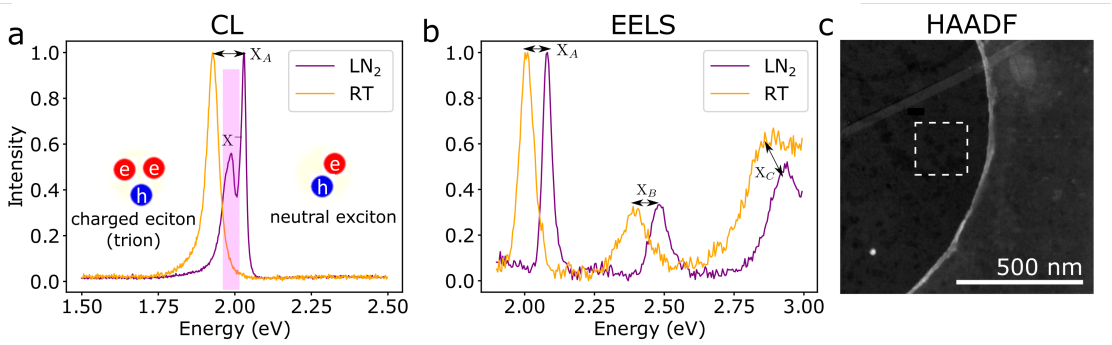

Figure 6.6: **CL and EELS spectra of WS_2 at RT and LN_2:** (a) the presence of X^- in the CL spectrum of monolayer WSe_2 is affected by temperature; (b) the EELS absorption spectrum corresponding to (a) does not observe the presence of X^-. (a) and (b) are measured from the white boxed region in (c). The energy difference between X_A in (a) and (b) corresponds to the Stokes shift. Reproduced from the supplementary information of ref. [28]. The experiments were performed within ChromaTEM, as with the other spectra presented in the next two chapters.

Among all the exciton species (X_A, X_B and X_C), only neutral and charged X_A exciton at the lowest band gap **K** can decay to photons, thus emitting light. In ref. [28], the extra peaks with a smaller energy than X_A in STEM-CL at 110 K was taken to be X^- rather than X^+ by default as shown in Fig. 6.6(a), because it assumed the undoped TMD materials is n-type. As shown in Fig. 6.6(a), only at low temperatures are the peaks of the trion present, due to the fact that the binding energy of the trion is of the order of 20-30 meV [28, 164, 165]: at T=110 K, phonon energy is 9.5 meV, much smaller than the bonding energy of trion, whereas phonon energy is 26 meV at room temperature is comparable to the binding energy of trions.

As shown in Fig. 6.6, trion peaks are rarely visible in the EELS absorption spectrum, this is probably due to the energy spacing between X^* and X_A at 110 K and the low oscillator strength, rather than X^* doesn't exist at 110 K. The reason for this is that the peak of the trion is distinguishable even at 190 K in the optical absorption spectrum [166]. However, nothing that can be done about this because the resolution of the EELS is limited by the energy spread of the electron, which is still extended to 5 meV at most, even under the operation of a monochromator in ChromaTEM. A possible way to detect trion peak in EELS is to decrease the temperature, because X^* is stronger and thus more prominent at low temperature. But the lowest temperature of our sample holder for ChromaTEM is 110 K though a liquid nitrogen cooling. It is impossible to study trion in EELS at the moment, but fortunately the information can be acquired through CL in the microscope

as a supplementary method. Therefore in all the EELS spectra of this thesis we do not consider trions and focus only on X_A and X_B .

6.2.5 Exciton quantum dynamics and linewidth limitation

Excitation quantum dynamics can be described by two fundamental parameters: i) **excited state population relaxation** with decay time T_1; ii) the **exciton dephasing** at timescale T_2 [167]. The first dynamics includes both radiative and non-radiative recombination, and do not provide any details of the exciton coherent dynamics, and give the excited state population relaxation rate Γ, which is inversely proportional to the population decay time T_1 as indicated by curved arrow in Fig. 6.7(a). Thus, luminescence is generally an incoherence emission process unless the coherence is enhanced by polishing the sample faces to form an optical cavity. It has a spontaneous tendency to decay to lower levels and randomly break the coherence of the wave function. And the rate of this damping process is governed by the lifetime T_1 as below:

$$\frac{1}{T_1} = \frac{1}{\tau_R} + \frac{1}{\tau_{NR}} \tag{6.14}$$

where T_1 is up limited by the radiative lifetime τ_R of the excited state ($|1\rangle$), and τ_{NR} is the non-radiative relaxation time for the non-radiative transition. According to the energy-time uncertainty principle, the excited state's finite lifetime causes the broadening of the resonance at low temperature [167]:

$$\Delta\omega = \frac{\Delta E}{\hbar} \geq \frac{1}{\tau}. \tag{6.15}$$

This broadening linwidthis intrinsic to the transition, and it is called **natural broadening** or alternatively**radiative broadening**.

The second process for the excitation quantum dynamics is the coherent superposition of the crystal ground ($|0\rangle$) and excited ($|1\rangle$) states with dephasing rate γ (black down arrows in Fig. 6.7(a)), which is responsible for the homogeneous linewidth of an exciton resonance as described below. The homogeneous linewidth is linked to population relaxation through [167]:

$$\gamma = \Gamma/2 + \gamma^* \tag{6.16}$$

where γ^* describes those elastic processes that interrupt phase coherence of wave function of the excited state without affecting excited-state occupation, such as exciton-exciton and exciton-photon scattering [35, 168, 169, 170]. In general, γ^* is a population-conserving scattering processes, while Γ is population decay. Based on the fact that

the exciton relaxation time for TMDs is longer than several ps [171] and according to Eq. 6.16, it can be assumed that exciton lifetime will have a negligible effect on linewidth (less than 1 meV), which indicates that the decoherence is governed primarily by scattering processes for excitons in TMDs rather than population relaxation. The homogeneous linewidth γ broadened can be estimated by exciton-phonon scattering [35, 17, 172]:

$$\gamma = \gamma_0 + AT + \frac{B}{exp(\hbar\omega_a/k_BT) - 1} \tag{6.17}$$

where γ_0 is the residual linewidth at T=0 K, A and B are exciton-phonon coupling for the low- and high-frequency modes, $\hbar\omega_a$ is the average energy of the relevant phonons. The parameters in Eq. (6.17) can be retrieved by fitting γ-T, for example by PL measurements [17, 172]. The exciton-phonon dephasing time (τ_{de}) and lifetime of TMD monolayers can be measured by four-wave mixing microscopy [173] at various temperatures, thus the homogeneous broadened linewidth can be directly determined by $\gamma = 2\hbar/\tau_{de}$.

Beside that, there is the **inhomogeneous broadening** (Γ_{in}) **that results from a varying local potential**, resulting in a distribution of exciton transition frequencies (energy centers) as shown in Fig. 6.7(b), which can broadening the linewidth of excitons larger than the linewidth value of homogeneous broadening limitation [173].

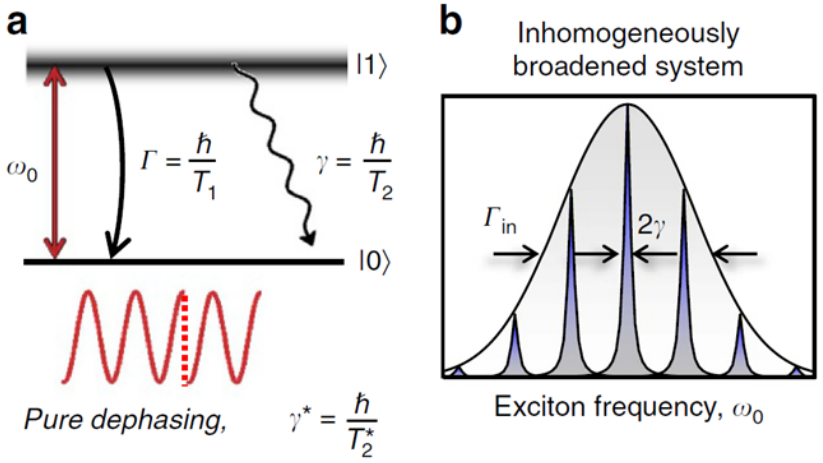

Figure 6.7: **Intrinsic exciton coherent dynamics and resonance broadening mechanisms:** (a) the quantum dynamics of an exciton with resonance frequency (ω_0) are characterized by two key parameters: the population decay rate Γ (population lifetime T_1) and the dephasing rate γ (coherence time T_2); (b) Inhomogeneous linewidth broadening (Γ_{in}) due to a varying local potential results in a distribution of exciton transition frequencies. Reproduced from ref. [169, 170].

6.3 Overall comparison of EELS&CL vs A(ω)&PL

The signals measured in CL and EELS were compared to $A(\omega)$ and PL for a hBN encapsulated WS_2 in Fig. 6.8. It is clear to note that the test results for PL vs CL and EELS vs $A(\omega)$ are very similar, while the transition process is not identical as discussed in section 6.1.3 and section 6.1.4. However, both electron spectroscopy and optical measurement revealed a certain amount of information on the energy band structure of WS_2: 1) charged (X^-) and neutral(X_A) exciton are observed in both CL and PL; 2) EELS (absorption) has a larger energy center than CL (PL) due to the Stokes shift. The larger Stokes shifts in the Fig. 6.8 (a) than 6.8 (b) is due to the energy dispersion of electrons is less accurate than that of light, and the energy center of EELS in Fig. 6.8 (a) has the precision about 1%.

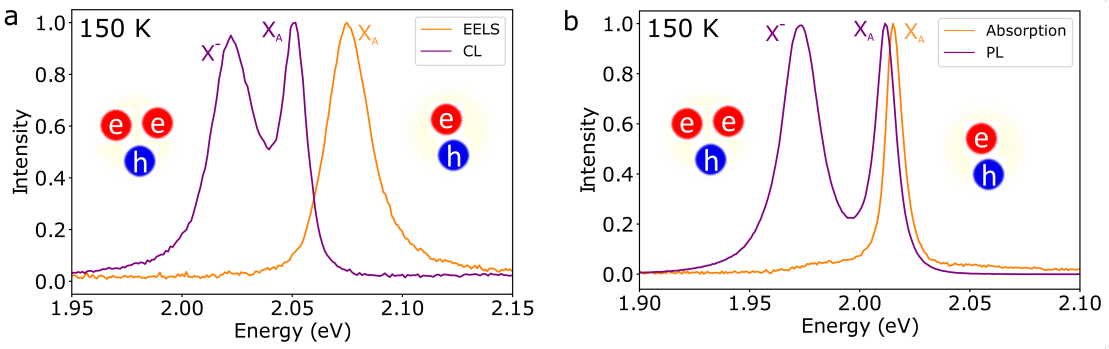

Figure 6.8: **Comparision between EELS&CL and absorption&PL:** (a) fast electron excited EELS and CL spectra; (b) optical absorption A(ω) and PL spectra. The optical measurments are made on two different samples of hBN encapsulated WS_2 at 150 K. The PL measurement was conducted by a continuous wave laser of 532 nm wavelenth. Optical measurement data courtesy of Ashish Arora and was reproduced from [35].

Electronic spectroscopy, however, provides optical information about the sample at the nanoscale due to its short wavelength (4.8 pm at 60 keV). In fact, EELS suffers from inelastic delocalization due to the long-range Coulomb interaction that limits its spatial resolution. In low-loss regions, its spatial resolution usually ranges from a few nanometers to tens of nanometers, depending on the specific values of energy being lost [68]. Despite this, EELS and CL are still therefore effective methods for inhomogeneous broadening investigation, since the measurmed spectra for PL and optical absorption are the total response over hundred nanometers.

In addition, the spectra of EELS is comparable to the optical absorption spectra attributed to the advanced monochromator and spectrometer design, as any peaks in EELS spectra cannot be sharper than ZLP. Under the experimental condition limitated of energy resolution (180 meV), even X_A and X_B are not so distinguishable [174]. Re-

cently, it has previously been observed that EELS and CL SPIM shown variations in TMDs down to 10 nm [28, 29] in a monochromated STEM (20 mev) at liquid nitrogen temperature.

The optical absorption spectra in this thesis are measured by Robert Schneider and Ashish Arora at University of Münster. The experiments were conducted at at normal incidence by measuring $\mathcal{A}(\omega) = 1 - \mathcal{R}(\omega) - \mathcal{T}(\omega)$ of TMD monolayers on top of sapphire substrate under a white light source transmitted across them. Light source is a broad-band LED source for WS_2 and a tungsten halogen lamp for WSe_2. The system response (reference spectrum) is measured by reflecting light from the bare sapphire substrate area close to the hBN/TMDC/hBN structure.

6.4 Summary

It is described in detail in this paper how light (or fast electrons) interacts with TMDs, as well as the resulting spectrum. In particular, the connection between energy band gap, absorption and emission spectra, complex dielectric function, complex refractive index is clarified. In addition, the differences and connections between EELS&CL and $A(\omega)$&PL are also explained in detail.

The energy band structure of TMDs is elucidated, and explained why the exciton resonance dominate the optical response of TMDs. The reason for the presence of multiple excitons in TMDs absorption/emission spectra is also addressed. Furthermore, it revealed in this chapter that the dephasing process determines the narrowest linewidth for homogeneous broadening, and it is the sharpest linewidth one can detect in TMDs. Finally, EELS&CL and $A(\omega)$&PL spectra of hBN/WS_2/hBN are compared, and why monochromated STEM/EELS/CL is a powerful experimental method for studying inhomogeneous broadening at the nanoscale is explained.

Chapter 7

The influence of heterostructures on the broadening of excitons in TMDs

The properties of 2D materials, in particular graphene and TMDs, are sensitive to their external environment. Therefore, realizing their full potential requires understanding and controlling the extrinsic disorders. It has been observed that the hBN encapsulate structures improves the properties of TMDs. For example, encapsulated 2D materials have better electronic mobility and sharper emission/absorption excitonic linewidths approaching the homogeneous broadening limit [17, 36]. Preliminary experiments have shown that strain, roughness, absorbates, surface cleanliness (impurities), trapped charges and oxidation are the main sources of extrinsic disorder for 2D materials. Moreover, suspended monolayers like graphene and MoS_2 have an intrinsic rippling nature as demonstrated in the previous chapter.

How does each of these disorders affect the exciton linewidth? Is there any direct connection between structural aspects, including material flatness and nanoscale strain homogeneity, and a narrower linewidth? One wonders how encapsulation with hBN improves the optical quality of TMDs. However, there are no comprehensive and systematically comparative experiments to reveal the specific role of hBN, although negative aspects such as exciton linewidth broadening induced by charge disorder [35], and dielectric environment variations [5] are discussed separately.

In fact, the mentioned external environment are mainly dependent on the substrate used [5, 35]. From this perspective, I focused on various wide bandgap dielectric materials in this chapter, namely hexagonal boron nitride (hBN) and amorphous silicon nitride (Si_3N_4), under different configurations as support or encapsulation material for WS_2 monolayers to disentangle the factors contributing to inhomogeneous broadening of exciton absorption peaks measured in EELS. The different roughness of Si_3N_4 and hBN can be used to investigated the effect of flatness on exciton linewidth of TMDs. The linewidth comparison among freestanding, support and encapsulation configuration could be applied for further exploring other broadening factors such as charging traps, surface cleanliness and sample degradation. The study was conducted in this chapter

using a combination of electron microscopy techniques to investigate the effect of different types of disorder on the TMD excitons absorption EELS linewidth. The effect on the exciton linewidth is described in detail for each of the underlying disorders.

The absorption linewidths for freestanding, 15-nm hBN supported, 5-nm and 15-nm hBN encapsulated, 15-nm Si_3N_4 supported, 15-nm Si_3N_4 and 50-nm hBN encapsulated WS_2 monolayers are presented in section 7.1. In section 7.2, core-loss EELS and t/λ thickness measurement are applied to determinate the composition and quantity of contamination. In section 7.3, I report on the effect of the electron beam scanning mode on the exciton EELS linewidth. Furthermore, because high-energy electrons are used as a probe, electron beam-induced damage on bare monolayer TMDs is also revealed to be responsible for irreversible linewidth increases in section 7.4.

In section 7.5, the conclusions of the previous chapter on the corrugation of monolayer TMDs in different heterostructures will be involved to discussion of dominant effect on the optical properties, especially exciton EELS linewidths. In the last section 7.6, I will summarize the importance of the hBN encapsulation structure in preserving optical properties.

7.1 EELS spectrum of monolayer WS_2 under diffraction configurations

Three exciton peaks, marked X_A, X_B and X_C in Fig. 7.1, can be distinguished in all WS_2 monolayers in different configurations: (i) freestanding, (ii) on hBN, (iii) hBN encapsulated, (iv) on Si_3N_4, and (v) Si_3N_4/hBN encapsulated. In the spectra, A and B excitons are associated to transitions at the direct band gap at the $\mathbf{K}^+$ and $\mathbf{K}^-$ points and are split due to spin-orbit coupling, denoted as X_A and X_B. C excitons are associated with direct transitions at the $\mathbf{Q}$ point between $\mathbf{\Gamma}$ and $\mathbf{K}$ point in the Brillouin zone [175], as introduced in section 6.2.2.

The absorption EELS spectra of WS_2 monolayer changes for different substrate configurations at 110 K as shown in Fig. 7.1. Small energy shifts occur due to different real parts of the dielectric function of the substrate and strain. Even for the same substrate the energy center of X_A is extended beyond 30 meV about its mean as the dot is extended in energy center axis in Fig. 7.1 (b), it is because of the contamination and strain is not even within the same sample.

Compared to absolute energy center of X_A, the large variation in width of the absorption peaks is more evident, in particular towards the lower-energy transition of X_A. This can be represented by the full width of half maximum (FWHM) measured from spectral fits using Lorentzian or Gaussian functions as shown in Fig. 7.2. The variation in linewidth

axis in Fig. 7.1 (b) is the same data as Fig. 7.1 (a). The linewidth differ slightly in the values by two methods. There is a slight difference in the linewidth between the two fitting methods. For the purpose of identifying the factors that influence exciton linewidth for brevity, the linewidth from Lorentzian fits are used for discussion, but in the summary section 7.5 both values will be presented.

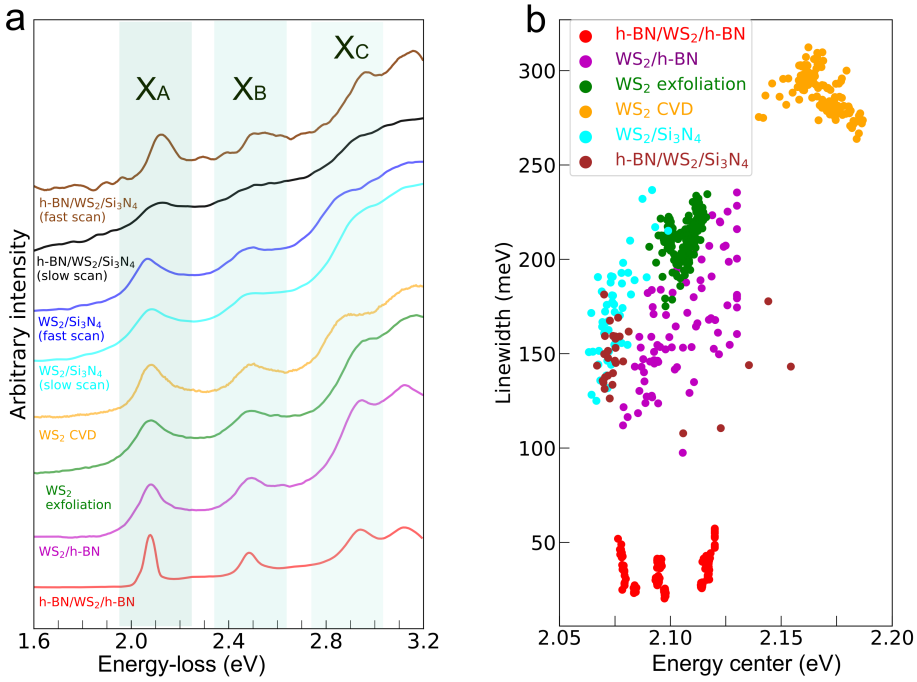

Figure 7.1: **EELS absorption spectrum and X_A FWHM and energy center distribution of monolayer WS_2 in various configurations.** (a) EELS absorption spectra are measured by STEM-EELS on different substrates at 110 K. EELS spectra are from WS_2 monolayers of hBN encapsulated (red), hBN supported (purple), freestanding exfoliated (green), freestanding CVD-grown (yellow), slow-scan Si_3N_4 supported (cyan), fast-scan Si_3N_4 supported (blue), slow-scan Si_3N_4/hBN encapsulated (black) and fast-scan Si_3N_4/hBN encapsulated (brown) cases, respectively. Each spectrum is normalized with respect to its X_A intensity after ZLP alignment and tail subtraction. All spectra are smoothed by a Savitzky-Golay filter of polynomial order 3. (b) Statistic plot of X_A energy center and linewidth, which are extracted from the Lorentzian fit of X_A exciton peak. Fast-scan and slow-scan of Si_3N_4 supported WS_2 monolayer are ploted in the same color in (b). Only the fast-scan data of Si_3N_4/hBN encapsulated WS_2 monolayer can be fitted, because slow-scan of that is too weak to fit with the strong background of hBN.

As shown in Fig. 7.2, the use of hBN induces an obvious improvement in optical quality in comparison to both freestanding and Si_3N_4 supported monolayers, despite Si_3N_4 also being a wide-gap dielectric material. For hBN encapsulated WS_2 monolayer, the sharpest X_A mean absorption FWHM is observed. This is significantly less than the mean linewidth for the hBN supported WS_2 monolayer which exhibits comparable monolayer TMDs roughness of h/L=0.002 (details for roughness measurement is de-

scribed in section 5.4.1). The energy center variations of hBN/WS_2/hBN is different from the result in Fig. 7.1 is bacause the results obtained from three different areas on the sample that they are mainly distributed on three concentrated values on the energy center axis. Also, for the narrow X_A spectra, I used the energy center as the most preferred parameter to restrict it to the extreme value point due to the accuracy of the fit. This results in a narrow distribution of energy centers for individual regions examined on the energy center axis as well.

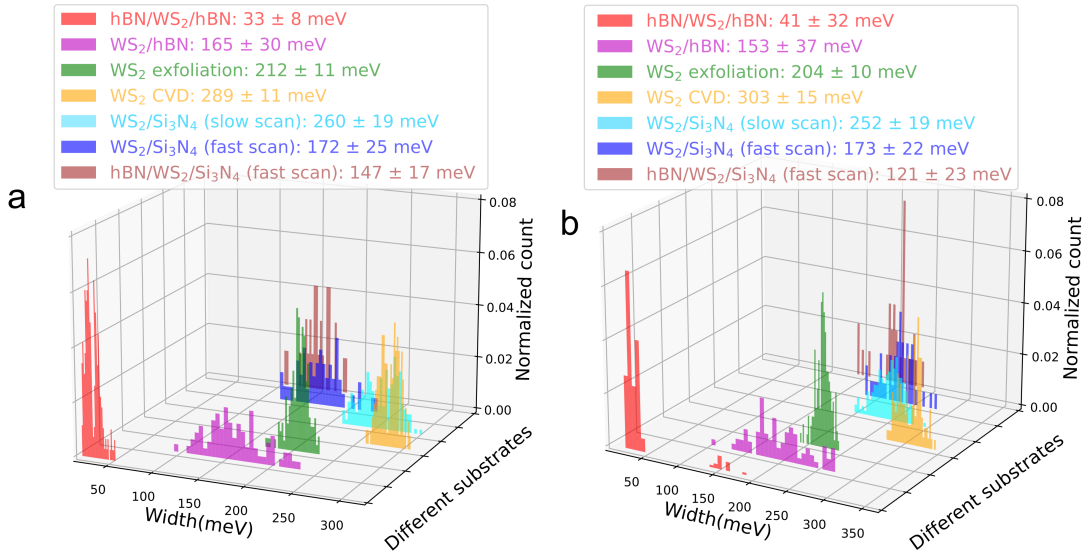

Figure 7.2: **Histograms of X_A linewidths measured from different positions of WS_2 monolayer on different substrates.** Linewidth is extracted from the FWHM of the (a) Lorentzian and (b) Gaussain fit of X_A exciton peak. The mean FWHM and standard deviation for each substrate is listed in the legend. Unfortunately, the excitons in slow-scan EELS spectrum of Si_3N_4/hBN encapsulated WS_2 monolayer is too weak to fit with the strong background of hBN, so there is no histogram for X_A in this configuration. The data in this figure is the same set and fit as that shown in Fig. 7.1 (b).

There is no complementary emission data from CL spectrum is available in this chapter because all samples except the hBN encapsulation did not exhibit measurable CL signals. For freestanding/suspended monolayer TMDs, it likely has to do with the low charge-carriers density produced by nanometer-sized electron beam on the thin sample, exciting insufficient electron-hole pairs in the thin material to produce detectable CL. For the sample with Si_3N_4 involved, sufficient electrons and holes are generalized, but the highest priority channel for de-excition is excitation non-radiative recombination through defects from the amorphous Si_3N_4. Consequently, these samples do not exhibit a measureable CL signal, and the CL study of the hBN-encapsulated vdWH will be discussed in the next chapter.

7.2 Surface/Interface cleanliness of TMDs

Firstly, the definition of interfaces and surfaces seems ambiguous. To specify, as these terminologies are in terms of the TMDs monolayers, when it is exposed in vacuum, it is called surface; when it is encapsulated or supported, the interior surface towards the substrate named as interface. Some contaminants are generated on the surface of TMDs during our sample preparation using tape exfoliation as well as material transfer with PDMS/PC stamp [28]. It is known that in vdWH, interfaces between materials tend to expel residues, which then coalesce into bubbles [94].

Contamination can alter the local dielectric function, such that the exciton peak center would shift, resulting in **inhomogeneous broadening from summation of different spectra with different energy centers**. Therefore, a monolayer that is only single-side supported has an exposed surface and it has directly contacted with the PDMS/PC stamp and chloroform. Thus the exposed surface contains inhomogeneously distributed residue and adsorbates, which would explain the difference in X_A mean FWHM between the hBN supported and encapsulated monolayers.

Secondly, the large spread in X_A energy center of ± 30 meV or more for hBN supported and Si_3N_4 supported (purple and blue in Fig. 7.1(b)) are also indicative of this hypothesis. Another supporting evidence is that the hBN/Si_3N_4 encapsulated WS_2 monolayer has sharper linewidth (147 meV) than hBN supported WS_2 (165 meV), since the encapsulated monolayer has better surface cleanliness than the supported monolayer. As for the containments outside the vdWH, the disorder is well screened by the top or bottom hBN flakes, thus having a minimal impact on the dielectric disorder.

Composition of the contaminants

The origin of these contaminants are the glue and tape residue components of different scotch tapes used during sample preparation. Core-loss EELS and log-ratio thickness measurements (introduced in section 3.4.3.4) of the regions using EELS scan can provide the the contamination composition and give an estimation of its thickness. The thickness of contamination varies from a few to tens of nanometers, which affect the dielectric function to different degrees.

The presence of carbon contaminants shows up in the thickness histograms as higher thickness tails beyond the normal distribution, as highlighted by the purple arrow in Fig. 7.3(c). For encapsulated samples, the histogram of thickness is a normal distribution (Fig. 7.4(c)). The thickness of the contamination can vary across the sample at the nanoscale.

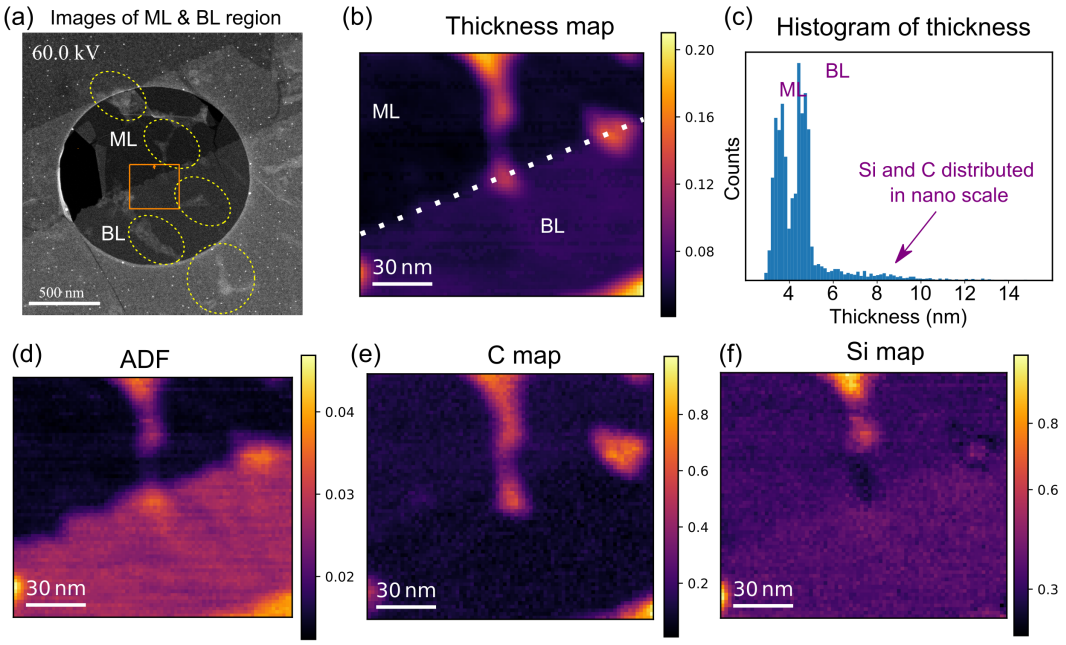

Figure 7.3: **Core-loss EELS map of bare TMDs:** (a) HAADF image of freestanding monolayer (ML) and bilayer (BL) TMD region. Visible contamination is marked by dotted yellow circles; (b) thickness measurement using EELS by log-ratio method corresponding to the region in (a) marked by the orange rectangle, the histogram is shown in (c); (d) is the ADF image of the scanned region marked in (a); (e) and (f) are the elemental maps of carbon and silicon. The EELS spectrum image was treated using PCA to improve the fidelity of the elemental maps.

In short, an ideal clean sample not only possess a symmetric histogram of thickness, but also should not have other common impurity elemental edges, such as Si-$L_{2,3}$, C-K and O-K in core-loss EELS. As shown in Fig. 7.4(f,g), the C-K signal intensity is much weaker in the encapsulated samples, at the limit of EELS detection, indicating few nanometers thick contamination exists at most. However, the freestanding monolayers shows C-K signal with clear fine-structure indicating amorphous-structured carbon, as presented in the comparison in Fig. 7.4(g).

One thing to note, in addition, is that the EELS measurements are summed through the sample thickness. Therefore, it is not trivial to differentiate exactly which surface/interface the contamination resides. The effect of an inhomogeenous contamination layer, indeed could change the local dielectric function. Thus, the exciton peak center would shift and lead to inhomogeneous broadening from summing up of different spectra with different energy centers. For sure, there is still some contamination even in hBN encapsulation, but the amount contacted with TMDs is significantly less compared to freestanding layers. This is because during the sample preparation, two flakes are brought into contact only partially, starting at one of its edges stamp first at 120°C. Thereafter, the contact front advances under a small pressure of the PDMS/PC stamp,

and the contact interface cross-section between the two flakes increases slowly. With the force applied at high temperature during the process, most of the contamination would be expelled outside the interior interface.

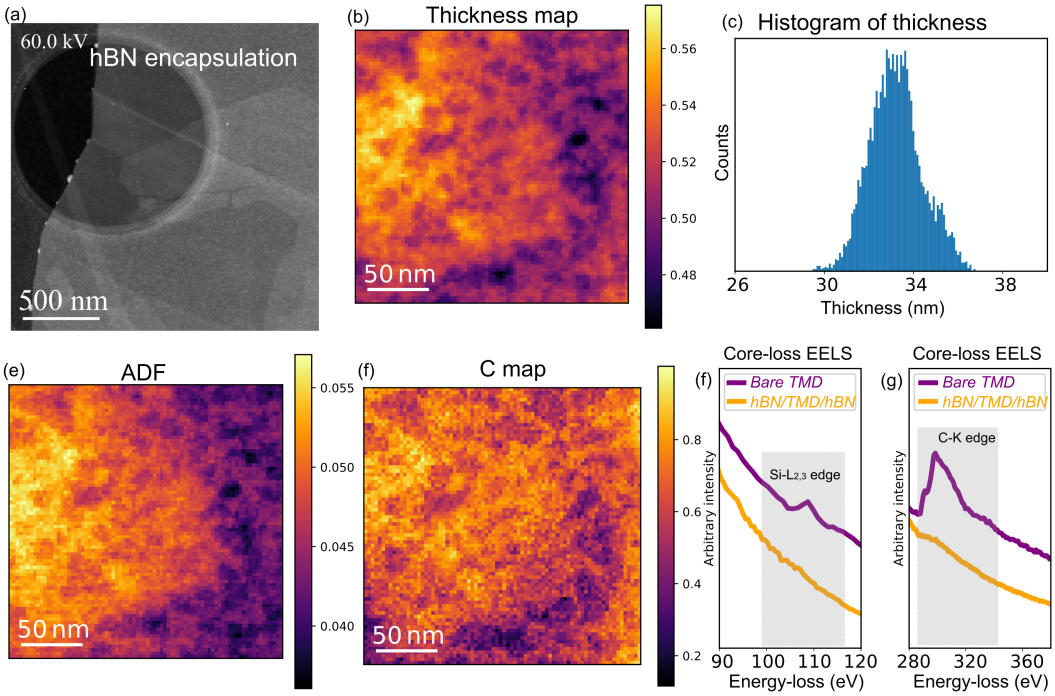

Figure 7.4: **Core-loss EELS map of hBN encapsulated TMDs:** (a) HAADF image of an hBN/TMD/hBN heterostructure: no visible contamination in the sample is seen; (b) thickness measurement by EELS log-ratio method, and (c) the corresponding histogram; (d) is the ADF images of the scanned area and (e) is the carbon elemental map; (f) and (g) are the spectra of Si-$L_{2,3}$ and C-K in bare TMD and hBN/TMD/hBN encapsulation sample; (a) was not acquired in the same region as (b-g), but it represents the general case. The EELS spectrum image was treated using principal components analysis for denoising to improve the fidelity of the elemental map.

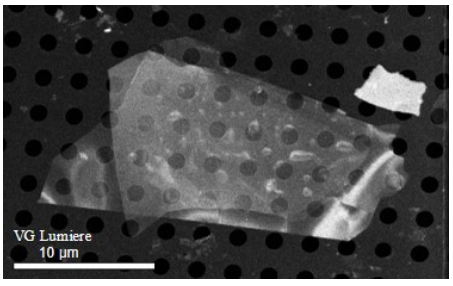

Figure 7.5: **Segregation of the impurities for hBN encapsulated TMDs.** Thw brighter region are the clusters of contamination at the interface of TMDs and hBN flake. The image is taken at BF mode, so that the contamination is lighter atoms, such as C and Si. Image courtesy of Jassem Baaboura.

There is still some residuals which is not expelled outside interface after encapsulation. This part of the residuals will be clustered together to form bubbles as shown in Fig. 7.5, while other surrounding areas are quite clean. If the linewidth spreading in freestanding WS_2 (212 meV) is attributed entirely to the contamination residues, then by comparing it to the ideal linewidth (33 meV), it can be concluded that the effect of the contamination at one side could change the energy center by approximately ± 100 meV.

In the following sections, the effect of different substrates will continually to be explored in greater detail to gather more evidence concerning the benefits of hBN encapsulation for TMD monolayers. In conclusion, a combination of factors play a role on the exciton linewidth, while some more than others, as explained in later sections.

7.3 Charging effect of electron dose rate

The monolayer supported by Si_3N_4 is not flat, as discussed in the previous chapter, which could be one of the explanations for its large X_A FWHM (blue and cyan dots in Fig. 7.2). However, if monolayer roughness was the only cause for the linewidth broadening, one would expect to measure sharper X_A absorption lines on the sample which is covered by a additional hBN layer which has similarly the lowest monolayer roughness (Fig. 5.6 data points in brown). A reduction is observed in Fig. 7.2(b) from 172 meV to 147 meV in FWHM (mean values of the histogram) when comparing the same fast-scan rates. However, the linewidth in FWHM still is significantly larger than observed in the hBN encapsulated sample.

7.3.1 Charging effect in the Si_3N_4-based TMD heterostructures

During the EELS experiments, it was observed that the measured FWHM of the X_A absorption peak for WS_2 across Si_3N_4 substrates depended on how the electron beam was scanned on the samples. The 15-nm thick Si_3N_4 layer used to support the WS_2 monolayer is an amorphous insulator, which is known to be prone to charge accumulation. The incident electrons are repelled by the accumulated charge (mainly electrons) on the sample, and this would lead to a local shift of the exciton line and inhomogeneous broadening, explaining the observations.

The important parameters here for the experiment are the **scan speed** (how long the beam dwells at a specific pixel before moving to next pixel), **spatial sampling** (the distance between neighboring pixels), and **total scanned area size**. To test and control this effect, spectra are measured with the same total acquisition times and total scanned area size, while the electron beam was scanned at different rates and sampling step on the monolayer TMDs.

Using acquisition settings typical to EELS spectrum imaging (slow-scan), a dwell time

of the 100 ms time scale, with an approximately 1-nm wide beam and a sampling of the order of 10 nm/pixel, the X_A was systematically broader than fast-scan as presented in Fig. 7.6(a-c) (green curves). In comparison to spectra acquired over identical regions where the electron beam was rastered at much faster speeds (sample dwell time of 1–16 μs/pixel for fast-scan) while keeping the exposure time constant, the linewidths can be decreased by more than half (orange curves in Fig. 7.6(a-c)). The spectral evolution due to these changes in scan parameters is summarized schematically in Fig. 7.6(d-f).

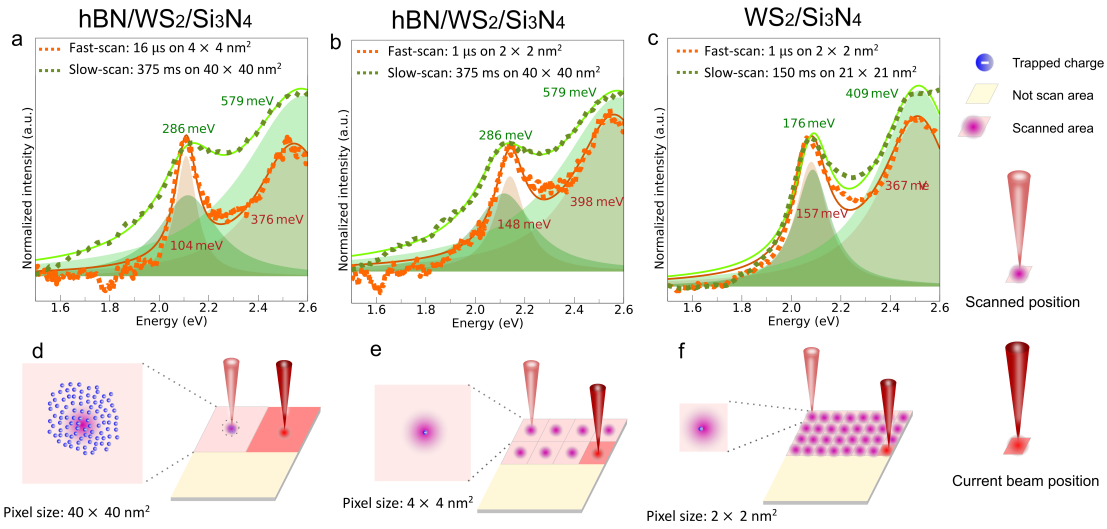

Figure 7.6: **Charging effect of EELS measurement for WS_2 on Si_3N_4:** (a) slow-scan versus fast-scan in hBN/WS_2/Si_3N_4: spectral comparison between slow-scan (green dotted line) and fast-scan (orange dotted line) acquisition. The pixel dwell times are 375 ms and 16 μs and the pixel sizes are $40\times40\,nm^2$ and $4\times4\,nm^2$, respectively. The linewidth is given by the FWHM of a Lorenzian fit of X_A and X_B peaks are as labelled, solid line is the sum of the fitted curves of the two excitations and the offset; (b) slow-scan vs fast-scan (1 μs on $2\times2\,nm^2$) in hBN/WS_2/Si_3N_4: The linewidth of X_A and X_B in fast-scan (1 μs on $2\times2\,nm^2$) is 148 meV and 398 meV. Linewidth of X_A is wider than long fast-scan (16 μs on $4\times4\,nm^2$), but sharper than slow-scan (375 ms on $40\times40\,nm^2$ area); (c) slow-scan vs fast-scan (1 μs on $2\times2\,nm^2$) in WS_2/Si_3N_4: The linewidth of X_A and X_B are as labelled; (d) the scan patterns correspond to slow-scan mode: 100 ms dwell time on a $40\times40\,nm^2$ sized pixel, the most residual charges induced by the beam; (e) the scan patterns correspond to large pixel scan patterns: μs dwell time on $4\times4\,nm^2$ pixel, the least residual charges induced by fast beam. The linewidth is the closest to intrinsic linewidth; (f) the scan patterns correspond to small pixel scan patterns: 1 μs dwell time on $2\times2\,nm^2$ pixel, less residual charges than slow-scan but more residual charges than large pixel fast-scan.

Typical EELS spectrum imaging acquisition leads to long dwell times for the electron beam, which allows the excess charges to be trapped (according to our interpretation) in the Si_3N_4 substrate, represented by little purple dots in Fig. 7.6(d). The pink and red cones represent the electron beam raster start and finish positions, respectively, while

the shaded pink and red areas in the specimen plane represent areas scanned by the electron beam and current scan areas. One immediately sees in Fig. 7.6(e,f) that increasing the scan speed and the sampling can distribute these trapped charges more homogeneously across a larger area, reducing their overall effect. 15-nm Si_3N_4-windowed TEM grids are routinely used for EELS experiments of plasmonic materials, with their charging under the electron irradiation a known limitation, which leads to electron beam displacement with respect to the sample (seen as spatial drift during data acquisition). hBN, while also an insulator on the other hand, has been shown to be a valid alternative, which does not possess this limitation [176].

However to quantify the dose-related effect without accounting for accumulated effects on identical areas proved to be very difficult, as the charging effect were not reversible. The difficulties come from how the trapped electrons can be discharged from the previously measured areas. Even though we controled of the beam current and dose rate, there are still residual trapped electrons from the previous scan. Further, the severity of this effect depends on the sample region are observed, probably due to different charge recombination rates.

It impossible to perform quantitative measurements of the amount and rate for dose on the linewidth, because it is difficult to control the charging effect systematically. There isn't any means to quantify the typical trapped charge lifetime in our microscope system. For an electron beam of 10 pA, the time delay between consecutive electrons is 16 ns. The beam distribution statistics is Poissonian (not evenly distributed). In any case, because of the lack of control on the effect itself, as described before, a quantitative measurement of dose influence on the linewidth was not possible.

To be less affected by the residue charge in this sample, I utilised scanning parameters denoted as fast-scan mode in section 3.5, in which the sampling is 4 nm/pixel and the scan speed 16 μs/pixel. At the same time, with the beam scanning, EELS spectra were acquired using the same detector accumulation time of 100 ms/spectrum as in the slow-scan mode. The X_A linewidth with the slow-scan scheme is 286 meV. The faster scan rate produces sharper X_A linewidth (104 meV). This is reproduced in different areas of the same sample, albeit with small changes in spatial sampling, showing similar behavior in Fig. 7.6(a,b).

To check if the residual X_A absorption broadening was due to the remaining roughness of the WS_2 monolayer on Si_3N_4, a part of this sample was covered with 50-nm thick hBN in Fig. 7.2. Indeed, roughness is reduced by the presence of hBN, as described in the previous chapter (Fig 5.4(c,d)). In these regions, the initial X_A FWHM for slow-scan acquisitions is narrower than in the regions only supported on Si_3N_4. Electron diffraction rules out a difference in roughness, but residual effects due to charge trapping accumulated between measurements over the same area without discharging, despite modifying the scanning parameters, appears to still increase the linewidth.

7.3.2 No charging effect in freestanding and hBN encapsulated WSe_2

Aside from the WS_2 monolayer samples supported on Si_3N_4 with or without additional hBN encapsulation, other samples were not sensitive to the scan mode in the WS_2 vdWH comparison series. In Fig. 7.7, both fast-scan and slow-scan are performed on freestanding WSe_2 and hBN/WSe_2/hBN, and their linewidths are the same irrespective of scan mode. The comparisons are conducted on areas that had never been scanned separately. Because the strain and contaminant disorders of the freestanding TMDs are greater than those of the encapsulated, there is a deviation in the energy centers of the different regions as shown in Fig. 7.7. Even so, the test results for both structures are not insensitive to the scanning mode.

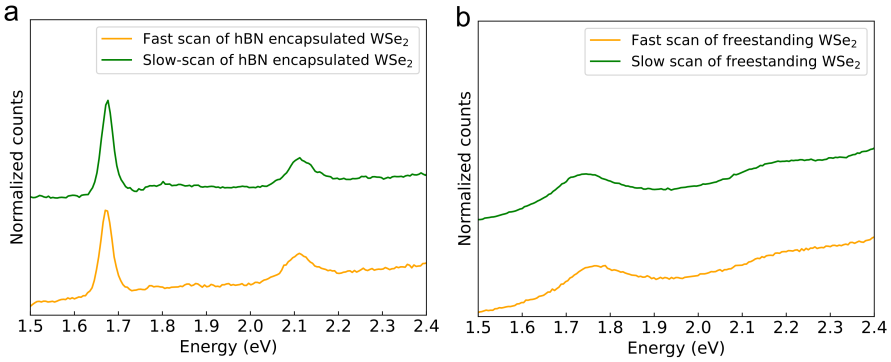

Figure 7.7: **Spectrum comparison between fast-scan (orange) and slow-scan (green):** (a) hBN encapsulated WSe_2; (b) freestanding WSe_2. The intensity is normalized with respected its X_A intensity maxima.

7.3.3 Other attributes affected by charge disorder

In this section, the effect of different scan rates on the X_A linewidth of a WS_2 monolayer supported by Si_3N_4 are discussed. Interestingly, the same charging effect is not observed on hBN supported or encapsulated monolayers, despite the fact that both materials are insulators and hBN has a larger band gap than Si_3N_4. Other factors such as the low intrinsic disorder of crystalline hBN, i.e. low density of atomic defects, makes it a better candidate to counteract against surface charge effects to TMDs. Amorphous Si_3N_4 on the other hand can exhibit extrinsic charge disorder similarly to SiO_2 substrates, depending on its defect density and impurities, including hosting trapped charges and surface adsorbates [7, 8]. The experiments conducted here is in a monochromated electron microscope with current of between 1-20 pA. Experiments were attempted to control reversibly the observed charge trapping. However, the magnitude of the broadening produced at fixed currents varied at different sample positions. The underlying reasons for these changes were not identified, so a quantitative assessment of charge trapping

was not possible.

This charge disorders induced inhomogeneous broadening is not only limited to EELS spectra, but is also applicable to optical measurements. In the light probe luminescence, the hBN encapsulated TMDs also shows a much sharp and strong peak than TMDs/SiO_2, as shown in Fig. 7.8. The PL linewidth can also be explained by the negative factors which were observed in the EELS linewidth as discussed in this section: i) hBN-encapsulation reduce the charge disorder by spatially separating the $MoSe_2$ from the charged SiO_2 surface; ii) passivation of the SiO_2 surface led to a reduction in substrate charge traps and static charges.

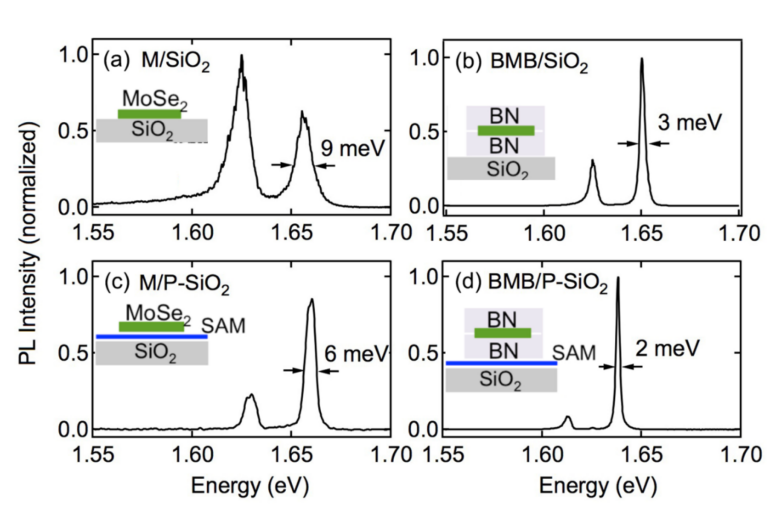

Figure 7.8: **PL spectra of $MoSe_2$ monolayer at 4 K on different substrates:** (a) on a SiO_2 substrate; (b) hBN encapsulated on SiO_2 substrate; (c) on a passivated SiO_2 substrate; (d) hBN encapsulated on a passivated SiO_2 substrate. The sharpest linewidth 2 meV is obtained from hBN/$MoSe_2$/hBN on cleaned SiO_2 surface with self-assembled monolayer (SAM) coating. Reproduced from ref. [50].

Besides, the charge disorders can also influence the carrier mobility of TMDs. A necessary step in device developments to achieve the current state-of-the-art optical properties was the production of field-effect transistor devices no longer on top of bare SiO_2 surfaces that suffer from charge impurities [177, 178], but encapsulated in hexagonal boron nitride (hBN) for its high-quality and atomically-flat surfaces with low trap density. Recently, extensive research has shown that the use of two-dimensional (2D) transition metal dichalcogenides in semiconductor devices may help overcome silicon complementary metal-oxide-semiconductor (CMOS) scaling limitations [179, 180]. In fact, SiN_x (with a dielectric constant $\epsilon = 7.5$) and silicon oxide ($\epsilon = 3.9$) are always be used as gate dielectric materials for TMDs-based metal–insulator–semiconductor field-effect transistors (MIS-FETs). But the charged defects at the contact between the channel TMDs and substrate (SiN_x or SiO_2) contact, as well as charge traps in the substrate,

can reduce FET electrical performance [181]. Experiment have shown that hBN encapsulated TMDs have better mobility than that on SiO_2 substrate [15, 9], so that hBN as the most common 2D insulator has been widely considered to be the most promising gate insulator in 2D material-based transistors [182, 183]. Ref. [184] has established that the trapped charge density is reduced to $1.9 \times 10^{11} cm^{-2}$ on hBN substate as compared to $1.1 \times 10^{12} cm^{-2}$ on SiO_2. However, one of the main obstacles concerned defect-free hBN as 2D gate insulators is that it caused excessive leakage currents than HfO_2 and CaF_2 [185]. It is therefore believed that an intensive search for suitable gate insulators and gate insulator stacks is required in order to deliver the performance boost expected by next-generation ultrascaled CMOS logic.

7.4 Effect of electron beam damage

A final linewidth broadening mechanism that was identified is irradiation damage on bare TMD monolayers including: i) Si_3N_4 supported under slow-scan and fast-scan mode at LN_2; ii) suspended monolayer TMDs at RT. However, no significant optical quality degradation occurs in the presence of hBN under the fast-scan mode. The structure of hBN/TMD/hBN does not suffer from any degradation of the optical quality even at slow-scan mode with exposure in the scale of 100 ms/nm^2 at LN_2. In fact, for the TMDs encapsulated between two hBN flakes, the optical properties of the exciton do not degrade even if repeatedly scan the same area, as evidenced by the constant X_A EELS linewidth and no decrease in the intensity of the CL emission [28].

7.4.1 Elastic and inelastic damage in TMDs

Electron beam-induced damage in the case of 60 keV and higher kinetic energy electrons are known to induce damage in TMD samples either through elastic or inelastic scattering. The first mechanism, known as knock-on [186, 187, 188], leads to the removal of atoms. It is more effective at higher kinetic energies [186] and should present a cutoff at lower energies, below which knock-on should not be possible, as not enough energy would be available to eject the atom. However, due to the thermal motion of atoms [187, 188], knock-on damage can still occur below this threshold. Electronic excitations can also induce below threshold atom removal [189].

The cutoff is proportional to the atomic mass, as the maximum energy transferred during elastic scattering decreases as the ratio between the mass of the electron and the target atom increases [186]. For this reason, knock-on of heavy transition metal atoms (compared to carbon, whose cutoff is 86 keV [190]) should be an ineffective damage mechanism, as in WS_2 and WSe_2. However, the pre-existence of defects can decrease the energy necessary for knock-on, allowing atom removal from edges or voids [191]. Inelastic scattering leads to the material modification through high energy transfer, which can lead to bond breaking and atomic motion. The cross-section for these events increase at lower kinetic energies for the incident electron beam [186] and is thus an ef-

fective mechanism for beam damage in TMDs. Typically for TMDs, it has been found that a good compromise for electron microscopy and spectroscopy experiments is to use electron beams with kinetic energy between 60 and 100 keV [28, 29]. Thus, I chose to measure TMDs all at 60 keV, which also minimizes damage on the hBN layers.

7.4.2 Beam damage on Si_3N_4 supported monolayers

In the experiments here and reported by others [28], in addition to the sharp linewidth of the X_A in hBN encapsulated structure, it was also seen that beam damage is significantly reduced, allowing even the imaging and spectroscopy of stable monolayer edges [28]. However, this is not true for all substrates. In the Si_3N_4 supported monolayers, beam damage does occur. This appears as a linewidth broadening as a function of repeated irradiation, which is not reversible by subsequently leaving the measured area unexposed to the electron beam for certain periods. This is in contrast to the mechanism described in the previous section 7.3, where trapped charges are recombined, leading to reduction of the X_A linewidth if the electron beam is moved away and then faster scan acquisitions are performed.

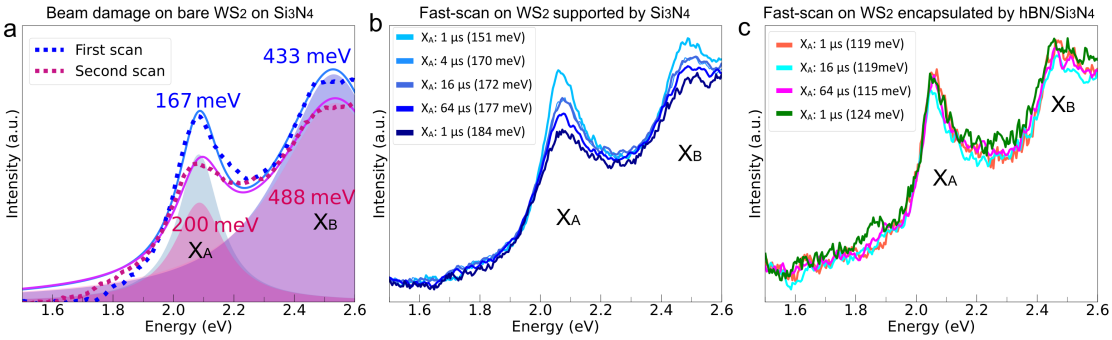

Figure 7.9: **Beam damage effect of EELS measurement for WS_2 on Si_3N_4:** (a) WS_2 on Si_3N_4: beam damage induces the broadening of WS_2 excitons under EELS slow-scan with pixel size 21×21 nm^2 at 150 ms exposure time; (b) 2×2 μm^2 area fast-scan with pixel size 2×2 nm^2 for WS_2/Si_3N_4, the area is scanned under the sample dwell time of 1, 4, 16, 64 μs and then back to 1 μs and its exciton peak broadening is because of charging and beam damage; (c) 2×2 μm^2 area fast-scan with pixel size 2×2 nm^2 for $hBN/WS_2/Si_3N_4$, the area is scanned under the sample dwell time of 1, 16, 64 μs and then back to 1 μs. There is no significant exciton peak broadening after several scans.

EELS spectra for the same region of WS_2 supported on Si_3N_4 acquired in series show an increase in the X_A linewidth as shown in Fig. 7.9(a). These spectra are averaged from 70×44 pixel EELS datacube with pixel size of 21×21 nm^2 and exposure time of 150 ms. The effect of the first scan was induced damage and increase the linewidth from 167 meV to 200 meV. One could argue that this was due to charge trapped in the Si_3N_4. However, this broadening is not recovered by subsequently discharging by leaving the area unexposed to the electron beam. Another test for this hypothesis is the sequential acquisition

of spectra in a fast-scan mode, with different scan rates. If the induced broadening is reversible, this would indicate that it was due to charging and not permanent crystal damage. This was not the case for the WS_2 monolayer on Si_3N_4. A sequence of acquisitions with fixed scan area and pixel size ($2 \times 2\,nm^2$) with sample dwell time in the order of 1, 4, 16, 64 and 1 μs show an increasingly broader X_A absorption peak (from 151 to 184 meV as shown Fig. 7.9(b)), which is not reduced during the last fast-scan acquisition. The irreversible X_A linewidth increase is not observed for the sample encapsulated in hBN/Si_3N_4as shown in Fig. 7.9(c).

7.4.3 No optical degradation at LN_2 in freestanding and hBN encapsulated TMDs

In contrast to the Si_3N_4 substrate, neither the freestanding nor the hBN-encapsulated TMD samples experienced any degradation in optical properties during the EELS measurement, as evidenced by the fact that even after multiple scans of the same region, the exciton spectra (including linewidths) did not change. In fact, the fast-scan mode does not appear to damage the suspended monolayer TMDs at all at LN_2. Therefor, it is necessary to investigate in greater detail why TMD monolayers supported by amorphous Si_3N_4 at LN_2 suffer significant damaging, for example whether it is directly related to the charging effect.

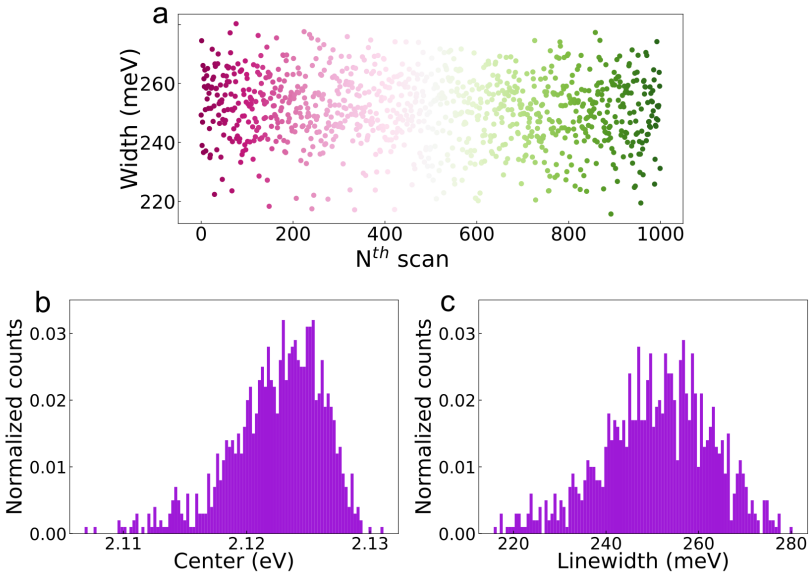

Figure 7.10: **Fast-scan EELS spectra of suspended WS_2:** (a) X_A linewidth does not vary with sequence of spectral fast-scans on suspended WS_2; the histogram of (b) linewidth and (c) energy center, which are extracted from the Lorentzian fit of X_A exciton peak.

As shown in Fig. 7.10, I have tested 1000 spectra on a $250 \times 250\,nm^2$ freestanding WS_2

region, but the linewidth of the X_A exciton does not change as the number of scans is superimposed. This indicates that the linewidth broadening of WS_2/Si_3N_4 in Fig. 7.9 (a,b) is caused by electron beam radiation damage on Si_3N_4 rather than WS_2. The damaged Si_3N_4 substrate has more defects trapping charge, which leads to the more inhomogeneous broadening caused by charge disorder on damaged Si_3N_4.

A noticeable feature in Fig. 7.11 (b) is that the X_A exciton energy centers are different from each other for the three time scans on the same area for freestanding WSe_2 unlike $hBN/WSe_2/hBN$. Due to the electron beam scanning, contaminants redistribution was conducted (Fig. 7.11 (c)) and it resulted in mainly a change in the energy center rather than variations in the linewidth. The largest energy center shift occurred at the slow-scan, this because the large dose rate induced the most local contaminant accumulation. When the TMDs are protected between two hBN flakes as shown in 7.11 (a), neither the energy center nor the linewidth of X_A changes with increasing number of scans. This is beneficial to the stability and reliability for the test results of optical properties of TMDs.

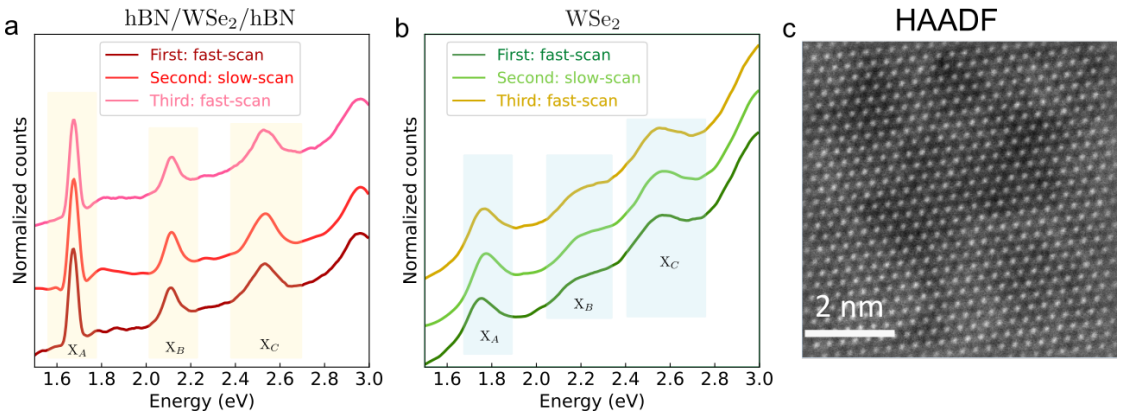

Figure 7.11: **EELS measurment for WSe_2 and hBN/WSe_2/hBN at 110 K:** the electron beam is scanned on the same region by fast-mode, then slow-mode, and finally fast-mode. The spectrum is measured on a (a) 80 × 80 nm^2 $hBN/WSe_2/hBN$ region and (b) 120 × 120 nm^2 freestanding WSe_2 region with a sampling 2 × 2nm^2. All spectra is normalized by its X_A intensity maxima. (c) An atom-resolved HAADF images of freestanding TMD monolayer (WS_2) inside UltraSTEM Nion microscope at 60 keV. The bright region is mainly caused by carbon contaminants, so that the contrast is different from the clean freestanding TMD regions.

The reason why electron microscopists prefer slow-scan is that this provides point-to-point spatial resolution and good signal-to-noise ratio, whereas fast-scan sacrifice some spatial resolution to get an average signal that is summed over the full scanned region (10-10^2 nm^2), which can decrease the sample damage and induce less charging effect. Therefore, when testing the EELS of materials, one can chooses the scan mode to their own requirements.

7.4.4 Optical degradation at room temperature of freestanding TMDs

The optical properties of freestanding TMDs exposed by electron beam at room temperature are severely degraded. When the sample is lowered to LN_2, the exciton signal in these regions is weak and the linewidth is wide. As shown in Fig. 7.12, EELS test is performed on the sample at room temperature (pink curves) with 300 ms dwell time and 4×4 nm^2 sampling. Then performed experiment on these areas for scanning nanodiffraction, and followed by EELS measurement at LN_2, the spectra is shown as grey curve in Fig. 7.12(a).

It is believed that this degradation of optical properties is caused primarily by carbon contamination, which is manifested by a large amount of carbon aggregation in the scanned area as shown in Fig. 7.12(d). The experiment with the highest dose exposure per area was nanodiffraction. The scanned area of nanodiffraction at RT is fully carbon covered, as indicated by its ADF image in Fig. B.1.

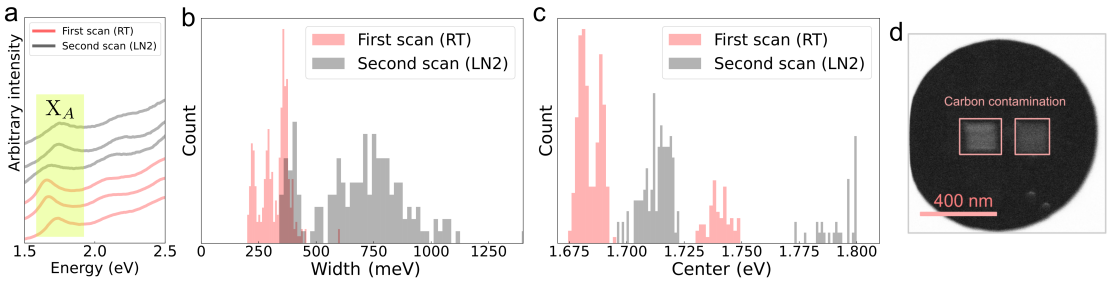

Figure 7.12: **Beam damage of freestanding WSe_2 at RT:** (a) is the comparison of first and second scan EELS spectra on suspended WSe_2 at RT and LN_2, respectively; the histogram of (b) linewidth and (c) energy center, which are extracted from the Lorentzian fit of X_A exciton peak. The exciton linewidth obtained from the damaged sample remained even largely broadened at LN_2 temperature, subsequently; (d) the ADF image shows a bright contrast boxes at the scanned areas due to carbon contamination caused by the electron beam scan on top of the sample at RT.

In order to present more clearly the linewidth variation due to electron beam damage, a Lorentzian fit was performed for all X_A, and the resulting statistical histogram Fig. 7.12(b) shows that the exciton linewidth of the second EELS scan at LN_2 is significantly higher at around 750 meV than that of the first scan 270 meV at RT and also other no-damaged areas as spectrum shown in Fig 7.11(b). Since the EELS signal is weak in suspended TMDs and increasing the exposure time would cause more damage for next measurement, the data here are treated by PCA for fitting to reduce noise and binned four pixel into one.

In this section, we can gain the summary that freestanding and hBN encapsulated TMDs measured at low temperature can effectively avoid the exciton linewidth spreading. To date, several studies have investigated the hBN encapsulation allowed the TMDs-based devices can functioning under severe environmental conditions. In ref. [192], it reports that the hBN encapsulated graphite/WSe_2 photodetectors can endure temperatures up to 700 °C in air (1000 °C in vacuum). Similarly, ref. [193] found that graphene-based devices are capable of performing in an extended temperature range up to 500 °C without noticeable thermally induced degradation when encapsulated by hBN. In terms of the photoluminescence, hBN encapsulated WS_2 still showed strong PL emission to 600 °C under N_2 flow [194].

7.5 Discussion of dominant effects on linewidth

In the previous sections how various effects influence the EELS linewidth of WS_2 excitons in different substrate configurations are described. By comparing the dominant effect from each substrate and the resulting linewidths (Table 7.1) a qualitative classification of the importance of TMD roughness can be reached as follows TMD surface cleanliness, and substrate charge trapping on linewidth broadening. The comparable roughness (corrugation amplitude, h, as a function of corrugation period, L) for hBN encapsulated, hBN supported and hBN/Si_3N_4 encapsulated WS_2 shows that the monolayer flatness is not the prevailing factor among those considered here on linewidth. For instance, the flatter hBN supported WS_2 shows linewidths (165 meV) comparable to that of the rougher Si_3N_4 supported WS_2 configurations (172 meV).

Table 7.1: **Summary of X_A linewidths of WS_2 monolayers in different configurations.**

Configuration	Surface cleanliness	Trapped charges	Roughness	Linewidth (Lorentizan)	Linewidth (Gaussian)
hBN/WS_2/hBN	both sides clean	few	0.002 × L	33 ± 8 meV	41 ± 32 meV
Si_3N_4/WS_2/hBN	both sides clean	many	0.002 × L	147 ± 17 meV (fast scan)	121 ± 23 meV (fast scan)
WS_2/hBN	one side clean, one side dirty	few	0.002 × L	165 ± 30 meV	153 ± 37 meV
WS_2/Si_3N_4	one side clean, one side dirty	many	0.02 × L	172 ± 25 meV (fast scan) 260 ± 19 meV (slow scan)	173 ± 22 meV (fast scan) 252 ± 19 meV (slow scan)
Exfoliated WS_2 (freestanding)	both sides dirty	some	0.01 × L	212 ± 11 meV	204 ± 10 meV
CVD-grown WS_2 (freestanding)	both sides dirty	some	0.01 × L	289 ± 11 meV	303 ± 15 meV

In fact, both surface cleanliness and charge disorder have substantial influence on the linewidth of TMD excitons. Only when the TMD is fully protected against surface charge disorder, presence of adsorbates and randomly distributed residue (due to clean interfaces) between two hBN flakes can the narrowest linewidth of 33 meV. The sharp linewidth in EELS is reproducible across repeated measurements of the same sample

area, different regions on sample areas, as well as different samples. The narrow EELS exciton peaks in other TMDs monolayers following hBN encapsulation, like $MoSe_2$ and WSe_2 is also observed. As shown in Fig. 7.13, the X_A linewidth of $MoSe_2$, WS_2 and WSe_2 in the hBN encapsulation structure are 20 meV, 35 meV and 41 meV, while 130 meV, 191 meV and 235 meV for suspended TMD monolayers. For X_B, the linewidth of hBN encapsulation is also much sharper than that of the freestanding monolayer TMDs. Also, there is no variation in the linewidth of the excitons for either fast-scan or slow-scan in hBN encapsulation, which can further support that the high quality hBN used is defect-free and therefore insensitive to residual charge from the electron beam.

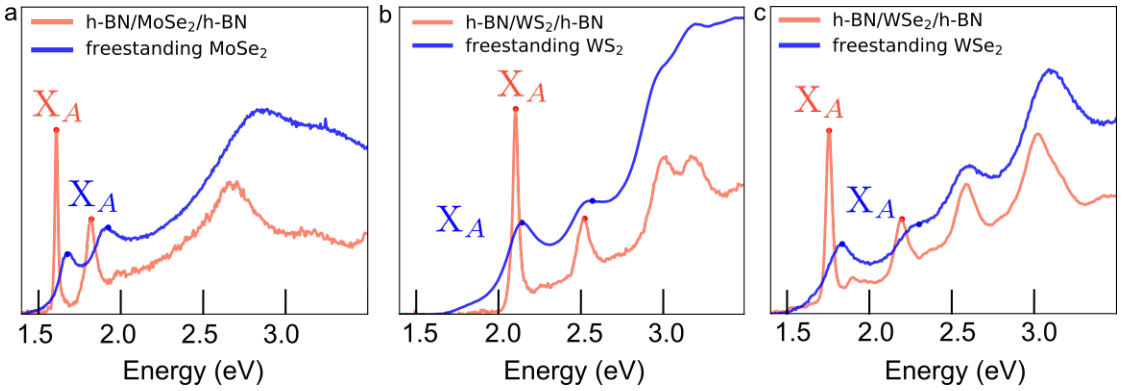

Figure 7.13: **EELS spectrum of freestanding and hBN encapsulated TMD monolayers:** (a) hBN/$MoSe_2$/hBN (red) and freestanding $MoSe_2$ (blue); (b) hBN/WS_2/hBN (red) and freestanding WS_2 (blue); (c) hBN/WSe_2/hBN (red) and freestanding WSe_2 (blue). The energy shift of X_A in (a-c) is due to the screening effect of hBN.

The linewidth broadening in the case of hBN supported WS_2 (165 meV) can be attributed mostly to the lack of cleanliness from its remaining exposed surface.For monolayer with comparable surface residue (WS_2 on Si_3N_4), charge trapping on the substrate can significantly increase the linewidth, leading to its linewidth being sensitive to electron beam scanning modes. The effect of the trapped charge on the linewidth is most obvious in the slow-scan mode because it is difficult to discharge at large electron doses. This leads to the local conductivity and dielectric variations and thus inhomogeneous linewidth broadening. In fact, any parameter modifying the energy position of the absorption peak will lead to linewidth broadening. For example, one can also cite dielectric disorder, strain, and proximity to extended defect voids or edges present in the monolayer as possible sources.

The charging effect is less pronounced under fast-scan, where linewidth reduced from 260 meV (slow-scan) to 172 meV (fast-scan). In the case where the charge effect is not obvious like fast-scan in WS_2 on Si_3N_4, its linewidth is similar to the linewidth of WS_2 on hBN, since they both have one clean interface and the other exposed. With an addition of a top-layer hBN, the linewidth is reduced to 147 meV, because both surfaces of WS_2 are now cleaner. However, the linewidth is still not as narrow as hBN encapsulated

WS_2, because residual charges is inevitable from the amorphous Si_3N_4 even in the case of fast-scan.

The exciton linewidth of WS_2 on Si_3N_4 (260 meV) under slow-scan mode is larger than freestanding exfoliated WS_2 (212 meV). This comparison should be taken cautiously, as too much surface residue coupled to high roughness (compared to freestanding CVD-grown WS_2) can lead to broader absorption lines (289 meV), although WS_2 monolayer corrugates more dramatically on Si_3N_4 than freestanding. With these comparisons we conclude that the increasing order of importance of these effect is: monolayer roughness, followed by monolayer cleanliness and substrate charge inhomogeneity. It should be noted that the latter two can be correlated, and not so straight-forwardly ranked in relation to the other in all situations.

Although I tried to relate the strain distribution map (Fig. B.1) to the exciton linewidth distribution map to observe the strain-induced change in the central energy or the exciton linewidth. As ref. [195] points out, 0.1% strain casues 6 meV energy center shift of X_A in monolayer WS_2. However, we did not find the correlation between strain distribution maps on the nanoscale in correspondence with EELS. In addition, there are many kinds of strain in materials including uni-axial strain, bi-axial strain and shear. Under current testing conditions inside ChromaTEM, it is difficult to control a single strain variable to study its effect on the absorption spectrum. However, by comparing Fig. 5.12 and Fig. 5.11, it can be seen that the strain is significantly smaller in the presence of hBN, which is one of the reasons for its narrower EELS linewidth.

7.6 Conclusion

In this chapter, the role of different substrates on the EELS absorption linewidths of WS_2 monolayers are explored. Four main possible broadening factors are identified: i) monolayer roughness, ii) surface cleanliness, iii) charge trapping in substrates, and iv) electron beam-induced damage. The first three have been considered and discussed in the past for optical spectroscopies extensively [17, 101, 50, 196]. The experiments described here give indications that these three effects on TMD absorption linewidth broadening are also applicable in electron spectroscopy, and can be ranked by decreasing order of dominance of substrate charge disorder, followed by surface cleanliness, then monolayer roughness. These findings conclude that hBN remains, so far, the most suitable substrate for both optical and electron spectroscopies with TMD monolayers and atomically thin layers for multiple reasons, as outlined below:

- Surface cleanliness is crucial: encapsulation with hBN on both surfaces is required to confine the surface residue into localized patches, as widely known in the 2D materials community. Moreover, monolayer flatness is influential to reducing X_A linewidth, as shown by our comparison of hBN supported, hBN encapsulated,

and Si_3N_4/hBN encapsulated WS_2 monolayer.

- Flatness and cleanliness are clearly not enough as WS_2 monolayer encapsulated in Si_3N_4/hBN is flat and sufficiently clean but still has a significantly broader X_A absorption linewidth than hBN encapsulated WS_2 monolayer.
- Charge trapping on substrates also plays a key role, as exemplified by the experiments on Si_3N_4. Trapping of charges in hBN seems to be ineffective, indicating why it is such a good substrate for 2D materials.
- Finally, electron beam-induced damage also plays a considerable role for electron spectroscopy of 2D materials, intrinsically hindered by the use of a high-energy electron beam, but this detriment could be minimized with ultra high vacuum of $3e^{-9}$ torr and cooling of the sample to LN_2. Carbon-contamination is harmful to the optical properties of the sample, and this damage is more pronounced at high temperatures. It implies that the optimal test conditions for TMDs vdWHs are at low temperatures in vacuum, and under this condition it allows repeated EELS on the same sample without optical properties degradation.

It needs to be emphasised that these effects are not intrinsic to electron spectroscopy, and broadly applicable in a similar manner for optical spectroscopies. The combination of these four characteristics explains the large linewidths observed in EELS experiments in the past [29, 38, 42, 40, 41, 37, 43]. The experiments described here indicate a viable path for electron spectroscopy experiments with comparable energy resolution to optical measurements in the available temperature and energy ranges.

In conclusion, the reasons why hBN is such an ideal candidate for supporting/encapsulating TMDs is that it not only provides clean surfaces of TMD monolayers and minimal charge disorder, but can also protect the TMDs from irradiation damage and strain disorder. This work provides a better understanding of the mechanisms by which hBN remains, to date, the most compatible material for 2D material encapsulation, facilitating the realization of intrinsic material properties to their full potential.

Chapter 8

Exciton in monolayer TMDs engineered by graphene/graphite

The integration of TMDs with other 2D materials of specific properties in the form of van der Waals heterostructures demonstrates unique light-matter interactions, and can be tailored to further obtain novel functionalities. In addition to sharp exciton linewidth [197], some remarkable advances on manipulating the optical properties of TMDs have been achieved so far through alloying [198, 199], chemical [47, 200] and electrical [201, 202] doping, and applied strain [203, 204, 205]. On top of that, interlayer coupling plays a determinant role in the performance of such vdWH, including charge transfer [206, 207, 208] and Förster-type energy transfer [64], across the interface when the excitons are excited in the TMD layer.

As explored in the previos chapter, TMDs encapsulated between two hBN flakes can preserve its best intrinsic properties resulting in neutral exciton linewidth approaching the radiative limit, and the neutral exciton linewidth measured by EELS is around 30 meV at 110 K (Fig. 7.13). Aside from hBN, which provides an ideal environment for TMDs, graphite, as a member of the 2D material family, is also capable of meeting all the essentially conditions, reducing roughness, uniform charge distribution, improving strain disorders, and providing clean surfaces/interfaces, protection TMD monolayer from radiation damage [209].

To continue my study on the substrate influence on the exciton, graphite as another viable substrate material that also satisfies the criteria of atomic flatness, low defect density, few charge disorders and effective sample protection is investigated in this chapter. Specifically, the effects of graphite (Gr) and graphene (gr) on the absorption and emission spectra of TMDs exciton in various encapsulated vdWHs are investigated. Overall, graphite can play an important role in addressing the exciton engineering as a result of **interlayer coupling and interaction** between graphite and TMDs in these vdWH.

First of all, section 8.1 reports the observation of Fano-like absorption lineshape in graphite-based TMDs vdWH for the first time, and this asymmetric lineshape is due

to the electronmagnetic coupling between TMDs and graphite. In addition, a model was established for interpreter the asymmetric excitonic lineshape though the complex dielectric functions of the vdWH in section 8.2, including the derivation of the model based on retardation in section 8.2.2 and non-retardation approximation in section 8.2.3.

. In addition, the EELS/CL spectra of hBN encapsulated WSe_2/graphene are presented in section 8.3, including a description of the logic behind this structure design (section 8.3.1), the single neutral exciton CL emission (section 8.3.2), and the exciton binding energy modified by graphene monolayer (section 8.3.3).

8.1 Fano-like asymmetric excitonic absorption lineshape

The modification of the optical extinction response of TMD monolayers in contact with graphene and thin (<10 nm) graphite layers is reported in this section. Optical extinction and electron energy-loss spectroscopy (EELS) spectra show asymmetric lineshapes, similar to Fano profiles at the energies expected of excitonic transitions in the TMD monolayers.

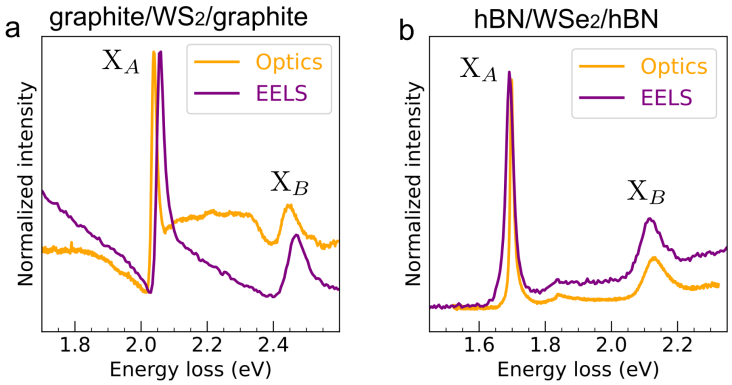

Figure 8.1: **Absorption spectra comparison between hBN and graphite encapsulated TMDs:** (a) EELS and optical extinction spectrum of graphite encapsulated monolayer WS_2 shows Fano-like asymetric lineshape for both X_A and X_B; (b) EELS and optical extinction spectrum of hBN encapsulated WSe_2 correspond to symmetric Lorentzian lineshape for both X_A and X_B. The background of EELS spectrum for hBN encapsulated WSe_2 is removed by power-law. The measurements were conducted on different samples so that not only the different samples but also different temperatures resulted in the different energy centers and line widths of X_A and X_B between optical absorption and EELS measurement.

As shown in Fig. 8.1, the hBN encapsulated TMDs have different Fano-like asymet-

ric lineshape from the symmetric graphite encapsulated TMDs. It is apparent in the figure that the observation of asymmetric Fano-like lineshape is not limited to methods, as it can be measured by both EELS and optical extinction spectra. The graphite/WS_2/graphite or hBN/WSe_2/hBN heterostructure supported on a sapphire substrate shows similar excitonic features at the X_A and X_B exciton energies in the optical extinction spectra (orange lines) measured at 5 K as EELS (purple lines) at 110 K as indicated in Fig. 8.1.

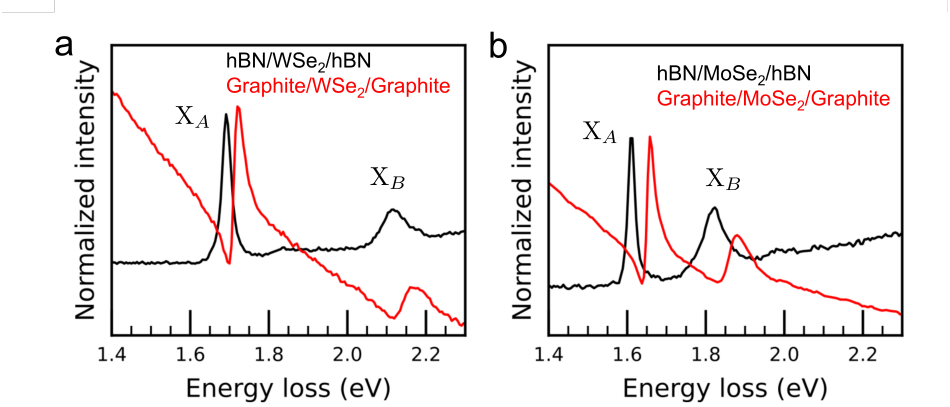

Figure 8.2: **EELS spectra comparison between hBN and graphite encapsulated TMDs:** electron energy-loss spectra comparison between hBn encapsulated TMDs and graphite encapsulated TMDs for monolayer (a) WSe_2 and (b) $MoSe_2$ at 110 K. hBN encapsulated TMDs have different asymmetric lineshape (red lines) from the symmetric graphite encapsulated TMDs (black lines). For hBN encapsulated TMDs, the background of the EELS spectrum is removed by a power-law, but not for graphite encapsulated TMDs. The exciton energy center shifts is due to the different screening from different thickness and dielectric of graphite and hBN.

The production of this asymmetric lineshape is due to the coupling between the TMDs and graphite so that it is supposed to be observed in all similar vdWH. In order to verify this, TMD species other than WS_2, WSe_2 and $MoSe_2$ encapsulated within graphite vdWH are produced and EELS measurements are performed on them as shown in Fig. 8.2. Here is an EELS data process note: for graphite involved vdWH, the background should not be subtracted, as the contribution of the graphite or ZLP tail to the background is ambiguous. Whereas for the hBN, it is transparent in the energy range below its energy gap, so that the power-law can be applied to background extraction, thus the treated spectra reveal the intrinsic optical response.

This section is organized as follows: in section 8.1.1, the optical response of various vdWH under fast electron excitation is presented and compared. In addition to the asymmetric line profiles, graphite encapsulated TMDs exhibit a similar linewidth as those encapsulated in hBN, as discussed in section 8.1.2. Then, EELS experiments at room temperature was performed to demonstrate the coupling between graphite and

TMDs as the cause of this Fano-like absorption lineshape in section 8.1.3. Apart from that, Fano-like line shapes were found to be correlated with graphite and TMD thickness as presented in section 8.1.4. In the last section 8.1.5, the asymmetric line pattern observed on Ni/hBN/$MoSe_2$/hBN is a strong indication that this electromagnetic coupling can extend beyond graphene to all metals.

8.1.1 EELS of TMDs encapsulated or supported by graphene or hBN

The EELS spectra of the TMD monolayers considered here (WS_2, $MoSe_2$, and WSe_2) in Fig. 8.3 contains a series of excitonic transitions [28, 35]. For TMD monolayers encapsulated in thin graphite, the lineshape is markedly different from those encapsulated in hBN . At slightly redshifted energies as the excitonic transitions of the freestanding TMD, most evident in the two lowest-energy excitons X_A and X_B in the insets, asymmetric lineshapes are observed, characteristic of Fano profiles [58].

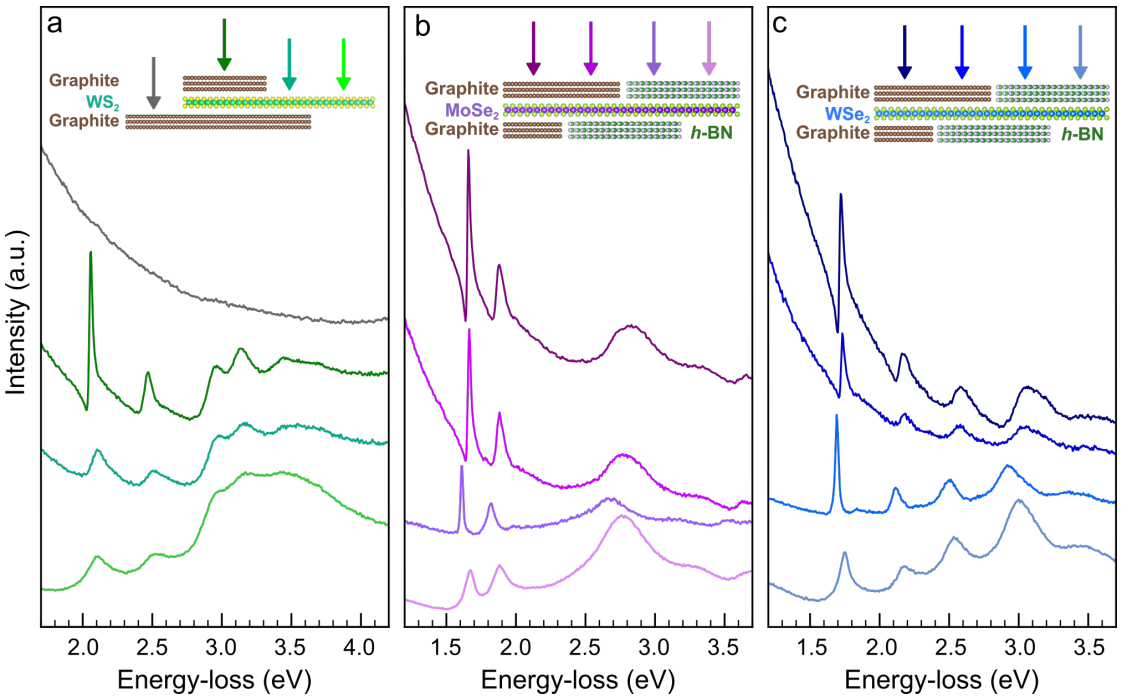

Figure 8.3: **TMD monolayer spectra with graphite and/or hBN encapsulation**: EELS spectra of WS_2 (a), $MoSe_2$ (b), and WSe_2 (c) monolayers in different configurations of freestanding, supported or encapsulated with hBN and/or thin graphite measured at T = 110 K. The configuration of each spectrum is color-coded by the arrows on the sketches in the upper part of the panels. All spectra are normalized with respect to the total intensity of the elastic (zero-loss) peak (ZLP).

It appears on top of the known continuous absorption of graphite, as shown in Fig.

8.3(a) by grey EELS spectrum for the bare and thin graphite. The exciton redshifts in graphite/TMD/graphite and hBN/TMD/hBN to the freestanding TMD monolayers arise from the dielectric screening, in which few layered graphene can tune the electronic gap and exciton binding energy as reported in ref. [63].

For those heterostructures with the TMD monolayers in contact with nm-thick graphite, no cathodoluminescence emission was observed, contrary to structures made with hBN encapsulation [28, 48]. This is because hBN is a high-gap band insulator, while graphite is a conductor. For the graphite encapsulation structure, electrons excited in graphite mainly go through non-radiative recombination without generating a large number of electron-hole pairs that can diffuse into the TMDs, and therefore no CL signal is measured so far in such structure. Recently, it was reported in literature TMDs monolayers contact with mono- or bi- layer graphene can produce quenched PL signal compared to TMDs monolayers [64, 18, 65], but this has not yet been observed in CL [1].

8.1.2 Exciton linewidth of TMDs inside encapsulated heterostructures

For the current samples, the evolution from suspended to hBN supported and encapsulated monolayer behaves as reported in the previous chapter and ref. [17, 28, 35, 197]: the ~100-150 meV broad peak sharpens, attaining a Lorentzian lineshape when encapsulated in hBN (Fig. 8.3(b-c)) with a full-width at half-maximum (FWHM) in the 20-40 meV range at 110 K. The similar linewidth in graphite encapsulated TMDs have similar value as hBN encapsulated indicates that energy dissipation and charge transfer to from TMDs the graphite layers do not modify the total lifetime and dephasing time of the exciton transitions (section 6.2.5).

From the perspective of inhomogeneous broadening, encapsulation between hBN and/or graphite ensures reduced monolayer corrugation (Fig. A.6) and reduction of adsorbates (Fig.7.4) on TMD surfaces. In Fig. A.6, when compared to the freestanding WS_2 monolayer, electron diffraction spots at high tilt-angle shows little to no broadening in the graphite/WS_2/graphite. This demonstrates that thin graphite materials has comparable capabilities to induce flatness in atomically-thin layers as hBN encapsulation (Fig. 5.6).

Interestingly, the asymmetric Fano-type lineshape is only observable with encapsulation. The asymmetric lineshape of the graphite supported TMDs in Fig. 8.3(a) is not very obvious because of the inhomogeneous broadening caused by the impurities on the remaining monolayer surface. **One of the significant findings to emerge from this study is that the sharp linewidth can be only preserved in encapsulation vdWH even in graphite encapsulation.** Therefore, encapsulation of TMDs is essential in order to

[1] Refer to section 8.3.2 for the WSe_2/graphene CL emission inside hBN encapsulation.

observe the fine asymmetric Fano-type lineshape features, regardless of whether it is hBN/graphite or graphite/graphite encapsulation.

8.1.3 Confirmation of the coupling between TMDs and graphite

Room-temperature (RT) absorption measurement on the identical areas from graphite/WS_2/graphite vdWH from Fig. 8.3(a) continues to exhibit the asymmetric Fano-like lineshape as presented in Fig. 8.4(b), albeit with significantly lower oscillator strength. A comparison of WS_2/graphite and freestanding WS_2 monolayer between LN_2 (110 K) and RT (300 K) also identifies the same decrease in EELS signal intensity, in addition to the expected exciton linewidth broadening, shown in Fig. 8.4(c,d).

Fano-type resonance at the X_A transition in $MoSe_2$ monolayers with a negative asymmetry parameter (dip at higher energy) has been previously reported by reflectance contrast at T = 5 K [210]. The progressive transition towards a Lorentzian lineshape and disappearance of the charged exciton (trion, X^*) peak with increasing temperature suggested the unusual lineshape is caused by the interaction of the ground-state $1s$ X_A^0 with the quasi-continuum of trion excited states. The binding energy of trions are of the order of ~35 meV for WS_2, and therefore diminishes in oscillator strength at room temperature [141].

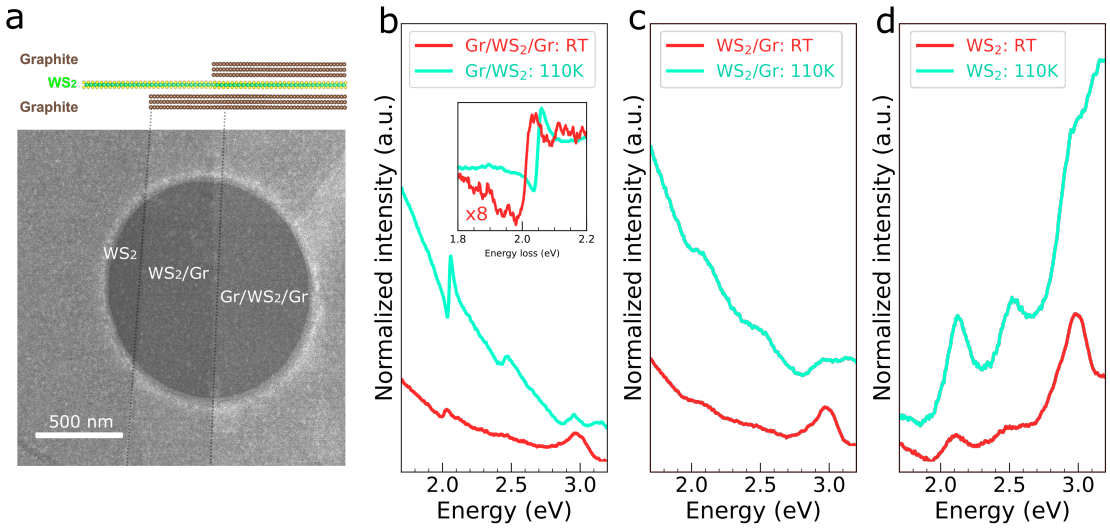

Figure 8.4: **An area including WS_2, WS_2/Gr, Gr/WS_2/Gr are measured by EELS both at RT and LN_2:** (a) ADF of the region with its partition on top; (b) EELS spectra of Gr/WS_2/Gr, the insert is background subtracted by power-law; (c) the spectra of WS_2/Gr; (d) the spectra of WS_2 monolayers. In the case of RT, the spectra are measured on the Princeton instrument KURO CMOS, while in the case of LN_2, the spectra are measured on the Merlin Medipix3.

The persistence of the asymmetric lineshape at RT for the graphite/WS_2/graphite heterostructure suggests the continuum of states that couple to the discrete excitonic states does not originate from the trions. Also, if the asymmetric lineshape is arise from the coupling between excited state trion and X_A, there should be Fano-like exciton peaks in hBN encapsulated TMD-based vdWH. It can therefore be unambiguously concluded that the Fano-like absorption lineshape observed in this chapter is caused by the coupling between the exciton resonance in TMDs and the continuous absorption background of graphite as illustrated later in section 8.2 with the theory of electromagnetic coupling.

8.1.4 Effect of graphene and TMD thickness on the Fano-like lineshape

It should also be noted that the electromagnetic coupling behavior applies to TMD layer thicknesses beyond monolayers. Discrete excitonic transitions in few-layered TMDs encapsulated in thin graphite also exhibit identical asymmetric lineshapes, as demonstrated for the X_A and X_B excitons in the graphite/WS_2/graphite heterostructure with 1-4 layers WS_2 as shown in Fig. 8.5(a). The thickness of graphite is different between 1-2 and 3-4 layers, so the coupling strength is not comparable. The current study found that asymmetric lineshapes do not significantly change when several layers of TMDs are applied to the similarly thickness graphite.

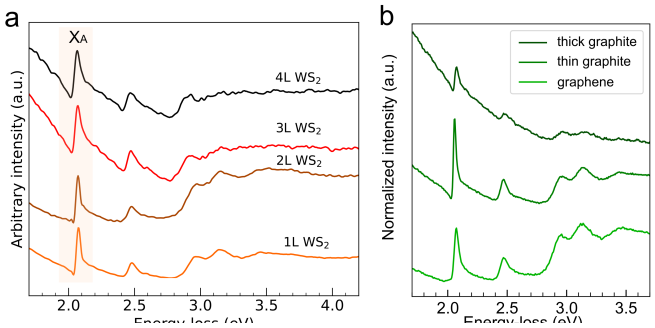

Figure 8.5: **EELS spectra of graphite/WS_2/graphite as the thickness variation:** (a) EELS spectra of one to four layers of WS_2 encapsulated within two graphite flakes are presented. The graphite thickness differs among them, so the coupling strength cannot be compared. One and two layers WS_2 have the same graphite thickness around 8 nm, and three and four layer WS_2 have the same thickness graphite; (b) Monolayer WS_2 coupling with different graphite thicknesses, from bottom to top: graphene (0.69 nm), thin (6.1 nm), and thick (17.5 nm) graphite. The intensity is normalized in the same manner for (b) as in Fig. 8.3.

As shown in Fig. 8.5(b), graphite thickness has a significant influence on this lineshape: i) as graphite thickness increases, the intensity of the exciton absorption peak decreases; ii) there is no significant difference in the exciton absorption linewidth when graphite

thickness is changed; iii) as the graphite thickness increases, the asymmetric line shape becomes increasingly evident, which suggests that the coupling strength increases (at least for thicknesses between 0.69 nm and 17.5 nm).

8.1.5 TMDs coupling with other metal: nickel

The electromagnetic coupling in vdWH is not limited to graphite and TMDs, but can be achieved by any metal that can provide a continuous absorption. In Fig. 8.6, EELS absorption spectra of $MoSe_2$ in proximity and seperated by a 5-nm hBN spacer from a Ni thin film are shown, where an asymmetric line shape can clearly be seen. Due to the fact that the thickness of the sample is much smaller than the wavelength of resonance, the metal film and TMD do not necessarily have to be in contact with each other, and coupling take place even outside the hBN.

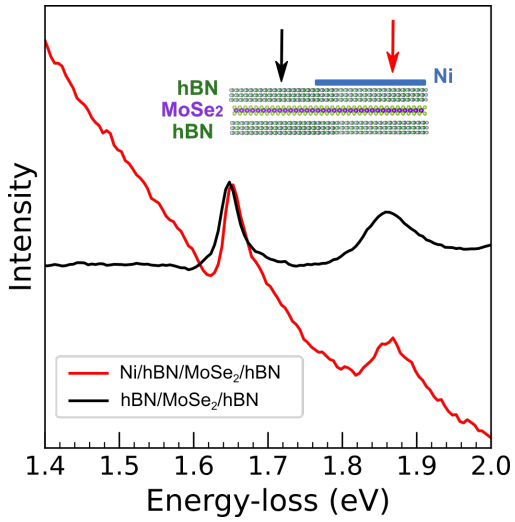

Figure 8.6: **The EELS spetrum comparision between Ni/hBN/$MoSe_2$/hBN and hBN/$MoSe_2$/hBN.**The configuration of each spectrum is color-coded by the arrows on the sketches in the upper part of the panels. Sample from Antoine Reserbat-Plantey et al. at ICFO-Institut de Ciencies Fotonique, Spain.

However, the Fano-like lineshape in hBN encapsulated TMDs on top of the amorphous carbon support (holey carbon of the grid) were not observed. This is not what one expected and it is not consistent with the results obtained for the Ni/hBN/$MoSe_2$/hBN. In this case, there are three possible explanations: i) the thickness of hBN between amorphous carbon and TMDs is greater (20 nm) than that of Ni and $MoSe_2$ (5 nm); ii) in comparison to graphite and nickel, amorphous carbon is not as effective a conductor; iii) the interface between hBN and amorphous carbon is not clean enough, so that the coupling efficiency is low.

8.2 Interpreting the origin of Fano-like lineshape based on theory

There is a type of resonant scattering phenomenon known as Fano resonance, which produces an asymmetric lineshape. It is the interference between a continuum and a discrete energy level that produces the asymmetric lineshape. Ugo Fano established a theoretical explanation of the scattering lineshape of electrons from helium caused by inelastic scattering [58]. This general wave phenomenon can be observed in many fields of physics and engineering [62, 211, 212, 213, 214, 215, 216].

Actually, Fano resonances have been observed in TMD and graphene, separately in the literature [60, 61, 210, 217]. For example, Fano-like resonance was reported in metal nanostructures on TMD monolayer due to plasmon–exciton coupling [61]. Phonon-exciton coupling in bilayer graphene has also been observed by means of electrical gating [217]. Since semiconductors and metals have discrete and continuous energy states, their combination is a good candidate system for optical Fano-type resonances [61, 217]. Although, the optical properties of TMDs/graphene van der Waals heterostructures (vdWH) possess all the elements to show Fano effects, this had not yet been explored.

As an explanation of this asymmetric lineshape response observed in vdWH consisting of graphite and TMDs, an electromagnetic theory based on optical conductivity is developed by F. Javier García de Abajo and Andrea Konečná, which can be applied to interpret the optical absorption spectrum of TMDs in section 8.2.1. Then, the expression of momentum-resolved (section 8.2.2) and analytical EELS probability (section 8.2.3) can be deviated based on retardation and non-retardation approximation. On top of that, the experimental data are fitted based on this model to retrieve the dielectric function of the TMDs and graphite in section 8.2.4. A simple harmonic oscillator systems driven by external forces provide a brief overview of the physics for such Fano resonance as presented in section 8.2.5. In the end, EELS absorption and the phase of optical conductivity are presented in section 8.2.6.

8.2.1 Response of thin semiconductor/metal film with swift electrons

In general, the TMD vdWH has a very thin thickness (≈ 30 nm) in comparison to their optical resonance wavelength (≈ 700 nm), allowing one to treat their surface conductivity $\sigma = \sum_j \sigma_j$, as a zero-thickness film, with σ_j originating from each layer. Thus in this subsection, we intend to calculate the EELS probability of a fast electron impinging on a zero-thickness film lying on the z=0 plane. According to ref. [34], the electron acts on the film with an external time-dependent electric field distribution given by:

$$\mathbf{E}^{\text{ext}}(\mathbf{r},t) = 2\,\text{Re}\left\{\int \frac{d^2\mathbf{k}_\parallel}{(2\pi)^2}\int \frac{d\omega}{2\pi}\,\mathrm{e}^{\mathrm{i}\mathbf{k}_\parallel\cdot\mathbf{R}-\mathrm{i}\omega t}\,\mathbf{E}(\mathbf{k}_\parallel,z,\omega)\right\}, \tag{8.1}$$

where

$$\mathbf{E}^{\text{ext}}(\mathbf{k}_\parallel,z,\omega) = \frac{4\pi \mathrm{i} e}{v}\,\frac{\mathbf{k}_\parallel - (\omega/v\gamma^2)\hat{\mathbf{z}}}{k_\parallel^2 + (\omega/v\gamma)^2}\,\mathrm{e}^{\mathrm{i}\omega z/v}, \tag{8.2}$$

$\gamma = 1/\sqrt{1-v^2/c^2}$ is the Lorentz factor, and $\mathbf{R} = (x,y)$ is the in-plane coordinates. The induced surface current can be written as $\mathbf{j}^{\text{ind}}(\mathbf{k}_\parallel,z,\omega) = \delta(z)\mathbf{j}^{\text{ind}}(\mathbf{k}_\parallel,\omega) \perp \hat{\mathbf{z}}$ in $\mathbf{k}_\parallel - \omega$ space, and

$$\mathbf{j}^{\text{ind}}(\mathbf{k}_\parallel,\omega) = \sigma(k_\parallel,\omega)\Big[\mathbf{E}^{\text{ext}}(\mathbf{k}_\parallel,0,\omega) + \mathbf{E}^{\text{ind}}(\mathbf{k}_\parallel,0,\omega)\Big], \tag{8.3}$$

where $\mathbf{E}^{\text{ind}}$ is the self-induced field acting on the film. According to the Maxwell equation [218], $\mathbf{E}^{\text{ind}}$ can be expressed in terms of $\mathbf{j}^{\text{ind}}$ in free space as:

$$\mathbf{E}^{\text{ind}}(\mathbf{k}_\parallel,z,\omega) = \frac{2\pi}{\omega k_z}\,\mathrm{e}^{\mathrm{i}k_z|z|}\left\{(\mathbf{k}_\parallel + \text{sign}(z)\,k_z\hat{\mathbf{z}})\Big[\mathbf{k}_\parallel\cdot\mathbf{j}^{\text{ind}}(\mathbf{k}_\parallel,\omega)\Big] - (\omega/c)^2\,\mathbf{j}^{\text{ind}}(\mathbf{k}_\parallel,\omega)\right\}, \tag{8.4}$$

where $k_z = \sqrt{(\omega/v)^2 - k_\parallel^2 + \mathrm{i}0^+}$ and the square root is taken to yield $\text{Re}\{k_z\} > 0$. Combining Eqs. (8.2-8.4) and assume the optical conductivity is isotropic in the directions parallel to the film:

$$\mathbf{j}^{\text{ind}}(\mathbf{k}_\parallel,\omega) = \frac{2\mathrm{i}e\omega}{vk_z}\,\frac{\mathbf{k}_\parallel}{k_\parallel^2 + (\omega/v\gamma)^2}\,r_p(k_\parallel,\omega) \tag{8.5}$$

where

$$r_p(k_\parallel,\omega) = \left[1 + \frac{\omega}{2\pi k_z \sigma(k_\parallel,\omega)}\right]^{-1} \tag{8.6}$$

is the Fresnel reflection coefficient for p polarization. The EELS probability $\Gamma_{\text{EELS}}(\omega)$,

corresponding to an energy loss $\hbar\omega$ is then:

$$\begin{aligned}\Gamma_{\mathrm{EELS}}(\omega) &= \frac{e}{\pi\hbar\omega}\int dz\,\mathrm{Re}\left\{e^{-i\omega z/v}\,E_z^{\mathrm{ind}}(0,0,z,\omega)\right\} \\ &= \frac{2e}{\hbar\omega^2}\int\frac{d^2\mathbf{k}_\parallel}{(2\pi)^2}\,\mathrm{Re}\left\{\int dz\,e^{ik_z|z|-i\omega z/v}\,\mathrm{sign}(z)\,\mathbf{k}_\parallel\cdot\mathbf{j}^{\mathrm{ind}}(\mathbf{k}_\parallel,\omega)\right\} \\ &= \frac{4e^2}{\pi\hbar v^2}\int_0^\infty\frac{k_\parallel^3\,dk_\parallel}{\left[k_\parallel^2+(\omega/v\gamma)^2\right]^2}\,\mathrm{Re}\left\{\frac{1}{k_z}\,r_p(k_\parallel,\omega)\right\}.\end{aligned} \tag{8.7}$$

8.2.2 Retardation expression: momentum-resolved EELS probability

This expression has been used in the past to model the optical response of graphene [219], which is extended to describe all 2D materials here. The model proposed here includes only the interaction of the probe (fast electron) with the heterostructure combined electromagnetic response and does not take into account possible electronic interactions between the TMD monolayers with the substrate.

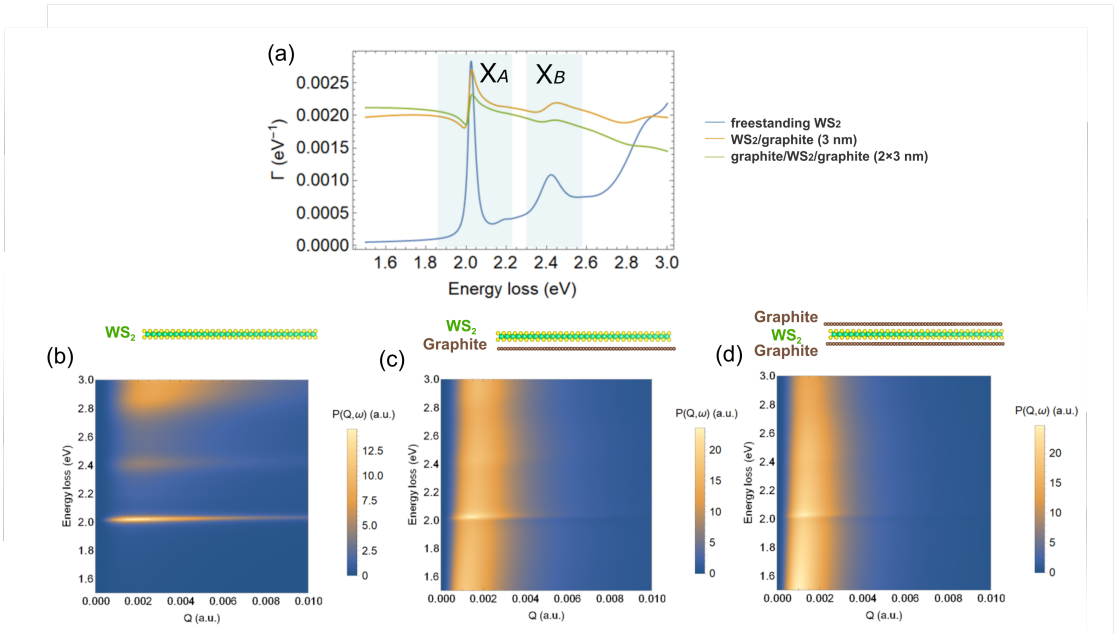

Figure 8.7: **Simulated EELS spectra:** (a) calculated EELS spectra of monolayer WS_2 (b) freestanding, (c) supported by graphite, (d) encapsulated between two graphite layers. The spectra in (a) is the integral of $k_\parallel$ (also called Q) in (b-d). The dielectric function of WS_2 and graphite are from ref. [220] and [221], respectively. Spectra courtesy of Andrea Konečná.

This model can already capture all the spectral features observed indicating that the electronic interaction between the layers is negligible in the energy range with the energy resolution probed. Similar electromagnetic coupling have been observed inside $Ge/Ag/TiO_2/Ag$ optical films, that can transmit and reflect light of the same wavelength within the visiable range [12].

The EELS absorption spectrum of freestanding WS_2 has a Lorentzian shape at X_A as shown in Fig. 8.7(a), while that supported/encapsulated by graphene has an asymmetric shape. The model indicates that the calculated/observed asymmetric profiles are not due to the classical Fano effect, as described by Fano [58], where the absorption lineshape of a discrete transition is modified by its coupling to a continuum of states. Graphene and TMDs have different coupling strengths at different in-plane momentum $k_\parallel$ as shown in Fig. 8.7(c-d). It makes the fitting of such lineshape not possible using either the general Fano formula or modified formula [222, 223], because the resulted lineshapes are the superposition of many different couplings.

8.2.3 Analytical EELS probability expression based on non-retardation approximation

An alternative expression for EELS possibility can be obtained by separating the $k_\parallel$ integral into the $(0, k)$ and (k, ∞) regions, where $k = \omega/c$, and additionally performing the changes of variable $q = k_z$ in the former and $q = -ik_z$ in the latter. Inserting Eq. (8.6) into Eq. (8.7), this leads to

$$\Gamma_{\mathrm{EELS}}(\omega) = \frac{4e^2}{\pi\hbar v^2}\left[\int_0^k \frac{(k^2-q^2)\,dq}{\left(q^2-\omega^2/v^2\right)^2}\,\mathrm{Re}\left\{\frac{q}{q-\mathrm{i}q_0}\right\} + \int_0^\infty \frac{(k^2+q^2)\,dq}{\left(q^2+\omega^2/v^2\right)^2}\,\mathrm{Im}\left\{\frac{q_0}{q-q_0}\right\}\right], \tag{8.8}$$

where $q_0 = \mathrm{i}\omega/2\pi\sigma$ and we have $\mathrm{Im}\{q_0\} > 0$ from the physical condition $\mathrm{Re}\{\sigma\} > 0$ (i.e., the system does not have optical gain). The integrals in this equation admit analytical solutions, although quite involved, in the local-response approximation (i.e., if $\sigma(k_\parallel, \omega) \equiv \sigma(\omega)$ is independent of $k_\parallel$).

In addition, we expect the first integral in Eq. (8.8) to produce a minor contribution that actually vanishes in the nonretarded limit and does not involve any surface mode (i.e., it is carried out within the light cone, where r_p is divergenceless). The second integral can be conveniently recast as the real part of

$$q_0 \int_0^\infty dq\,(q+q_0)(k^2+q^2)\left[q^2+\omega^2/v^2\right]^{-2}(q^2-q_0^2)^{-1}, \tag{8.9}$$

which can in turn be calculated by changing the variable of integration to q^2 in the terms proportional to odd powers of q, while the remaining part can be expressed as half of the $\int_{-\infty}^{\infty} dq$ integral, which we evaluate through complex residues. We finally find

$$\Gamma_{\mathrm{EELS}}(\omega) = \frac{e^2}{\hbar v\omega}\left[\mathcal{I} + \frac{4}{\pi}\int_0^\beta \frac{(\beta^2-x^2)\,dx}{\left(x^2-1\right)^2}\,\mathrm{Re}\left\{\frac{x}{x-\mathrm{i}/\vartheta}\right\}\right], \tag{8.10}$$

where

$$\begin{aligned}\mathcal{I} &= \frac{4}{\pi}\int_0^\infty \frac{(\beta^2+x^2)\,dx}{\left(1+x^2\right)^2}\,\mathrm{Im}\left\{\frac{1}{x\vartheta-1}\right\} \\ &= \mathrm{Im}\left\{\frac{\vartheta}{\left(1+\vartheta^2\right)^2}\left[\vartheta(3-\beta^2)+\vartheta^3(1+\beta^2)+\frac{2}{\pi\gamma^2}\left(1+\vartheta^2\right)+\frac{4}{\pi}\left(1+\beta^2\vartheta^2\right)(\mathrm{i}\pi+\ln\vartheta)\right]\right\}\end{aligned} \tag{8.11}$$

$\beta = v/c$, and $\vartheta = \omega/vq_0 = -2\pi\mathrm{i}\sigma(\omega)/v$. Because $\mathrm{Re}\{\sigma\} > 0$, we have that $\mathrm{Im}\{\vartheta\} < 0$, and the imaginary part of $\ln\vartheta$ needs to be taken as the argument of ϑ in the $(-\pi, 0)$ branch. By this analytical solution, the EELS probability is not momentum dependent.

8.2.4 Theoretical fit based on linear optical conductivity system

The response of the TMD heterostructure is modelled by frequency-dependent optical conductivity $\sigma(\omega)$ here, which can be expressed as the sum of the conductivity of each component of the heterostructure $\sigma(\omega) = \sum_j \sigma_j(\omega)$, where each $j-$th layer forming the heterostructures is so thin that the finite-thickness effects can be neglected. The optical conductivity of each layer can be modelled as

$$\sigma_j(\omega) = \frac{\omega t_j}{4\pi}[\epsilon_{j,2}(\omega) + \mathrm{i}(1-\epsilon_{j,1}(\omega))], \tag{8.12}$$

where t_j is the thickness of $j-$th layer, and $\epsilon_{j,1}$ and $\epsilon_{j,2}$ are the real and imaginary parts of its dielectric function, respectively. One can simply consider the dielectric function

of TMDs and substrate (graphite and hBN) as a Lorentz oscillator oscillator and a continuum damper in the energy range of TMD exciton resonance, respectively. Thus their dielectric function is

$$\epsilon_{sub} = \epsilon_1 + i\epsilon_2, \tag{8.13}$$

$$\epsilon_{TMDs} = 1 + \frac{f_{TMDs}}{{\omega_0}^2 - \omega^2 - i\omega\gamma}, \tag{8.14}$$

where ϵ_1 and ϵ_2 are the real and imaginary part of the dielectric constant for the substrate, f_S is related to the thickness of the substrate. f_{TMDs}, ω_R, γ are the parameters of the harmonic oscillator for TMDs.

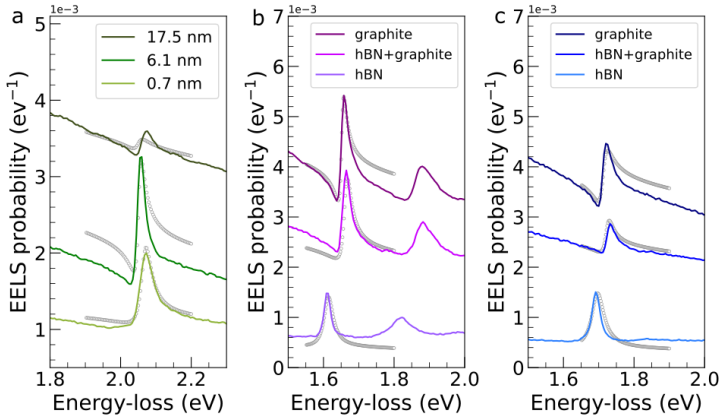

Figure 8.8: **Plot of experimental spectra and their fitted data:** (a) graphite encapsulated WS_2 spectra as the thickness of the graphite decreases; (b) and (c) are spectra of mixed encapsulation of $MoSe_2$ and WSe_2, and they are the same experiemntal data as in Fig. 8.3(b,c). The fitted data are plotted in grey. The experimental data is plotted as EELS probability $\Gamma_{\mathrm{EELS}}(\omega_i) = \frac{I(\omega_i)}{\int_0^{\omega_i} I(\omega)d\omega}$, where $\mathcal{I}(\omega)$ is the measured EELS intensity at energy ω. Fitted spectra courtesy of Andrea Konečná.

Based on above equations and Eq. (8.11), we have fitted the experimental data and retrived the complex dielectric function as shown in Fig. 8.8. The dielectric function of hBN is constant $\epsilon_{hBN} = 4 + i0.5$, and the parameters of TMDs and graphite are listed below in order from of Fig. 8.8 top to bottom, from left to right:

Table 8.1: **The dielectric function of TMDs and graphite retrieved by fitting.**

vdWH configuration	ω_R eV	f_{TMD} ev^2	γ eV	$\epsilon_{graphite}$	$\epsilon_{graphite}$	t_{TMDs} nm	t_{sub} nm
graphite/WS_2/graphite	2.05	1.6	0.03	5.34	8.74	0.6	17.5
graphite/WS_2/graphite	2.05	2.8	0.015	5.34	8.74	0.6	6.1
graphite/WS_2/graphite	2.06	0.6	0.03	5.34	8.74	0.6	0.7
graphite/$MoSe_2$/graphite	1.65	3.0	0.01	5.91	10.13	0.6	8.0
graphite/$MoSe_2$/hBN	1.66	3.0	0.02	5.91	10.13	0.6	4.0
hBN/$MoSe_2$/hBN	1.61	3.0	0.02	N	N	0.6	28.0
graphite/WSe_2/graphite	1.71	10	0.02	5.84	9.92	0.6	20.0
graphite/WSe_2/hBN	1.72	10	0.02	5.84	9.92	0.6	20.0
hBN/WSe_2/hBN	1.69	5.7	0.04	N	N	0.6	32.0

The fitted data are only valid in the energy range of the X_A resonance, which means that only in this energy range can TMDs be regarded as Lorentzian harmonic oscillators, where the dielectric of the substrate is constant. The difference between the experimental data and the fitted data in Fig 8.8 is due to the background generated by the X_B exciton and the excited state of the X_A exciton. This fit method can be used to quantify the exciton energy centres and linewidths in the Fano resonance. From the results in the Table 8.1, it can be shown again that the linewidths of the TMDs in encapsulation are very similar.

8.2.5 Harmonic oscillator systems driven by an external force

In order to grasp the essence of Fano resonance, one can consider the dynamics of two classical oscillators coupled by a weak spring [59]. As shown in Fig. 8.9(a), the equation of motion can be written by:

$$\begin{aligned} \ddot{x}_1 + \gamma_1 \dot{x}_1 + \omega_1^2 x_1 + v_{12} x_2 &= a e^{i\omega t} \\ \ddot{x}_2 + \gamma_2 \dot{x}_2 + \omega_2^2 x_2 + v_{12} x_1 &= 0 \end{aligned} \tag{8.15}$$

where ω_1 and ω_2 are the two normal eigenmodes of this coupled oscillators, v_{12} is the coupling of the two oscillators, γ_1 and γ_2 are the frictional parameters, a is the amplitude of the external harmonic force. One can obtain the solutions for the displacement of the two oscillators as:

$$x_1 = \frac{\left(\omega_2^2 - \omega^2 + i\gamma_2\omega\right) a e^{i\omega t}}{\left(\omega_1^2 - \omega^2 + i\gamma_1\omega\right)\left(\omega_2^2 - \omega^2 + i\gamma_2\omega\right) - v_{12}^2} = |c_1(\omega)| e^{i\omega t - i\varphi_2(\omega)}$$
$$x_2 = \frac{-v_{12} a e^{i\omega t}}{\left(\omega_1^2 - \omega^2 + i\gamma_1\omega\right)\left(\omega_2^2 - \omega^2 + i\gamma_2\omega\right) - v_{12}^2} = |c_2(\omega)| e^{i\omega t - i\varphi_2(\omega)} \tag{8.16}$$

The phase difference between oscillators is:

$$\varphi_2 - \varphi_1 = \pi - \theta = \pi - \tan^{-1}\left(\frac{\gamma_2\omega}{\omega_2^2 - \omega^2}\right) \tag{8.17}$$

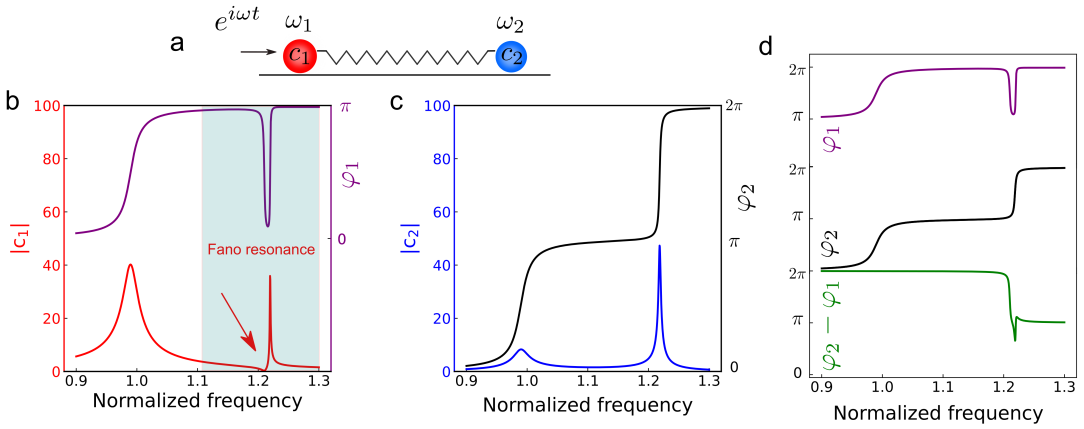

Figure 8.9: **Two coupled damped oscillators:** (a) schematic view of two coupled damped oscillators with one (in red) oscillator being driven by an external force; the resonant dependence of the amplitude and phase of the oscillator with force applied (b) and the coupled one (c); (d) is the phase comparision among the φ_2, φ_1 and $\varphi_2 - \varphi_1$. The frequency in (b-d) is normalized by the ω_1. Here, $\omega_1 = 1$, $\omega_2 = 1.21$, $\gamma_1 = 0.025$, $\gamma_2 = 0.0025$, $v_{12} = 0.1$.

There is a spectral signature to the response of oscillator as shown in Fig. 8.9(a), and this asymmetric amplitude response is called the **Fano resonance**. There is a special characteristic of Fano resonance in that the first oscillator (in red) does not have a response at the frequency of $\omega \approx \omega_2$. In order to explain this 'null' response, one should examine the phase of the first oscillator, which drops rapidly to minimum when the resonant frequency near $\omega = 1.21$ is approached. As a consequence, the first oscillator is experiencing two out-of-phase driving forces: one from the external source and the other from the coupled oscillator, and **as a result of this destructive interference, the coupled resonator exhibits a minimum response.**

8.2.6 Fano-like lineshape and phase in TMDs/graphite

By plotting the EELS probability and the phase of the optical conductivity as shown in Fig. 8.10, it can be seen that: i) for bare TMD, the ω is in phase before the resonance and out of phase at the resonance, and keep out of phase after the resonance; ii) for TMD/graphite vdWH, the ω drop and increase rapidly at the resonance energy; iii) for TMD/hBN vdWH, the ω is in phase before the resonance and out of phase at the resonance, and back to in phase after the resonance. This indicates that the model here is a pure electromagnetic coupling through optical conductivity like the two harmonic oscillator systems driven by an external force (as described in section 8.2.5).

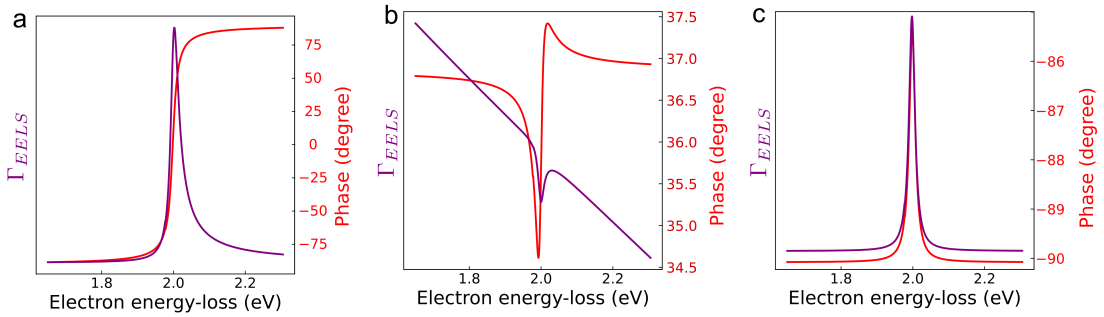

Figure 8.10: **The EELS probability Γ_{EELS} and corresponding phase plot:** (a) bare TMDs; (b) TMDs/graphite; (c) TMDs/hBN. The parameters for TMDs are $f_{\mathrm{TMDs}} = 0.01$, $\omega_{\mathrm{R}} = 2\,eV$, $\gamma = 0.02$. For graphite, $f_{\mathrm{S}} = 2$, $\epsilon_1 = -2.5$, $\epsilon_2 = 1.5$. For hBN, $f_{\mathrm{S}} = 2$,$\epsilon_1 = 2.5$, $\epsilon_2 = 0$. The EELS absorption possibility is in arbitrary units.

8.2.7 Summary

In this section, a TMD monolayer with a conductive or dielectric environment explains the Fano-like lineshapes by a 2D sheet optical conduction model [219], indicating that:

- vdWH is a linear optical conductivity system;
- coupling occurs only through the electromagnetic field, without modifications to the TMD band structure;
- dissipation on and charge transfer to the graphite layers do not modify the exciton absorption linewidth, which will be discussed from the perspective of lifetime and energy level in next section.

8.3 EELS and CL of hBN/WSe_2/graphene/hBN

In TMD-based vdWH, energy and charge transfer between adjacent layers of the TMD directly affects the performance of excitons [206, 207, 208, 64]. It is important to note that charge transfer is much shorter-range (1 nm) and plays a more dominant role in the property of exciton when compared to energy transfer (1 μm) in hBN and graphite encapsulated TMDs.

The charge transfer is very important for generating CL emission from TMD monolayers: i) for hBN encapsulated TMDs, electrons and holes transfer from the hBN to the TMDs enable such vdWH to emit detectable CL signals (section 8.3.1); ii) for TMDs/graphene, native dopants in the TMDs transfer to graphene lead to the trion-free emission (section 8.3.2). In addition to its effect on charge transfer, graphene as a semi-metal can also decrease the exciton binding energy and energy bandgap of TMDs, as introduced insection 8.3.3.

8.3.1 Energy band structure of hBN encapsulated TMDs

A description of the design employed in the CL study for TMD exciton emission will be provided in this section. By combining the fact that TMD/graphene vdWH can suppress trion (charged exciton) emission [18] in PL, and the fact that CL from the excitons in TMD monolayers is only detectable inside hBN encapsulation [48], a new vdWH is proposed: hBN/TMD/graphene/hBN in this section.

TMD/graphene

A complex series of peaks can be observed at cryogenic temperatures in the emission spectra of TMDs. [19, 20, 28, 224]. Especially in the case of tungsten-based TMDs, whose spin-dark state X^D is lower in energy than its spin-bright X_A (as explained in section 6.2.1). As shown in Fig. 8.11, the multiple emission peakas in WS_2 are assigned in increasing order of energy as: several defect-induced local excitons (X_{L1}, X_{L2}), spin-dark excitons (X^D), charged biexcitons (XX^*), singlet trions (X_S^*), triplet trions (X_T^*) and neutral excitons (X_A). Despite its complicated emission spectrum, it remains a goal of many scientists to obtain a single, narrow emission line from TMDs. There is an attractive solution in the form of TMD/graphene coupling, which can result in narrow-line emission resulting solely from neutral excitons [18, 51].

This is because the Dirac crossover of graphene is always located in the middle of the energy gap of TMDs [225], so it can be used as a doping acceptor that can neutralize charge density below $10^{13}\,cm^{-2}$ [225, 51] result in complete filtering of charged excitons or charged biexcitons. In addition, non-radiative recombination to graphene is sufficiently fast to quench emissions from all excitonic species other than X_A. It has been proven that the lifetime of X_A in $MoSe_2$/graphene and bare $MoSe_2$ is the same at 2.3 ps, which is in

accordance with the radiative lifetime [18]. Consequently, TMD/graphene emit only a neutral exciton X_A peak with sharp linewidth and damped intensity, while other species are screened out. Exciton emission intensity dampening mechanisms by graphene including tunneling of charges (Dexter-type charge transfer) [226], asynchronous charge transfer [206, 64], long-range interactions between dipoles (Föster-type energy transfer) [227]. The PL intensity of hBN encapsulated TMD monolayers damped by the graphene is indicated in Fig. 8.11.

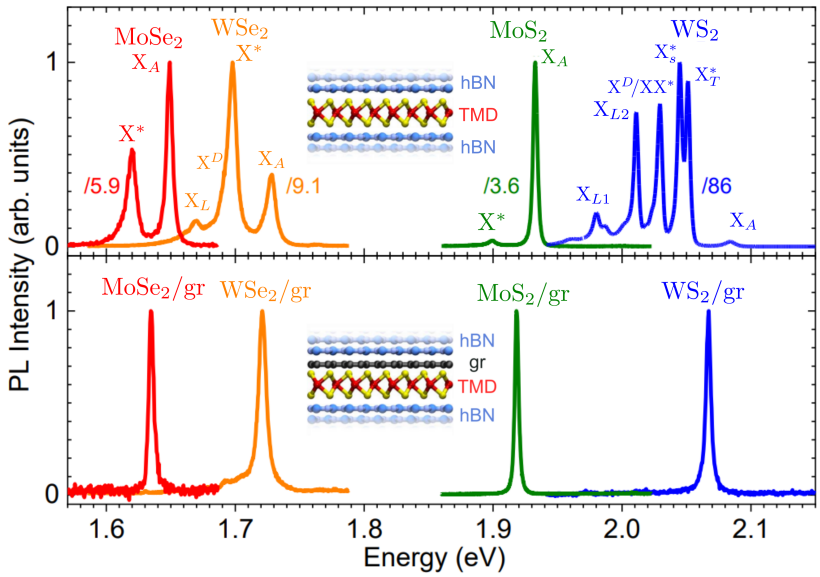

Figure 8.11: **PL spectra of hBN/TMDs/hBN and hBN/grephene/TMDs at around 20 K.** The scaling factors indicate a direct PL intensity comparison between TMD and TMD/graphene encapsulated between hBN flakes. Normalizing all spectra to unity is done by taking the most intense feature as the reference. Reproduced from ref. [18].

hBN/TMDs/hBN

It was not until 2017 that Zheng et al. [48] detected CL signals from excitons in TMD monolayers only within hBN encapsulated structures for the first time in a scanning electron microscope. For the following reasons, CL has not been reported for bare monolayer TMDs: i) electron beams can damage bare TMDs and lead to degradation of optical properties; ii) nanoscale electron beams can not produce enough emission signal to be detected by CL detectors due to their low cross-section of the electron-hole generation process (short action time and small cross section), when passing through very thin monolayer TMDs. The interaction volume can be increased about one hundred times, as thickness of the sample increased from 0.6 nm to 20 nm, and it is the typical thickness of the hBN encapsulation vdWH sample in this chapter.

The charge transfer concept can be applied here to understand the energy band structure of hBN/TMD/hBN as shown in Fig. 8.12(b). hBN applied on both sides of the

TMDs increase the time that electrons spend in the system, resulting in a large number of electrons and holes being generated in the hBN, which diffused into the TMDs, where radiative recombination occurs. This structure makes it possible to study the optical properties of TMDs at the nanoscale with electron beams, one can refer to ref. [28] for the origins of nanoscale CL and EELS variations.

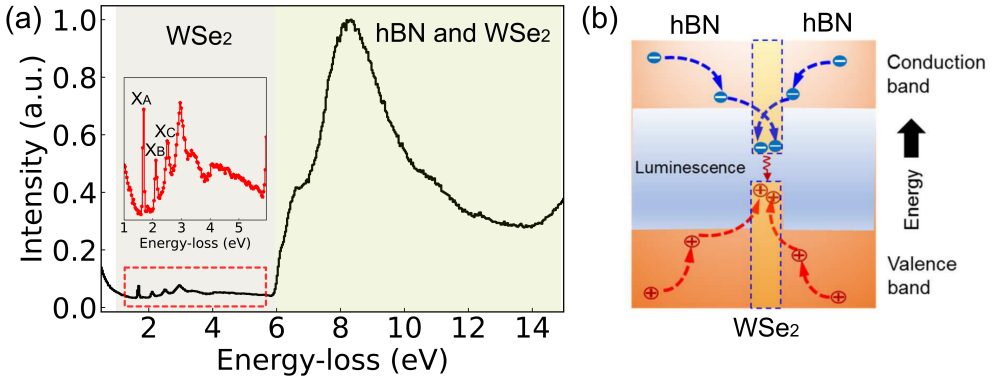

Figure 8.12: **Illustration of cathodoluminescence dynamics for hBN/TMDs/hBN:** (a) EELS spectra of hBN/WSe_2/hBN: indicate that the majority of the absorption occurs in the low-loss range in hBN. The insert shows the EELS spectra of the dotted box marked by red; (b) the energy absorption by the hBN flakes creates many electron and holes which then diffuse into the TMDs monolayer, leading to binding electron-hole pair (exciton) recombination. (b) is reproduced from ref. [48].

hBN/TMD/graphene/hBN for CL experiment

The main challenge faced by performing CL experiment on TMDs/graphene is that its emission efficiency is lower than that from bare TMDs (Fig. 8.11), so there is no measurable CL signal. TMDs on top of graphene and bi-layer graphene have been extensively studied by PL [18, 64, 65], however, without hBN encapsulation, there is not enough signal for CL detection as mentioned. With the aim to study the CL emssion from TMDs/graphene, I encapsulated WSe_2/graphene inside hBN to increase the emission intensity. A decision was made to use WSe_2 is because it is the available strong trion emission TMDs source at LPS. The optical image and diffraction pattern of this four-layered stack vdWH is presented in Fig. 8.13.

In comparison with WSe_2 only encapsulated between two hBN flakes, the optical response of hBN/graphene/WSe_2/hBN exhibits a very different characteristic in CL and EELS. Briefly, it can be concluded that graphene opens up non-radiative decay pathways which mitigate the recombination of ground-state X_A radiation, but not considerably inhibit the formation of X_A. Specifically, the presence of graphene results in: i) X_A red-shifts arise from additional dielectric screening; ii) damping emission X_A intensity in CL; iii) no trion emission. The next two sections will address the difference of CL and

EELS spectra between hBN/WSe_2/hBN and hBN/WSe_2/graphene/hBN in detail.

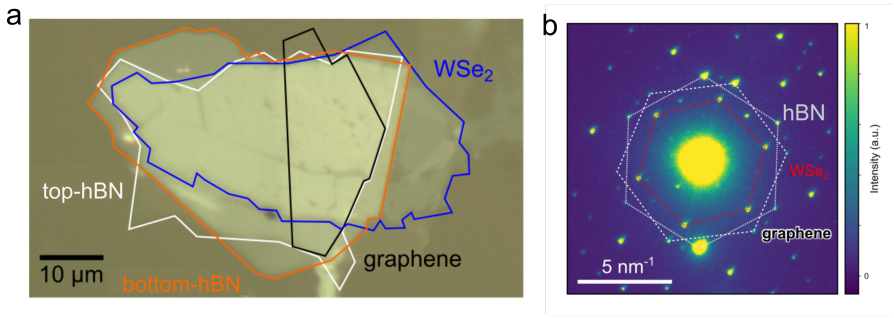

Figure 8.13: **hBN/graphene/WSe_2/hBN vdWH sample:** (a) optical image of hBN/graphene/WSe_2/hBN vdWH with the different constituents outlined during assembly; (b) diffraction pattern of the sample from a hBN/graphene/WSe_2/hBN region measured inside ChromaTEM.

8.3.2 Single exciton emission from hBN/WSe_2/graphene/hBN

The CL spectrum of vdWH made from monolayer WSe_2 stacked onto graphene and encapsulated in hBN at 110 K is shown in Fig. 8.14. This spectrum is compared to its neighboring only hBN encapsulated spectrum (in purple). The CL spectrum of hBN/WSe_2/hBN is composed of two peaks, shifted by 27 meV. The high and low energy line are assigned to neutral exciton X_A (linewidth: 12 meV) and trion X^* (linewidth: 30 meV), filled by the shaded blue curves in Fig. 8.14(a), respectively.

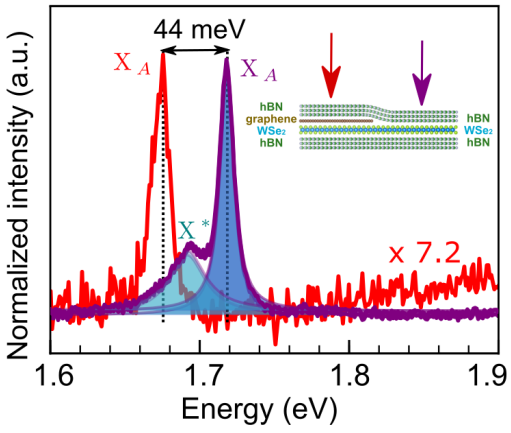

Figure 8.14: **CL spectra comparision between:** (a) hBN/WSe_2/hBN (purple); (b) hBN/WSe_2/graphene/hBN (red). The insets shows the EELS spectra measured from the arrows on the sketches in the upper part of the panels. The linewidth of X_A in hBN/WSe_2/hBN and hBN/WSe_2/graphene/hBN is 12 meV and 15 meV, respectively.

In contrast, the WSe_2/graphene spectrum only display one single and narrow emission line, with a FWHM of 15 meV (Lorentzian fit), suggesting the negligible dephasing time and lifetime changed by graphene. The CL line in WSe_2/graphene is redshifted (by 44 meV) with respect to in the WSe_2 reference due to the additional dielectric screening. However, this study at 110 K has been unable to replicate that the graphene can reduce the inhomogeneous broadening more effectively than hBN encapsulation [51].

There are two likely causes for the differences between the linewidth observe in CL and PL. Firstly, the linewidth of $MoSe_2$/hBN (35 meV) and graphene/$MoSe_2$/hBN (36 meV) in ref. [51] are similar at room-temperature, while the difference observed at 14 K is much more drastic with 7.5 meV for $MoSe_2$/hBN and 1.9 meV graphene/$MoSe_2$/hBN. The CL experiments are carried out at an intermediate temperature where one cannot draw equivalent conclusions. Furthermore, this reduction can also be explained by the sample cleanliness, since $MoSe_2$/hBN has one bare surface compared to graphene/$MoSe_2$/hBN. In this case, the net linewidth reduced by the intervalley scattering and dephasing process cannot be determined with certainty. There is no doubt that the presence of graphene can eliminate the charging effect for inhomogeneous broadening, which hBN as an insulator cannot do as well. Thus, further research is needed to determine the effect of graphene on linewidth compared to hBN.

As a result of this single line emission, it is suggested that the absence of trion emissions can be exploited as a valid indicator of the coupling between WSe_2 and graphene. All dopants in WSe_2 have been transferred to graphene (charge transfer), thus leading to the absence of trion emission. Fast electrons generate a population of hot electron-hole pairs inside hBN and monolayer TMDs, and the presence of graphene increases the non-radiative decay of hot electron-hole pairs and X_A.

From time resolved PL experiment in ref. [18], the lifetime of cold exciton [2] energy level is 2.2 ps and 2.4 ps for hBN/graphene/$MoSe_2$ and hBN/$MoSe_2$, respectively. The presence of graphene decreases the relaxation time of the hot electron-hole pairs to the ground state, thus less of them undergo thermalization to X_A, which make the X_A peak less intense than its counterpart without graphene. From the CL measurement under same large area and electron beam dwell time, the intensity is quenched by a factor of 7.2.

8.3.3 Exciton binding energy

EELS spectra for hBN/WSe_2/hBN and hBN/WSe_2/graphene/hBN vdWH measured at 110 K is presented in Fig. 8.15. The major difference is that the exciton peaks X_A and X_B in the WSe_2/graphene is red-shifted. Different regions on the sample all have similar redshifts as shown in Fig. 8.15, with X_A at around 1.72 eV and 1.68 eV for WSe_2 and

[2] Cold exciton refer to the exciton at band-edge states. When high excitation energy is implied, hot excitons are created, and these excitons thermalize to the cold excitons.

WSe_2/graphene, respectively.

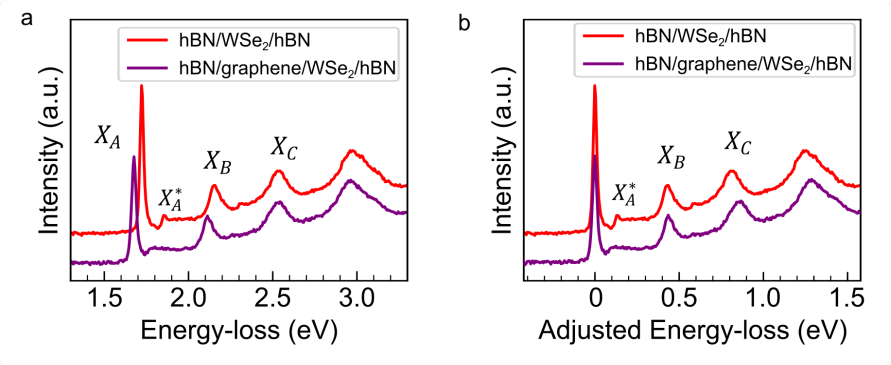

Figure 8.15: **EELS spectra comparison between of hBN/WSe_2/graphene/hBN and hBN/WSe_2/hBN:** (a) EELS spectra of hBN/WSe_2/hBN (in red) and hBN/WSe_2/graphene/hBN (in purple); (b) offset-adjusted EELS spectra by shift the X_A exciton to the offset. The background of the EELS spectra is subtracted by power-law method.

The small peak after the X_A is assigned to X_A^*, which is the first excited Rydberg states of X_A exciton. The energy difference Δ_{12} between the X_A (quantum number n=1) and X_A^* (quantum number n = 2) scales with the ground state exciton binding energy E_b, that $E_b \approx 2\Delta_{12}$ [157]. In Fig. 8.15(b), the EELS offset are all shifted to its X_A, the energy separation between the two states of Δ_{12} is 135 meV and 115 meV for WSe_2 and WSe_2/graphene, respectively. According to ref. [63] that $E_{gap} = E_{X_A} + E_b$, one can infer a bandgap 1.99 eV for WSe_2, reducing to 1.91 eV in the WSe_2/graphene under hBN encapsulation. Thus a 80 mev decrease in the bandgap energy from the presence of graphene can be deduced.

Further comparison of the binding energy with freestanding or graphite encapsulated WSe_2 is not feasible by EELS, as the X_A^* in freestanding WSe_2 is indiscernible due to the peak broadening caused by disorder and intensity of X_A^* in graphite/WSe_2/graphite is highly damped in graphite of all thickness. However, in ref. [63], it was observed that the binding energy of X_A keep decreasing with increasing graphene thickness by reflectance contrast spectra. TMD/graphite coupling offers a means of tuning the electronic state energy based on the magnitude of Coulomb interaction in different vdWH configurations.

It is necessary to recall, in order to interpret these experimental results more intuitively, that while the excitons are contained within the WSe_2 layer, their electric field penetrate both hBN and the local external environment. There is an increasing influence of the dielectric properties of the environment on the screening for larger electron-hole separations [228]. By adding a semi-metallic graphene layer on top of WSe_2, the Coulomb

interaction strength is reduced, resulting in a decrease in both the exciton binding energy and the bandgap. Whether WSe_2 on top of graphene has a more stable exciton energy than hBN requires further statistical analysis. This may be due to the fact that graphene, as a metal, is able to confine the external electric field of exciton, thereby reducing the impact of dielectric disorder outside the vdWHs on the exciton.

8.4 Conclusion

The purpose of the study in this chapter was to determine the effect of graphite as a substrate for TMDs. Various encapsulated vdWH were designed to determine the effect of near-field coupling between graphite and TMDs. The most obvious finding to emerge from the graphite encapsulated TMDs is that the observation of Fano-like lineshape in both optical absorption and EELS. To verify the reliability of this asymmetric line shape, three different TMDs including $MoSe_2$, WSe_2 and WS_2 were tested, inside graphite supported and encapsulated heterostructures. Similar lineshape was observed for TMDs close to Ni film. Therefore, the findings provide insights on the influence of a metal film on TMDs, which would have near-field electromagnetic coupling with excitons, thus forming the Fano-like asymmetric absorption lineshape. Furthermore, the thickness of graphene has an more dominant effect on the lineshape than that of TMDs. The study contributes to our understanding of electron-matter and photon-matter interaction of TMDs based vdWH.

The second aim of this study was to investigate the effects of graphene on the CL of monolayer TMDs. This study has raised important questions about the nature of hBN encapsulation for CL detection on TMDs. The investigation of hBN/WSe_2/graphene/hBN has shown that graphene only affects the intensity of the luminescence (produced a 70% reduction) and exciton species (filter out exciton species other than neutral exciton), but not the linewidth (lifetime) of the exciton. This result is clearly supported by existing findings in PL measurement on TMDs/graphene [18, 65]. But it was not possible to assess the nanoscale varision in CL emission on such structures; currently only a significant signal can be detected on the 0.03 μm^2 area. And because of the thickness of hBN, the electromagnetic coupling effect of graphene and TMDs is not obvious, i.e., the exciton absorption peak is more Lorentzian rather than Fano-like. This study lays the groundwork for future spectroscopy research into TMDs on top of graphene.

Chapter 9

Conclusion

In this thesis, how heterostructures of 2D materials and disorder modify the optical properties of TMDs are examined. To probe these, electron spectroscopies in STEM: EELS and CL, are employed. Experiments were performed inside ChromaTEM using focused electron beams in transmission to achieve the nanometer spatial resolution required to probe heterogeneities in these materials. In the optical response, the important quantities are the lineshape and linewidth of excitonic transitions.

I started considering different substrates, attempting to understand why hBN encapsulation leads to the best optical response. So in the first part of the thesis we explore different substrates and heterostructures configurations, including freestanding, hBN and Si_3N_4 supported or encapsulated TMD monolayers, with the objective to understand the possible effects leading to exciton absorption linewidth broadening in EELS. The ultimate goal was to understand the role of disorders and their degree of importance. This is achieved in part because a STEM microscope enables the measurement of multiple signals, including low-loss EELS for optical absorption, core-loss EELS for chemistry and dielectric environments, scanning nanodiffraction for strain mapping and wide-beam diffraction for roughness on the same areas. Thus we could probe disorder and the optical response of materials with nanoscale spatial resolution. Finally, it is clarified that the negative effects of these substrates on exciton linewidth. The overall conclusion is that, indeed, hBN preserves the optical quality of TMD monolayers and thin flakes as best as possible.

Along this search, the optical response (EELS and CL) in various graphite-based TMD monolayers vdWH are investigated, such as hBN/TMD/graphite/hBN, hBN/TMD/graphite and graphite/TMD/graphite. A substantial modification of the exciton transition due to the near-field coupling between TMDs and graphene/graphite is observed, which leads to Fano-like profiles in absorption and to only an emission spectrum which contains a single quenched but sharp neutral exciton.

In the experiments, we observed that the presence of graphite close to TMD monolayers led to a significant modification of the excitonic lineshape in EELS spectra. Given the

novelty of the Fano-like lineshape, I attempted to understand the interaction leading to these lineshapes and their evolution as a function of the dielectric function of the encapsulating material. The original idea was that the semiconductor (TMD monolayer)-metal (graphite) heterostructure combine a discrete (neutral excition) and a continuous of energy levels (graphite), leading to an asymmetric line shape, as original described by Fano. However, in collaboration with Andrea Konečná and Javier F. García de Abajo, we realized that this interaction was not necessary to explain the effect. In a model describing the EELS response of the heterostructure as that of a zero-thickness 2D sheet, in which the total optical conductivity is simply the sum of the optical conductivity of the substrate and the monolayer, we were able to show that the asymmetry can be understood.

To unveil in detail the role of graphite in both surface of the monolayer (encapsulation), the evolution of the excitonic lineshapes as a function of different encapsulation schemes with graphite and hBN are studied. The general conclusion is that encapsulation is necessary to ensure clean surfaces and that at least one layer of graphite or graphene is needed to produce the asymmetric absorption lineshapes. These conclusions are supported by the theoretical model. In addition, WSe_2/graphene heterostructures encapsulated in hBN showed emission spectra with only a single damped and sharp neutral exciton. This filtering effect has been observed in PL experiments, but this is the first time that is observed in CL. Also in these structures, the neutral exciton exhibits redshift and a reduction of its binding energy compared to hBN/WSe_2/hBN in EELS, in accordance with previous optical measurements.

This thesis has highlighted the importance of encapsulation for TMD monolayers in defining their optical response in different vdWHs. The flexibility of its building blocks combination can bring many new features to the optical properties. The work has opened many perspectives for the research on 2D vdWH as described in next chapter.

Chapter 10

Perspectives

In this chapter, some perspective are presented that can be applied to the study of TMDs in various configurations based on this PhD research. It involves the preparation of several new vdWH samples as well as the use of several advanced electron microscopy and spectroscopy techniques.

Momentum-resolved EELS for graphite/TMDs

In Chapter 8, according to the discussion, it was not possible to fit the asymmetric lineshape of the excitons observed in EELS spectra of graphite-encapsulated TMDs, even considering a modified Fano model [222, 223]. This occurs because the coupling strength between graphite and TMDs depends on the scattering wavevector (Q).

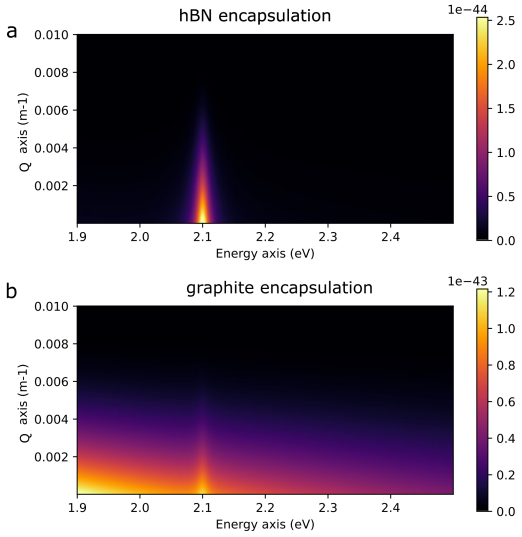

Figure 10.1: **Calculated momentum-resolved EELS probability:** (a) hBN/$MoSe_2$/hBN, (b) graphite/$MoSe_2$/graphite. The dielectric function of hBN end graphite is $\varepsilon_{hBN} = 4 + 0.5i$ and $\varepsilon_{graphite} = 3 + 11i$, and the dielectric function of TMDs is $\varepsilon_{MoSe_2} = 1 + \frac{1.1(eV^2)}{1.66^2 - \omega^2 - i\omega 0.03(eV)}$. The thickness of hBN graphite and $MoSe_2$ is 5, 25, and 0.6 nm.

As an EELS spectrum ($\Gamma_{EELS}(E)$) is the result of the summation over different Q, fitting with a simple expression is not possible. Using momentum-resolved electron energy loss spectroscopy (Q-EELS) to measure the energy-momentum distribution ($\Gamma_{EELS}(Q,E)$), this problem can be overcome through determining both the energy and momentum transferred by an electron to a sample by using the wide parallel electron beam. Thus, Q-EELS is a valuable tool to map the Q-space EELS for graphite/TMDs systems up to large wavevectors (high-Q) and can give key insights into their coupling. Calculation have showed that the coupling strength is small at large Q (Fig. 10.1), further experiment is necessary to prove it.

Electric field mapping of hBN/TMD/hBN

The ratio between the trion and neutral exciton emission intensity in CL experiments on WSe_2 encapsulated in hBN varies at the nanoscale significantly. It is believed that this is primarily due to variations in doping. Previous studies have demonstrated that charge accumulation and the dielectric environment can contribute to trion emission enhancement [28]. However, doping density and trion emission intensity have not yet been directly correlated at the nanoscale. A technique called differential phase contrast (DPC) based on spatially-resolved nanodiffraction can be used to measure electric and magnetic fields at the atomic level. Therefore, one could perform EELS, CL, and DPC on the same region to map both the trion to neutral exciton emission intensity along with the local doping.

As bare TMDs do not exhibit a CL signal, DPC must be performed on hBN encapsulated TMD monolayers. In particular, the analysis of DPC could be problematic as the electric field and potential distribution include the contribution of the hBN layers. It is also possible to investigate the filtering effect of graphene on charged excitons by DPC. Even so, as of the date of the writing of this thesis, no study of DPC analysis has been performed on hBN encapsulated TMD monolayers.

Enhance the emission signal for hBN/TMD/graphene/hBN

To further study the filtering effect of graphene on excitons in CL experiments, stronger signals need to be achieved. Right now, the signal cannot be mapped spatially with nanometer resolution, as their intensity is too weak. We could only get a relatively good signal-to-noise ratio spectrum by accumulating slow-scan signal on a 160 nm × 160 nm region.

The initial aim of the hBN/WSe_2/graphene/hBN sample was to observe a Fano-type EELS and a single neutral exciton peak CL on same sample, therefore this sample does not have a particularly thick hBN so that it does not lead to double scattering events on the EELS spectrum. Furthermore, having a limited supply of the $MoSe_2$ supply with strong trion emission, we chose WSe_2 to study the filtering effect on trion. It is possible to

increase the CL signal for further studies by increasing the thickness of hBN or selecting a TMD monolayer with stronger luminescence than WSe_2, such as $MoSe_2$. Another possible solution for this might be that the graphene is placed outside of the hBN, away from the TMD, thus the vdWH would be hBN/TMD/hBN/graphene.

Filtering effect and coupling distance

In the absence of direct contact between TMDs and graphite, it is unclear whether there is a exciton filtering effect. In particular, whether the charges on TMDs can be neutralized in this case and how graphite influences the lifetime of various exciton species. In ref. [64, 151], there is no measurement of whether a nanometer distance separating $MoSe_2$ and graphene by air or hBN exhibit filtering of exciton species or not, since the spectra are only measured at room temperature.

Ref. [224] has revealed that hBN/graphene/WS_2/hBN (or WSe_2) exhibits multiple species in PL and electroluminescence (EL) at 5 K. Experiments in an electron microscope would be ideal for the study of optical properties of such vdWH interfaces due to its ability to obtain extinction/emission spectra at nanoscale. A new sample containing graphene/hBN/TMD itself encapsulated inside hBN need to be prepared. A varying internal hBN thickness would help to investigate the role the energy and charge transfer mechanism between graphene and TMD. It is encouraging to make this sample, as graphene/hBN(monolayer)/TMDs has been shown to have PL emission four times stronger than graphene/TMDs [151].

Decouple corrugation and strain by scanning nanodiffraction

By conventional spatially-resolved nanodiffraction, lattice strain measurements of TMD monolayers are not accurate due to the corrugation of monolayers. It is possible to obtain full information regarding the location and direction β of the diffraction rods by performing two diffraction measurements with specimen tilts at α and $-\alpha$ as shown in Fig. 10.2. This method has been developed and used to study the corrugation and strain on folded regions of 2D monolayers in 2022 [229].

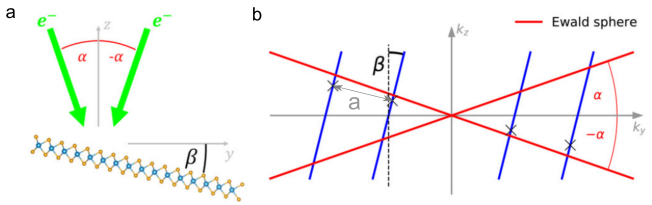

Figure 10.2: **Double tilt nanodifraction experiment:** (a) the electron beam and the tilted sample in real space and (b) the Ewald reconstruction of the 2D materials. Ewald spheres are approximated locally by plans. Reproduced from ref. [229].

Moiré excitons modified by graphite

The model used to understand the TMD/graphite heterostructure coupling is purely electromagnetic that neglects electronic interaction (e.g. orbital hybridization) between the layers. It also holds true for multilayer TMDs. Moiré excitons such as in WSe_2/WS_2 heterostructure with zero twist angle shows multiple peaks around the X_A in WSe_2 with comparable oscillator strength in the absorption spectrum [230, 231, 232]. In order to understand how graphite manipulates these excitons, which are derived from periodic potential energy, further research is required. For example, whether the dielectric function of these interlayer excitons can be represented by a simple dipole harmonic model, and whether the electromagnetic coupling model is still applicable for such vdWH.

Chapter A

Diffraction patterns of TMD monolayers

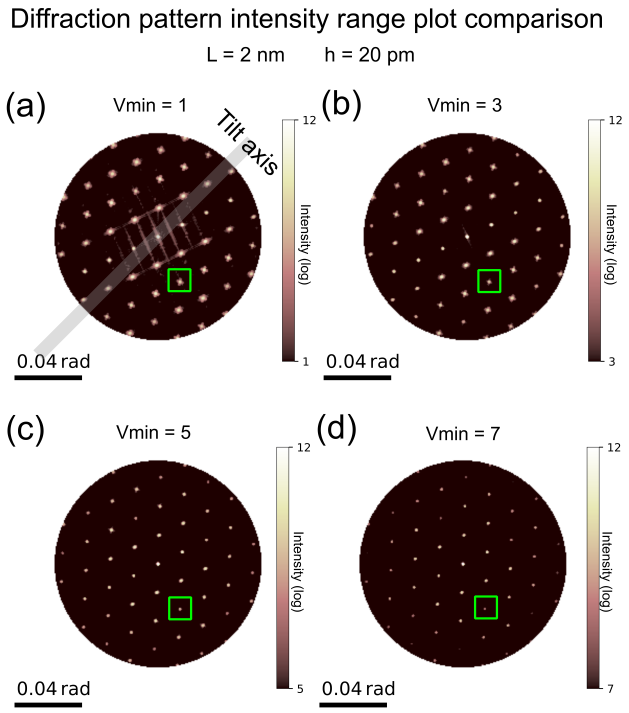

Figure A.1: **Different minimum scaling of the log intensity plot comparison of corrugated WS_2 monolayer simulated diffraction pattern, where L = 2 nm and h = 20 pm.** (a), (b), (c) and (d) are the same simulation plot with V_{min}= 1, 3, 5, 7, respectively.

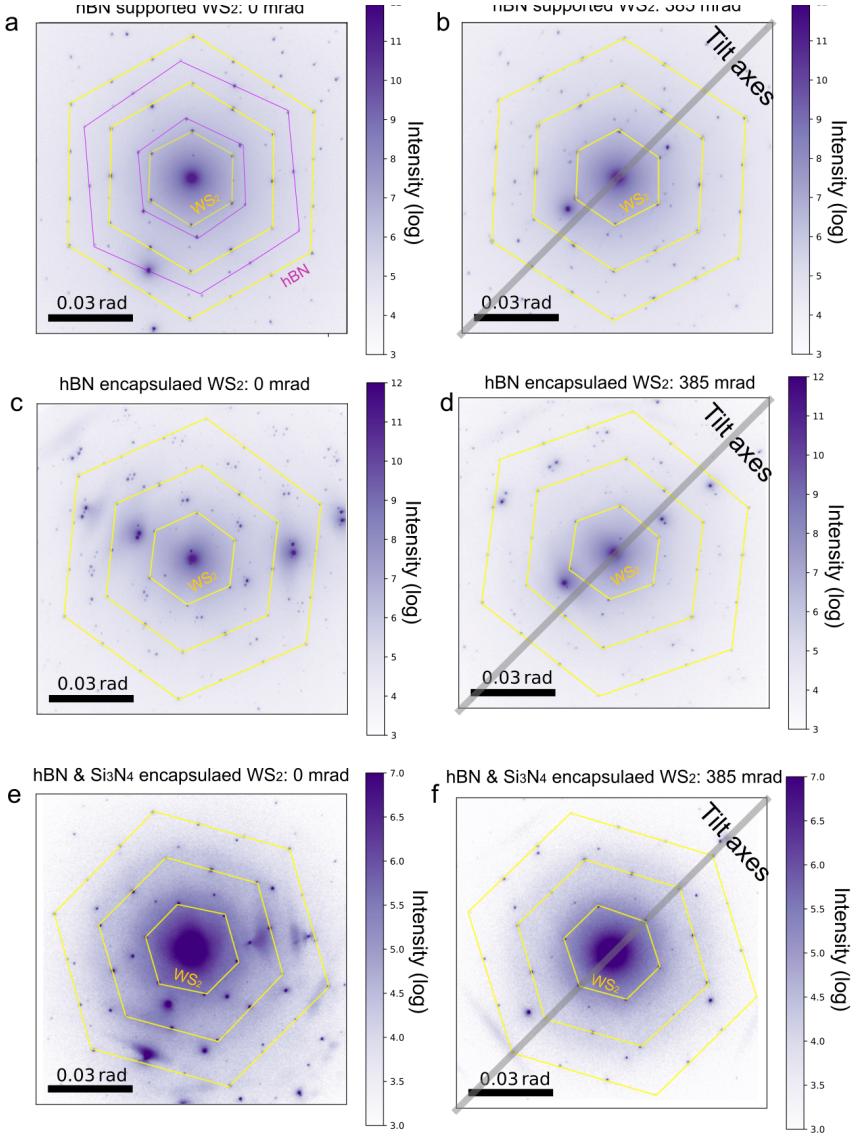

Figure A.2: **hBN supported and encapsulated WS_2 monolayer diffraction patterns:** (a) and (b) are experimental diffraction patterns of hBNsupported WS_2 monolayer at 0 and 385 mrad; (c) and (d) are experimental diffraction patterns of hBNencapsulated WS_2 monolayer at 0 and 385 mrad; (e) and (f) are experimental diffraction pattern of *h*-BN/Si_3N_4 encapsulated WS_2 monolayer at 0 and 385 mrad. The tilt axes are denoted in (b), (d) and (f) by the grey line.

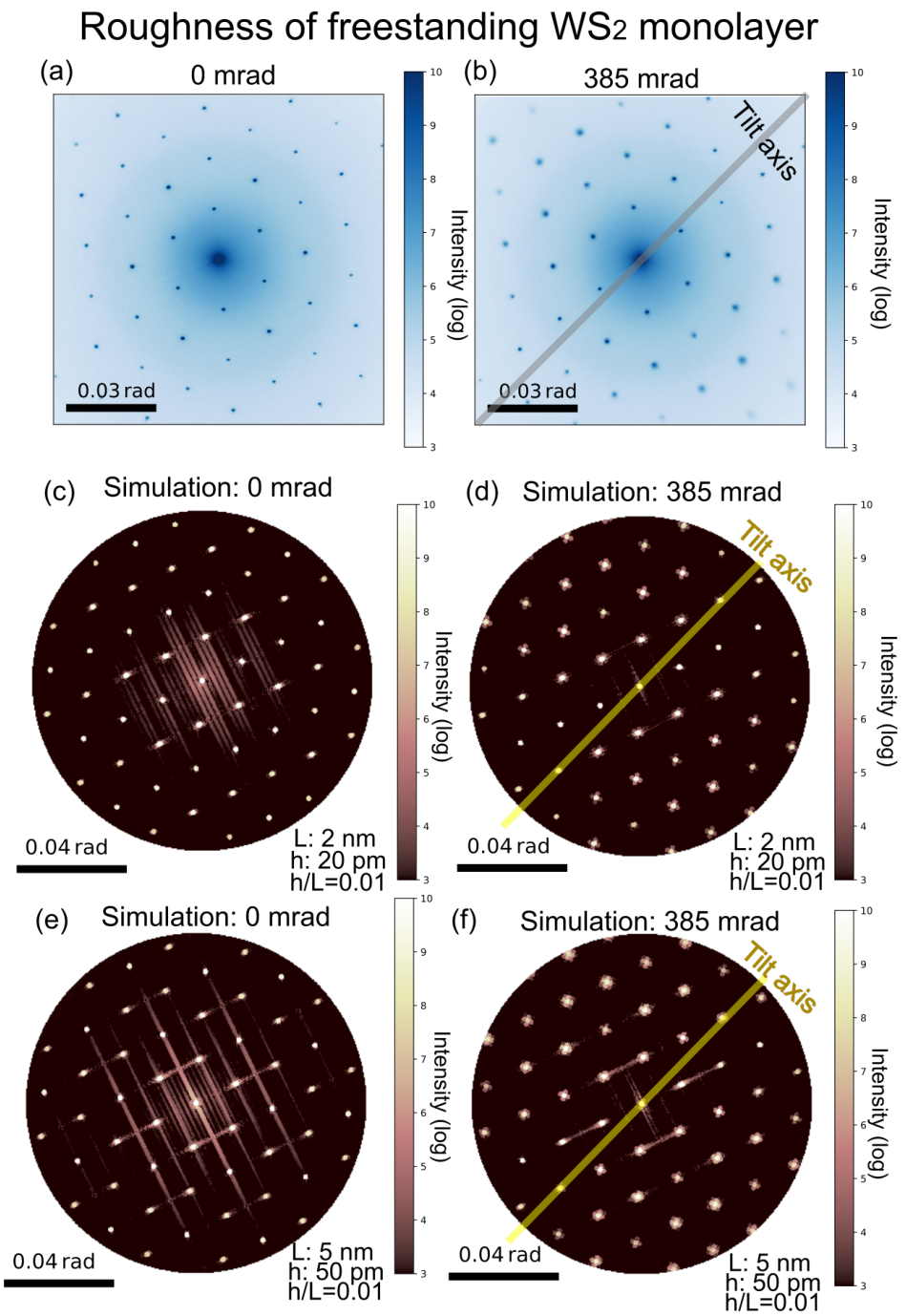

Figure A.3: **Diffraction patterns of freestanding WS_2 monolayer.** (a) and (b) are experimental diffraction patterns at 0 and 385 mrad tilt angles. (c) and (d) are the simulation results of h/L = 0.01 with period of L = 2 nm. (e) and (f) are the simulation results of h/L= 0.01 with period of L = 5 nm.

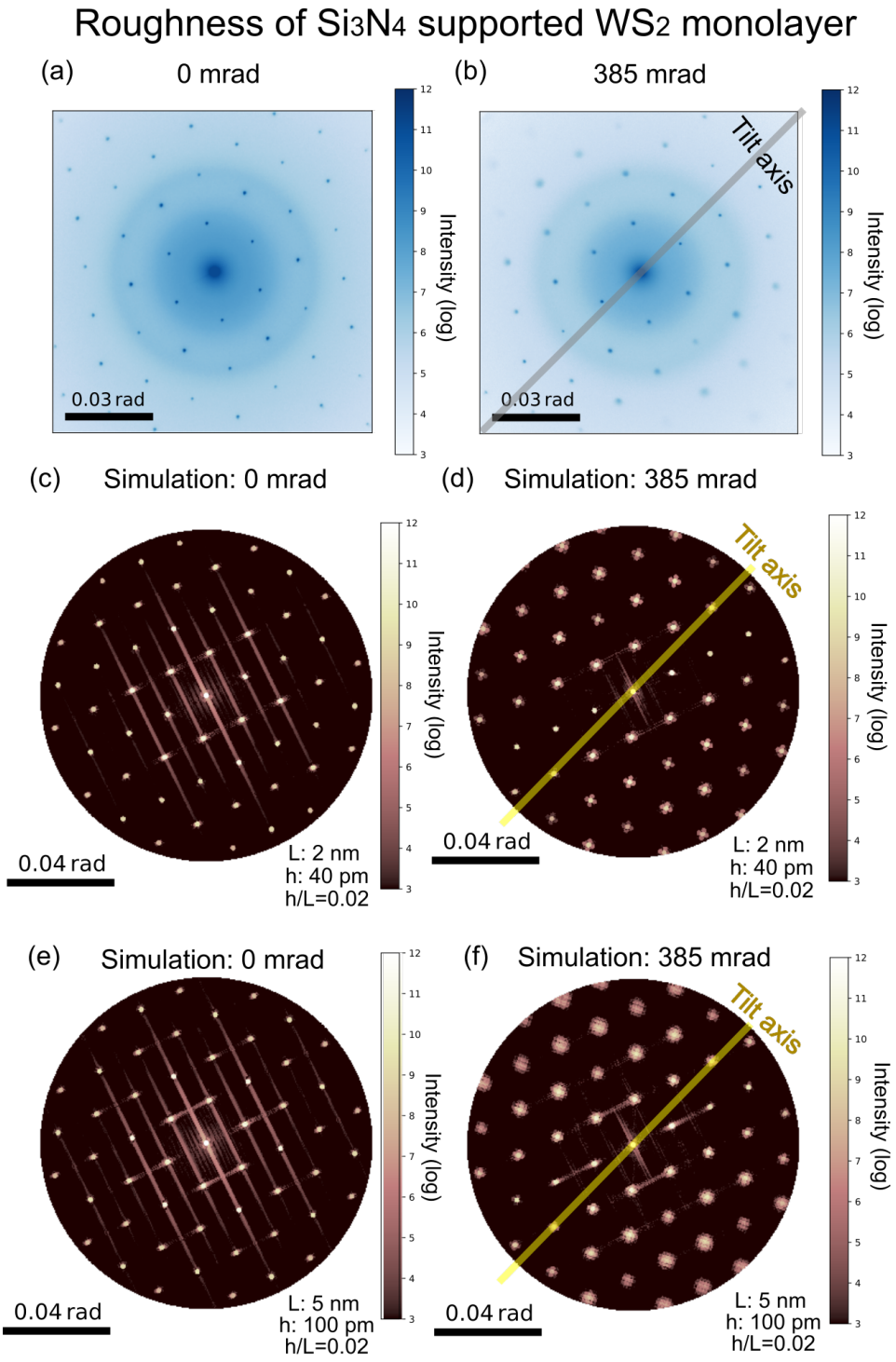

Figure A.4: **Roughness of Si_3N_4 supported WS_2 monolayer:** (a) and (b) are experimental results of diffraction patterns at 0 and 385 mrad tilt angles; (c) and (d) are the simulation results of h/L= 0.02 with period of L = 2 nm; (e) and (f) are the simulation results of h/L = 0.02 with period of L = 5 nm.

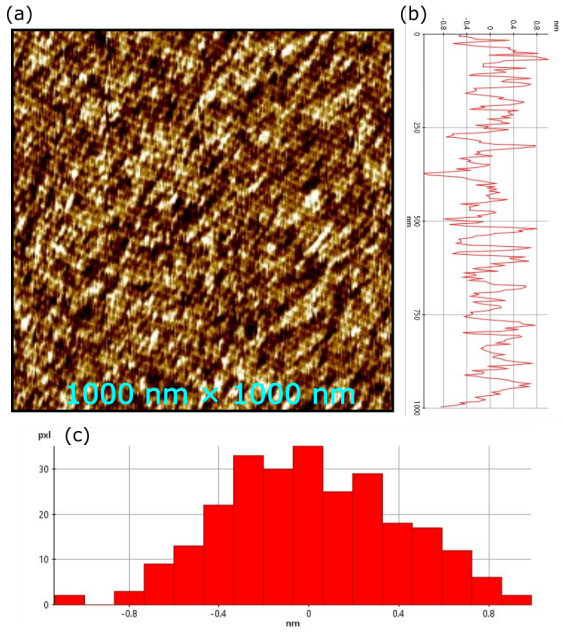

Figure A.5: **AFM measurement the roughness of S_3N_4 membrane:**(a) AFM mapping of 1000 nm × 1000 nm area of 15 nm-S_3N_4 TEM support windows; (b) the height of 1000 nm line profile; (c) histogram of (a), the amplitude is in the range of -0.8 nm to 0.8 nm

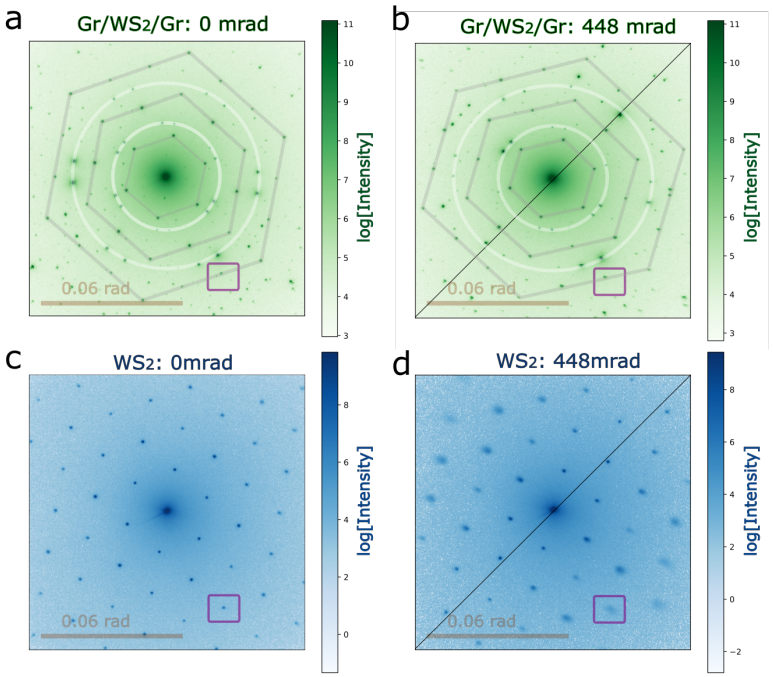

Figure A.6: **Electron diffraction patterns of WS_2 monolayer in graphite/WS_2/graphite and freestanding WS_2 configurations at sample tilt angles of 0 and 448 mrad.** The diffraction spot as boxed in purple are the same index order used to identify the roughness of WS_2 monolayer. Spots highlighted by grey hexagon and white circle are from WS_2 and graphite, respectively.

Chapter B

Strain mapping comparison at different temperatures

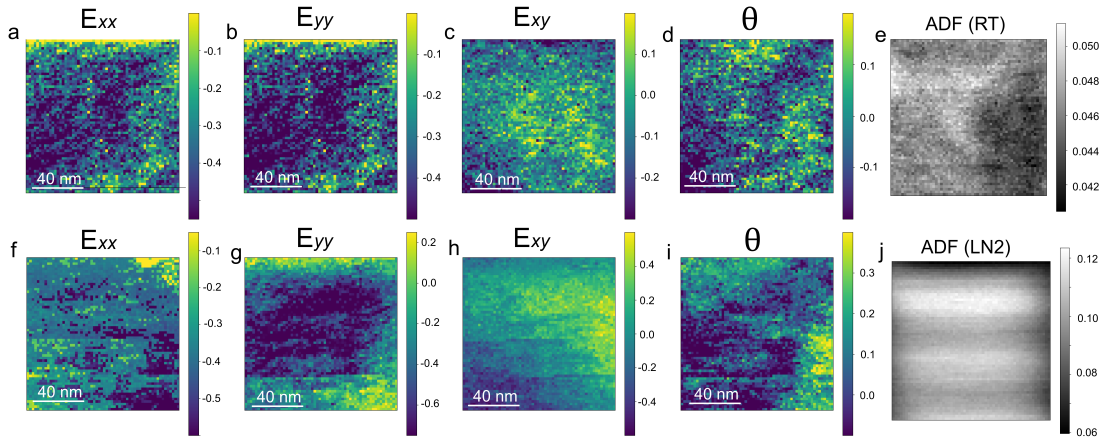

Figure B.1: **Strain mapping of monolayer WSe_2:** (a-d) and (f-i) are the strain component of freestanding WSe_2 for E_{xx}, E_{yy}, E_{xy}, rotation on the same region at RT and LN_2. (a-d) and (f-i) are measured from a same region. (e) and (j) are the ADF images of the RT and LN_2 on the region. As a result of the first scanning nanodiffraction at RT, (j) is the contrast from the carbon on the sample at LN_2.

Bibliography

[1] Thomas Mueller and Ermin Malic. Exciton physics and device application of two-dimensional transition metal dichalcogenide semiconductors. *NPJ 2D Mater. Appl.*, 2:29, 2018. doi: 10.1038/s41699-018-0074-2.

[2] Gang Wang, Alexey Chernikov, Mikhail M. Glazov, Tony F. Heinz, Xavier Marie, Thierry Amand, and Bernhard Urbaszek. Colloquium: excitons in atomically thin transition metal dichalcogenides. *Rev. Mod. Phys.*, 90:021001, 2018. doi: 10.1103/RevModPhys.90.021001.

[3] Zhiwei Peng, Xiaolin Chen, Yulong Fan, David J. Srolovitz, and Dangyuan Lei. Strain engineering of 2D semiconductors and graphene. *Light Sci. Appl.*, 9:1–25, 2020. doi: 10.1038/s41377-020-00421-5.

[4] Andrea Locatelli, Kevin R Knox, Dean Cvetko, Tevfik Onur Mentes, Miguel Angel Nino, Shancai Wang, Mehmet B Yilmaz, Philip Kim, Richard M Osgood Jr, and Alberto Morgante. Corrugation in exfoliated graphene: an electron microscopy and diffraction study. *ACS Nano*, 4:4879–4889, 2010. doi: 10.1021/nn101116n.

[5] Archana Raja, Lutz Waldecker, Jonas Zipfel, Yeongsu Cho, Samuel Brem, Jonas D. Ziegler, Marvin Kulig, Takashi Taniguchi, Kenji Watanabe, Ermin Malic, Tony F. Heinz, Timothy C. Berkelbach, and Alexey Chernikov. Dielectric disorder in two-dimensional materials. *2D Mater.*, 14:832–837, 2019. doi: 10.1038/s41565-019-0520-0.

[6] Peiliang Zhao, Jin Yu, H Zhong, M Rösner, Mikhail I Katsnelson, and Shengjun Yuan. Electronic and optical properties of transition metal dichalcogenides under symmetric and asymmetric field-effect doping. *New J. Phys.*, 22:083072, 2020. doi: 10.1088/1367-2630/aba8d2.

[7] Changhee Lee, Servin Rathi, Muhammad Atif Khan, Dongsuk Lim, Yunseob Kim, Sun Jin Yun, Doo-Hyeb Youn, Kenji Watanabe, Takashi Taniguchi, and Gil-Ho Kim. Comparison of trapped charges and hysteresis behavior in hBN encapsulated single MoS_2 flake based field effect transistors on SiO_2 and hBN substrates. *Nanotechnology*, 29:335202, 2018. doi: 10.1088/1361-6528/aac6b0.

[8] Yury Yu Illarionov, Gerhard Rzepa, Michael Waltl, Theresia Knobloch, Alexander Grill, Marco M Furchi, Thomas Mueller, and Tibor Grasser. The role of charge trapping in MoS_2/SiO_2 and MoS_2/hBN field-effect transistors. *2D Mater.*, 3:035004, 2016. doi: 10.1088/2053-1583/3/3/035004.

[9] Daniel Rhodes, Sang Hoon Chae, Rebeca Ribeiro-Palau, and James Hone. Disorder in van der Waals heterostructures of 2D materials. *Nat. Mater.*, 18:541–549, 2019. doi: 10.1038/s41563-019-0366-8.

[10] Jannik C Meyer, Andre K Geim, Mikhail I Katsnelson, Konstantin S Novoselov, Tim J Booth, and Siegmar Roth. The structure of suspended graphene sheets. *Nature*, 446:60–63, 2007. doi: 10.1038/nature05545.

[11] Joachim Dahl Thomsen, Tue Gunst, Søren Schou Gregersen, Lene Gammelgaard, Bjarke Sørensen Jessen, David M. A. Mackenzie, Kenji Watanabe, Takashi Taniguchi, Peter Bøggild, and Timothy J. Booth. Suppression of intrinsic roughness in encapsulated

graphene. *Phys. Rev. B*, 96:014101, 2017. doi: 10.1103/PhysRevB.96.014101.

[12] Mohamed ElKabbash, Theodore Letsou, Sohail A. Jalil, Nathaniel Hoffman, Jihua Zhang, James Rutledge, Andrew R. Lininger, Chun-Hao Fann, Michael Hinczewski, Giuseppe Strangi, and et al. Fano-resonant ultrathin film optical coatings. *Nat. Nanotechnol.*, 16: 440–446, 2021. doi: 10.1038/s41565-020-00841-9.

[13] Zhihao Yu, Zhun-Yong Ong, Yiming Pan, Yang Cui, Run Xin, Yi Shi, Baigeng Wang, Yun Wu, Tangsheng Chen, Yong-Wei Zhang, and et al. Realization of room-temperature phonon-limited carrier transport in monolayer mos_2 by dielectric and carrier screening. *Adv. Mater.*, 28:547–552, 2015. doi: 10.1002/adma.201503033.

[14] Britton W. Baugher, Hugh O. Churchill, Yafang Yang, and Pablo Jarillo-Herrero. Intrinsic electronic transport properties of high-quality monolayer and bilayer MoS_2. *Nano Lett.*, 13:4212–4216, 2013. doi: 10.1021/nl401916s.

[15] Branimir Radisavljevic and Andras Kis. Mobility engineering and a metal–insulator transition in monolayer MoS_2. *Nat. Mater.*, 12:815–820, 2013. doi: 10.1038/nmat3687.

[16] Xiaoxiang Xi, Zefang Wang, Weiwei Zhao, Ju-Hyun Park, Kam Tuen Law, Helmuth Berger, László Forró, Jie Shan, and Kin Fai Mak. Ising pairing in superconducting $NbSe_2$ atomic layers. *Nat. Phys.*, 12:139–143, 2015. doi: 10.1038/nphys3538.

[17] Fabian Cadiz, Emmanuel Courtade, Cédric Robert, Gang Wang, Y Shen, Hui Cai, Takashi Taniguchi, Kenji Watanabe, Helene Carrere, Delphine Lagarde, M. Manca, T. Amand, P. Renucci, S. Tongay, X. Marie, and B Urbaszek. Excitonic linewidth approaching the homogeneous limit in MoS_2-based van der Waals heterostructures. *Phys. Rev. X*, 7:021026, 2017. doi: 10.1103/PhysRevX.7.021026.

[18] Etienne Lorchat, Luis E Parra López, Cédric Robert, Delphine Lagarde, Guillaume Froehlicher, Takashi Taniguchi, Kenji Watanabe, Xavier Marie, and Stéphane Berciaud. Filtering the photoluminescence spectra of atomically thin semiconductors with graphene. *Nat. Nanotechol.*, 15:283–288, 2020. doi: 10.1038/s41565-020-0644-2.

[19] M. Koperski, K. Nogajewski, A. Arora, V. Cherkez, P. Mallet, J.-Y. Veuillen, J. Marcus, P. Kossacki, and M. Potemski. Single photon emitters in exfoliated WSe_2 structures. *Nat. Nanotechol.*, 10:503–506, 2015. doi: 10.1038/nnano.2015.67.

[20] Lukas Linhart, Matthias Paur, Valerie Smejkal, Joachim Burgdörfer, Thomas Mueller, and Florian Libisch. Localized intervalley defect excitons as single-photon emitters in WSe_2. *Phys. Rev. Lett.*, 123:146401, 2019. doi: 10.1103/PhysRevLett.123.146401.

[21] Zhiwei Li, Yawei Lv, Liwang Ren, Jia Li, Lingan Kong, Yujia Zeng, Quanyang Tao, Ruixia Wu, Huifang Ma, Bei Zhao, Di Wang, Weiqi Dang, Keqiu Chen, Lei Liao, Xidong Duan, Xiangfeng Duan, and Yuan Liu. Efficient strain modulation of 2D materials via polymer encapsulation. *Nat. Commun.*, 11:1151, 2020. doi: 10.1038/s41467-020-15023-3.

[22] Adeline Huiling Loo, Alessandra Bonanni, Adriano Ambrosi, and Martin Pumera. Molybdenum disulfide (MoS_2) nanoflakes as inherently electroactive labels for DNA hybridization detection. *Nanoscale*, 6:11971–11975, 2014. doi: 10.1039/C4NR03795B.

[23] Changli Li, Qi Cao, Faze Wang, Yequan Xiao, Yanbo Li, Jean-Jacques Delaunay, and Hongwei Zhu. Engineering graphene and TMDs based van der waals heterostructures for photovoltaic and photoelectrochemical solar energy conversion. *Chem. Soc. Rev.*, 47:4981–5037, 2018. doi: 10.1039/C8CS00067K.

[24] Limits of resolution: The Rayleigh criterion, Douglas College Physics and OpenStax. URL `https://pressbooks.bccampus.ca/introductorygeneralphysics2phys1207/chapter/27-6-limits-of-resolution-the-rayleigh-criterion/`.

[25] Eva Rittweger, Kyu Young Han, Scott E. Irvine, Christian Eggeling, and Stefan W. Hell. STED microscopy reveals crystal colour centres with nanometric resolution. *Nat. Photon-*

ics, 3:144–147, 2009. doi: 10.1038/nphoton.2009.2.

[26] R. Marty, C. Girard, A. Arbouet, and G. Colas des Francs. Near-field coupling of a point-like dipolar source with a thin metallic film: Implication for STM plasmon excitations. *Chem. Phys. Lett.*, 532:100–105, 2012. doi: 10.1016/j.cplett.2012.02.058.

[27] Rachel A Oliver. Advances in AFM for the electrical characterization of semiconductors. *Rep. Prog. Phys.*, 71:076501, 2008. ISSN 0034-4885, 1361-6633. doi: 10.1088/0034-4885/71/7/076501.

[28] Noémie Bonnet, Hae Yeon Lee, Fuhui Shao, Steffi Y. Woo, Jean-Denis Blazit, Kenji Watanabe, Takashi Taniguchi, Alberto Zobelli, Odile Stéphan, Mathieu Kociak, Silvija Gradečak, and Luiz H. G. Tizei. Nanoscale modification of WS_2 trion emission by its local electromagnetic environment. *Nano Lett.*, 21:10178–10185, 2021. doi: 10.1021/acs.nanolett.1c02600.

[29] Luiz HG Tizei, Yung-Chang Lin, Masaki Mukai, Hidetaka Sawada, Ang-Yu Lu, Lain-Jong Li, Koji Kimoto, and Kazu Suenaga. Exciton mapping at subwavelength scales in two-dimensional materials. *Phys. Rev. Lett.*, 114:107601, 2015. doi: 10.1103/PhysRevLett.114.107601.

[30] Mathieu Kociak and Odile Stéphan. Mapping plasmons at the nanometer scale in an electron microscope. *Chem. Soc. Rev.*, 43:3865, 2014. doi: 10.1039/c3cs60478k.

[31] Colin Ophus. Four-dimensional scanning transmission electron microscopy (4D-STEM). *Microsc. Microanal.*, 25:563–582, 2019. doi: 10.1017/S1431927619000497.

[32] Benjamin H. Savitzky, Steven E. Zeltmann, Lauren A. Hughes, Hamish G. Brown, Shiteng Zhao, Philipp M. Pelz, Thomas C. Pekin, Edward S. Barnard, Jennifer Donohue, Luis Rangel DaCosta, Ellis Kennedy, Yujun Xie, Matthew T. Janish, Matthew M. Schneider, Patrick Herring, Chirranjeevi Gopal, Abraham Anapolsky, Rohan Dhall, Karen C. Bustillo, Peter Ercius, Mary C. Scott, Jim Ciston, Andrew M. Minor, and Colin Ophus. py4DSTEM: A software package for four-dimensional scanning transmission electron microscopy data analysis. *Microsc. Microanal.*, 27:712–743, 2021. doi: 10.1017/S1431927621000477.

[33] Albert Polman, Mathieu Kociak, and F Javier García de Abajo. Electron-beam spectroscopy for nanophotonics. *Nat. Mater.*, 18:1158–1171, 2019. doi: 10.1038/s41563-019-0409-1.

[34] F. J. García de Abajo. Optical excitations in electron microscopy. *Rev. Mod. Phys.*, 82:209–275, 2010. doi: 10.1103/RevModPhys.82.209.

[35] Ashish Arora, Nils Kolja Wessling, Thorsten Deilmann, Till Reichenauer, Paul Steeger, Piotr Kossacki, Marek Potemski, Steffen Michaelis de Vasconcellos, Michael Rohlfing, and Rudolf Bratschitsch. Dark trions govern the temperature-dependent optical absorption and emission of doped atomically thin semiconductors. *Phys. Rev. B*, 101:241413, 2020. doi: 10.1103/PhysRevB.101.241413.

[36] Jakob Wierzbowski, Julian Klein, Florian Sigger, Christian Straubinger, Malte Kremser, Takashi Taniguchi, Kenji Watanabe, Ursula Wurstbauer, Alexander W. Holleitner, Michael Kaniber, Kai Müller, and Jonathan J. Finley. Direct exciton emission from atomically thin transition metal dichalcogenide heterostructures near the lifetime limit. *Sci. Rep.*, 7:12383, 2017. doi: 10.1038/s41598-017-09739-4.

[37] Jinhua Hong, Masanori Koshino, Ryosuke Senga, Thomas Pichler, Hua Xu, and Kazu Suenaga. Deciphering the intense postgap absorptions of monolayer transition metal dichalcogenides. *ACS Nano*, 15:7783–7789, 2021. doi: 10.1021/acsnano.1c01868.

[38] Luiz H. G. Tizei, Yung-Chang Lin, Ang-Yu Lu, Lain-Jong Li, and Kazu Suenaga. Electron energy loss spectroscopy of excitons in two-dimensional-semiconductors as a function of temperature. *Appl. Phys. Lett.*, 108:163107, 2016. doi: 10.1063/1.4947058.

[39] Jinhua Hong, Ryosuke Senga, Thomas Pichler, and Kazu Suenaga. Probing exciton dis-

persions of freestanding monolayer WSe_2 by momentum-resolved electron energy-loss spectroscopy. *Phys. Rev. Lett.*, 124:087401, 2020. doi: 10.1103/PhysRevLett.124.087401.

[40] Kumar Gogoi Pranjal, Yung-Chang Lin, Senga Ryosuke, Komsa Hannu-Pekka, Liang Wong Swee, Chi Dongzhi, Krasheninnikov Arkady, V., Li Lain-Jong, Breese Mark, B. H., Pennycook Stephen, J., Wee Andrew, T. S., and Suenaga Kazu. Layer rotation-angle-dependent excitonic absorption in van der Waals heterostructures revealed by electron energy loss spectroscopy. *ACS Nano*, 13:9541–9550, 2019. doi: 10.1021/acsnano.9b04530.

[41] Eoin Moynihan, Stefan Rost, Eoghan O'Connell, Quentin Ramasse, Christoph Friedrich, and Ursel Bangert. Plasmons in MoS_2 studied via experimental and theoretical correlation of energy loss spectra. *J. Microsc.*, 279:256–264, 2020. doi: 10.1111/jmi.12900.

[42] Hannah Catherine Nerl, Kirsten Trøstrup Winther, Fredrik S Hage, Kristian Sommer Thygesen, Lothar Houben, Claudia Backes, Jonathan N Coleman, Quentin M Ramasse, and Valeria Nicolosi. Probing the local nature of excitons and plasmons in few-layer MoS_2. *NPJ 2D Mater. Appl.*, 1:2, 2017. doi: 10.1038/s41699-017-0003-9.

[43] Sandhya Susarla, Lucas M. Sassi, Alberto Zobelli, Steffi Y. Woo, Luiz HG Tizei, Odile Stéphan, and Pulickel M. Ajayan. Mapping modified electronic levels in the moiré patterns in MoS_2/WSe_2 using low-loss EELS. *Nano Lett.*, 21:4071–4077, 2021. doi: 10.1021/acs.nanolett.1c00984.

[44] Andreas V. Stier, Kathleen M. McCreary, Berend T. Jonker, Junichiro Kono, and Scott A. Crooker. Exciton diamagnetic shifts and valley Zeeman effects in monolayer WS_2 and MoS_2 to 65 Tesla. *Nat. Commun.*, 7:10643, 2016. doi: 10.1038/ncomms10643.

[45] A. A. Mitioglu, K. Galkowski, A. Surrente, L. Klopotowski, D. Dumcenco, A. Kis, D. K. Maude, and P. Plochocka1. Magnetoexcitons in large area CVD-grown monolayer MoS_2 and $MoSe_2$ on sapphire. *Phys. Rev. B*, 93:165412, 2016. doi: 10.1103/PhysRevB.93.165412.

[46] J Jadczak, J Kutrowska-Girzycka, P Kapuściński, Y S Huang, A Wójs, and L Bryja1. Probing of free and localized excitons and trions in atomically thin WSe_2, WS_2, $MoSe_2$ and MoS_2 in photoluminescence and reflectivity experiments. *Nanotechnology*, 28:395702, 2017. doi: 10.1088/1361-6528/aa87d0.

[47] Shinichiro Mouri, Yuhei Miyauchi, and Kazunari Matsuda. Tunable photoluminescence of monolayer MoS_2 via chemical doping. *Nano Lett.*, 13:5944–5948, 2013. doi: 10.1021/nl403036h.

[48] Shoujun Zheng, Jin-Kyu So, Fucai Liu, Zheng Liu, Nikolay Zheludev, and Hong Jin Fan. Giant enhancement of cathodoluminescence of monolayer transitional metal dichalcogenides semiconductors. *Nano Lett.*, 17:6475–6480, 2017. doi: 10.1021/acs.nanolett.7b03585.

[49] Jason S. Ross, Sanfeng Wu, Hongyi Yu, Nasim Nirmal J. Ghimire, Aaron M. Jones, Grant Aivazian, Jiaqiang Yan, David G. Mandrus, Di Xiao, Wang Yao, and Xiaodong Xu. Electrical control of neutral and charged excitons in a monolayer semiconductor. *Nat. Commun.*, 4:1–6, 2013. doi: 0.1038/ncomms2498.

[50] Obafunso A Ajayi, Jenny V Ardelean, Gabriella D Shepard, Jue Wang, Abhinandan Antony, Takeshi Taniguchi, Kenji Watanabe, Tony F Heinz, Stefan Strauf, X-Y Zhu, and James C Hone. Approaching the intrinsic photoluminescence linewidth in transition metal dichalcogenide monolayers. *2D Mater.*, 4:031011, 2017. doi: 10.1088/2053-1583/aa6aa1.

[51] Luis Enrique Parra López, Loïc Moczko, Joanna Wolff, Aditya Singh, Etienne Lorchat, Michelangelo Romeo, Takashi Taniguchi, Kenji Watanabe, and Stéphane Berciaud. Single- and narrow-line photoluminescence in a boron nitride-supported $MoSe_2$ /graphene heterostructure. *C R Phys*, 22:77–88, 2022. doi: 10.5802/crphys.58.

[52] Akshay Singh, Hae Yeon Lee, and Silvija Gradečak. Direct optical-structure correlation in atomically thin dichalcogenides and heterostructures. *Nano Res.*, 13:1363–1368, 2019. doi: 10.1007/s12274-019-2601-7.

[53] Tong Ye, Junze Li, and Dehui Li. Charge-accumulation effect in transition metal dichalcogenide heterobilayers. *1902424*, 15:C39, 2019. doi: 10.1002/smll.201902424.

[54] Liheng Zheng, Zhixin Liu, Donglin Liu, Xingguo Wang, Yu Li, Meiling Jiang, Feng Lin, Han Zhang, Bo Shen, Xing Zhu, Yongji Gong, and Zheyu Fang. Deep subwavelength control of valley polarized cathodoluminescence in h-BN/WSe_2/h-BN heterostructure. *Nat. Commun.*, 12:291, 2021. doi: 10.1038/s41467-020-20545-x.

[55] Wang G., Marie X., Gerber I., Amand T., Lagarde D., Bouet L., Vidal M., Balocchi A., and Urbaszek B. Giant enhancement of the optical second-harmonic emission of WSe_2 monolayers by laser excitation at exciton resonances. *Phys. Rev. Lett.*, 114:097403, 2015. doi: 10.1103/PhysRevLett.114.097403.

[56] J.C. Meyer, A.K. Geim, M.I. Katsnelson, K.S. Novoselov, D. Obergfell, S. Roth, C. Girit, and A. Zettl. On the roughness of single- and bi-layer graphene membranes. *Solid State Commun*, 143:101–109, 2007. doi: 10.1016/j.ssc.2007.02.047.

[57] Beidou Guo, Baohong Zhang Liang Fang and, and Jianru Gong. Graphene doping: a review. *Insciences*, 1:80–89, 2011. doi: 10.5640/insc.010280.

[58] U. Fano. Effects of configuration interaction on intensities and phase shifts. *Phys. Rev.*, 124:1866–1878, 1961. doi: 10.1103/PhysRev.124.1866.

[59] Yong S Joe, Arkady M Satanin, and Chang Sub Kim. Classical analogy of fano resonances. *Phys. Scr.*, 74:259–266, 2006. doi: 10.1088/0031-8949/74/2/020.

[60] Mingsong Wang, Alex Krasnok, Tianyi Zhang, Leonardo Scarabelli, He Liu, Zilong Wu, Luis M. Liz-Marzán, Mauricio Terrones, Andrea Alù, and Yuebing Zheng. Tunable fano resonance and plasmon–exciton coupling in single au nanotriangles on monolayer WS_2 at room temperature. *Adv. Mater.*, 30:1705779, 2018. doi: 10.1002/adma.201705779.

[61] Bumsu Lee, Joohee Park, Gang Hee Han, Ho-Seok Ee, Carl H. Naylor, Wenjing Liu, A.T. Charlie Johnson, and Ritesh Agarwal. Fano resonance and spectrally modified photoluminescence enhancement in monolayer MoS_2 integrated with plasmonic nanoantenna array. *Nano Lett.*, 15:3646–3653, 2015. doi: 10.1021/acs.nanolett.5b01563.

[62] Wei Zhang, Alexander O. Govorov, and Garnett W. Bryant. Semiconductor-metal nanoparticle molecules: hybrid excitons and non-linear fano effect. *Phys. Rev. Lett.*, 97: 146804, 2006. doi: 10.1103/PhysRevLett.97.146804.

[63] A. Raja, A. Chaves, J. Yu, G. Arefe, H. M. Hill, A. F. Rigosi, T. C. Berkelbach, P. Nagler, C. Schüller, T. Korn, C. Nuckolls, J. Hone, L. E. Brus, T.F. Heinz, D. R. Reichman, and A. Chernikov. Coulomb engineering of the bandgap and excitons in two-dimensional materials. *Nat. Commun.*, 8:15251, 2017. doi: 10.1038/ncomms15251.

[64] G. Froehlicher, E. Lorchat, and S. Berciaud. Charge versus energy transfer in atomically thin graphene-transition metal dichalcogenide van der Waals heterostructures. *Phys. Rev. X*, 8:011007, 2018. doi: 10.1103/PhysRevX.8.011007.

[65] Phan Thi Kim Loan, Wenjing Zhang, Cheng-Te Lin, Kung-Hwa Wei, Lain-Jong Li, and Chang-Hsiao Chen. Graphene/MoS_2 heterostructures for ultrasensitive detection of DNA hybridisation. *Adv. Mater.*, 26:4838–4844, 2014. doi: 10.1002/adma.201401084.

[66] Alexandre Gloter, Vincent Badjeck, Laura Bocher, Nathalie Brun, Katia March, Maya Marinova, Marcel Tencé, Michael Walls, Alberto Zobelli, Odile Stéphan, and Christian Colliex. Atomically resolved mapping of EELS fine structures. *Mater Sci Semicond Process*, 65:2–17, 2017. doi: 10.1016/j.mssp.2016.07.006.

[67] Hans Paetz gen. Schieck. *Key Nuclear Reaction Experiments*. IOP, 2015. doi: 10.1088/978-0-7503-1173-1.

[68] Ray F. Egerton. Electron energy-loss spectroscopy in the tem. *Reports on Progress in Physics*, 72:1–25, 2008. doi: 10.1088/0953-8984/27/31/315301.

[69] Steven H. Simon. *The Oxford solid state basics*. OUP Oxford, 2013. ISBN 978-0-19-968077-1 978-0-19-968076-4.

[70] Mark Fox. *Optical properties of solids*. Oxford University Press, 2010. ISBN 978-0-19-957336-3 978-0-19-957337-0.

[71] R.F. Egerton. *Electron Energy-Loss Spectroscopy in the Electron Microscope*. Springer, 2011. doi: 10.1007/978-1-4419-9583-4.

[72] Hennyz sample holder. URL `http://www.hennyz.com/`.

[73] Direct electron and pixel detector: MerlinEM (quantum detectors). URL `https://quantumdetectors.com`.

[74] Z.L. Wang and J.M. Cowley. Simulating high-angle annular dark-field stem images including inelastic thermal diffuse scattering. *Ultramicroscopy*, 31:437–453, 1989. doi: 10.1016/0304-3991(89)90340-9.

[75] David B Williams and C Barry Carter. *Transmission electron microscopy*. Springer, 2009. doi: 10.1007/978-0-387-40093-8.

[76] Earl J. Kirkland. *Advanced computing in electron microscopy*. Springer Nature, 2010. doi: 10.1007/978-1-4419-6533-2.

[77] Yuanyuan Zhu, Colin Ophus, Jim Ciston, and Haiyan Wang. Interface lattice displacement measurement to 1pm by geometric phase analysis on aberration-corrected HAADF stem images. *Acta Mater.*, 61:5646–5663, 2013. doi: 10.1016/j.actamat.2013.06.006.

[78] Martin J. Hÿtch and Andrew M. Minor. Observing and measuring strain in nanostructures and devices with transmission electron microscopy. *MRS Bull.*, 39:138–146, 2014. doi: 10.1557/mrs.2014.4.

[79] M.J. Hÿtch, E. Snoeck, and R. Kilaas. Quantitative measurement of displacement and strain fields from HREM micrographs. *Ultramicroscopy*, 74:131–146, 1998. doi: 10.1016/S0304-3991(98)00035-7.

[80] A. Béché, J.L. Rouvière, J.P. Barnes, and D. Cooper. Strain measurement at the nanoscale: comparison between convergent beam electron diffraction, nano-beam electron diffraction, high resolution imaging and dark field electron holography. *Ultramicroscopy*, 131: 10–23, 2013. doi: 10.1016/j.ultramic.2013.03.014.

[81] Humboldt-Universität zu Berlin. QSTEM: Quantitative TEM/STEM simulations, 2017. URL `https://www.physik.hu-berlin.de/en/sem/software/software_qstem`.

[82] Christoph Tobias Koch. *Determination of core structure periodicity and point defect density along dislocations*. Thesis (Ph.D.) Arizona State University, 2002.

[83] Toma Susi Jacob Madsen. The abTEM code: transmission electron microscopy from first principles. *Open Research Europe*, 2021. doi: 10.12688/openreseurope.13015.1.

[84] Ask Hjorth Larsen, Jens Jørgen Mortensen, Jakob Blomqvist, Ivano E. Castelli, and et al. Christensen. The atomic simulation environment—a Python library for working with atoms. *J. Phys. Condens. Matter*, 29:273002, 2017. doi: 10.1088/1361-648X/aa680e.

[85] K3 cameras: the new imaging performance benchmark for direct detection cameras., Gatan. URL `https://www.gatan.com/products/tem-imaging-spectroscopy/k3-cameras`.

[86] Francisco de la Peña, Tomas Ostasevicius, Vidar Tonaas Fauske, Pierre Burdet, Petras Jokubauskas, Mike Sarahan, Duncan Johnstone, Magnus Nord, Josh Taillon, Jan Caron, and et al. Hyperspy. *Zenodo*, 2016. doi: 10.5281/zenodo.60697.

[87] EELS Spectrum, Practical Electron Microscopy and Database. URL https://www.globalsino.com/EM/page4780.html.

[88] Ondrej L Krivanek, Tracy C Lovejoy, Matthew F Murfitt, Gwyn Skone, Philip E Batson, and Niklas Dellby. Towards sub-10 mev energy resolution STEM-EELS. *J Phys Conf Ser*, 522:012023, 2014. doi: 10.1088/1742-6596/522/1/012023.

[89] Marian Mankos, Khashayar Shadman, and Vladimir Kolarik. Novel electron monochromator for high resolution imaging and spectroscopy. *J. Vac. Sci. Technol. B*, 34, 2016. doi: 10.1116/1.4962383.

[90] T. Malis, S. C. Cheng, and R. F. Egerton. EELS log-ratio technique for specimen-thickness measurement in the TEM. *Journal of Electron Microscopy Technique*, 8:193–200, 1988. doi: 10.1002/jemt.1060080206.

[91] Wavelength of electron, JEOL. URL https://www.jeol.co.jp/en/words/emterms/search_result.html?keyword=wavelength+of+electron.

[92] Jonas Lähnemann; Jordi Ferrer Orri; Eric Prestat; Duncan N. Johnstone; Nicolas Tappy. Lumispy. *Zenodo*, 2022. doi: 10.5281/zenodo.6506534.

[93] Andres Castellanos-Gomez, Michele Buscema, Rianda Molenaar, Vibhor Singh, Laurens Janssen, Herre S J van der Zant, and Gary A Steele. Deterministic transfer of two-dimensional materials by all-dry viscoelastic stamping. *2D Mater.*, 1:011002, 2014. doi: 10.1088/2053-1583/1/1/011002.

[94] D. G. Purdie, N. M. Pugno, T. Taniguchi, K. Watanabe, A. C. Ferrari, and A. Lombardo. Cleaning interfaces in layered materials heterostructures. *Nat. Commun.*, 9:5387, 2018. doi: 10.1038/s41467-018-07558-3.

[95] Sujay B. Desai, Surabhi R. Madhvapathy, Matin Amani, Daisuke Kiriya, Mark Hettick, Mahmut Tosun, Yuzhi Zhou, Madan Dubey, Joel W. Ager, Daryl Chrzan, and et al. Gold-mediated exfoliation of ultralarge optoelectronically-perfect monolayers. *Adv. Mater.*, 28: 4053–4058, 2016. doi: 10.1002/adma.201506171.

[96] Matthew A. Meitl, Zheng-Tao Zhu, Vipan Kumar, Keon Jae Lee, Xue Feng, Yonggang Y. Huang, Ilesanmi Adesida, Ralph G. Nuzzo, and John A. Rogers. Transfer printing by kinetic control of adhesion to an elastomeric stamp. *Nat. Mater.*, 5:33–38, 2006. doi: 10.1038/nmat1532.

[97] Glass transition temperatures. URL https://polymerdatabase.com.

[98] Rieger Bernhard, Künkel Andreas, Geoffrey W. Coates, Reichardt Robert, Dinjus Eckhard, and Thomas A. Zevaco. *Synthetic biodegradable polymers*. Springer, 2012. doi: 10.1007/122011126.

[99] P. J. Zomer, M. H. D. Guimarães, J. C. Brant, N. Tombros, and B. J. van Wees. Fast pick up technique for high quality heterostructures of bilayer graphene and hexagonal boron nitride. *Appl. Phys. Lett.*, 105:013101, 2014. doi: 10.1063/1.4886096.

[100] Alexander S. Mayorov, Roman V. Gorbachev, Sergey V. Morozov, Liam Britnell, Rashid Jalil, Leonid A. Ponomarenko, Peter Blake, Kostya S. Novoselov, Kenji Watanabe, Takashi Taniguchi, and A. K. Geim. Micrometer-scale ballistic transport in encapsulated graphene at room temperature. *Nano Lett.*, 11:2396–2399, 2011. doi: 10.1021/nl200758b.

[101] Cory R Dean, Andrea F Young, Inanc Meric, Chris Lee, Lei Wang, Sebastian Sorgenfrei, Kenji Watanabe, Takashi Taniguchi, Phillip Kim, Kenneth L Shepard, and Hone J. Boron nitride substrates for high-quality graphene electronics. *Nat. Nanotechol.*, 5:722–726, 2010.

doi: 10.1038/nnano.2010.172.

[102] Filippo Pizzocchero, Lene Gammelgaard, Bjarke S. Jessen, José M. Caridad, Lei Wang, James Hone, Peter Bøggild, and Timothy J. Booth. The hot pick-up technique for batch assembly of van der waals heterostructures. *Nat. Commun.*, 7:11894, 2016. doi: 10.1038/ncomms11894.

[103] L. Wang, I. Meric, P. Y. Huang, Q. Gao, Y. Gao, H. Tran, T. Taniguchi, K. Watanabe, L. M. Campos, D. A. Muller, J. Guo, P. Kim, J. Hone, K. L. Shepard, and C. R. Dean. One-Dimensional Electrical Contact to a Two-Dimensional Material. *Science*, 342:614–617, 2013. doi: 10.1126/science.1244358.

[104] Yuto Anzai, Mahito Yamamoto, Shingo Genchi, Kenji Watanabe, Takashi Taniguchi, Shuhei Ichikawa, Yasufumi Fujiwara, and Hidekazu Tanaka. Broad range thickness identification of hexagonal boron nitride by colors. *Appl. Phys. Express*, 12:055007, 2019. doi: 10.7567/1882-0786/ab0e45.

[105] Hai Li, Jumiati Wu, Xiao Huang, Gang Lu, Jian Yang, Xin Lu, Qihua Xiong, and Hua Zhang. Rapid and reliable thickness identification of Two-Dimensional nanosheets using optical microscopy. *ACS Nano*, 7:10344–10353, 2013. doi: 10.1021/nn4047474.

[106] A Castellanos-Gomez, N Agraït, and G Rubio-Bollinger. Optical identification of atomically thin dichalcogenide crystals. *Appl. Phys. Lett.*, 96:213116, 2010. doi: 10.1063/1.3442495.

[107] S. Roddaro, P. Pingue, V. Piazza, V. Pellegrini, and F. Beltram. The optical visibility of graphene: interference colors of ultrathin graphite on sio$_2$. *Nano Lett.*, 7:2707–2710, 2007. doi: 10.1021/nl071158l.

[108] P. Blake, K. S. Novoselov, A. H. Castro Neto, D. Jiang, R. Yang, T. J. Booth, A. K. Geim, and E. W. Hill. Making graphene visible. *Appl. Phys. Lett.*, 91:063124, 2007. doi: 10.1063/1.2768624.

[109] Iacopi Francesca, Boeckl John, and Jagadish Chennupati. *2D Materials*. Elsevier, 2016. ISBN 978-0-12-804272-4.

[110] Xue Bai Xiaofei Zhou, Hainan Sun. *Two dimensional transition metal dichalcogenides: synthesis, properties, and applications*. Springer, 2019. ISBN 9789811390449 9789811390456. doi: 10.1007/978-981-13-9045-6.

[111] K S Novoselov, D Jiang, F Schedin, T J Booth, V V Khotkevich, S V Morozov, and A K Geim. Two-dimensional atomic crystals. *Proc. Natl. Acad. Sci. U.S.A.*, page 3, 2015. doi: 10.1073/pnas.0502848102.

[112] Yumeng Shi, Li Henan, and Li Lain-Jong. Recent advances in controlled synthesis of two-dimensional transition metal dichalcogenides via vapour deposition techniques. *Chem. Soc. Rev.*, 44, 2015. doi: 10.1039/C4CS00256C.

[113] Ji Won Suk, Alexander Kitt, Carl W. Magnuson, Yufeng Hao, Samir Ahmed, Jinho An, Anna K. Swan, Bennett B. Goldberg, and Rodney S. Ruoff. Transfer of CVD-grown monolayer graphene onto arbitrary substrates. *ACS Nano*, 5:6916–6924, 2011. doi: 10.1021/nn201207c.

[114] Yuan Huang, Yu-Hao Pan, Rong Yang, Li-Hong Bao, Lei Meng, Hai-Lan Luo, Yong-Qing Cai, Guo-Dong Liu, Wen-Juan Zhao, Zhang Zhou, Liang-Mei Wu, Zhi-Li Zhu, Ming Huang, Li-Wei Liu, Lei Liu, Peng Cheng, Ke-Hui Wu, Shi-Bing Tian, Chang-Zhi Gu, You-Guo Shi, Yan-Feng Guo, Zhi Gang Cheng, Jiang-Ping Hu, Lin Zhao, Guan-Hua Yang, Eli Sutter, Peter Sutter, Ye-Liang Wang, Wei Ji, Xing-Jiang Zhou, and Hong-Jun Gao. Universal mechanical exfoliation of large-area 2D crystals. *Nat. Commun.*, 11:2453, 2020. doi: 10.1038/s41467-020-16266-w.

[115] David Nelson, Tsvi Piran, and Steven Weinberg. *Statistical Mechanics Of Membranes And*

Surfaces. World Scientific, 2004. doi: 10.1142/5473.

[116] P. M. Chaikin and T. C. Lubensky. *Principles of Condensed Matter Physics*. Cambridge University Press, 1995. doi: 10.1017/CBO9780511813467.

[117] Zhiping Xu and Markus J. Buehler. Geometry controls conformation of graphene sheets: Membranes, ribbons, and scrolls. *ACS Nano*, 4:3869–3876, 2010. doi: 10.1021/nn100575k.

[118] A. Fasolino, J. H. Los, and M. I. Katsnelson. Intrinsic ripples in graphene. *Nat. Mater.*, 6: 858–861, 2017. doi: 10.1038/nmat2011.

[119] Mieko Takagi. Electron-diffraction study of liquid-solid transition of thin metal films. *J. Phys. Soc. Jpn.*, 9:359–363, 1954. doi: 10.1143/JPSJ.9.359.

[120] DA Kirilenko, AT Dideykin, and G Van Tendeloo. Measuring the corrugation amplitude of suspended and supported graphene. *Phys. Rev. B*, 84:235417, 2011. doi: 10.1103/PhysRevB.84.235417.

[121] A. Zugarramurdi, M. Debiossac, P. Lunca-Popa, A. J. Mayne, A. Momeni, A. G. Borisov, Z. Mu, P. Roncin, and H. Khemliche. Determination of the geometric corrugation of graphene on SiC(0001) by grazing incidence fast atom diffraction. *Appl. Phys. Lett.*, 106: 101902, 2015. doi: 10.1063/1.4914178.

[122] Carsten Busse, Predrag Lazić, Rabie Djemour, Johann Coraux, Timm Gerber, Nicolae Atodiresei, Vasile Caciuc, Radovan Brako, Alpha T. N'Diaye, Stefan Blügel, Jörg Zegenhagen, and Thomas Michely. Graphene on Ir(111): physisorption with chemical modulation. *Phys. Rev. Lett.*, 107:036101, 2011. doi: 10.1103/PhysRevLett.107.036101.

[123] Chun Hung Lui, Li Liu, Kin Fai Mak, George W. Flynn, and Tony F. Heinz. Ultraflat graphene. *Nature*, 462:339–341, 2009. doi: 10.1038/nature08569.

[124] Zhao Deng, Nikolai N. Klimov, Santiago D. Solares, Teng Li, Hua Xu, and Rachel J. Cannara. Nanoscale interfacial friction and adhesion on supported versus suspended monolayer and multilayer graphene. *Langmuir*, 29:235–243, 2013. doi: 10.1021/la304079a.

[125] Jannik C. Meyer, C. O. Girit, M. F. Crommie, and A. Zettl. Hydrocarbon lithography on graphene membranes. *Appl. Phys. Lett.*, 92:123110, 2008. doi: 10.1063/1.2901147.

[126] Shanshan Chen, Arden L. Moore, Weiwei Cai, Ji Won Suk, Jinho An, Columbia Mishra, Charles Amos, Carl W. Magnuson, Junyong Kang, Li Shi, and Rodney S. Ruoff. Raman measurements of thermal transport in suspended monolayer graphene of variable sizes in vacuum and gaseous environments. *ACS Nano*, 5:321–328, 2011. doi: 10.1021/nn102915x.

[127] Sergey Mikhailov. *Physics and applications of graphene*. InTech, 2011. doi: 10.5772/590.

[128] Kin Fai Mak, Changgu Lee, James Hone, Jie Shan, and Tony F. Heinz. Atomically thin MoS_2: A new direct-gap semiconductor. *Phys. Rev. Lett.*, 105:136805, 2010. doi: 10.1103/PhysRevLett.105.136805.

[129] Alejandro Molina-Sánchez, Kerstin Hummer, and Ludger Wirtz. Vibrational and optical properties of MoS_2: from monolayer to bulk. *Surf. Sci. Rep.*, 70:554–586, 2015. doi: 10.1016/j.surfrep.2015.10.001.

[130] Zhiming M. Wang, editor. *MoS_2: Materials, Physics, and Devices*. Springer, 2014. doi: 10.1007/978-3-319-02850-7.

[131] Anubhav Jain, Shyue Ping Ong, Geoffroy Hautier, Wei Chen, William Davidson Richards, Stephen Dacek, Shreyas Cholia, Dan Gunter, David Skinner, Gerbrand Ceder, and Kristin A. Persson. Commentary: The Materials Project: A materials genome approach to accelerating materials innovation. *APL Mater.*, 1:011002, 2013. doi: 10.1063/1.4812323.

[132] Darshana Wickramaratne, Leigh Weston, and Chris G. Van de Walle. Monolayer to bulk properties of hexagonal boron nitride. *J. Phys. Chem. C*, 122:25524–25529, 2018. doi:

10.1021/acs.jpcc.8b09087.

[133] K. S. Novoselov, A. K. Geim, S. V. Morozov, D. Jiang, Y. Zhang, S. V. Dubonos, I. V. Grigorieva, and A. A. Firsov. Electric field effect in atomically thin carbon films. *Science*, 306: 666–669, 2004. doi: 10.1126/science.1102896.

[134] Yenny Hernandez, Valeria Nicolosi, Mustafa Lotya, Fiona M. Blighe, Zhenyu Sun, Sukanta De, I. T. McGovern, Brendan Holland, Michele Byrne, Yurii K. Gun'Ko, John J. Boland, Peter Niraj, Georg Duesberg, Satheesh Krishnamurthy, Robbie Goodhue, John Hutchison, Vittorio Scardaci, Andrea C. Ferrari, and Jonathan N. Coleman. High-yield production of graphene by liquid-phase exfoliation of graphite. *Nat. Nanotechnol.*, 3:563–568, 2008. doi: 10.1038/nnano.2008.215.

[135] A. K. Geim and I. V. Grigorieva. Van der waals heterostructures. *Nature*, 499:419–425, 2013. doi: 10.1038/nature12385.

[136] Zhongwei Dai, Wencan Jin, Maxwell Grady, Jerzy T Sadowski, Jerry I Dadap, Richard M Osgood Jr, and Karsten Pohl. Surface structure of bulk 2H-MoS_2 (0001) and exfoliated suspended monolayer MoS_2. *Surf Sci*, 660:16–21, 2017. doi: 10.1016/j.susc.2017.02.005.

[137] Koichi Momma and Fujio Izumi. VESTA 3 for three-dimensional visualization of crystal, volumetric and morphology data. *J Appl Crystallogr*, 44:1272–1276, 2011. doi: 10.1107/S0021889811038970.

[138] Pratiti Deb, Michael C. Cao, Yimo Han, Megan E. Holtz, Saien Xie, Jiwoong Park, Robert Hovden, and David A. Muller. Imaging polarity in two dimensional materials by breaking Friedel's law. *Ultramicroscopy*, 215:113019, 2020. doi: 10.1016/j.ultramic.2020.113019.

[139] Jian Min Zuo and John C. H. Spence. *Advanced Transmission Electron Microscopy*. Springer, 2017. doi: 10.1007/978-1-4939-6607-3_13.

[140] J. M. Cowley. *Diffraction Physics*. Elsevier, 1995. ISBN 978-0-444-82218-5. doi: 10.1016/B978-0-444-82218-5.X5000-7.

[141] Ashish Arora, Thorsten Deilmann, Till Reichenauer, Johannes Kern, Steffen Michaelis de Vasconcellos, Michael Rohlfing, and Rudolf Bratschitsch. Excited-state trions in monolayer WS_2. *Phys. Rev. Lett.*, 123:167401, 2019. doi: 10.1103/PhysRevLett.123.167401.

[142] Lei Wang, Zheyuan Chen, Cory R Dean, Takashi Taniguchi, Kenji Watanabe, Louis E. Brus, and James Hone. Negligible environmental sensitivity of graphene in a hexagonal boron nitride/graphene/h-BN sandwich structure. *ACS Nano*, 6:9314–9319, 2012. doi: 10.1021/nn304004s.

[143] Maxim A Stolyarov, Guanxiong Liu, Sergey L Rumyantsev, Michael Shur, and Alexander A Balandin. Suppression of 1/f noise in near-ballistic h-BN-graphene-h-BN heterostructure field-effect transistors. *Appl. Phys. Lett.*, 107:023106, 2015. doi: 10.1063/1.4926872.

[144] Joo Han Kim and Ki Woong Chung. Microstructure and properties of silicon nitride thin films deposited by reactive bias magnetron sputtering. *J. Appl. Phys.*, 83:5831, 1998. doi: 10.1063/1.367440.

[145] Duhee Yoon, Young-Woo Son, and Hyeonsik Cheong. Negative thermal expansion coefficient of graphene measured by raman spectroscopy. *Nano Lett.*, 11:3227–3231, 2011. doi: 10.1021/nl201488g.

[146] Wenzhong Bao, Kevin Myhro, Zeng Zhao, Zhen Chen, Wanyoung Jang, Lei Jing, Feng Miao, Hang Zhang, Chris Dames, Chun Ning Lau, and et al. In situ observation of electrostatic and thermal manipulation of suspended graphene membranes. *Nano Lett.*, 12: 5470–5474, 2012. doi: 10.1021/nl301836q.

[147] Vibhor Singh, Shamashis Sengupta, Hari S Solanki, Rohan Dhall, Adrien Allain, Sajal

Dhara, Prita Pant, and Mandar M Deshmukh. Probing thermal expansion of graphene and modal dispersion at low-temperature using graphene nanoelectromechanical systems resonators. *Nanotechnology*, 21:165204, 2010. doi: 10.1088/0957-4484/21/16/165204.

[148] Lenan Zhang, Zhengmao Lu, Youngsup Song, Lin Zhao, Bikram Bhatia, Kevin R. Bagnall, and Evelyn N. Wang. Thermal expansion coefficient of monolayer molybdenum disulfide using micro-raman spectroscopy. *Nano Lett.*, 19:4745–4751, 2019. doi: 10.1021/acs.nanolett.9b01829.

[149] Rui Zhang, Vasileios Koutsos, and Rebecca Cheung. Elastic properties of suspended multilayer WSe_2. *Appl. Phys. Lett.*, 108:042104, 2016. doi: 10.1063/1.4940982.

[150] Andrea Splendiani, Liang Sun, Yuanbo Zhang, Tianshu Li, Jonghwan Kim, Chi-Yung Chim, Giulia Galli, and Feng Wang. Emerging photoluminescence in monolayer MoS_2. *Nano Lett.*, 10:1271–1275, 2010. doi: 10.1021/nl903868w.

[151] Yunjeong Hwang, Taehun Kim, and Naechul Shin. Interlayer energy transfer and photoluminescence quenching in $MoSe_2$/graphene van der Waals heterostructures for optoelectronic devices. *ACS Appl. Nano Mater*, 4:9, 2021. doi: 10.1021/acsanm.1c02599.

[152] Solid state physics ii, MIT. URL `https://web.mit.edu/6.732/www/texts.html`.

[153] H. Sahin, S. Tongay, S. Horzum, W. Fan, J. Zhou, J. Li, J. Wu, and F. M. Peeters. Anomalous raman spectra and thickness dependent electronic properties of WSe_2. *Phys. Rev. B*, 87: 165409, 2013. doi: 10.1103/PhysRevB.87.165409.

[154] Alex Krasnok, Sergey Lepeshov, and Andrea Alú. Nanophotonics with 2D transition metal dichalcogenides. *Opt. Express*, 26, 2015. doi: 10.1364/OE.26.015972.

[155] Helena Bragança, Fanyao Qu Flávio Riche, Victor Lopez-Richard, and Gilmar Eugenio Marques. Dark-exciton valley dynamics in transition metal dichalcogenide alloy monolayers. *Sci. Rep.*, 9:4575, 2019. doi: 10.1038/s41598-019-40932-9.

[156] M. Bayer and A. Forchel. Temperature dependence of the exciton homogeneous linewidth in in0.6ga0.4as/GaAs self-assembled quantum dots. *Phys. Rev. B*, 65:041308, 2002. doi: 10.1103/PhysRevB.65.041308.

[157] Alexey Chernikov, Timothy C Berkelbach, Heather M Hill, Albert Rigosi, Yilei Li, Ozgur Burak Aslan, David R Reichman, Mark S Hybertsen, and Tony F Heinz. Exciton binding energy and nonhydrogenic rydberg series in monolayer WS_2. *Phys. Rev. Lett.*, 113: 076802, 2014. doi: 10.1103/PhysRevLett.113.076802.

[158] David K. Zhang, Daniel W. Kidd, and Kalman Varga. Excited biexcitons in transition metal dichalcogenides. *Nano Lett.*, 15:7002–7005, 2015. doi: 10.1021/acs.nanolett.5b03009.

[159] Kristian Sommer Thygesen. Calculating excitons, plasmons, and quasiparticles in 2D materials and van der Waals heterostructures. *2D Mater.*, 4:022004, 2017. doi: 10.1088/2053-1583/aa6432.

[160] Michele Cotrufo, Junho Choi Liuyang Sun, Andrea Alù, and Xiaoqin Li. Enhancing functionalities of atomically thin semiconductors with plasmonic nanostructures. *Nanophotonics*, 8:577–598, 2019. doi: 10.1515/nanoph-2018-0185.

[161] Archana Raja, Andrey Chaves, Jaeeun Yu, Ghidewon Arefe, Heather M. Hill, Albert F. Rigosi, Timothy C. Berkelbach, Philipp Nagler, Christian Schüller, Tobias Korn, Colin Nuckolls, James Hone, Louis E. Brus, Tony F. Heinz, David R. Reichman, and Alexey Chernikov. Coulomb engineering of the bandgap and excitons in two-dimensional materials. *Nat. Commun.*, 8:15251, 2017. doi: 10.1038/ncomms15251.

[162] M V Durnev and M M Glazov. Excitons and trions in two-dimensional semiconductors based on transition metal dichalcogenides. *Physics-Uspekhi*, 61:22, 2018. doi: 10.3367/UFNr.2017.07.038172.

[163] Zhipeng Li, Tianmeng Wang, Zhengguang Lu, Chenhao Jin, Yanwen Chen, Yuze Meng, Zhen Lian, Takashi Taniguchi, Kenji Watanabe, Shengbai Zhang, Dmitry Smirnov, and Su-Fei Shi. Revealing the biexciton and trion-exciton complexes in BN encapsulated WSe_2. *Nat. Commun.*, 9:3719, 2018. doi: 10.1038/s41467-018-05863-5.

[164] Akshay Singh, Galan Moody, Kha Tran, Marie E. Scott, Vincent Overbeck, Gunnar Berghäuser, John Schaibley, Edward J. Seifert, Dennis Pleskot, Nathaniel M. Gabor, Jiaqiang Yan, David G. Mandrus, Marten Richter, Ermin Malic, Xiaodong Xu, and Xiaoqin Li. Trion formation dynamics in monolayer transition metal dichalcogenides. *Phys. Rev. B*, 93:041401, 2016. doi: 10.1103/PhysRevB.93.041401.

[165] Timothy C. Berkelbach, Mark S. Hybertsen, and David R. Reichman. Theory of neutral and charged excitons in monolayer transition metal dichalcogenides. *Phys. Rev. B*, 88: 045318, 2013. doi: 10.1103/PhysRevB.88.045318.

[166] Changjian Zhang, Haining Wang, Weimin Chan, Christina Manolatou, and Farhan Rana. Absorption of light by excitons and trions in monolayers of metal dichalcogenide MoS_2: experiments and theory. *Phys. Rev. B*, 89:205436, 2014. doi: 10.1103/PhysRevB.89.205436.

[167] Mark Fox. *Quantum Optics*. Oxford University Press, 2006. ISBN 0–19–856672–7.

[168] O. Scully Marlan and Zubairy Scully, M. Suhail. *Quantum Optics*. Cambridge University Press, 1997. doi: 10.1017/CBO9780511813993.

[169] Galan Moody, John Schaibley, and Xiaodong Xu. Exciton dynamics in monolayer transition metal dichalcogenides. *J Opt Soc Am*, 33:C39, 2016. doi: 10.1364/JOSAB.33.000C39.

[170] Galan Moody, Chandriker Kavir Dass, Kai Hao, Chang-Hsiao Chen, Lain-Jong Li, Akshay Singh, Kha Tran, Genevieve Clark, Xiaodong Xu, Gunnar Berghäuser, Ermin Malic, Andreas Knorr, and Xiaoqin Li. Intrinsic homogeneous linewidth and broadening mechanisms of excitons in monolayer transition metal dichalcogenides. *Nat. Commun.*, page 8315, 2015-11. doi: 10.1038/ncomms9315.

[171] C. Poellmann, P. Steinleitner, U. Leierseder, P. Nagler, G. Plechinger, M. Porer, R. Bratschitsch, C. Schüller, T. Korn, and R. Huber. Resonant internal quantum transitions and femtosecond radiative decay of excitons in monolayer WSe_2. *Nat. Mater.*, 14:889–893, 2015. doi: 10.1038/nmat4356.

[172] Sandhaya Koirala, Shinichiro Mouri, Yuhei Miyauchi, and Kazunari Matsuda. Homogeneous linewidth broadening and exciton dephasing mechanism in $MoTe_2$. *Phys. Rev. B*, 93:075411, 2016. doi: 10.1103/PhysRevB.93.075411.

[173] Tomasz Jakubczyk, Valentin Delmonte, Maciej Koperski, Karol Nogajewski, Clément Faugeras, Wolfgang Langbein, Marek Potemski, and Jacek Kasprzak. Radiatively limited dephasing and exciton dynamics in $MoSe_2$ monolayers revealed with four-wave mixing microscopy. *Nano Lett.*, 16:5333–5339, 2016. doi: 10.1021/acs.nanolett.6b01060.

[174] Mario Pelaez-Fernandez, Yung-Chang Lin, and Kazu Suenaga andRaul Arenal. Optoelectronic properties of atomically thin $Mo_xW_{(1-x)}S_2$ nanoflakes probed by spatially-resolved monochromated eels. *Nanomaterials*, 11:1–17, 2021. doi: 10.3390/nano11123218.

[175] Diana Y. Qiu, Felipe H. da Jornada, and Steven G. Louie. Optical spectrum of MoS_2: many-body effects and diversity of exciton states. *Phys. Rev. Lett.*, 111:216805, 2013. doi: 10.1103/PhysRevLett.111.216805.

[176] Luiz Henrique Galvão Tizei, Hugo Lourenço-Martins, Pabitra Das, Steffi Y Woo, Leonardo Scarabelli, Christoph Hanske, Luis M Liz-Marzán, Kenji Watanabe, Takashi Taniguchi, and Mathieu Kociak. Monolayer and thin h-BN as substrates for electron spectromicroscopy analysis of plasmonic nanoparticles. *Appl. Phys. Lett.*, 113:231108, 2018. doi: 10.1063/1.5054751.

[177] Mei Yin Chan, Katsuyoshi Komatsu, Song-Lin Li, Yong Xu, Peter Darmawan, Hiromi Ku-

ramochi, Shu Nakaharai, Alex Aparecido-Ferreira, Kenji Watanabe, Takashi Taniguchi, and Kazuhito Tsukagoshi. Suppression of thermally activated carrier transport in atomically thin MoS_2 on crystalline hexagonal boron nitride substrates. *Nanoscale*, 5:9572–9576, 2013. doi: 10.1039/C3NR03220E.

[178] Freddie Withers, Thomas Hardisty Bointon, David Christopher Hudson, Monica Felicia Craciun, and Saverio Russo. Electron transport of WS_2 transistors in a hexagonal boron nitride dielectric environment. *Sci. Rep.*, 4:4967, 2014. doi: 10.1038/srep04967.

[179] Alwin Daus, Sam Vaziri, Victoria Chen, Çağıl Köroğlu, Ryan W. Grady, Connor S. Bailey, Hye Ryoung Lee, Kirstin Schauble, Kevin Brenner, and Eric Pop. High-performance flexible nanoscale transistors based on transition metal dichalcogenides. *Nat. Electron*, 4: 495–501, 2021. doi: 10.1038/s41928-021-00598-6.

[180] Guangjian Wu, Lan Liu Bobo Tian, Wei Lv, Shuang Wu, Xudong Wang, Yan Chen, Jingyu Li, Zhen Wang, Shuaiqin Wu, Hong Shen, Tie Lin, Peng Zhou, Qi Liu, Chungang Duan, Shantao Zhang, Xiangjian Meng, Shiwei Wu, Weida Hu, Xinran Wang, Junhao Chu, and Jianlu Wang. Programmable transition metal dichalcogenide homojunctions controlled by nonvolatile ferroelectric domains. *Nat. Electron*, 3:43–50, 2020. doi: 10.1038/s41928-019-0350-y.

[181] Abdelkader Abderrahmane, Pan-Gum Jung, Changlim Woo, and Pil Ju Ko. Effect of gate dielectric material on the electrical propertiesof $MoSe_2$-based metal–insulator–semiconductorfield-effect transistor. *Reports on Progress in Physics*, 12:1–7, 2022. doi: 10.3390/cryst12091301.

[182] Yuan Liu, Nathan O. Weiss, Xidong Duan, Hung-Chieh Cheng, Yu Huang, and Xiangfeng Duan. Van der waals heterostructures and devices. *Nat. Rev. Mater.*, 1:1–17, 2006. doi: 10.1038/natrevmats.2016.42.

[183] Saptarshi Das, Amritanand Sebastian, Eric Pop, Connor J. McClellan, Aaron D. Franklin, Tibor Grasser, Theresia Knobloch, Yury Illarionov, Ashish V. Penumatcha, Joerg Appenzeller, Zhihong Chen, Wenjuan Zhu, Inge Asselberghs, Lain-Jong Li, Uygar E. Avci, Navakanta Bhat, Thomas D. Anthopoulos, and Rajendra Singh. Transistors based on two-dimensional materials for future integrated circuits. *Nat. Electron*, 4:786–799, 2021. doi: 110.1038/s41928-021-00670-1.

[184] Changhee Lee, Servin Rathi, Muhammad Atif Khan, Dongsuk Lim, Yunseob Kim, Sun Jin Yun, Doo-Hyeb Youn, Kenji Watanabe, Takashi Taniguchi, and Gil-Ho Kim. Comparison of trapped charges and hysteresis behavior in hBN encapsulated single MoS_2 flake based field effect transistors on SiO_2 and hBN substrates. *Nanotechnology*, 29:1–8, 2018. doi: 10.1088/1361-6528/aac6b0.

[185] Theresia Knobloch, Yury Yu. Illarionov, Christian Schleich Fabian Ducry, Stefan Wachter, Kenji Watanabe, Takashi Taniguchi, Thomas Mueller, Michael Waltl, Mario Lanza, Mikhail I. Vexler, Mathieu Luisier, and Tibor Grasser. The performance limits of hexagonal boron nitride as an insulator for scaled CMOS devices based on two-dimensional materials. *Nat. Electron*, 4:98–108, 2021. doi: 10.1038/s41928-020-00529-x.

[186] Helmut Kohl and Ludwig Reimer. *Transmission Electron Microscopy*. Springer, 2008. doi: 10.1007/978-0-387-40093-8.

[187] Jannik C Meyer, Franz Eder, Simon Kurasch, Viera Skakalova, Jani Kotakoski, Hye Jin Park, Siegmar Roth, Andrey Chuvilin, Sören Eyhusen, Gerd Benner, Krasheninnikov Arkady, and Kaiser Ute. Accurate measurement of electron beam induced displacement cross sections for single-layer graphene. *Phys. Rev. Lett.*, 108:196102, 2012. doi: 10.1103/PhysRevLett.108.196102.

[188] Alexandru Ionut Chirita Mihaila, Toma Susi, and Jani Kotakoski. Influence of temperature on the displacement threshold energy in graphene. *Sci. Rep.*, 9:12981, 2019. doi:

10.1038/s41598-019-49565-4.

[189] Silvan Kretschmer, Tibor Lehnert, Ute Kaiser, and Arkady V. Krasheninnikov. Formation of defects in two-dimensional MoS_2 in the transmission electron microscope at electron energies below the knock-on threshold: the role of electronic excitations. *Nano Lett.*, 20: 2865–2870, 2020. doi: 10.1021/acs.nanolett.0c00670.

[190] Brian W. Smith and David E. Luzzi. Electron irradiation effects in single wall carbon nanotubes. *J. Appl. Phys.*, 90:3509–3515, 2001. doi: 10.1063/1.1383020.

[191] Jani Kotakoski, David Santos-Cottin, and Arkady V Krasheninnikov. Stability of graphene edges under electron beam: equilibrium energetics versus dynamic effects. *ACS Nano*, 6: 671–676, 2012. doi: 10.1021/nn204148h.

[192] Yixuan Zou, Zekun Zhang, Jiawen Yan, Linhan Lin, Guanyao Huang, Yidong Tan, Zheng You, and Peng Li. High-temperature flexible WSe_2 photodetectors with ultrahigh photoresponsivity. *Nat. Commun.*, 13:4972, 2022. doi: 10.1038/s41467-022-32062-0.

[193] Makars Šiškins1, Ciaran Mullan, Seok-Kyun Son, Jun Yin, Kenji Watanabe, Takashi Taniguchi, Davit Ghazaryan, Kostya S. Novoselov, and Artem Mishchenko. High-temperature electronic devices enabled by hBN-encapsulated graphene. *Appl. Phys. Lett.*, 114:123104, 2019. doi: 10.1063/1.5088587.

[194] Xiang Hua, Datong Zhang, Bumho Kim, Dongjea Seo, Kyungnam Kang, Eui-Hyeok Yang, Jiayang Hu, Xianda Chen, Haoran Liang, Kenji Watanabe, Takashi Taniguchi, James Hone, Young Duck Kim, and Irving Herman. Stabilization of chemical-vapor-deposition-grown WS_2 monolayers at elevated temperature with hexagonal boron nitride encapsulation. *ACS Appl. Mater. Interfaces*, 13:31271, 2021. doi: 10.1021/acsami.1c06348.

[195] Martin E. P. Tweedie, Yuewen Sheng, Syed Ghazi Sarwat, Wenshuo Xu, Harish Bhaskaran, and Jamie H. Warner. Inhomogeneous strain release during bending of WS_2 on flexible substrates. *ACS Appl. Mater. Interfaces*, 10:39177–39186, 2018. doi: 10.1021/acsami.8b12707.

[196] Michael K. L. Man, Skylar Deckoff-Jones, Andrew Winchester, Guangsha Shi, Gautam Gupta, Aditya D Mohite, Swastik Kar, Emmanouil Kioupakis, Saikat Talapatra, and Keshav M Dani. Protecting the properties of monolayer MoS_2 on silicon based substrates with an atomically thin buffer. *Sci. Rep.*, 6:20890, 2016. doi: 10.1038/srep20890.

[197] Fuhui Shao, Steffi Y Woo, Nianjheng Wu, Robert Schneider, Andrew J Mayne, Steffen Michaelis de Vasconcellos, Ashish Arora, Benjamin J Carey, Johann A Preuß, Noémie Bonnet, Och Mauro, Mattevi Cecilia, Taniguchi Kenji, Watanabe andTakashi, Niu Zhichuan, Bratschitsch Rudolf, and Tize Luiz. Substrate influence on transition metal dichalcogenide monolayer exciton absorption linewidth broadening. *Phys. Rev. Mater.*, 6: 074005, 2022. doi: 10.1103/PhysRevMaterials.6.074005.

[198] G. Wang, C. Robert, A. Suslu, B. Chen, S. Yang, S. Alamdari, I. C. Gerber, T. Amand, X. Marie, S. Tongay, and B. Urbaszek. Spin-orbit engineering in transition metal dichalcogenide alloy monolayers. *Nat. Commun.*, 6:10110, 2015. doi: 10.1038/ncomms10110.

[199] A.-Y. Lu, H. Zhu, J. Xiao, C.-P. Chuu, Y. Han, M.-H. Chiu, C.-C. Cheng, C.-W. Yang, K.-H. Wei, Y. Yang, Y. Wang, D. Sokaras, D. Nordlund, P. Yang, D. A. Muller, M.-Y. Chou, X. Zhang, and L.-J. Li. Janus monolayers of transition metal dichalcogenides. *Nat. Nanotechnol.*, 12:744–749, 2017. doi: 10.1038/nnano.2017.100.

[200] Ah Ra Kim, Yonghun Kim, Jaewook Nam, Hee-Suk Chung, Dong Jae Kim, Jung-Dae Kwon, Sang Won Park, Jucheol Park, Sun Young Choi, Byoung Hun Lee, Ji Hyeon Park, Kyu Hwan Lee, Dong-Ho Kim, Sung Mook Choi, Pulickel M. Ajayan, Myung Gwan Hahm, and Byungjin Cho. Alloyed 2D metal–semiconductor atomic layer junctions. *Nano Lett.*, 16:1890–1895, 2016. doi: 10.1021/acs.nanolett.5b05036.

[201] Kin Fai Mak, Keliang He, Changgu Lee, Gwan Hyoung Lee, James Hone, Tony F. Heinz, and Jie Shan. Tightly bound trions in monolayer MoS_2. *Nat. Mater.*, 12:207–211, 2013. doi: 10.1038/nmat3505.

[202] Alexey Chernikov, Arend M. van der Zande, Heather M. Hill, Albert F. Rigosi, Ajanth Velauthapillai, James Hone, and Tony F. Heinz. Electrical tuning of exciton binding energies in monolayer WS_2. *Phys. Rev. Lett.*, 115:126802, 2015. doi: 10.1103/PhysRevLett.115.126802.

[203] Keliang He, Charles Poole, Kin Fai Mak, and Jie Shan. Experimental demonstration of continuous electronic structure tuning via strain in atomically thin MoS_2. *Nano Lett.*, 13: 2931–2936, 2013. doi: 10.1021/nl4013166.

[204] R. Schmidt, I. Niehues, R. Schneider, M. Drüppel, T. Deilmann, M. Rohlfing, S. Michaelis de Vasconcellos, A. Castellanos-Gomez, and R. Bratschitsch. Reversible uniaxial strain tuning in atomically thin WSe_2. *2D Mater.*, 3:021011, 2016. doi: 10.1088/2053-1583/3/2/021011.

[205] M. G. Harats, J. N. Kirchhof, M. Qiao, K. Greben, and K. I. Bolotin. Dynamics and efficient conversion of excitons to trions in non-uniformly strained monolayer WS_2. *Nature Photonics*, 14:324–329, 2020. doi: 10.1038/s41566-019-0581-5.

[206] Hongzhi Zhou, Yuzhong Chen, and Haiming Zhu. Deciphering asymmetric charge transfer at transition metal dichalcogenide–graphene interface by helicity-resolved ultrafast spectroscopy. *Sci. Adv.*, 7:eabg2999, 2021. doi: 10.1126/sciadv.abg2999.

[207] Chen Yingying, Liu Zeyi, Li Junze, Cheng Xue, Ma Jiaqi, Wang Haizhen, and Li Dehui. Robust interlayer coupling in two-dimensional perovskite/monolayer transition metal dichalcogenide heterostructures. *ACS Nano*, 14:10258–10264, 2020. doi: 10.1021/acsnano.0c03624.

[208] Ranjit Kashid, Jayanta Kumar Mishra, Avradip Pradhan, Tanweer Ahmed, Saloni Kakkar, Pranav Mundada, Preeti Deshpande, Kallol Roy, Ambarish Ghosh, and Arindam Ghosh. Observation of inter-layer charge transmission resonance at optically excited graphene–TMDC interfaces. *APL Mater.*, 8:091114, 2020. doi: 10.1063/5.0020396.

[209] Recep Zan, Quentin M. Ramasse, Rashid Jalil, Thanasis Georgiou, Ursel Bangert, and Konstantin S. Novoselov. Control of radiation damage in MoS_2 by graphene encapsulation. *ACS Nano*, 7:10167–10174, 2013. doi: 10.1021/nn4044035.

[210] Ashish Arora, Karol Nogajewski, Maciej Molas, Maciej Koperski, and Marek Potemski. Exciton band structure in layered $MoSe_2$: from a monolayer to the bulk limit. *Nanoscale*, 7:20769–20775, 2015. doi: 10.1039/C5NR06782K.

[211] Chengcong Cui, Chaobiao Zhou, Shuai Yuan, Xingzhi Qiu, Liangqiu Zhu, Yuxi Wang, Yi Li, Jinwen Song, Qingzhong Huang, Yi Wang, Cheng Zeng, and Jinsong Xia. Multiple fano resonances in symmetry-breaking silicon metasurface for manipulating light emission. *ACS Photonics*, 5:4074–4080, 2018. doi: 10.1021/acsphotonics.8b00754.

[212] Shanhui Fan. Sharp asymmetric line shapes in side-coupled waveguide-cavity systems. *Appl. Phys. Lett.*, 80:908–910, 2002. doi: 10.1063/1.1448174.

[213] Ora Bitton, Satyendra Nath Gupta, and Gilad Haran. Quantum dot plasmonics: from weak to strong coupling. *Nanophotonics*, 8:559–575, 2019. doi: 10.1515/nanoph-2018-0218.

[214] Yong He and Ka-Di Zhu. Fano effect and quantum entanglement in hybrid semiconductor quantum dot-metal nanoparticle system. *Sensors*, 17:1445, 2017. doi: 10.3390/s17061445.

[215] Byungjun Kang, Kengo Motokura, Minoru Fujii, Dmitry V. Nesterenko, Zouheir Sekkat, and Shinji Hayashi. Observation of Fano line shape in directional fluorescence emission mediated by coupled planar waveguide modes and interpretation based on Lorentz reciprocity. *AIP Adv.*, 10:075302, 2020. doi: 10.1063/5.0010930.

[216] Shanhui Fan and J. D. Joannopoulos. Analysis of guided resonances in photonic crystal slabs. *Phys. Rev. B*, 65:235112, 2002-06-07. doi: 10.1103/PhysRevB.65.235112.

[217] Tsung-Ta Tang, Yuanbo Zhang, Cheol-Hwan Park, Baisong Geng, Caglar Girit, Zhao Hao, Michael C. Martin, Alex Zettl, Michael F. Crommie, Steven G. Louie, Y. Ron Shen, and Feng Wang. A tunable phonon–exciton Fano system in bilayer graphene. *Nat. Nanotechnol.*, 5:32–36, 2010. doi: 10.1038/nnano.2009.334.

[218] John David Jackson. *Classical Electrodynamics*. Wiley, 1999. ISBN 978-0471309321.

[219] F. J. García de Abajo. Multiple excitation of confined graphene plasmons by single free electrons. *ACS Nano*, 7:11409–11419, 2013. doi: 10.1021/nn405367e.

[220] Yilei Li, Alexey Chernikov, Xian Zhang, Albert Rigosi, Heather M. Hill, Arend M. van der Zande, Daniel A. Chenet, En-Min Shih, James Hone, and Tony F. Heinz. Measurement of the optical dielectric function of monolayer transition-metal dichalcogenides: MoS_2, $MoSe_2$, WS_2, and $WSe2_2$. *Phys. Rev. B*, 90:205422, 2014. doi: 10.1103/PhysRevB.90.205422.

[221] Aleksandra B Djurišić and E Herbert Li. Optical properties of graphite. *J. Appl. Phys.*, 85: 8, 1999. doi: 10.1103/PhysRev.138.A197.

[222] Benjamin Gallinet and Olivier J. F. Martin. Influence of electromagnetic interactions on the line shape of plasmonic Fano resonances. *ACS Nano*, 5:8999–9008, 2011. doi: 10.1021/nn203173r.

[223] Benjamin Gallinet and Olivier J. F. Martin. *Ab initio* theory of fano resonances in plasmonic nanostructures and metamaterials. *Phys. Rev. B*, 83:235427, 2011. doi: 10.1103/PhysRevB.83.235427.

[224] Matthias Paur, Aday J. Molina-Mendoza, Rudolf Bratschitsch, Kenji Watanabe, Takashi Taniguchi, and Thomas Mueller. Electroluminescence from multi-particle exciton complexes in transition metal dichalcogenide semiconductors. *Nat. Commun.*, 10:1709, 2019. doi: 10.1038/s41467-019-09781-y.

[225] Neil R. Wilson, Paul V. Nguyen, Kyle Seyler, Pasqual Rivera, Alexander J. Marsden, Zachary P. L. Laker, Gabriel C. Constantinescu, Viktor Kandyba, Alexei Barinov, Nicholas D. M. Hine, Xiaodong Xu, and David H. Cobden. Determination of band offsets, hybridization, and exciton binding in 2D semiconductor heterostructures. *Sci. Adv.*, 3: e1601832, 2017. doi: 10.1126/sciadv.1601832.

[226] Shuwen Zheng, Hai Wang, Lei Wang, and Hai-Yu Wang. Dexter-type exciton transfer in van der waals heterostructures. *Adv. Funct. Mater.*, 32:2201123, 2022. doi: 10.1002/adfm.202201123.

[227] Jinwei Shi, Meng-Hsien Lin, I-Tung Chen, Nasim Mohammadi Estakhri, Xin-Quan Zhang, Yanrong Wang, Hung-Ying Chen, Chun-An Chen, Chih-Kang Shih, Andrea Alù, Xiaoqin Li, Yi-Hsien Lee, and Shangjr Gwo. Cascaded exciton energy transfer in a monolayer semiconductor lateral heterostructure assisted by surface plasmon polariton. *Nat. Commun.*, 8: 35, 2017. doi: 10.1038/s41467-017-00048-y.

[228] Lutz Waldecker, Archana Raja, Malte Rösner, Christina Steinke, Aaron Bostwick, Roland J. Koch, Chris Jozwiak, Takashi Taniguchi, Kenji Watanabe, Eli Rotenberg, Tim O. Wehling, and Tony F. Heinz. Rigid band shifts in two-dimensional semiconductors through external dielectric screening. *Phys. Rev. Lett.*, 123:206403, 2019. doi: 10.1103/PhysRevLett.123.206403.

[229] Julian Sickel, Marcel Asbach, Christoph Gammer, Rudolf Bratschitsch, and Helmut Kohl. Quantitative strain and topography mapping of 2D materials using nanobeam electron diffraction. *Microsc. Microanal.*, 28:701–715, 2022. doi: 10.1017/S1431927622000502.

[230] Chenhao Jin, Emma C. Regan, Aiming Yan, M. Iqbal Bakti Utama, Danqing Wang, Sihan Zhao, Ying Qin, Sijie Yang, Zhiren Zheng, Shenyang Shi, Kenji Watanabe, Takashi

Taniguchi, Sefaattin Tongay, Alex Zettl, and Feng Wang. Observation of moiré excitons in WSe_2/WS_2 heterostructure superlattices. *Nature*, 567:76–80, 2019. doi: 10.1038/s41586-019-0976-y.

[231] Kha Tran, Galan Moody, Fengcheng Wu, Xiaobo Lu, Junho Choi, Kyounghwan Kim, Amritesh Rai, Daniel A. Sanchez, Jiamin Quan, Akshay Singh, Jacob Embley, André Zepeda, Marshall Campbell, Travis Autry, Takashi Taniguchi, Kenji Watanabe, Nanshu Lu, Sanjay K. Banerjee, Kevin L. Silverman, Suenne Kim, Emanuel Tutuc, Li Yang, Allan H. MacDonald, and Xiaoqin Li. Evidence for moiré excitons in van der waals heterostructures. *Nature*, 567:71–75, 2019. doi: 10.1038/s41586-019-0975-z.

[232] Emma C. Regan, Danqing Wang, Eunice Y. Paik, Yongxin Zeng, Long Zhang, Jihang Zhu, Allan H. MacDonald, Hui Deng, and Feng Wang. Emerging exciton physics in transition metal dichalcogenide heterobilayers. *Nat. Rev. Mater.*, 7:778–795, 2022. doi: 10.1038/s41578-022-00440-1.